

Flavour anomalies meet flavour symmetry

Innes Bigaran¹, Tobias Felkl², Claudia Hagedorn^{3,4}, Michael A. Schmidt²

¹ ARC Centre of Excellence for Dark Matter Particle Physics, School of Physics, The University of Melbourne, Victoria 3010, Australia

² Sydney Consortium for Particle Physics and Cosmology, School of Physics, The University of New South Wales, Sydney, NSW 2052, Australia

³ Instituto de Física Corpuscular, Universidad de Valencia and CSIC, Edificio Institutos Investigación, Catedrático José Beltrán 2, 46980 Paterna, Spain

⁴ Istituto Nazionale di Fisica Nucleare, Sezione di Padova, Via F. Marzolo 8, 35131 Padua, Italy

E-mail: `ibigaran@fnal.gov`, `t.felkl@unsw.edu.au`, `claudia.hagedorn@ific.uv.es`,
`m.schmidt@unsw.edu.au`

Abstract

We construct an extension of the Standard Model with a scalar leptoquark $\phi \sim (3, 1, -\frac{1}{3})$ and the discrete flavour symmetry $G_f = D_{17} \times Z_{17}$ to explain anomalies observed in charged-current semi-leptonic B meson decays and in the muon anomalous magnetic moment, together with the charged fermion masses and quark mixing. The symmetry Z_{17}^{diag} , contained in G_f , remains preserved by the leptoquark couplings, at leading order, and efficiently suppresses couplings of the leptoquark to the first generation of quarks and/or electrons, thus avoiding many stringent experimental bounds. The strongest constraints on the parameter space are imposed by the radiative charged lepton flavour violating decays $\tau \rightarrow \mu\gamma$ and $\mu \rightarrow e\gamma$. A detailed analytical and numerical study demonstrates the feasibility to simultaneously explain the data on the lepton flavour universality ratios $R(D)$ and $R(D^*)$ and the muon anomalous magnetic moment, while passing the experimental bounds from all other considered flavour observables.

Contents

1	Introduction	2
2	Setup of model	3
2.1	Choice of flavour symmetry and fermion assignment	4
2.2	Leptoquark couplings	4
2.3	Viable textures of leptoquark couplings	5
2.4	Flavour structure of Yukawa couplings	9
2.5	Summary of flavour symmetry, particle content and spurions	12
3	Mass matrices and leptoquark couplings	12
3.1	Quark sector	14
3.2	Charged lepton sector	19
3.3	Leptoquark couplings	21
4	Outline of phenomenological study	25
5	Primary observables: anomalies and constraints	27
5.1	Analytic estimates	28
5.2	Numerical study	36
6	Comprehensive study	48
6.1	Fit of charged fermion masses and quark mixing	48
6.2	Biases from primary scan	49
6.3	Conventions for plots presented in this section	50
6.4	Numerical results for primary observables	51
6.5	Analytic estimates for secondary observables	63
6.6	Numerical results for secondary observables	65
6.7	Comment on tertiary observables	68
7	Summary and outlook	69
A	Group theory of D_{17}	73
B	Relations between Lagrangian and effective parameters	74
C	Formulae for phenomenology	77
C.1	Correction to charged lepton masses	77
C.2	Leptonic processes	77
C.3	Semi-leptonic processes	80
C.4	Z decays to fermions	85
D	Supplementary information for section 5	86
E	Supplementary information for section 6	88
E.1	Details of method of comprehensive scan	88
E.2	Additional plots	88
E.3	Tertiary observables	89

1 Introduction

The Standard Model (SM) has been very successful in describing the gauge interactions involving SM fermions, the Higgs and gauge bosons. However, the observed values of fermion masses and mixing can only be accommodated with a judicious choice of free parameters, appearing in the Yukawa matrices, and cannot be predicted. In particular, the strong hierarchy among charged fermion masses, the potentially different type of mass spectrum in the neutrino sector, as well as the fact that only the Cabibbo angle is sizeable among quarks, while two of the mixing angles in the lepton sector are large, necessitate a profound explanation.

Given the success of symmetries in describing the gauge interactions of the SM particles, it is tempting to also employ a symmetry G_f , acting on the flavour (or generation) space, in order to explain the features of fermion masses and mixing. Abelian symmetries, such as a $U(1)$ group [1], have turned out to be sufficient in order to correctly accommodate the hierarchy among charged fermion masses by an appropriate choice of the $U(1)$ charges of the different generations of the species of SM fermions. However, fermion mixing, especially the striking difference between the mixing among quarks and leptons as well as the possibility to predict a certain mixing pattern (e.g. tri-bimaximal mixing among leptons [2–5]), points towards a non-abelian, discrete group as flavour symmetry which can be broken non-trivially. For reviews about the application of these groups in high energy particle physics, see references [6–9].

In recent years there have been several anomalous measurements in flavour physics which deviate from the SM predictions and hint at a non-trivial flavour structure. BaBar [10; 11], Belle [12–15] and LHCb [16–18] have measured the ratios¹

$$R(D^{(*)}) = \frac{\Gamma(B \rightarrow D^{(*)}\tau\nu)}{\Gamma(B \rightarrow D^{(*)}\ell\nu)} \quad (1)$$

with $\ell = e, \mu$ which are sensitive probes of lepton flavour universality (LFU). The result of the combined fit leads to larger values for $R(D)$ and $R(D^*)$ and exhibits a tension with the SM prediction at the 3.4σ level [19]. There is also a long-standing discrepancy between the measured value [20; 21] and the theoretical prediction [22–57] of the anomalous magnetic moment (AMM) of the muon, $a_\mu = (g - 2)_\mu/2$. The combined fit to the experimental data shows a 4.2σ tension [21] in $\Delta a_\mu = a_\mu^{\text{exp}} - a_\mu^{\text{SM}}$.² These three anomalies are summarised in table 1.

ANOMALIES					
Observable	SM prediction		Experiment		Significance
$R(D)$	0.297 ± 0.008	[62–64]	$0.340 \pm 0.027 \pm 0.013$	[19]	1.4σ
$R(D^*)$	0.245 ± 0.008	[62–64]	$0.295 \pm 0.010 \pm 0.010$	[19]	2.9σ
Δa_μ	0		$(2.51 \pm 0.59) \times 10^{-9}$	[21; 57]	4.2σ

Table 1: **Overview of the three anomalies to be addressed in this work and their present significance.** The experimental values for $R(D)$ and $R(D^*)$ are quoted from the Heavy Flavour Averaging Group (HFLAV) fit *circa* 2021, and the combined significance of these two anomalies is 3.4σ , with a correlation of $\rho = -0.38$ [19].

¹For brevity, we do not indicate antiparticles by overbars unless required for clarity.

²There is an ongoing debate about the theoretical prediction of the hadronic vacuum polarisation. While the current determination of the leading-order hadronic vacuum polarisation is obtained using dispersion relations, c.f. reference [57], recent lattice calculations [58–61] predict a value consistent with the experimental result of the AMM of the muon.

In reference [65] Bauer and Neubert have proposed a simultaneous explanation of the flavour anomalies in terms of the scalar leptoquark (LQ) ϕ transforming as $(3, 1, -\frac{1}{3})$ under the SM gauge group. The importance of LQ couplings to right-handed (RH) fermions has been emphasised in reference [66] and it has been demonstrated that the LQ ϕ cannot explain the discrepancies in $b \rightarrow s\mu\mu$ which requires the introduction of additional particles, see e.g. references [67–78]. In the vast majority of these studies only the couplings which are needed to explain the flavour anomalies are introduced, while all other couplings are set to zero without providing any explanation for the vanishing couplings nor for the size of the non-zero ones.

In this work, we construct a model with a discrete flavour symmetry to explain the observed flavour anomalies in $R(D)$, $R(D^*)$ and in the AMM of the muon. This model is also capable of correctly describing the strong hierarchy among charged fermion masses as well as the quark mixing, leaving aside neutrino masses and lepton mixing. Given this focus, the three generations of SM fermions are (mostly) assigned to a doublet and a singlet of G_f . For this reason, we choose a dihedral group as flavour symmetry. Both single-valued dihedral groups, D_n , as well as double-valued dihedral groups, D'_n , form series of groups that feature one- and two-dimensional irreducible representations in case the index n of the group D_n (D'_n) is at least $n = 3$ ($n = 2$), see e.g. references [79–82] for their application to fermion mixing. A thorough analysis shows that a model with the flavour group $G_f = D_{17} \times Z_{17}$ can pass all requirements, e.g. coming from the non-observation of charged lepton flavour violating (cLFV) decays such as $\tau \rightarrow \mu\gamma$. The residual symmetry Z_{17}^{diag} , the diagonal subgroup of G_f , which is preserved by the LQ couplings to the SM fermions, at leading order, is crucial in order to appropriately suppress those to the first generation of quarks and/or electrons. The breaking of the flavour symmetry is achieved with the help of four spurions that acquire a certain vacuum expectation value (VEV), given in terms of the expansion parameter λ , $\lambda \approx 0.22$, of the model. For related studies on the use of flavour symmetries to explain the anomalies observed in semi-leptonic B meson decays, see references [83–85].

The paper is organised as follows. In section 2 the model is introduced, the choice of G_f , its residual symmetry, and the particle assignment are explained as well as the spurions necessary in order to achieve viable textures for the LQ couplings and the charged fermion mass matrices are specified. The explicit form of the mass matrices and the LQ couplings in both the interaction basis and the charged fermion mass basis is derived in section 3. Analytical expressions for charged fermion masses and quark mixing are also given. Section 4 serves as introduction to the phenomenological study which includes the analytical estimates, the numerical scan of the primary observables in section 5 and the comprehensive numerical analysis of all observables in section 6. We summarise and give an outlook in section 7. Technical details and supplementary material are collected in appendices A to E.

2 Setup of model

In section 2.1, we first argue for the choice of the flavour symmetry to be a dihedral group, and establish assignments under this group for the three generations of different SM fermion species. We continue in section 2.2 with the introduction of the LQ and its relevant couplings. In section 2.3, we focus on particular textures of the LQ couplings and further specify the transformation properties of the fields of the model, as well as the employed flavour symmetry and its breaking. In section 2.4, we turn to the Yukawa sector and ensure that the observed charged fermion mass hierarchies and the Cabibbo-Kobayashi-Maskawa (CKM) mixing matrix are correctly generated. For convenience, in section 2.5, we summarise the choice of the flavour symmetry G_f , all fields and their transformation properties under G_f , as well as the employed spurions and their assumed VEVs.

2.1 Choice of flavour symmetry and fermion assignment

We choose a member of the series of dihedral groups D_n with $n \geq 3$ as candidate flavour symmetry, as these groups contain several inequivalent one- and two-dimensional irreducible representations. This permits two distinct assignments of the three generations of SM fermions: either $\mathbf{1} + \mathbf{1} + \mathbf{1}$ or $\mathbf{2} + \mathbf{1}$. Both assignments prove to be useful for our purposes.

For the charged fermions, we are motivated to use the assignment $\mathbf{2} + \mathbf{1}$ as much as possible, since the heaviest masses are associated with the third generation, and the mixing between the first (second) and third generations of quarks is small. The doublets and singlets used for the different fermion species, left-handed (LH) quark doublets Q_i , RH down-type quarks d_{Ri} , LH lepton doublets L_i and RH charged leptons e_{Ri} , are in general inequivalent.³ We, consequently, expect that the index n of the dihedral group should be at least $n = 9$ in order to offer a minimum of four inequivalent two-dimensional representations.

For the RH up-type quarks u_{Ri} , we choose to assign each generation to a singlet, $\mathbf{1} + \mathbf{1} + \mathbf{1}$, which may or may not be inequivalent.⁴ This can facilitate the accommodation of the very pronounced mass hierarchy among the up-type quarks. Such an assignment also simplifies the achievement of the desired texture of the LQ coupling to RH charged leptons e_{Ri} and up-type quarks u_{Ri} , \mathbf{y} , see eq. (9). Thus, we are able to partially unify the three generations of four of the five different SM fermion species.

We do not discuss neutrino masses nor lepton mixing in this work, which may otherwise hint at a different assignment of the three generations of LH leptons under the flavour symmetry.

Furthermore, we consider a Two Higgs Doublet Model (2HDM) of type-II [86; 87], in which one of the Higgs fields, H_u , is responsible for the masses of up-type quarks, while the other one, H_d , provides the masses of down-type quarks and charged leptons.⁵ This simplifies the search for and, at the same time, amplifies the choice of a suitable flavour symmetry, as we see below.

We can, thus, write the Lagrangian containing the Yukawa couplings of the charged fermions as follows

$$\mathcal{L}_{\text{Yuk}} = -Y_{ij}^u \overline{Q}_i H_u u_{Rj} - Y_{ij}^d \overline{Q}_i H_d d_{Rj} - Y_{ij}^e \overline{L}_i H_d e_{Rj} + \text{h.c.} \quad (2)$$

with the Yukawa coupling matrices Y^u , Y^d and Y^e being, in general, complex three-by-three matrices.

2.2 Leptoquark couplings

The main topic of this study is, however, *not* the correct description of charged fermion masses and quark mixing with the help of a flavour symmetry. Rather, it is exploring the possibilities of capturing the main features of a particular flavour structure of the couplings of the LQ, ϕ , to the SM fermions, which satisfactorily explains (some of) the present flavour anomalies, while also passing existing phenomenological constraints.

³The fields d_{Li} (u_{Li}) denote the LH down-type (up-type) quarks that are the lower (upper) component of the LH quark doublets Q_i . Similarly, the fields e_{Li} (ν_{Li}) are the LH charged leptons (neutrinos), being the lower (upper) component of the LH lepton doublets L_i .

⁴Whether or not all RH up-type quarks can be assigned to inequivalent one-dimensional representations of the dihedral group depends on whether the index n of the chosen group is even or odd, since in the case of even n the group has four inequivalent singlets, while D_n with n odd only comprises two inequivalent singlets [81]. One could also consider double-valued dihedral groups D'_n , n integer, which all provide four inequivalent one-dimensional representations [81].

⁵We assume the decoupling limit, in which the lightest Higgs is SM-like and the further scalars are decoupled. This can be achieved, e.g. in case one of the VEVs is induced [88]. The potential of the two Higgs doublets H_u and H_d is not discussed and might require adding further scalar fields and/or terms, softly breaking the imposed symmetries, in order to correctly achieve the VEVs of H_u and H_d , shown in eq. (15).

For this reason, we begin with the Lagrangian containing the two relevant LQ couplings, before electroweak symmetry breaking

$$\mathcal{L}_{\text{LQ}}^{\text{int}} = \hat{x}_{ij} \overline{L_i^c} \phi^\dagger Q_j + \hat{y}_{ij} \overline{e_{Ri}^c} \phi^\dagger u_{Rj} + \text{h.c.} , \quad (3)$$

where \hat{x}_{ij} and \hat{y}_{ij} are, in general, complex numbers. We define $\hat{\mathbf{x}}$ and $\hat{\mathbf{y}}$ as complex three-by-three matrices whose elements are denoted as \hat{x}_{ij} and \hat{y}_{ij} , respectively. The hatted notation $\hat{}$ is used to indicate that these LQ couplings are given in the interaction basis of the SM fermions.

The quantum numbers of ϕ^\dagger coincide with those of the scalar LQ conventionally denoted S_1 [89], i.e. under the SM gauge group, $\phi \sim (3, 1, -\frac{1}{3})$. In contrast to reference [89], we omit the possible coupling to RH neutrinos which are absent in this model, as well as diquark couplings, since the latter can induce proton decay if not appropriately constrained. Imposing baryon number conservation forbids such diquark couplings. Additionally, we neglect possible couplings between the LQ ϕ and the Higgs doublets H_u and H_d and assume that ϕ does not acquire a non-vanishing VEV. In this way, the LQ does not impact the potential of H_u and H_d .

In the following, we use the results of reference [66] to derive suitable textures of the LQ couplings as a starting point for this model. In order to match the convention of reference [66], we change to the charged fermion mass basis

$$\mathcal{L}_{\text{LQ}}^{\text{mass}} = x_{ij} \overline{(\nu_{Li}^m)^c} \phi^\dagger d_{Lj}^m + y_{ij} \overline{(e_{Ri}^m)^c} \phi^\dagger u_{Rj}^m - z_{ij} \overline{(e_{Li}^m)^c} \phi^\dagger u_{Lj}^m + \text{h.c.} . \quad (4)$$

The fields with the superscript m , u_{Li}^m , u_{Ri}^m , d_{Li}^m , d_{Ri}^m , e_{Li}^m , e_{Ri}^m and ν_{Li}^m , represent the SM fermion fields in the mass basis. These are related to the fields, u_{Li} , u_{Ri} , d_{Li} , d_{Ri} , e_{Li} , e_{Ri} and ν_{Li} , in the interaction basis as follows, formulated in matrix-vector notation,

$$u_L = L_u u_L^m , \quad u_R = R_u u_R^m , \quad d_L = L_d d_L^m , \quad d_R = R_d d_R^m , \quad (5)$$

$$e_L = L_e e_L^m , \quad e_R = R_e e_R^m \quad \text{and} \quad \nu_L = L_e \nu_L^m . \quad (6)$$

We reiterate that the basis change of LH neutrinos coincides with the one of LH charged leptons, since neutrinos are massless in this model and thus lepton mixing is unphysical. The couplings x_{ij} , y_{ij} and z_{ij} in eq. (4) are, in general, complex numbers, like \hat{x}_{ij} and \hat{y}_{ij} , and we define the LQ couplings \mathbf{x} , \mathbf{y} and \mathbf{z} as complex three-by-three matrices with elements x_{ij} , y_{ij} and z_{ij} , respectively. The two LQ couplings \mathbf{x} and \mathbf{z} in eq. (4) both stem from the LQ coupling $\hat{\mathbf{x}}$ in eq. (3) and are, consequently, related by the quark mixing matrix V_{CKM} .

2.3 Viable textures of leptoquark couplings

Possible textures of the LQ couplings \mathbf{x} and \mathbf{y} that permit an explanation of the flavour anomalies in $R(D)$, $R(D^*)$ and in the AMM of the muon have been proposed and studied in numerous publications. The study in reference [66] has performed two separate scans of these couplings, each assuming a slightly different texture for \mathbf{y} . We use the results of the scan in which the form of the LQ couplings \mathbf{x} and \mathbf{y} has been fixed to

$$\mathbf{x} = \begin{pmatrix} 0 & 0 & 0 \\ 0 & x_{22} & x_{23} \\ 0 & x_{32} & x_{33} \end{pmatrix} \quad \text{and} \quad \mathbf{y} = \begin{pmatrix} 0 & 0 & 0 \\ 0 & 0 & y_{23} \\ 0 & y_{32} & 0 \end{pmatrix} , \quad (7)$$

where, a priori, all non-vanishing entries of \mathbf{x} and y_{32} can be of order one (or even larger), while y_{23} is bounded as $|y_{23}| \leq 0.05$. A detailed analysis of the results of this scan shows that for $\hat{m}_\phi \lesssim 5$, where \hat{m}_ϕ measures the mass m_ϕ of the LQ ϕ in TeV, the textures of \mathbf{x} and \mathbf{y} can be expressed in terms of the expansion parameter λ

$$\lambda \approx 0.2 . \quad (8)$$

One viable set of textures is

$$\mathbf{x} \sim \begin{pmatrix} 0 & 0 & 0 \\ 0 & \lambda^3 & \lambda \\ 0 & \lambda^2 & 1 \end{pmatrix} \text{ and } \mathbf{y} \sim \begin{pmatrix} 0 & 0 & 0 \\ 0 & 0 & \lambda^3 \\ 0 & 1 & 0 \end{pmatrix}, \quad (9)$$

where each non-zero element is accompanied by a complex order-one number.⁶ In particular, $x_{33} \sim 1$ and $y_{32} \sim 1$ facilitate the explanation of the anomalies in $R(D)$ and $R(D^*)$, while $z_{23} y_{23} \sim x_{23} y_{23} \sim \lambda^4$ helps to achieve $\Delta a_\mu \sim 10^{-9}$. We concentrate on achieving these textures of \mathbf{x} and \mathbf{y} , with the zeros denoting elements (much) smaller than $\lambda^4 \sim 10^{-3}$.

These couplings are specified in the basis where the down-type quark mass matrix, M_d , and the charged lepton mass matrix, M_e , are (nearly) diagonal, whereas the up-type quark mass matrix, M_u , is the origin of the CKM mixing matrix. The unitary transformation associated with the RH up-type quarks is assumed to be (close to) the identity matrix in flavour space. Furthermore, all fermion masses are canonically ordered, so that no additional permutations of columns and/or rows of the mass matrices are necessary.

In order to proceed with the assignment of the particles to representations of the flavour symmetry, we first fix the transformation properties of the LQ ϕ . We choose it to be in the trivial singlet of the entire flavour symmetry G_f . The elements x_{33} and y_{32} are both of order one, and thus should be non-zero in the limit of an unbroken flavour symmetry. More generally, this should be true for all couplings, including the Yukawa couplings of the charged fermions of order one, e.g. the Yukawa coupling that gives rise to the top quark mass. Otherwise large flavour symmetry breaking effects would be needed, which are difficult to control. We discuss this issue, when addressing the charged fermion mass matrices in section 2.4.

To achieve $x_{33} \sim 1$ constrains us to assign the third generation of LH lepton doublets, L_3 , and of LH quark doublets, Q_3 , to complex conjugated representations of the flavour symmetry. Furthermore, $y_{32} \sim 1$ requires that the third generation of RH charged leptons, e_{R3} , and the second generation of RH up-type quarks, u_{R2} , also transform as complex conjugated representations. Note that they should be in complex conjugated representations given the form of the LQ couplings in eq. (3). However, as all representations of (single-valued) dihedral groups are real, complex conjugation refers to an external Z_N symmetry with $N > 2$, whose purpose becomes clear in the following. Indeed, we can fix, without loss of generality, $L_3 \sim \mathbf{1}_1$, $Q_3 \sim \mathbf{1}_1$, $e_{R3} \sim \mathbf{1}_1$, and $u_{R2} \sim \mathbf{1}_1$ under the dihedral group.

2.3.1 Flavour symmetry breaking in leptoquark couplings

The other non-zero elements of the LQ couplings \mathbf{x} and \mathbf{y} are achieved by breaking the flavour symmetry with some spurion, acquiring a suitably aligned VEV. The largest non-zero element of \mathbf{x} and \mathbf{y} that is not of order one is of order λ . This determines the size of the symmetry breaking parameter, at least for the LQ couplings. We follow a minimalistic approach by generating all elements, x_{22} , x_{23} , x_{32} and y_{23} , with the help of a single spurion, called S . Since these non-zero elements have different orders of magnitude in λ , we expect that $x_{ij}, y_{ij} \sim \lambda^k$ arise from the insertion of k powers of the spurion.⁷

The insertion of a single spurion S for $x_{23} \sim \lambda$ forces us to assign the spurion S to the same (real) two-dimensional representation of the dihedral group as the first two generations of LH

⁶We note that many phenomenological analyses take the elements of the LQ couplings \mathbf{x} and \mathbf{y} to be real for simplicity. We refrain from doing so, since we do not include a CP symmetry in this model.

⁷Since we work in a non-supersymmetric model, it can also be the conjugated spurion and/or some suitable combination of both.

lepton doublets, L . This two-dimensional representation can be chosen without loss of generality as $\mathbf{2}_1$ of the dihedral group. Clearly, the VEV of the spurion also needs to be aligned in a specific way in order to only generate the element $x_{23} \sim \lambda$, and not x_{13} at the same or similar level. We come back to this point in section 2.3.2.

Knowing that $x_{32} \sim \lambda^2$ and thus is due to two spurion insertions, we have to have the first two generations of LH quark doublets, Q , in a representation different from $\mathbf{2}_1$ and, indeed, a suitable choice is $\mathbf{2}_2$, since the product of $\mathbf{2}_1$ with itself contains as irreducible two-dimensional representation $\mathbf{2}_2$, see appendix A. Choosing $L \sim \mathbf{2}_1$, but $Q \sim \mathbf{2}_2$, also ensures that no large elements are generated among x_{11} , x_{12} , x_{21} and x_{22} .

At the level of three spurion insertions, S^3 , however, $x_{22} \sim \lambda^3$ can be generated, as desired, compare eq. (9). This is possible, since the product of $\mathbf{2}_1 \times \mathbf{2}_1 \times \mathbf{2}_1$ can contain the doublet $\mathbf{2}_3$.

Finally, we note that also y_{23} should be generated at order λ^3 . So, the combination of the first two generations of RH charged leptons, e_R , and of the RH up-type quark u_{R3} should transform as the same two-dimensional representation $\mathbf{2}_3$ (and possibly with an appropriate charge under an external Z_N symmetry). We arrive at the conclusion that e_R has to be in $\mathbf{2}_3$. We remind that it remains to be checked explicitly that only the element $y_{23} \sim \lambda^3$ is generated, and not y_{13} as well. Whether or not this happens, depends on the alignment of the VEV of the three spurion insertion and the relevant Clebsch-Gordan coefficients, see appendix A.

At the same time, we have to ensure that the elements y_{21} and y_{22} (and also y_{11} and y_{12}) are not generated at order λ^3 or larger. The best option in order to achieve this goal is to assign different charges under an external Z_N symmetry to the RH up-type quarks. This is in general also required in order to keep $y_{32} \sim 1$ and y_{31} and y_{33} (much) suppressed, since the dihedral group might not offer enough inequivalent one-dimensional representations to achieve this.

In summary, we are able to generate all non-zero elements of the LQ couplings \mathbf{x} and \mathbf{y} of their correct order in λ . Since we are in a non-supersymmetric context, also the conjugated spurion S^\dagger can couple. Indeed, this cannot be avoided by the dihedral group as part of the flavour symmetry, since it only provides real representations. This is one of the arguments for considering as flavour symmetry the direct product of a dihedral group D_n and an external Z_N symmetry with $N > 2$.

Due to the size of the symmetry breaking parameter, $\lambda \approx 0.2$, the spurion S might not be suitable for generating charged fermion masses. Since these follow a stronger hierarchy, this would not be possible unless we could achieve this by multiple insertions of the spurion. As we see in section 2.4, it is necessary to introduce three further spurions, T , U and W , with different transformation properties under the flavour symmetry and with different VEVs (in size and/or alignment), for correctly describing the charged fermion masses and quark mixing.

2.3.2 Protecting textures of leptoquark couplings with a residual symmetry

It is well-known that the zero elements in the first column and row of the LQ couplings \mathbf{x} and \mathbf{y} should be preserved to a high degree. As these couplings induce interactions involving the first generation of leptons and/or quarks, experimental bounds on them are particularly strong. In this model, we ensure such a suppression by a residual symmetry, i.e. the vanishing elements in \mathbf{x} and \mathbf{y} in eq. (7) are protected from becoming non-zero, so long as the residual symmetry is intact.

This residual symmetry is a subgroup of the flavour symmetry $D_n \times Z_N$ of the model. As residual symmetry, we use an abelian symmetry because a non-abelian one can easily become too constraining. A type of residual symmetry which has been successfully employed in approaches with flavour symmetries of the form $X \times Z_N$ is Z_N^{diag} . The symmetry Z_N^{diag} corresponds to the diagonal subgroup of a Z_N symmetry, contained in the non-abelian group X , and the external Z_N

symmetry [90; 91]. We, hence, choose $N = n$ in the following, i.e.

$$G_f = D_n \times Z_n \text{ with a single index } n. \quad (10)$$

Furthermore, we assume that the Z_n symmetry contained in D_n is generated by the generator a of D_n – see appendix A for the generators of the dihedral group D_{17} . Since the residual symmetry Z_n^{diag} should be preserved by the textures of the LQ couplings \mathbf{x} and \mathbf{y} , all non-vanishing elements of \mathbf{x} and \mathbf{y} in eq. (7) should correspond to combinations of SM fermions (and the LQ ϕ) with zero charge under Z_n^{diag} . At the same time, the spurion S should acquire a VEV that is compatible with the preservation of this residual symmetry.

We make the eventual choice⁸

$$n = 17. \quad (11)$$

It is straightforward to derive a set of charges under the external Z_{17} symmetry in order to ensure the preservation of the residual symmetry in the LQ coupling \mathbf{x} , given that we have already fixed that $L_3 \sim \mathbf{1}_1$, $Q_3 \sim \mathbf{1}_1$, $L \sim \mathbf{2}_1$, $Q \sim \mathbf{2}_2$, as well as $S \sim \mathbf{2}_1$.

Let us set the charge of L_3 under the external Z_{17} symmetry to 1.⁹ Then, we have to have that Q_3 carries the Z_{17} charge 16. Since L_3 and Q_3 are both singlets under D_{17} , their charge under the external Z_{17} symmetry coincides with their charge under the residual symmetry Z_{17}^{diag} . Furthermore, the fact that both x_{23} and x_{32} in the LQ coupling \mathbf{x} should be allowed as well, compare eq. (7), requires L_2 and Q_2 to transform in the same way under the residual symmetry Z_{17}^{diag} as L_3 and Q_3 , respectively. Knowing this, we can compute the charge of $L \sim \mathbf{2}_1$, whose second component is L_2 , under the external Z_{17} symmetry, and arrive at 2 as Z_{17} charge for L . Similarly, we have for $Q \sim \mathbf{2}_2$, whose second component is Q_2 , that its charge under the external Z_{17} symmetry is 1. Then, automatically also the element x_{22} in the LQ coupling \mathbf{x} is invariant under the residual symmetry Z_{17}^{diag} . Additionally, we can check that L_1 and Q_1 both have the charge 3 under the residual symmetry Z_{17}^{diag} and hence none of the elements of the first column and row of the LQ coupling \mathbf{x} is allowed in the limit of the residual symmetry Z_{17}^{diag} being preserved.

In order to couple the spurion S in an Z_{17} -invariant way to the combination $\overline{L^c} \phi^\dagger Q_3$ we have to assign the Z_{17} charge 16 to S . For $S \sim \mathbf{2}_1$ thus its first component S_1 carries no charge under the residual symmetry Z_{17}^{diag} . Consequently, this has to be the component which acquires a non-zero VEV, while the VEV of the other one, S_2 , has to vanish

$$\langle S \rangle = \begin{pmatrix} \lambda \\ 0 \end{pmatrix}. \quad (12)$$

By explicit computation one can check that the other two operators, $\overline{L_3^c} \phi^\dagger Q S^2$ as well as $\overline{L^c} \phi^\dagger Q S^3$, generating x_{32} and x_{22} of the appropriate size, are invariant as well.¹⁰

In order to protect the vanishing elements in the LQ coupling \mathbf{y} , we appeal to the residual symmetry Z_{17}^{diag} as well. To do so, we have to assign appropriate charges to the RH fermions u_{Ri} ,

⁸We do not comment further about this choice. However, we mention that we have studied different values of the index n of the dihedral group D_n with regard to the possibility to generate all operators needed for the LQ couplings \mathbf{x} and \mathbf{y} and for a valid description of charged fermion masses and quark mixing and, at the same time, not to give rise to other contributions to the LQ couplings and the charged fermion mass matrices which strongly perturb the leading-order results.

⁹Other choices are possible at this point. A valid choice is determined by the requirement that no contribution to the LQ couplings \mathbf{x} and \mathbf{y} nor to the charged fermion mass matrices, when including the spurions T , U and W beyond S as well as their conjugated fields, is generated which perturbs the leading-order structure of these and thus leads to unacceptably large flavour violation and/or wrong results for charged fermion masses and quark mixing. The presented set of charges under the external Z_{17} symmetry is such a valid choice.

¹⁰The spurions are treated as dimensionless flavour symmetry breaking fields. Thus, we do not need to introduce a cutoff scale in order to restore the correct mass dimension of the operators.

Field	Z_{17}^{diag}	Field	Z_{17}^{diag}	Field	Z_{17}^{diag}	Field	Z_{17}^{diag}	Field	Z_{17}^{diag}
Q_1	3	d_{R1}	5	e_{R1}	5	S_1	0	W_1	14
Q_2	16	d_{R2}	14	e_{R2}	16	S_2	15	W_2	10
Q_3	16	d_{R3}	7	e_{R3}	9	T_1	10		
u_{R1}	13	L_1	3	H_u	15	T_2	6		
u_{R2}	8	L_2	1	H_d	9	U_1	10		
u_{R3}	1	L_3	1	ϕ	0	U_2	6		

Table 2: **Charge under residual symmetry Z_{17}^{diag}** . We list the charge of the different fermions, scalar fields and spurions under the residual symmetry Z_{17}^{diag} , preserved by the leading-order structure of the LQ couplings \mathbf{x} and \mathbf{y} , see eq. (9). This residual symmetry Z_{17}^{diag} is the diagonal subgroup of the Z_{17} symmetry, contained in D_{17} and generated by the generator a , compare appendix A, and the external Z_{17} symmetry.

e_R and e_{R3} . Given that only two elements are non-zero in the limit of unbroken Z_{17}^{diag} , we can only fix a certain combination of Z_{17} charges. Therefore, the Z_{17} charges of the D_{17} singlets e_{R3} and u_{R2} should be opposite, e.g. for 9 being the Z_{17} charge of e_{R3} , that of u_{R2} should be 8. Also, the charges of e_{R2} , the second component of $e_R \sim \mathbf{2}_3$, and of the D_{17} singlet u_{R3} should be opposite under the residual symmetry. A possible choice is that e_{R2} has the Z_{17}^{diag} charge 16, since e_R has the charge 2 under the external Z_{17} symmetry and, thus, u_{R3} carries the Z_{17}^{diag} charge 1 – which also corresponds to its charge under the external Z_{17} symmetry.

With this Z_{17} charge assignment, we can check that apart from the elements y_{32} and y_{23} no other element of the second and third columns of the LQ coupling \mathbf{y} is invariant under the residual symmetry Z_{17}^{diag} . We can, furthermore, explicitly check that the operator $\bar{e}_R^c \phi^\dagger u_{R3} S^3$ is invariant under the external Z_{17} symmetry. In order to avoid letting any element of the first column of \mathbf{y} be invariant under Z_{17}^{diag} , we choose the charge of the D_{17} singlet u_{R1} under the external Z_{17} symmetry to be 13.

The presented choice of Z_{17} charge assignments also takes constraints into account from the requirement of a correct description of charged fermion masses and quark mixing. It, furthermore, suppresses flavour violation, in particular involving the first lepton and/or quark generation, by limiting the contributions to the LQ coupling \mathbf{y} from operators involving the other spurions T , U , W , and their conjugated fields.

In table 2, the chosen charges of the different fermions, scalar fields and spurions under the residual symmetry Z_{17}^{diag} have been collected.

2.4 Flavour structure of Yukawa couplings

In the next step, we turn to the construction of the charged fermion mass matrices and complete the assignment of the SM fermions under the flavour symmetry $G_f = D_{17} \times Z_{17}$ by also fixing the transformation properties of the RH down-type quarks. We introduce three further spurions, T , U and W , all transforming as doublets under D_{17} . These are responsible for the generation of the correct charged fermion mass hierarchy and the Cabibbo angle θ_C of the order of λ . By contrasting eqs. (16, 17, 18) with eq. (12), we note that the size of their VEVs is (significantly) smaller than that of the spurion S .

We recall that the LQ couplings \mathbf{x} and \mathbf{y} are given in the mass basis of charged leptons and down-type quarks. This means M_e and M_d should be (almost) diagonal, while the CKM mixing matrix should arise from the up-type quark mass matrix M_u , and the unitary transformation

relating the interaction and mass bases of the RH up-type quarks should be (close to) the identity matrix. The approximate form of the mass matrices M_e , M_d and M_u in terms of λ is therefore

$$M_e \sim \begin{pmatrix} \lambda^4 & 0 & 0 \\ 0 & \lambda^2 & 0 \\ 0 & 0 & 1 \end{pmatrix} \langle H_d^0 \rangle, \quad M_d \sim \begin{pmatrix} \lambda^4 & 0 & 0 \\ 0 & \lambda^2 & 0 \\ 0 & 0 & 1 \end{pmatrix} \langle H_d^0 \rangle, \quad (13)$$

$$\text{and} \quad M_u \sim \begin{pmatrix} \lambda^8 & \lambda^5 & \lesssim \lambda^3 \\ 0 & \lambda^4 & \lambda^2 \\ 0 & 0 & 1 \end{pmatrix} \langle H_u^0 \rangle. \quad (14)$$

In eqs. (13, 14) all non-vanishing elements are accompanied by complex order-one coefficients, and the vanishing elements imply that these entries are (strongly) suppressed.

As discussed in section 2.1, we work in a 2HDM: H_u gives masses to up-type quarks, and H_d to down-type quarks as well as charged leptons. Therefore, the hierarchy between the bottom quark (tau lepton) mass and the mass of the top quark can be generated via an appropriate hierarchy among the VEVs of the two Higgs doublets H_d and H_u . Typical values of these VEVs are

$$\langle H_d^0 \rangle = \frac{v_d}{\sqrt{2}} \sim 2.4 \text{ GeV} \quad \text{and} \quad \langle H_u^0 \rangle = \frac{v_u}{\sqrt{2}} \sim 174 \text{ GeV} \quad (15)$$

so that $v_d^2 + v_u^2 = v^2 \sim (246 \text{ GeV})^2$. Both Higgs doublets transform as trivial singlet $\mathbf{1}_1$ under D_{17} , but need to carry a non-trivial charge under the external Z_{17} symmetry to allow for the generation of the top quark and tau lepton mass at tree level.

2.4.1 Generation of down-type quark and charged lepton masses

The invariance of the operator $\overline{L}_3 H_d e_{R3}$ under the external Z_{17} symmetry requires that the charge of H_d is 9.¹¹ Since the size of the bottom quark mass is similar to that of the tau lepton, we also require that the operator $\overline{Q}_3 H_d d_{R3}$ is invariant. This fixes the transformation properties of d_{R3} to $d_{R3} \sim \mathbf{1}_1$ under D_{17} , and the charge of d_{R3} under the external Z_{17} symmetry to be 7.

In order to generate the mass of the muon and of the strange quark, we invoke a further spurion, T . One relevant operator is thus $\overline{L} H_d e_R T$, requiring that the spurion T carries the charge 8 under the external Z_{17} symmetry. We can determine the transformation properties of T under D_{17} to be $T \sim \mathbf{2}_2$ by noting that the second component of the covariant in $\mathbf{2}_2$ is $\overline{L}_2 H_d e_{R2}$. Furthermore, we know then also that the first component of T should acquire a non-zero VEV of order λ^2

$$\langle T \rangle = \begin{pmatrix} \lambda^2 \\ 0 \end{pmatrix}. \quad (16)$$

For details about the necessary Clebsch-Gordan coefficients, see appendix A. We can check that this VEV breaks the residual symmetry Z_{17}^{diag} , invoked to protect the form of the LQ couplings \mathbf{x} and \mathbf{y} . This is not unexpected, but indicates that couplings of this spurion to the LQ ϕ should be appropriately suppressed by the flavour symmetry $G_f = D_{17} \times Z_{17}$.

At the same time, the spurion T should generate the strange quark mass, i.e. the operator $\overline{Q} H_d d_R T$ should be invariant under G_f . For this to work, we have to fix the transformation properties of d_R accordingly. Its charge under the external Z_{17} symmetry should be 1, and $d_R \sim \mathbf{2}_4$ under D_{17} such that the second component of the covariant in $\mathbf{2}_2$ reads $\overline{Q}_2 H_d d_{R2}$. This completes the fixing of the transformation properties of the three generations of all SM fermion species.

¹¹We do not consider it an issue that the VEV of H_d (and also of H_u) spontaneously breaks the external Z_{17} symmetry because it is broken anyway (at a higher scale) by the VEVs of the spurions S , T , U and W .

The simplest way to generate the mass of the electron and of the down quark would be to modify the VEV of the spurion T so that its second component acquires a VEV of order λ^4 . We do not pursue this possibility and instead introduce a further spurion, U , which transforms in the same way under G_f as T , but acquires a VEV of the form

$$\langle U \rangle = \begin{pmatrix} 0 \\ \lambda^4 \end{pmatrix}. \quad (17)$$

Similar to the VEV of T , this VEV does not preserve the residual symmetry Z_{17}^{diag} , maintained in the LQ couplings \mathbf{x} and \mathbf{y} (at leading order). The two relevant operators for the mass of the electron and of the down quark are $\overline{L} H_d e_R U$ and $\overline{Q} H_d d_R U$, respectively.

The reason for employing the further spurion U is twofold. Firstly, it allows the undetermined order-one coefficients accompanying the aforementioned operators to be used to correctly achieve the masses of both the electron and the down quark. This would not be possible with only the spurion T . Secondly, in this way the computation of higher-order operators with several insertions of the spurions T and U is simplified, and their number can be controlled better.

This concludes the discussion of the generation of the charged lepton and the down-type quark mass matrices. In the end, both mass matrices are not exactly diagonal, since further operators are always induced.¹² We show in the next section that this neither poses a problem for the charged fermion mass matrices nor for achieving the textures of the LQ couplings \mathbf{x} and \mathbf{y} .

2.4.2 Generation of up-type quark masses and quark mixing matrix

The invariance of the operator $\overline{Q}_3 H_u u_{R3}$ under the external Z_{17} symmetry requires that the charge of H_u is 15. In the limit of unbroken flavour symmetry, the only up-type quark mass generated is the one of the top quark. In order to arrive at a non-zero mass for the charm quark, and to generate the Cabibbo angle of the correct order of magnitude, we introduce a last spurion, W . It should couple to $\overline{Q} H_u u_{R2}$ and, hence, W has to carry the charge 12 under the external Z_{17} symmetry and transform like Q under D_{17} , $W \sim \mathbf{2}_2$. Since the purpose of introducing W is to generate the charm quark mass as well as the Cabibbo angle, both its components should acquire a non-vanishing VEV

$$\langle W \rangle = \begin{pmatrix} \lambda^5 \\ \lambda^4 \end{pmatrix}. \quad (18)$$

Indeed, given the structure of the covariant $\overline{Q} H_u u_{R2}$, the lower component of the VEV of W generates the charm quark mass, while the upper one is responsible for the size of the Cabibbo angle, which is $\theta_C \approx \lambda$. As can be shown, the VEV of the spurion W also breaks the residual symmetry Z_{17}^{diag} . This completes the set of spurions we use in this model.

Two points still need to be addressed, namely the generation of the two smaller quark mixing angles and of the mass of the up quark. The former issue can be solved by noting that in this non-supersymmetric model also the conjugated spurions contribute to the charged fermion mass matrices and LQ couplings \mathbf{x} and \mathbf{y} . Indeed, one can check that with the assigned transformation properties the operator $\overline{Q} H_u u_{R3} (S^\dagger)^2$ leads to an element $M_{u,23}$ in the up-type quark mass matrix

¹²One example is the operator $\overline{L} H_d e_{R3} S^\dagger$. It is invariant because $\overline{L}_3 H_d e_{R3}$ is generated at tree level, L transforms as the same doublet of D_{17} as the spurion $S^{(\dagger)}$ and the piece $\overline{L}_2 H_d e_{R3}$ is like $\overline{L}_3 H_d e_{R3}$ invariant under the residual symmetry Z_{17}^{diag} which is also left unbroken by the VEV of the spurion $S^{(\dagger)}$. We, hence, already know that the element $M_{e,23}$ of the charged lepton mass matrix must arise at the order $\lambda \langle H_d^0 \rangle$ from the operator $\overline{L} H_d e_{R3} S^\dagger$.

which is of the order $\lambda^2 \langle H_u^0 \rangle$ and thus can correctly generate $\theta_{23} \sim \lambda^2$.¹³ At the same time, this induces $\theta_{13} \sim \lambda^3$, where the additional suppression factor λ arises from the Cabibbo angle.¹⁴

The correct order of the up quark mass arises from the operator $\bar{Q} H_u u_{R1} T^2 U$ which is automatically invariant under the flavour symmetry G_f and leads to the term $\bar{u}_{L1} \langle H_u^0 \rangle u_{R1} \lambda^8$, after flavour and electroweak symmetry breaking.

2.5 Summary of flavour symmetry, particle content and spurions

In this section, we briefly summarise the essential information about the model. The flavour symmetry is

$$G_f = D_{17} \times Z_{17} \quad (19)$$

and the particle content is given in table 3. The VEVs of the spurions are

$$\langle S \rangle = \begin{pmatrix} \lambda \\ 0 \end{pmatrix}, \quad \langle T \rangle = \begin{pmatrix} \lambda^2 \\ 0 \end{pmatrix}, \quad \langle U \rangle = \begin{pmatrix} 0 \\ \lambda^4 \end{pmatrix}, \quad \langle W \rangle = \begin{pmatrix} \lambda^5 \\ \lambda^4 \end{pmatrix}. \quad (20)$$

Since we do not address the potential of these spurions and thus also not how their VEVs can be correctly aligned, we also do not discuss possible perturbations of these VEVs and their potential impact on the results for charged fermion masses, quark mixing and the form of the LQ couplings \mathbf{x} and \mathbf{y} in terms of the symmetry breaking parameter λ .

3 Mass matrices and leptoquark couplings

In this section, we list the operators contributing to the charged fermion mass matrices M_u , M_d and M_e , and to the LQ couplings $\hat{\mathbf{x}}$ and $\hat{\mathbf{y}}$ from eq. (3). We do so for operators that contribute up to and including order λ^{12} in the symmetry breaking parameter, and assume that the VEVs of the spurions S , T , U and W are of the form given in eq. (20). Each operator is accompanied by a complex order-one coefficient. The lists of operators are usually ordered according to the number of spurion insertions. We further emphasise that the spurions are treated as dimensionless flavour symmetry breaking fields. Thus, no cutoff scale needs to be introduced to achieve the correct mass dimension of the operators.

In the lists, the operators stand for all possible combinations of the involved fields which lead to an invariant of the flavour symmetry G_f . Thus, they can correspond to more than one independent contribution to the charged fermion mass matrices M_u , M_d and M_e or the LQ couplings $\hat{\mathbf{x}}$ and $\hat{\mathbf{y}}$. We take this into account in the computation, and signal them by using primed coefficients in those instances, e.g. α_8^d , $(\alpha_8^d)'$ – see eq. (120) in appendix B.

¹³We note that also $\bar{Q} H_d d_{R3} (S^\dagger)^2$ is invariant, since the combinations $H_u u_{R3}$ and $H_d d_{R3}$ transform in the same way. This is due to the fact that both operators $\bar{Q}_3 H_u u_{R3}$ and $\bar{Q}_3 H_d d_{R3}$ are generated at tree level. As we show in the analysis of quark masses and mixing, this does not pose a problem. It is also not an obstacle for achieving the texture of the LQ coupling \mathbf{x} , as shown in eq. (9). From the viewpoint of the residual symmetry Z_{17}^{diag} , one can argue that not only the mass of the top and of the bottom quark are invariant under Z_{17}^{diag} , but also the elements $M_{u,23}$ and $M_{d,23}$ of the up-type and down-type quark mass matrix.

¹⁴This leads to issues with generating a large enough value for V_{td} and for the Jarlskog invariant J_{CP} [92] as well as to a too tight relation between the CKM mixing matrix elements V_{us} , V_{ub} and V_{cb} , as we comment in section 3.1.3. However, generating θ_{13} directly through an element $M_{u,13}$ of the up-type quark mass matrix of the order $\lambda^3 \langle H_u^0 \rangle$ would have as immediate consequence that also an element $M_{d,13}$ of the order $\lambda^3 \langle H_d^0 \rangle$ is produced in the down-type quark mass matrix, since the combination of fields $\bar{Q} H_u u_{R3}$ and $\bar{Q} H_d d_{R3}$ transforms in the same way. Such a large element in the down-type quark mass matrix leads, upon re-diagonalisation of the latter, to rather large elements in the first column of the LQ coupling \mathbf{x} . For this reason, we prefer to neither generate the element $M_{u,13}$ nor $M_{d,13}$ through operators, respecting all symmetries of the model.

Field	SU(3)	SU(2)	U(1)	D_{17}	Z_{17}
$Q = \begin{pmatrix} Q_1 \\ Q_2 \end{pmatrix}$	3	2	$\frac{1}{6}$	$\mathbf{2}_2$	1
Q_3	3	2	$\frac{1}{6}$	$\mathbf{1}_1$	16
u_{R1}	3	1	$\frac{2}{3}$	$\mathbf{1}_2$	13
u_{R2}	3	1	$\frac{2}{3}$	$\mathbf{1}_1$	8
u_{R3}	3	1	$\frac{2}{3}$	$\mathbf{1}_1$	1
$d_R = \begin{pmatrix} d_{R1} \\ d_{R2} \end{pmatrix}$	3	1	$-\frac{1}{3}$	$\mathbf{2}_4$	1
d_{R3}	3	1	$-\frac{1}{3}$	$\mathbf{1}_1$	7
$L = \begin{pmatrix} L_1 \\ L_2 \end{pmatrix}$	1	2	$-\frac{1}{2}$	$\mathbf{2}_1$	2
L_3	1	2	$-\frac{1}{2}$	$\mathbf{1}_1$	1
$e_R = \begin{pmatrix} e_{R1} \\ e_{R2} \end{pmatrix}$	1	1	-1	$\mathbf{2}_3$	2
e_{R3}	1	1	-1	$\mathbf{1}_1$	9
H_u	1	2	$-\frac{1}{2}$	$\mathbf{1}_1$	15
H_d	1	2	$\frac{1}{2}$	$\mathbf{1}_1$	9
ϕ	3	1	$-\frac{1}{3}$	$\mathbf{1}_1$	0
$S = \begin{pmatrix} S_1 \\ S_2 \end{pmatrix}$	1	1	0	$\mathbf{2}_1$	16
$T = \begin{pmatrix} T_1 \\ T_2 \end{pmatrix}$	1	1	0	$\mathbf{2}_2$	8
$U = \begin{pmatrix} U_1 \\ U_2 \end{pmatrix}$	1	1	0	$\mathbf{2}_2$	8
$W = \begin{pmatrix} W_1 \\ W_2 \end{pmatrix}$	1	1	0	$\mathbf{2}_2$	12

Table 3: **Particle content of the model.** The fermions, scalar fields and spurions (flavour symmetry breaking fields) and their transformation properties under the SM gauge group $SU(3) \times SU(2) \times U(1)$ as well as the flavour symmetry $G_f = D_{17} \times Z_{17}$ are given. Particles in a two-dimensional irreducible representation of D_{17} are evidenced as two-component vector.

We generally omit all operators with insertions of powers of SS^\dagger , TT^\dagger , UU^\dagger and WW^\dagger , and products thereof. Typically, these duplicate the contribution from the operator without this insertion, but have at least an additional suppression of order λ^2 , λ^4 and $\lesssim \lambda^8$, respectively. There

are two exceptions to this rule: *a*) the subleading-order (in λ , SLO) contribution to the elements $M_{u,12}$ and $M_{u,22}$ of the up-type quark mass matrix involving $S S^\dagger$, and *b*) operators involving the insertion $W W^\dagger$. For exception *a*), the elements $M_{u,12}$ and $M_{u,22}$ carry the same parameter dependence at leading order (in λ , LO), generated by the second operator in eq. (21), but they receive partially different SLO corrections at relative order λ^2 from the first and second operators in eq. (22), seen explicitly in eq. (119) in appendix B. For exception *b*), $W W^\dagger$ also contains a covariant in $\mathbf{2}_4$ with a non-vanishing VEV, so some operators with this insertion can lead to non-redundant contributions – although they are always suppressed by at least λ^8 with respect to contributions from operators without this insertion.

After listing the operators, we present the form of the charged fermion mass matrices M_u , M_d and M_e , analytic formulae for charged fermion masses, and the unitary matrices for LH and RH fermions, needed in order to arrive at the charged fermion mass basis. The latter are necessary to compute the LQ couplings \mathbf{x} and \mathbf{y} in eq. (4) from $\hat{\mathbf{x}}$ and $\hat{\mathbf{y}}$, respectively, in eq. (3). We also explicitly detail the form of the LQ coupling \mathbf{z} , appearing in eq. (4).

All matrices, M_u , M_d , M_e , $\hat{\mathbf{x}}$, $\hat{\mathbf{y}}$, \mathbf{x} , \mathbf{y} and \mathbf{z} , are given in an effective parametrisation, where the parameters are related to the coefficients of the contributing operators. For completeness, these relations can be found in appendix B. For the analytic computations in this section we assume all parameters to be real, but note that they are taken to be complex-valued in subsequent phenomenological studies.

When computing the CKM mixing matrix V_{CKM} , we find analytically and numerically that this model (as outlined so far) cannot be in full agreement with experimental data. Specifically, we find that a large enough value for V_{td} and for the Jarlskog invariant J_{CP} , as well as a correct value of V_{ub} (with V_{us} and V_{cb} already fixed) cannot be produced. We comment on this in section 3.1, and point out how this issue can be solved with a slight change in the form of the up-type quark mass matrix M_u , i.e. by enhancing the element $M_{u,13}$ to be of the order $\lambda^3 \langle H_u^0 \rangle$. We call the results obtained in this model *without* modification of M_u ‘scenario A’, and those *with* the modification of M_u ‘scenario B’. The form of the LQ couplings \mathbf{x} , \mathbf{y} and \mathbf{z} is computed in both scenarios.

The quark sector is discussed in section 3.1, while the charged lepton sector is addressed in section 3.2. Section 3.3 is dedicated to the LQ couplings.

3.1 Quark sector

Here we discuss the results for the up-type quark mass matrix M_u and the down-type quark mass matrix M_d . We then move on to address the CKM mixing matrix in the aforementioned scenarios A and B.

3.1.1 Up quark sector

In the up quark sector, we consider four operators at LO that generate the up-type quark masses and the three quark mixing angles. These four operators read

$$\mathcal{L}_{\text{Yuk,LO}}^u = \alpha_1^u \overline{Q}_3 H_u u_{R3} + \alpha_2^u \overline{Q} H_u u_{R2} W + \alpha_3^u \overline{Q} H_u u_{R3} (S^\dagger)^2 + \alpha_4^u \overline{Q} H_u u_{R1} T^2 U. \quad (21)$$

At SLO, the following operators give contributions up to and including λ^{12} to the up-type quark mass matrix

$$\begin{aligned} \mathcal{L}_{\text{Yuk,SLO}}^u &= \alpha_5^u \overline{Q} H_u u_{R2} S S^\dagger W + \alpha_6^u \overline{Q} H_u u_{R2} (S^\dagger)^4 T + \alpha_7^u \overline{Q}_3 H_u u_{R2} (S^\dagger)^2 T \\ &+ \alpha_8^u \overline{Q}_3 H_u u_{R2} (W^\dagger)^2 + \alpha_9^u \overline{Q} H_u u_{R2} W^2 W^\dagger + \alpha_{10}^u \overline{Q} H_u u_{R1} T U^2 \\ &+ \alpha_{11}^u \overline{Q}_3 H_u u_{R2} S^2 W + \alpha_{12}^u \overline{Q} H_u u_{R2} T^\dagger U W + \alpha_{13}^u \overline{Q} H_u u_{R2} T U^\dagger W \end{aligned} \quad (22)$$

$$\begin{aligned}
& + \alpha_{14}^u \bar{Q} H_u u_{R3} T^\dagger (W^\dagger)^2 + \alpha_{15}^u \bar{Q} H_u u_{R3} (S^\dagger)^2 T U^\dagger + \alpha_{16}^u \bar{Q} H_u u_{R3} S^2 T^\dagger W \\
& + \alpha_{17}^u \bar{Q} H_u u_{R3} S^2 U^\dagger W + \alpha_{18}^u \bar{Q} H_u u_{R2} S^2 T^\dagger W^\dagger + \alpha_{19}^u \bar{Q} H_u u_{R2} S^2 U^\dagger W^\dagger \\
& + \alpha_{20}^u \bar{Q} H_u u_{R2} (S^\dagger)^2 (W^\dagger)^2 + \alpha_{21}^u \bar{Q} H_u u_{R3} (S^\dagger)^2 W W^\dagger \\
& + \alpha_{22}^u \bar{Q}_3 H_u u_{R1} S^2 T U^2 + \alpha_{23}^u \bar{Q}_3 H_u u_{R1} (S^\dagger)^4 (U^\dagger)^2 \\
& + \alpha_{24}^u \bar{Q}_3 H_u u_{R3} S^4 T^\dagger W + \alpha_{25}^u \bar{Q}_3 H_u u_{R3} (S^\dagger)^4 T W^\dagger \\
& + \alpha_{26}^u \bar{Q}_3 H_u u_{R2} S^4 T^\dagger W^\dagger + \alpha_{27}^u \bar{Q} H_u u_{R2} (S^\dagger)^4 T^2 U^\dagger \\
& + \alpha_{28}^u \bar{Q} H_u u_{R3} S^4 (T^\dagger)^2 W^\dagger + \alpha_{29}^u \bar{Q} H_u u_{R2} S^6 (T^\dagger)^2 \\
& + \alpha_{30}^u \bar{Q} H_u u_{R3} (S^\dagger)^6 T W^\dagger .
\end{aligned}$$

Of the operators in eq. (22), the first two are the most important, since they contribute at relative order λ^2 to the elements $M_{u,12}$ and $M_{u,22}$. The operators with the coefficients α_6^u and α_7^u are examples of operators that appear automatically once the field content of the LO operators is determined. We note that several of these operators lead to two independent contributions to the up-type quark mass matrix M_u . The operator with the coefficient α_5^u induces contributions of order λ^6 to the element $M_{u,22}$ and of λ^7 to the element $M_{u,12}$, but with a different relative sign; the one with α_{14}^u gives contributions of order λ^{10} and λ^{11} ; the one with α_{16}^u yields contributions of order λ^8 and λ^9 ; the one with α_{18}^u leads to contributions of order λ^8 and λ^9 ; finally, the operator with the coefficient α_{20}^u gives rise to two independent contributions of order λ^{10} and λ^{11} , respectively.

The up-type quark mass matrix can thus be effectively parametrised, up to and including order λ^{12} , as

$$M_u = \begin{pmatrix} f_{11} \lambda^8 & f_{12} \lambda^5 & f_{13} \lambda^8 \\ f_{21} \lambda^{10} & f_{22} \lambda^4 & f_{23} \lambda^2 \\ f_{31} \lambda^{12} & f_{32} \lambda^4 & f_{33} \end{pmatrix} \langle H_u^0 \rangle , \quad (23)$$

where f_{ij} are generally independent, complex order-one numbers, apart from f_{12} and f_{22} . The latter fulfil the relation

$$f_{12} - f_{22} \sim c \lambda^2 \quad (24)$$

with c being complex.¹⁵ As mentioned above, the first two operators in eq. (22), with the coefficients α_5^u and α_6^u , are the source of this difference – see also eq. (119) in appendix B. The expressions for the other parameters f_{ij} in terms of the coefficients α_i^u are given in eq. (119) in appendix B as well.

From the effective parametrisation of M_u , we can derive expressions for the up-type quark masses. Note that in order to clearly show these results here (and in the following), we only explicitly mention the most relevant terms. Thus, the quark masses can be expressed as

$$\begin{aligned}
m_u & = |f_{11} \lambda^8 + \mathcal{O}(\lambda^{10})| \langle H_u^0 \rangle , \\
m_c & = \left| f_{22} \lambda^4 + \left(\frac{f_{12}^2}{2 f_{22}} - \frac{f_{23} f_{32}}{f_{33}} \right) \lambda^6 + \mathcal{O}(\lambda^8) \right| \langle H_u^0 \rangle , \\
m_t & = \left| f_{33} + \frac{f_{23}^2}{2 f_{33}} \lambda^4 + \mathcal{O}(\lambda^8) \right| \langle H_u^0 \rangle .
\end{aligned} \quad (25)$$

We confirm that the dominant contributions to the three different masses come from the first, second and fourth operator in eq. (21), as expected from the construction of the model. The matrices L_u and R_u transforming LH and RH up-type quarks from the interaction to the mass

¹⁵In order to reflect this relation better in the effective parametrisation of M_u , one can express the element $M_{u,12}$ as $(f_{22} + \hat{f}_{12} \lambda^2) \lambda^5 \langle H_u^0 \rangle$ instead, where \hat{f}_{12} is a complex order-one number.

basis read, up to and including order λ^{12} ,

$$L_u = \begin{pmatrix} 1 - \frac{f_{12}^2}{2f_{22}^2} \lambda^2 + \mathcal{O}(\lambda^4) & \frac{f_{12}}{f_{22}} \lambda + \mathcal{O}(\lambda^3) & \frac{f_{13}}{f_{33}} \lambda^8 + \mathcal{O}(\lambda^9) \\ -\frac{f_{12}}{f_{22}} \lambda + \mathcal{O}(\lambda^3) & 1 - \frac{f_{12}^2}{2f_{22}^2} \lambda^2 + \mathcal{O}(\lambda^4) & \frac{f_{23}}{f_{33}} \lambda^2 + \mathcal{O}(\lambda^6) \\ \frac{f_{12}f_{23}}{f_{22}f_{33}} \lambda^3 + \mathcal{O}(\lambda^5) & -\frac{f_{23}}{f_{33}} \lambda^2 + \mathcal{O}(\lambda^4) & 1 - \frac{f_{23}^2}{2f_{33}^2} \lambda^4 + \mathcal{O}(\lambda^8) \end{pmatrix} \quad (26)$$

and

$$R_u = \begin{pmatrix} 1 + \mathcal{O}(\lambda^{10}) & \frac{f_{11}f_{12}}{f_{22}^2} \lambda^5 + \mathcal{O}(\lambda^6) & \frac{f_{21}f_{23}+f_{31}f_{33}}{f_{33}^2} \lambda^{12} + \mathcal{O}(\lambda^{12}) \\ -\frac{f_{11}f_{12}}{f_{22}^2} \lambda^5 + \mathcal{O}(\lambda^6) & 1 + \mathcal{O}(\lambda^8) & \frac{f_{32}}{f_{33}} \lambda^4 + \mathcal{O}(\lambda^6) \\ \frac{f_{11}f_{12}f_{32}}{f_{22}^2f_{33}} \lambda^9 + \mathcal{O}(\lambda^{10}) & -\frac{f_{32}}{f_{33}} \lambda^4 + \mathcal{O}(\lambda^6) & 1 + \mathcal{O}(\lambda^8) \end{pmatrix}. \quad (27)$$

We note that L_u is the primary source of the CKM mixing matrix, whereas the matrix R_u should be close to the identity matrix – in accordance with the basis in which the textures of the LQ couplings \mathbf{x} and \mathbf{y} are given in eq. (9). The obtained forms of L_u and R_u fulfil these requirements to a good degree.

The largest deviation of R_u from the identity matrix is of order λ^4 , due to the operator with the coefficient α_7^u that appears automatically. As can be seen below, this deviation in R_u is partly responsible for the generation of the element y_{33} of the LQ coupling $\hat{\mathbf{y}}$ in the charged fermion mass basis of order λ^4 – compare eq. (58) and eq. (126) in appendix B. Furthermore, $R_{u,21} \sim \lambda^5$ together with $\hat{y}_{32} \sim 1$, see eq. (53), has particular relevance for the texture of the same LQ coupling \mathbf{y} , leading to $y_{31} \sim \lambda^5$, see eq. (58) and eq. (126) in appendix B.

Introducing scenario B

One can already infer from the form of the matrix L_u in eq. (26) that the CKM mixing matrix element V_{td} as well as the Jarlskog invariant, J_{CP} , are likely to be very suppressed. This suppression originates from the entry $L_{u,13}$, which is only of order λ^8 . Furthermore, the tight relation between the elements $L_{u,21}$, $L_{u,31}$ and $L_{u,32}$ leads to a too-strong correlation between V_{us} , V_{ub} and V_{cb} . These points are discussed further in section 3.1.3.

A simple way to resolve these issues is to enhance the element $M_{u,13}$ in the up-type quark mass matrix M_u , namely

$$M_u = \begin{pmatrix} f_{11} \lambda^8 & f_{12} \lambda^5 & \tilde{f}_{13} \lambda^3 \\ f_{21} \lambda^{10} & f_{22} \lambda^4 & f_{23} \lambda^2 \\ f_{31} \lambda^{12} & f_{32} \lambda^4 & f_{33} \end{pmatrix} \langle H_u^0 \rangle \quad (28)$$

with \tilde{f}_{13} being a complex order-one number. Adding *ad hoc* a further contribution to the element $M_{u,13}$ is not explained by an appropriate operator in the context of this model. From the arguments given in footnote 14, it is, however, likely that such a contribution can only be generated by either an operator which explicitly breaks the flavour symmetry G_f or by changing at least part of the fermion assignment and/or G_f .

The up-type quark masses are mostly unaffected by this change, except that the SLO term in the top quark mass, see eq. (25), is slightly enhanced and of order λ^6 . The matrices L_u and R_u read

$$L_u = \begin{pmatrix} 1 - \frac{f_{12}^2}{2f_{22}^2} \lambda^2 + \mathcal{O}(\lambda^4) & \frac{f_{12}}{f_{22}} \lambda + \mathcal{O}(\lambda^3) & \frac{\tilde{f}_{13}}{f_{33}} \lambda^3 + \mathcal{O}(\lambda^7) \\ -\frac{f_{12}}{f_{22}} \lambda + \mathcal{O}(\lambda^3) & 1 - \frac{f_{12}^2}{2f_{22}^2} \lambda^2 + \mathcal{O}(\lambda^4) & \frac{f_{23}}{f_{33}} \lambda^2 + \mathcal{O}(\lambda^6) \\ \left(\frac{f_{12}f_{23}}{f_{22}f_{33}} - \frac{\tilde{f}_{13}}{f_{33}} \right) \lambda^3 + \mathcal{O}(\lambda^5) & -\frac{f_{23}}{f_{33}} \lambda^2 + \mathcal{O}(\lambda^4) & 1 - \frac{f_{23}^2}{2f_{33}^2} \lambda^4 + \mathcal{O}(\lambda^6) \end{pmatrix} \quad (29)$$

and

$$R_u = \begin{pmatrix} 1 + \mathcal{O}(\lambda^{10}) & \frac{f_{11}f_{12}}{f_{22}^2} \lambda^5 + \mathcal{O}(\lambda^6) & \frac{f_{11}\tilde{f}_{13}}{f_{33}^2} \lambda^{11} + \mathcal{O}(\lambda^{12}) \\ -\frac{f_{11}f_{12}}{f_{22}^2} \lambda^5 + \mathcal{O}(\lambda^6) & 1 + \mathcal{O}(\lambda^8) & \frac{f_{32}}{f_{33}} \lambda^4 + \mathcal{O}(\lambda^6) \\ \frac{f_{11}f_{12}f_{32}}{f_{22}^2f_{33}} \lambda^9 + \mathcal{O}(\lambda^{10}) & -\frac{f_{32}}{f_{33}} \lambda^4 + \mathcal{O}(\lambda^6) & 1 + \mathcal{O}(\lambda^8) \end{pmatrix}. \quad (30)$$

As expected, the element $L_{u,13}$ in the matrix L_u is now of order λ^3 and the tight relation between the elements $L_{u,21}$, $L_{u,31}$ and $L_{u,32}$ is relaxed. In this way, all mentioned short-comings of the resulting CKM mixing matrix are remedied – see further discussion in section 3.1.3. The matrix R_u is very mildly affected by this change in M_u , since only the element $R_{u,13}$ is enhanced to order λ^{11} .

3.1.2 Down quark sector

At LO there are three operators responsible for the generation of the down-type quark masses: one arising at tree level, and the other two requiring the insertion of one spurion, T or U . Thus, we have

$$\mathcal{L}_{\text{Yuk,LO}}^d = \alpha_1^d \overline{Q}_3 H_d d_{R3} + \alpha_2^d \overline{Q} H_d d_R T + \alpha_3^d \overline{Q} H_d d_R U. \quad (31)$$

At SLO, we find several more operators

$$\begin{aligned} \mathcal{L}_{\text{Yuk,SLO}}^d &= \alpha_4^d \overline{Q} H_d d_{R3} (S^\dagger)^2 + \alpha_5^d \overline{Q}_3 H_d d_R S^2 T + \alpha_6^d \overline{Q} H_d d_R T^\dagger U^2 \\ &+ \alpha_7^d \overline{Q} H_d d_R T^2 U^\dagger + \alpha_8^d \overline{Q} H_d d_{R3} T^\dagger (W^\dagger)^2 + \alpha_9^d \overline{Q} H_d d_R T W W^\dagger \\ &+ \alpha_{10}^d \overline{Q} H_d d_{R3} (S^\dagger)^2 T U^\dagger + \alpha_{11}^d \overline{Q} H_d d_{R3} S^2 T^\dagger W + \alpha_{12}^d \overline{Q} H_d d_{R3} S^2 U^\dagger W \\ &+ \alpha_{13}^d \overline{Q} H_d d_R S^2 (W^\dagger)^2 + \alpha_{14}^d \overline{Q} H_d d_{R3} (S^\dagger)^2 W W^\dagger + \alpha_{15}^d \overline{Q}_3 H_d d_R S^2 T^\dagger U^2 \\ &+ \alpha_{16}^d \overline{Q} H_d d_R S^4 W + \alpha_{17}^d \overline{Q}_3 H_d d_R (S^\dagger)^2 T^2 W^\dagger + \alpha_{18}^d \overline{Q}_3 H_d d_{R3} S^4 T^\dagger W \\ &+ \alpha_{19}^d \overline{Q}_3 H_d d_{R3} (S^\dagger)^4 T W^\dagger + \alpha_{20}^d \overline{Q}_3 H_d d_R S^6 W + \alpha_{21}^d \overline{Q} H_d d_R (S^\dagger)^4 T^2 W^\dagger \\ &+ \alpha_{22}^d \overline{Q} H_d d_{R3} S^4 (T^\dagger)^2 W^\dagger + \alpha_{23}^d \overline{Q} H_d d_{R3} (S^\dagger)^6 T W^\dagger \\ &+ \alpha_{24}^d \overline{Q} H_d d_R S^6 T^\dagger W^\dagger + \alpha_{25}^d \overline{Q} H_d d_R (S^\dagger)^7 (T^\dagger)^2. \end{aligned} \quad (32)$$

The first operator in eq. (32) has been discussed already, since it is automatically present once the corresponding operator in the up quark sector is considered. Similarly, the existence of the second operator in this list (with the coefficient α_5^d) is automatic, once we have accounted for the LO operators generating the dominant structures in the charged fermion mass matrices and in the LQ couplings $\hat{\mathbf{x}}$ and $\hat{\mathbf{y}}$.

We note that the operators with the following coefficients lead to more than one independent contraction, and hence contribution, to the down-type quark mass matrix. The operator with α_8^d leads to two independent contributions of order λ^{10} and λ^{11} ; the one with α_9^d yields two contributions, both of order λ^{11} ; the operator with α_{11}^d gives two contributions of order λ^8 and λ^9 ; the one with α_{13}^d leads to three contributions of order λ^{10} , λ^{11} and λ^{12} ; finally, the operator with the coefficient α_{16}^d leads to two contributions of order λ^8 and λ^9 .

The effective parametrisation of the down-type quark mass matrix, including all contributions up to and including order λ^{12} , therefore reads

$$M_d = \begin{pmatrix} d_{11} \lambda^4 & d_{12} \lambda^8 & d_{13} \lambda^8 \\ d_{21} \lambda^{10} & d_{22} \lambda^2 & d_{23} \lambda^2 \\ d_{31} \lambda^{12} & d_{32} \lambda^4 & d_{33} \end{pmatrix} \langle H_d^0 \rangle \quad (33)$$

with d_{ij} being, in general, independent complex order-one numbers, related to the coefficients α_i^d as shown in eq. (120) in appendix B. Furthermore, we arrive at the down-type quark masses

$$\begin{aligned} m_d &= |d_{11} \lambda^4 + \mathcal{O}(\lambda^{12})| \langle H_d^0 \rangle, \\ m_s &= \left| d_{22} \lambda^2 - \frac{d_{23}(d_{22}d_{23} + 2d_{32}d_{33})}{2d_{33}^2} \lambda^6 + \mathcal{O}(\lambda^{10}) \right| \langle H_d^0 \rangle, \\ m_b &= \left| d_{33} + \frac{d_{23}^2}{2d_{33}} \lambda^4 + \mathcal{O}(\lambda^8) \right| \langle H_d^0 \rangle, \end{aligned} \quad (34)$$

with the dominant contributions, arising from the three operators in eq. (31), as expected from the construction of the model.

For the matrices L_d for LH, and R_d for RH down-type quarks we have up to and including order λ^{12}

$$L_d = \begin{pmatrix} 1 - \frac{d_{12}^2}{2d_{22}^2} \lambda^{12} + \mathcal{O}(\lambda^{12}) & \frac{d_{12}}{d_{22}} \lambda^6 + \mathcal{O}(\lambda^{10}) & \frac{d_{13}}{d_{33}} \lambda^8 + \mathcal{O}(\lambda^{12}) \\ -\frac{d_{12}}{d_{22}} \lambda^6 + \mathcal{O}(\lambda^{10}) & 1 - \frac{d_{23}^2}{2d_{33}^2} \lambda^4 + \mathcal{O}(\lambda^8) & \frac{d_{23}}{d_{33}} \lambda^2 + \mathcal{O}(\lambda^6) \\ -\frac{(d_{13}d_{22} - d_{12}d_{23})}{d_{22}d_{33}} \lambda^8 + \mathcal{O}(\lambda^{12}) & -\frac{d_{23}}{d_{33}} \lambda^2 + \mathcal{O}(\lambda^6) & 1 - \frac{d_{23}^2}{2d_{33}^2} \lambda^4 + \mathcal{O}(\lambda^8) \end{pmatrix} \quad (35)$$

and

$R_d =$

$$\begin{pmatrix} 1 + \mathcal{O}(\lambda^{12}) & \frac{(d_{11}d_{12} + d_{21}d_{22})}{d_{22}^2} \lambda^8 + \mathcal{O}(\lambda^{12}) & \frac{d_{11}d_{13} + d_{21}d_{23} + d_{31}d_{33}}{d_{33}^2} \lambda^{12} + \mathcal{O}(\lambda^{12}) \\ -\frac{(d_{11}d_{12} + d_{21}d_{22})}{d_{22}^2} \lambda^8 + \mathcal{O}(\lambda^{12}) & 1 + \mathcal{O}(\lambda^8) & \frac{(d_{22}d_{23} + d_{32}d_{33})}{d_{33}^2} \lambda^4 + \mathcal{O}(\lambda^8) \\ \mathcal{O}(\lambda^{12}) & -\frac{(d_{22}d_{23} + d_{32}d_{33})}{d_{33}^2} \lambda^4 + \mathcal{O}(\lambda^8) & 1 + \mathcal{O}(\lambda^8) \end{pmatrix}. \quad (36)$$

We can see that both matrices, L_d and R_d , are close to the identity matrix, except for the (23)-block in L_d where a rotation of order λ^2 is present. This result has been anticipated in the preceding section, see footnote 13. The effect of this rotation is twofold. On the one hand, it leads to an additional contribution to the quark mixing angle θ_{23} , which is of the same order as the contribution arising from the up quark sector, see L_u in eq. (26) and eq. (29) and compare the form of the CKM mixing matrix in eq. (37) (scenario A) and eq. (40) (scenario B). On the other hand, it induces contributions to the elements x_{22} and x_{32} of the LQ coupling $\hat{\mathbf{x}}$ in the charged fermion mass basis, which are of the same order as the elements \hat{x}_{22} and \hat{x}_{32} of the LQ coupling $\hat{\mathbf{x}}$ itself, see eq. (54) and eq. (124) in appendix B.

3.1.3 Quark mixing

We first present the CKM mixing matrix, V_{CKM} , as obtained from the matrices L_u and L_d , shown in eq. (26) and eq. (35). This reflects the result of the model without modification of the up-type quark mass matrix M_u , i.e. in scenario A. Here, we find

$$V_{\text{CKM}} = L_u^\dagger L_d =$$

$$\begin{pmatrix} 1 - \frac{f_{12}^2}{2f_{22}^2} \lambda^2 + \mathcal{O}(\lambda^4) & -\frac{f_{12}}{f_{22}} \lambda + \mathcal{O}(\lambda^3) & \frac{f_{12}(d_{33}f_{23} - d_{23}f_{33})}{d_{33}f_{22}f_{33}} \lambda^3 + \mathcal{O}(\lambda^5) \\ \frac{f_{12}}{f_{22}} \lambda + \mathcal{O}(\lambda^3) & 1 - \frac{f_{12}^2}{2f_{22}^2} \lambda^2 + \mathcal{O}(\lambda^4) & \left(\frac{d_{23}}{d_{33}} - \frac{f_{23}}{f_{33}} \right) \lambda^2 + \mathcal{O}(\lambda^4) \\ \frac{d_{22}d_{33}f_{13} - d_{12}d_{33}f_{23} - d_{13}d_{22}f_{33} + d_{12}d_{23}f_{33}}{d_{22}d_{33}f_{33}} \lambda^8 + \mathcal{O}(\lambda^9) & -\left(\frac{d_{23}}{d_{33}} - \frac{f_{23}}{f_{33}} \right) \lambda^2 + \mathcal{O}(\lambda^6) & 1 - \frac{(d_{33}f_{23} - d_{23}f_{33})^2}{2d_{33}^2f_{33}^2} \lambda^4 + \mathcal{O}(\lambda^8) \end{pmatrix}. \quad (37)$$

There is an obvious suppression of the CKM mixing matrix element $V_{td} \sim \lambda^8$ compared to its experimentally measured value, $|V_{td}| = 0.00854_{-0.00016}^{+0.00023} \sim \lambda^3$ [93]. Furthermore, assuming that the effective parameters d_{ij} and f_{ij} are complex, we can estimate the size of the Jarlskog invariant J_{CP} and see that it is of order $J_{CP} = \text{Im}(V_{ud}V_{ub}^*V_{td}^*V_{tb}) \sim \lambda^{11}$. This is in conflict with the measured value, $J_{CP} = \left(3.00_{-0.09}^{+0.15}\right) \times 10^{-5} \sim \lambda^6$ [93].

In addition, we note that the relation between V_{us} , V_{cb} and V_{ub} is too tight to accommodate all three CKM mixing matrix elements in accordance with the experimental data [93]. In this model we have

$$|V_{us}| \approx \left| \frac{f_{12}}{f_{22}} \right| \lambda \sim \lambda \quad \text{and} \quad |V_{cb}| \approx \left| \frac{d_{23}}{d_{33}} - \frac{f_{23}}{f_{33}} \right| \lambda^2 \sim \lambda^2 \quad (38)$$

and as well

$$|V_{ub}| \approx \left| \frac{f_{12}}{f_{22}} \left(\frac{d_{23}}{d_{33}} - \frac{f_{23}}{f_{33}} \right) \right| \lambda^3 \approx |V_{us}| |V_{cb}| \quad (39)$$

which leads with $|V_{us}| = 0.22650$ and $|V_{cb}| = 0.04053$ [93] to $|V_{ub}| \approx 0.0092$. This is about a factor of 2.5 wrong with respect to the experimental best-fit value of V_{ub} , $|V_{ub}| = 0.00361_{-0.00009}^{+0.00011}$ [93], and clearly outside the range preferred at the 3σ level.

We have confirmed these findings with a chi-squared fit – while the charged fermion masses are fitted well at the scale $\mu = 1$ TeV [94], quark mixing cannot be brought into full agreement with experimental data [93].

In scenario B

Using instead the matrix L_u as given in eq. (29), we have for the CKM mixing matrix

$$V_{\text{CKM}} = \begin{pmatrix} 1 - \frac{f_{12}^2}{2f_{22}^2} \lambda^2 + \mathcal{O}(\lambda^4) & -\frac{f_{12}}{f_{22}} \lambda + \mathcal{O}(\lambda^3) & \left(\frac{f_{12}(d_{33}f_{23} - d_{23}f_{33})}{d_{33}f_{22}f_{33}} - \frac{\tilde{f}_{13}}{f_{33}} \right) \lambda^3 + \mathcal{O}(\lambda^5) \\ \frac{f_{12}}{f_{22}} \lambda + \mathcal{O}(\lambda^3) & 1 - \frac{f_{12}^2}{2f_{22}^2} \lambda^2 + \mathcal{O}(\lambda^4) & \left(\frac{d_{23}}{d_{33}} - \frac{f_{23}}{f_{33}} \right) \lambda^2 + \mathcal{O}(\lambda^4) \\ \frac{\tilde{f}_{13}}{f_{33}} \lambda^3 + \mathcal{O}(\lambda^7) & -\left(\frac{d_{23}}{d_{33}} - \frac{f_{23}}{f_{33}} \right) \lambda^2 + \mathcal{O}(\lambda^6) & 1 - \frac{(d_{33}f_{23} - d_{23}f_{33})^2}{2d_{33}^2f_{33}^2} \lambda^4 + \mathcal{O}(\lambda^6) \end{pmatrix}. \quad (40)$$

As we can clearly see, the anticipated changes in the CKM mixing matrix are achieved: the enhancement of V_{td} , which is now of order λ^3 , and in turn the enhancement of the Jarlskog invariant to $J_{CP} \sim \lambda^6$, as well as the loosening of the tight relation between V_{us} , V_{cb} and V_{ub} ,

$$|V_{ub}| \approx \left| \frac{f_{12}}{f_{22}} \left(\frac{d_{23}}{d_{33}} - \frac{f_{23}}{f_{33}} \right) + \frac{\tilde{f}_{13}}{f_{33}} \right| \lambda^3. \quad (41)$$

Indeed, a chi-squared fit shows that scenario B leads to an excellent agreement with the experimental data – not only of the quark mixing parameters [93], but also all charged fermion masses are fitted very well at the scale $\mu = 1$ TeV [94].

3.2 Charged lepton sector

Like we did for the quark sector, here we first present the list of operators. We then give the form of the charged lepton mass matrix M_e in the effective parametrisation, and extract analytical formulae for the charged lepton masses and the matrices L_e and R_e of LH and RH charged leptons, respectively, needed in order to arrive at the mass basis.

Three operators are mainly responsible for the generation of the charged lepton masses, like in the case of the down-type quark masses, namely

$$\mathcal{L}_{\text{Yuk,LO}}^e = \alpha_1^e \bar{L}_3 H_d e_{R3} + \alpha_2^e \bar{L} H_d e_R T + \alpha_3^e \bar{L} H_d e_R U. \quad (42)$$

As envisaged in the construction of this model, these have the analogous form as those found in the down quark sector, compare eq. (31). The operators, arising at SLO, differ in general

$$\begin{aligned}
\mathcal{L}_{\text{Yuk,SLO}}^e &= \alpha_4^e \bar{L} H_d e_{R3} S^\dagger + \alpha_5^e \bar{L}_3 H_d e_R S T + \alpha_6^e \bar{L} H_d e_R T W W^\dagger \\
&+ \alpha_7^e \bar{L}_3 H_d e_R S^\dagger (T^\dagger)^2 W^\dagger + \alpha_8^e \bar{L}_3 H_d e_R S^\dagger T^\dagger U^\dagger W^\dagger + \alpha_9^e \bar{L} H_d e_R S^2 (W^\dagger)^2 \\
&+ \alpha_{10}^e \bar{L} H_d e_{R3} S T^\dagger (W^\dagger)^2 + \alpha_{11}^e \bar{L} H_d e_R S^2 (T^\dagger)^3 + \alpha_{12}^e \bar{L} H_d e_R S^2 T^\dagger (U^\dagger)^2 \\
&+ \alpha_{13}^e \bar{L} H_d e_R S^4 W + \alpha_{14}^e \bar{L} H_d e_{R3} S^3 T^\dagger W + \alpha_{15}^e \bar{L}_3 H_d e_R (S^\dagger)^3 T^\dagger W \\
&+ \alpha_{16}^e \bar{L}_3 H_d e_R (S^\dagger)^3 U^\dagger W + \alpha_{17}^e \bar{L} H_d e_R (S^\dagger)^2 (T^\dagger)^2 W^\dagger \\
&+ \alpha_{18}^e \bar{L}_3 H_d e_R S^3 (W^\dagger)^2 + \alpha_{19}^e \bar{L}_3 H_d e_R S^3 (T^\dagger)^3 + \alpha_{20}^e \bar{L}_3 H_d e_R S^5 W \\
&+ \alpha_{21}^e \bar{L}_3 H_d e_{R3} S^4 T^\dagger W + \alpha_{22}^e \bar{L} H_d e_R (S^\dagger)^4 T^\dagger W + \alpha_{23}^e \bar{L} H_d e_R (S^\dagger)^4 U^\dagger W \\
&+ \alpha_{24}^e \bar{L}_3 H_d e_{R3} (S^\dagger)^4 T W^\dagger + \alpha_{25}^e \bar{L}_3 H_d e_R (S^\dagger)^3 T^2 W^\dagger \\
&+ \alpha_{26}^e \bar{L} H_d e_{R3} (S^\dagger)^5 T W^\dagger + \alpha_{27}^e \bar{L} H_d e_R (S^\dagger)^4 T^2 W^\dagger .
\end{aligned} \tag{43}$$

We briefly comment on the first two of these operators. The first one with the coefficient α_4^e has already been identified in the preceding section, compare footnote 12. The second one with α_5^e also turns out to be an operator that is automatically induced, once the field content of the LO operators, responsible for the dominant contributions to the charged fermion mass matrices and the LQ couplings $\hat{\mathbf{x}}$ and $\hat{\mathbf{y}}$, has been fixed. We note that only the operator with the coefficient α_9^e leads to two independent contributions to the charged lepton mass matrix M_e : one of order λ^{11} and another one of λ^{12} , compare also eq. (121) in appendix B.

For the charged lepton mass matrix M_e the following effective parametrisation is found

$$M_e = \begin{pmatrix} e_{11} \lambda^4 & e_{12} \lambda^{12} & \mathcal{O}(\lambda^{12}) \\ e_{21} \lambda^8 & e_{22} \lambda^2 & e_{23} \lambda \\ e_{31} \lambda^9 & e_{32} \lambda^3 & e_{33} \end{pmatrix} \langle H_d^0 \rangle \tag{44}$$

with e_{ij} being complex order-one numbers that are related to the coefficients α_i^e as shown in eq. (121) in appendix B. We emphasise that the element $M_{e,13}$ is only generated at an order higher than λ^{12} .

From M_e in eq. (44), we can derive for the charged lepton masses

$$\begin{aligned}
m_e &= |e_{11} \lambda^4 + \mathcal{O}(\lambda^{12})| \langle H_d^0 \rangle , \\
m_\mu &= \left| e_{22} \lambda^2 - \frac{e_{23}(e_{22}e_{23} + 2e_{32}e_{33})}{2e_{33}^2} \lambda^4 + \mathcal{O}(\lambda^6) \right| \langle H_d^0 \rangle , \\
m_\tau &= \left| e_{33} + \frac{e_{23}^2}{2e_{33}} \lambda^2 + \mathcal{O}(\lambda^4) \right| \langle H_d^0 \rangle .
\end{aligned} \tag{45}$$

These results match the expectations from the construction of the model, since the three operators in eq. (42) dominantly generate the three different charged lepton masses. We note that, in particular, the muon mass can receive sizeable contributions from the LQ at one-loop level, if the observed value of the AMM of the muon is explained in this model. These contributions can be compensated by adjusting the effective parameter e_{22} appropriately, see eq. (45). For formulae and estimates of these contributions, see section 5.1.2 and appendix C.1.

The matrices L_e and R_e read

$$L_e = \begin{pmatrix} 1 + \mathcal{O}(\lambda^{12}) & \frac{e_{11}e_{21}}{e_{22}^2} \lambda^8 + \mathcal{O}(\lambda^{10}) & \mathcal{O}(\lambda^{12}) \\ -\frac{e_{11}e_{21}}{e_{22}^2} \lambda^8 + \mathcal{O}(\lambda^{10}) & 1 - \frac{e_{23}^2}{2e_{33}^2} \lambda^2 + \mathcal{O}(\lambda^4) & \frac{e_{23}}{e_{33}} \lambda + \mathcal{O}(\lambda^3) \\ \frac{e_{11}e_{21}e_{23}}{e_{22}^2e_{33}} \lambda^9 + \mathcal{O}(\lambda^{11}) & -\frac{e_{23}}{e_{33}} \lambda + \mathcal{O}(\lambda^3) & 1 - \frac{e_{23}^2}{2e_{33}^2} \lambda^2 + \mathcal{O}(\lambda^4) \end{pmatrix} \tag{46}$$

and

$R_e =$

$$\left(\begin{array}{ccc} 1 - \frac{e_{21}^2}{2e_{22}^2} \lambda^{12} + \mathcal{O}(\lambda^{12}) & \frac{e_{21}}{e_{22}} \lambda^6 + \mathcal{O}(\lambda^8) & \frac{(e_{21}e_{23}+e_{31}e_{33})}{e_{33}^2} \lambda^9 + \mathcal{O}(\lambda^{11}) \\ -\frac{e_{21}}{e_{22}} \lambda^6 + \mathcal{O}(\lambda^8) & 1 - \frac{(e_{22}e_{23}+e_{32}e_{33})^2}{2e_{33}^4} \lambda^6 + \mathcal{O}(\lambda^8) & \frac{(e_{22}e_{23}+e_{32}e_{33})}{e_{33}^2} \lambda^3 + \mathcal{O}(\lambda^5) \\ -\frac{(e_{22}e_{31}-e_{21}e_{32})}{e_{22}e_{33}} \lambda^9 + \mathcal{O}(\lambda^{11}) & -\frac{(e_{22}e_{23}+e_{32}e_{33})}{e_{33}^2} \lambda^3 + \mathcal{O}(\lambda^5) & 1 - \frac{(e_{22}e_{23}+e_{32}e_{33})^2}{2e_{33}^4} \lambda^6 + \mathcal{O}(\lambda^8) \end{array} \right). \quad (47)$$

We reiterate that the matrix L_e is also applied to the LH neutrinos in order to transform from the interaction to the mass basis, since neutrinos are massless in this model and thus lepton mixing is unphysical.

In both matrices, L_e and R_e , the (23)-block deviates from being close to the identity matrix. These deviations are induced by the operators with the coefficients α_4^e and α_5^e which have been identified as automatically allowed, if the LO operators for the charged fermion mass matrices and the LQ couplings $\hat{\mathbf{x}}$ and $\hat{\mathbf{y}}$ are accounted for.

The effect of the rotation of order λ in L_e is to also contribute to the elements x_{22} and x_{23} of the LQ coupling $\hat{\mathbf{x}}$ in the charged fermion mass basis and to do so at the same order as the elements \hat{x}_{22} and \hat{x}_{23} of the LQ coupling $\hat{\mathbf{x}}$ itself, compare eq. (54) and eq. (124) in appendix B. The impact of the rotation of order λ^3 in R_e is to also generate the element y_{22} of the LQ coupling $\hat{\mathbf{y}}$ in the charged fermion mass basis of order λ^3 in addition to the element $\hat{y}_{22} \sim \lambda^3$ of the LQ coupling $\hat{\mathbf{y}}$ itself – see eq. (58) and eq. (126) in appendix B.

3.3 Leptoquark couplings

We first list the operators, contributing to the LQ couplings $\hat{\mathbf{x}}$ and $\hat{\mathbf{y}}$, up to and including order λ^{12} , and then discuss the form of \mathbf{x} , \mathbf{y} and \mathbf{z} , the LQ couplings $\hat{\mathbf{x}}$ and $\hat{\mathbf{y}}$ in the charged fermion mass basis, in the two different scenarios, scenario A and scenario B.

3.3.1 Couplings in interaction basis

We begin with the LO operators, responsible for the main structure of the LQ coupling $\hat{\mathbf{x}}$. There are four of them

$$\mathcal{L}_{\hat{\mathbf{x}},\text{LO}}^{\text{int}} = \beta_1^L \overline{L}_3^c \phi^\dagger Q_3 + \beta_2^L \overline{L}^c \phi^\dagger Q_3 S + \beta_3^L \overline{L}_3^c \phi^\dagger Q S^2 + \beta_4^L \overline{L}^c \phi^\dagger Q S^3. \quad (48)$$

They coincide with those, anticipated in the construction of the model in the preceding section. At SLO, there are several more operators

$$\begin{aligned} \mathcal{L}_{\hat{\mathbf{x}},\text{SLO}}^{\text{int}} &= \beta_5^L \overline{L}_3^c \phi^\dagger Q T W^2 + \beta_6^L \overline{L}^c \phi^\dagger Q S^\dagger T W^\dagger + \beta_7^L \overline{L}^c \phi^\dagger Q S^\dagger U W^\dagger \\ &+ \beta_8^L \overline{L}_3^c \phi^\dagger Q S^2 T^\dagger U + \beta_9^L \overline{L}^c \phi^\dagger Q S^\dagger (T^\dagger)^2 W + \beta_{10}^L \overline{L}^c \phi^\dagger Q S^\dagger T^\dagger U^\dagger W \\ &+ \beta_{11}^L \overline{L}^c \phi^\dagger Q S T W^2 + \beta_{12}^L \overline{L}^c \phi^\dagger Q_3 S^\dagger T W^2 + \beta_{13}^L \overline{L}_3^c \phi^\dagger Q (S^\dagger)^2 T W^\dagger \\ &+ \beta_{14}^L \overline{L}_3^c \phi^\dagger Q (S^\dagger)^2 U W^\dagger + \beta_{15}^L \overline{L}_3^c \phi^\dagger Q S^2 W W^\dagger + \beta_{16}^L \overline{L}^c \phi^\dagger Q S^3 T^\dagger U \\ &+ \beta_{17}^L \overline{L}^c \phi^\dagger Q_3 (S^\dagger)^3 T W^\dagger + \beta_{18}^L \overline{L}^c \phi^\dagger Q S (T^\dagger)^3 W^\dagger + \beta_{19}^L \overline{L}^c \phi^\dagger Q S^3 W W^\dagger \\ &+ \beta_{20}^L \overline{L}^c \phi^\dagger Q (S^\dagger)^5 U^\dagger + \beta_{21}^L \overline{L}^c \phi^\dagger Q (S^\dagger)^3 T^2 W + \beta_{22}^L \overline{L}_3^c \phi^\dagger Q_3 S^4 T^\dagger W \\ &+ \beta_{23}^L \overline{L}_3^c \phi^\dagger Q_3 (S^\dagger)^4 T W^\dagger + \beta_{24}^L \overline{L}_3^c \phi^\dagger Q (S^\dagger)^4 T^2 W + \beta_{25}^L \overline{L}^c \phi^\dagger Q_3 S^5 T^\dagger W \\ &+ \beta_{26}^L \overline{L}_3^c \phi^\dagger Q S^6 T^\dagger W. \end{aligned} \quad (49)$$

All couplings β_i^L are complex order-one coefficients. Like before, we note that several of these operators lead to two independent contributions to the LQ coupling $\hat{\mathbf{x}}$. The operator with the

coefficient β_5^L leads to contributions of order λ^{10} and λ^{11} ; the one with β_6^L gives contributions of order λ^7 and λ^8 ; the operator with β_{10}^L induces two of order λ^{11} and λ^{12} ; the one with β_{11}^L yields contributions of order λ^{11} and λ^{12} ; the one with β_{13}^L gives rise to two of order λ^8 and λ^9 ; finally, the operator with the coefficient β_{21}^L leads to two independent contributions of order λ^{11} and λ^{12} .

From the contributions of these operators, we can deduce the form of the LQ coupling $\hat{\mathbf{x}}$, up to and including order λ^{12} ,

$$\hat{\mathbf{x}} = \begin{pmatrix} \hat{a}_{11} \lambda^9 & \hat{a}_{12} \lambda^{12} & \mathcal{O}(\lambda^{12}) \\ \hat{a}_{21} \lambda^8 & \hat{a}_{22} \lambda^3 & \hat{a}_{23} \lambda \\ \hat{a}_{31} \lambda^8 & \hat{a}_{32} \lambda^2 & \hat{a}_{33} \end{pmatrix} \quad (50)$$

with the effective parameters \hat{a}_{ij} being, in general, complex order-one numbers. How these are related to the coefficients β_i^L can be found in eq. (122) in appendix B. We note that the element \hat{x}_{13} is only generated at an order higher than λ^{12} .

Although not yet in the charged fermion mass basis, we can already compare this form of the LQ coupling with the texture, envisaged in eq. (9). We clearly see that the elements of the first column and row are protected well by the residual symmetry Z_{17}^{diag} , while the elements in the (23)-block of the LQ coupling $\hat{\mathbf{x}}$ all have the desired order of magnitude in λ , see the texture in eq. (9).

In the end, we also discuss the operators, contributing to the LQ coupling $\hat{\mathbf{y}}$, up to and including order λ^{12} . We identify only two operators as LO ones

$$\mathcal{L}_{\hat{\mathbf{y}},\text{LO}}^{\text{int}} = \beta_1^R \overline{e_{R3}^c} \phi^\dagger u_{R2} + \beta_2^R \overline{e_R^c} \phi^\dagger u_{R3} S^3, \quad (51)$$

which are expected from the construction of the model. At SLO, several more operators are found

$$\begin{aligned} \mathcal{L}_{\hat{\mathbf{y}},\text{SLO}}^{\text{int}} &= \beta_3^R \overline{e_R^c} \phi^\dagger u_{R2} S T + \beta_4^R \overline{e_{R3}^c} \phi^\dagger u_{R3} S^2 T^\dagger + \beta_5^R \overline{e_{R3}^c} \phi^\dagger u_{R3} W^2 \\ &+ \beta_6^R \overline{e_R^c} \phi^\dagger u_{R1} S^\dagger (U^\dagger)^2 + \beta_7^R \overline{e_R^c} \phi^\dagger u_{R1} S U W + \beta_8^R \overline{e_{R3}^c} \phi^\dagger u_{R3} (S^\dagger)^2 W^\dagger \\ &+ \beta_9^R \overline{e_R^c} \phi^\dagger u_{R3} S^\dagger T W^\dagger + \beta_{10}^R \overline{e_R^c} \phi^\dagger u_{R3} S^\dagger (T^\dagger)^2 W + \beta_{11}^R \overline{e_R^c} \phi^\dagger u_{R3} S^\dagger T^\dagger U^\dagger W \\ &+ \beta_{12}^R \overline{e_R^c} \phi^\dagger u_{R3} S T W^2 + \beta_{13}^R \overline{e_R^c} \phi^\dagger u_{R2} S^\dagger (T^\dagger)^2 W^\dagger + \beta_{14}^R \overline{e_R^c} \phi^\dagger u_{R2} S^\dagger T^\dagger U^\dagger W^\dagger \\ &+ \beta_{15}^R \overline{e_R^c} \phi^\dagger u_{R1} (S^\dagger)^3 T U + \beta_{16}^R \overline{e_{R3}^c} \phi^\dagger u_{R1} (S^\dagger)^2 T^\dagger (U^\dagger)^2 + \beta_{17}^R \overline{e_R^c} \phi^\dagger u_{R2} (S^\dagger)^3 T^\dagger W \\ &+ \beta_{18}^R \overline{e_R^c} \phi^\dagger u_{R2} (S^\dagger)^3 U^\dagger W + \beta_{19}^R \overline{e_R^c} \phi^\dagger u_{R3} S (T^\dagger)^3 W^\dagger + \beta_{20}^R \overline{e_R^c} \phi^\dagger u_{R2} S^3 (W^\dagger)^2 \\ &+ \beta_{21}^R \overline{e_R^c} \phi^\dagger u_{R2} S^3 (T^\dagger)^3 + \beta_{22}^R \overline{e_{R3}^c} \phi^\dagger u_{R1} S^4 U^2 + \beta_{23}^R \overline{e_R^c} \phi^\dagger u_{R3} (S^\dagger)^5 U^\dagger \\ &+ \beta_{24}^R \overline{e_R^c} \phi^\dagger u_{R2} S^5 W + \beta_{25}^R \overline{e_{R3}^c} \phi^\dagger u_{R3} (S^\dagger)^4 T W + \beta_{26}^R \overline{e_R^c} \phi^\dagger u_{R3} (S^\dagger)^3 T^2 W \\ &+ \beta_{27}^R \overline{e_{R3}^c} \phi^\dagger u_{R2} S^4 T^\dagger W + \beta_{28}^R \overline{e_{R3}^c} \phi^\dagger u_{R2} (S^\dagger)^4 T W^\dagger + \beta_{29}^R \overline{e_R^c} \phi^\dagger u_{R2} (S^\dagger)^3 T^2 W^\dagger, \end{aligned} \quad (52)$$

with all coefficients β_i^R being complex order-one numbers. The presence of the first and the second operator is automatic after having fixed the transformation properties of the fields which are relevant for the LO terms of the charged fermion mass matrices M_u , M_d , M_e and the LQ couplings $\hat{\mathbf{x}}$ and $\hat{\mathbf{y}}$. We note that all listed operators give rise to a single (independent) contribution to the LQ coupling $\hat{\mathbf{y}}$.

We arrive at the effective parametrisation for $\hat{\mathbf{y}}$ to be of the form

$$\hat{\mathbf{y}} = \begin{pmatrix} \hat{b}_{11} \lambda^9 & \hat{b}_{12} \lambda^9 & \hat{b}_{13} \lambda^9 \\ \hat{b}_{21} \lambda^9 & \hat{b}_{22} \lambda^3 & \hat{b}_{23} \lambda^3 \\ \hat{b}_{31} \lambda^{12} & \hat{b}_{32} & \hat{b}_{33} \lambda^4 \end{pmatrix}. \quad (53)$$

The parameters \hat{b}_{ij} are, in general, complex order-one numbers and are related to the coefficients β_i^R as shown in eq. (123) in appendix B.

We may already compare this result to the texture of the LQ coupling \mathbf{y} in eq. (9) and see that it contains the same two dominant terms, \hat{y}_{32} and \hat{y}_{23} , like the texture with $y_{32} \sim 1$ and $y_{23} \sim \lambda^3$. At the same time, however, the form of the LQ coupling $\hat{\mathbf{y}}$ in eq. (53) also has rather large elements $\hat{y}_{22} \sim \lambda^3$ and $\hat{y}_{33} \sim \lambda^4$. These arise from the operators with the coefficients β_3^R and β_4^R which have been identified as automatically allowed, once the LO operators, contributing to the charged fermion mass matrices and LQ couplings $\hat{\mathbf{x}}$ and $\hat{\mathbf{y}}$ and their particle content are fixed. We note that none of the elements of the first column and row of the LQ coupling $\hat{\mathbf{y}}$ is larger than λ^9 , showing the effectiveness of the residual symmetry Z_{17}^{diag} . Couplings to electrons and/or up quarks are thus suppressed.

3.3.2 Couplings in charged fermion mass basis

In this section, we display the results for the LQ couplings \mathbf{x} , \mathbf{y} and \mathbf{z} , namely the LQ couplings $\hat{\mathbf{x}}$ and $\hat{\mathbf{y}}$ in the charged fermion mass basis, compare eq. (4). The LQ coupling \mathbf{x} is obtained by applying the matrices L_e and L_d to $\hat{\mathbf{x}}$, while \mathbf{z} by applying L_e and L_u to $\hat{\mathbf{x}}$. The LQ coupling \mathbf{y} is generated from $\hat{\mathbf{y}}$ by applying the matrices R_e and R_u . In doing so, we distinguish between the two different scenarios, scenario A and scenario B, for the LQ couplings \mathbf{z} and \mathbf{y} .

We use the matrices L_e and L_d in eqs. (35,46) and arrive at the LQ coupling \mathbf{x} . This matrix can be parametrised as

$$\mathbf{x} = L_e^T \hat{\mathbf{x}} L_d = \begin{pmatrix} a_{11} \lambda^9 & a_{12} \lambda^{11} & a_{13} \lambda^9 \\ a_{21} \lambda^8 & a_{22} \lambda^3 & a_{23} \lambda \\ a_{31} \lambda^8 & a_{32} \lambda^2 & a_{33} \end{pmatrix}, \quad (54)$$

where the effective parameters a_{ij} are related to the parameters \hat{a}_{ij} , d_{ij} and e_{ij} , found in the matrix $\hat{\mathbf{x}}$ in eq. (50), M_d in eq. (33) and M_e in eq. (44), respectively. The explicit form of these relations is given in eq. (124) in appendix B. In general, they can also be expected to be complex order-one numbers.

Comparing the form of the LQ coupling \mathbf{x} in eq. (54) to the texture of \mathbf{x} in eq. (9), we clearly see that all elements of the first column and row are suppressed, i.e. none of them is larger than λ^8 . At the same time, the elements x_{33} , x_{23} , x_{32} and x_{22} have the expected order of magnitude in λ .

In scenario A

In scenario A, i.e. the model without any modification of the up-type quark mass matrix M_u , we find the form of the LQ coupling \mathbf{z} , when applying the matrices L_e and L_u , see eqs. (46,26), to the LQ coupling $\hat{\mathbf{x}}$ in eq. (50). It is

$$\mathbf{z} = L_e^T \hat{\mathbf{x}} L_u = \begin{pmatrix} c_{11} \lambda^9 & c_{12} \lambda^{10} & c_{13} \lambda^9 \\ c_{21} \lambda^4 & c_{22} \lambda^3 & c_{23} \lambda \\ c_{31} \lambda^3 & c_{32} \lambda^2 & c_{33} \end{pmatrix}. \quad (55)$$

The effective parameters c_{ij} are related to \hat{a}_{ij} , e_{ij} and f_{ij} from eqs. (50,44,23). Again, the explicit form of these relations can be found in appendix B, see eq. (125).

We note that it might be useful to evidence the strong correlation between the LQ couplings \mathbf{x} and \mathbf{z} by using a different parametrisation for \mathbf{z} , namely

$$\mathbf{z} = \begin{pmatrix} (a_{11} - \frac{(c_{12}^A)^2}{2a_{11}} \lambda^2 + c_{11}^A \lambda^3) \lambda^9 & c_{12}^A \lambda^{10} & a_{13} \lambda^9 \\ (-\frac{c_{12}^A}{a_{11}} (a_{22} + a_{23} \tilde{c}) + c_{21}^A \lambda) \lambda^4 & (a_{22} + a_{23} \tilde{c} + c_{22}^A \lambda^2) \lambda^3 & (a_{23} + c_{23}^A \lambda^4) \lambda \\ (-\frac{c_{12}^A}{a_{11}} (a_{32} + a_{33} \tilde{c}) + c_{31}^A \lambda) \lambda^3 & (a_{32} + a_{33} \tilde{c} + c_{32}^A \lambda^2) \lambda^2 & a_{33} + c_{33}^A \lambda^4 \end{pmatrix}, \quad (56)$$

where a_{ij} are the same parameters as in \mathbf{x} in eq. (54). The new effective parameters c_{ij}^A and \tilde{c} are rather involved expressions in the other parameters so that we just take them to be complex order-one numbers, apart from

$$c_{12}^A = \frac{\hat{a}_{11} f_{12}}{f_{22}} + \mathcal{O}(\lambda) \quad \text{and} \quad \tilde{c} = \frac{d_{23}}{d_{33}} - \frac{f_{23}}{f_{33}}. \quad (57)$$

We use the matrices R_e and R_u in eqs.(47,27) and $\hat{\mathbf{y}}$ in eq. (53) in order to arrive at the form of the LQ coupling $\hat{\mathbf{y}}$ in the charged fermion mass basis

$$\mathbf{y} = R_e^T \hat{\mathbf{y}} R_u = \begin{pmatrix} b_{11} \lambda^9 & b_{12} \lambda^9 & b_{13} \lambda^9 \\ b_{21} \lambda^8 & b_{22} \lambda^3 & b_{23} \lambda^3 \\ b_{31} \lambda^5 & b_{32} & b_{33} \lambda^4 \end{pmatrix}. \quad (58)$$

The effective parameters b_{ij} are related to \hat{b}_{ij} from the LQ coupling $\hat{\mathbf{y}}$ in eq. (53), to e_{ij} of the charged lepton mass matrix M_e in eq. (44) and to f_{ij} of the up-type quark mass matrix M_u in eq. (23). These relations are given in eq. (126) in appendix B.

Comparing this form of the LQ coupling \mathbf{y} with the texture in eq. (9), we see that in the charged fermion mass basis not only the elements $y_{22} \sim \lambda^3$ and $y_{33} \sim \lambda^4$ turn out to be larger, but also the element $y_{31} \sim \lambda^5$. As we see in section 5.1, these couplings do not enter the analytic estimates for the strongest (primary) constraints on this model. We find that they generally lead to subleading contributions to these estimates, or appear in the estimates for secondary/tertiary observables, discussed further in section 6. For example, y_{22} contributes to the process $b \rightarrow c\mu\nu$, relevant for subdominant contributions to the LFU ratios $R(D)$ and $R(D^*)$, and for the secondary observables $R_D^{\mu/e}$ and $R_{D^*}^{e/\mu}$. The LQ coupling y_{33} relates the top quark to the tau lepton, and shows up in subdominant loop-level contributions to tau lepton decays including $\tau \rightarrow \mu\gamma$. The LQ coupling y_{31} is relevant for subleading contributions to the decay $B \rightarrow \tau\nu$, representing a secondary observable, and to tau lepton decays to light mesons, e.g. $\tau \rightarrow \pi\mu$, which correspond to tertiary observables. The LQ couplings y_{1j} involving the electron are still suppressed.

In scenario B

In scenario B, where the element $M_{u,13}$ of the up-type quark mass matrix M_u is enhanced, see eq. (28), the matrices L_u and R_u are found in eqs. (29,30). When using these in order to compute the form of the LQ coupling \mathbf{z} , we find the following: while the order of magnitude in λ of the different elements of \mathbf{z} is not changed with respect to the matrix shown in eq. (55), the relations of the effective parameters c_{ij} to the parameters \hat{a}_{ij} , e_{ij} , f_{ij} and \tilde{f}_{13} are to some extent altered. If we compare to the ones given in eq. (125) in appendix B, we now have for c_{21} and c_{31}

$$\begin{aligned} c_{21} &= -\frac{f_{12}}{e_{33} f_{22} f_{33}} (\hat{a}_{33} e_{23} f_{23} - \hat{a}_{23} e_{33} f_{23} - \hat{a}_{32} e_{23} f_{33} + \hat{a}_{22} e_{33} f_{33}) \\ &\quad - \frac{\tilde{f}_{13}}{f_{33}} \left(\hat{a}_{23} - \frac{\hat{a}_{33} e_{23}}{e_{33}} \right) + \mathcal{O}(\lambda^2), \\ c_{31} &= \frac{f_{12} (\hat{a}_{33} f_{23} - \hat{a}_{32} f_{33})}{f_{22} f_{33}} - \frac{\tilde{f}_{13}}{f_{33}} \hat{a}_{33} + \mathcal{O}(\lambda^2). \end{aligned} \quad (59)$$

As a consequence, the correlation between the LQ couplings \mathbf{x} and \mathbf{z} leads to a slightly different parametrisation than the one, displayed in eq. (56), i.e.

$$\mathbf{z} = \begin{pmatrix} (a_{11} - \frac{(c_{12}^B)^2}{2a_{11}} \lambda^2 + c_{11}^B \lambda^3) \lambda^9 & c_{12}^B \lambda^{10} & (a_{13} + c_{13}^B \lambda^3) \lambda^9 \\ (-\frac{c_{12}^B}{a_{11}} (a_{22} + a_{23} \tilde{c}) - a_{23} \tilde{c} + c_{21}^B \lambda) \lambda^4 & (a_{22} + a_{23} \tilde{c} + c_{22}^B \lambda^2) \lambda^3 & (a_{23} + c_{23}^B \lambda^4) \lambda \\ (-\frac{c_{12}^B}{a_{11}} (a_{32} + a_{33} \tilde{c}) - a_{33} \tilde{c} + c_{31}^B \lambda) \lambda^3 & (a_{32} + a_{33} \tilde{c} + c_{32}^B \lambda^2) \lambda^2 & a_{33} + c_{33}^B \lambda^4 \end{pmatrix}. \quad (60)$$

Most of the parameters c_{ij}^B are complex order-one numbers. Their expressions in terms of the other parameters are rather lengthy,¹⁶ apart from $c_{12}^B = c_{12}^A$, \tilde{c} and \bar{c} . The former two are still of the form as given in eq. (57), while the further parameter \bar{c} is defined as

$$\bar{c} = \frac{\tilde{f}_{13}}{f_{33}}. \quad (61)$$

Coming to the form of the LQ coupling \mathbf{y} , when using R_u in eq. (30), we see that neither its form, found in eq. (58), nor the definition of the effective parameters b_{ij} , given in eq. (126) in appendix B, are altered. Nevertheless, the change in the up-type quark mass matrix M_u in scenario B also leaves a slight imprint at higher order in λ on the LQ coupling \mathbf{y} with the maximum change in y_{31} at order λ^7 .

4 Outline of phenomenological study

In the following, we outline the strategy for the phenomenological study of the aforementioned model. In particular, we highlight the important features common to the studies detailed in sections 5 and 6.

Classification of observables. We classify all analysed observables to one of the following three categories: primary, secondary or tertiary observables. The primary observables comprise the anomalies in $R(D)$, $R(D^*)$ and in the AMM of the muon, as well as the observables for which contributions generated in this model can (substantially) violate the current experimental bounds and/or are accessible in upcoming experiments. Examples of the former are the radiative cLFV decays $\mu \rightarrow e\gamma$ and $\tau \rightarrow \mu\gamma$, while processes such as $\mu \rightarrow 3e$ and $\mu - e$ conversion in aluminium belong to the latter. These observables are studied analytically in section 5, and numerically in sections 5 and 6. Secondary observables, for instance $B \rightarrow \tau\nu$, do not presently provide any competitive constraint, but are expected to offer an opportunity to further test this model in the mid-term future. These are discussed both analytically and numerically in section 6. Tertiary observables, such as the AMM of the electron, do not lead to any restriction on the parameter space of the model given the present experimental status. We find analytically that they do not deviate significantly from the SM predictions. The projected sensitivity for these observables is thus not sufficient to probe a signal consistent with this model. However, if a deviation from the SM prediction is observed, this could challenge the model. We mention them in section 6 and appendix E.3, and incorporate them in the second numerical scan.

Implemented model setup. As mentioned in section 2.1, the presented model contains two Higgs doublets, H_u and H_d , that give masses to up-type quarks as well as to down-type quarks and charged leptons, respectively, upon electroweak symmetry breaking. Nevertheless, we simplify the model in the phenomenological study and consider it as model with one SM-like Higgs doublet, i.e. we only take into account one SM-like Higgs, ignoring effects due to scalars other than the LQ ϕ , and appropriately rescale the effective parameters f_{ij} , d_{ij} and e_{ij} , contained in the up-type quark, down-type quark and charged lepton mass matrices M_u , M_d and M_e , respectively.

Since only in scenario B the results for quark mixing are in full agreement with experimental data, c.f. section 3.1.3, we focus on this scenario in the phenomenological study. For scenario A, we note that only the form of the effective parameters c_{21} and c_{31} is slightly different, see section 3.3.2. According to the analytic results, the parameter c_{21} only contributes at SLO to $\mu - e$ conversion in

¹⁶The parameter c_{13}^B is new with respect to the parametrisation of \mathbf{z} in eq. (56).

nuclei, see section 5.1.5 and also table 5, while c_{31} is relevant for the computation of the secondary observable $B \rightarrow \tau\nu$, compare section 6.5. We, thus, do not expect any significant differences in the phenomenological results for these two scenarios. This expectation is, indeed, confirmed with a smaller data sample of the first numerical scan.

Bases of LQ couplings. The form of the LQ couplings is presented in two different bases, the interaction basis as well as the charged fermion mass basis, see section 3.3. The former basis refers to the *hatted* LQ couplings $\hat{\mathbf{x}}$ and $\hat{\mathbf{y}}$ with effective parameters \hat{a}_{ij} and \hat{b}_{ij} , see definition in eq. (3) and explicit forms in eq. (50) and eq. (53), while the latter basis corresponds to the *unhatted* LQ couplings \mathbf{x} , \mathbf{y} and \mathbf{z} with effective parameters a_{ij} , b_{ij} and c_{ij} or c_{ij}^B , \tilde{c} and \bar{c} , see definition in eq. (4) and explicit forms in eqs. (54), (58) and (55) or (60) (for scenario B). Each of the parameters a_{ij} , b_{ij} and c_{ij} is (at LO) given by a linear combination of some of the effective parameters \hat{a}_{ij} and \hat{b}_{ij} with coefficients constituted by f_{ij} , d_{ij} and e_{ij} , which parametrise the mass matrices M_u , M_d and M_e , respectively. The explicit relations between the parameters in the two bases can be found in appendix B.

While the interaction basis directly reflects the impact of the imposed flavour symmetry, the charged fermion mass basis is usually employed in phenomenological studies that focus on the effects of the LQ. For this reason, unhatted LQ couplings are used in analytic computations with \mathbf{z} being parametrised in terms of the effective parameters c_{ij} , see sections 5.1 and 6.5, as well as in the first numerical scan with the LQ coupling \mathbf{z} given in terms of c_{ij}^B , \tilde{c} and \bar{c} , c.f. section 5.2. On the other hand, the second numerical scan is performed in the interaction basis, see section 6 and appendix E.

Strategy of numerical scans. In order to study the phenomenology of the model in depth, we perform two numerical scans. In the following, we give details about the employed strategy.

For the first scan, discussed in section 5.2, we only consider primary observables, and thus refer to it as the *primary* scan. Since the LQ couplings in the model span a parameter space of high dimensionality, it is reasonable to first establish which of the effective parameters prove most relevant for the induced phenomenology. The main purpose of constructing the model is generating textures of the LQ couplings which are suitable to explain the currently observed flavour anomalies in $R(D)$, $R(D^*)$ and in the AMM of the muon. So, as a first step we deem it sufficient to only consider the effective parameters, contained in the LQ couplings \mathbf{x} , \mathbf{y} and \mathbf{z} , without making explicit reference to the interaction basis. We investigate the capability of the model to explain the mentioned anomalies and how the imposed current experimental bounds shape the viable parameter space. We also establish biases on the relevant effective parameters a_{ij} and b_{ij} that are applied in the second numerical scan, see section 6.2. The contributions to the relevant observables are computed with the help of the analytic expressions given in appendix C. In addition, we use Wilson [95] to account for renormalisation group (RG) running under QCD.

For the second scan, detailed in section 6, we take into account all observables, primary, secondary, and tertiary, and thus refer to it as *comprehensive*. In particular, we include secondary observables and outline how they can provide tangible signals for this model in the future, see section 6.6. Tertiary observables are also cross-checked and the generated ranges for these observables are summarised in appendix E.3. In order to ensure that this model accommodates charged fermion masses and quark mixing, we fix the effective parameters f_{ij} , d_{ij} and e_{ij} by performing a chi-squared fit, see details in section 6.1. Furthermore, we vary most of the effective parameters, contained in the LQ couplings $\hat{\mathbf{x}}$ and $\hat{\mathbf{y}}$, in the ranges laid out in eq. (62) and eq. (63), apart from the ones which are identified as playing a dominant role for the phenomenology of the model. For these effective parameters, we apply a suitable biasing in order to more efficiently target the

parameter space preferred by the primary observables, as detailed in section 6.2. As computational tools, we use SARAH, SPheno [96; 97] and flavio [62; 63] in the comprehensive scan.

Range of LQ couplings. In agreement with the expansion in λ , we assume the magnitude of an unbiased parameter s_{ij} to be in the range

$$\lambda = 0.2265 \leq |s_{ij}| \leq \frac{1}{\lambda} \approx 4.42, \quad (62)$$

and its phase to lie in the interval

$$0 \leq \text{Arg}(s_{ij}) < 2\pi. \quad (63)$$

Here, s_{ij} corresponds to any of the parameters a_{ij} , b_{ij} and c_{ij} or c_{ij}^B (except for c_{12}^B , see below), while working in the charged fermion mass basis, and to any of the parameters \hat{a}_{ij} and \hat{b}_{ij} , in the case of the interaction basis. In two instances, different choices for certain parameters are made. In the primary scan, employing the charged fermion mass basis, smaller ranges for the magnitudes of the effective parameters c_{12}^B , \bar{c} and \tilde{c} are used in order to better approximate the relation of the LQ couplings \mathbf{x} and \mathbf{z} that is determined by the CKM mixing matrix, see section 5.2.1. In the comprehensive scan, using the interaction basis, biases on certain effective parameters a_{ij} and b_{ij} are imposed that are derived from the results of the primary scan, see section 6.2.

In the analytic study, it is assumed that all effective parameters vary as indicated in eq. (62) and eq. (63). Depending on the studied observable, we either give an approximate relation based on the LO in λ or an estimate accounting only for the correct order of magnitude.

Inspecting the relations between the parameters in the interaction and charged fermion mass basis that are given in appendix B, we conclude that the value of an unhatted parameter can significantly differ from the value of the corresponding hatted parameter. Consequently, the results of the primary scan over the LQ couplings \mathbf{x} , \mathbf{y} and \mathbf{z} do not entirely agree with those obtained from the comprehensive scan over the LQ couplings $\hat{\mathbf{x}}$ and $\hat{\mathbf{y}}$, see discussion in section 6.4.

Range of LQ masses. We consider the following three values of the LQ mass m_ϕ as benchmarks

$$\hat{m}_\phi = \frac{m_\phi}{\text{TeV}} = 2, 4 \text{ and } 6. \quad (64)$$

These choices are compatible with current constraints from direct searches for LQs. The flavour structure of the LQ couplings predicts the dominant decays to be to τt , τc and νb , while branching ratios (BRs) of decays with muons and electrons as final states are suppressed by at least a further λ^2 . ATLAS [98] has constrained LQ masses to fulfil $\hat{m}_\phi \gtrsim 1.2$ at 95% C.L. for $\text{BR}(\phi \rightarrow t\tau) \sim \text{BR}(\phi \rightarrow b\nu)$. The choice of benchmark values for the LQ masses is even consistent with the strongest present limits on LQ masses from searches for LQs exclusively coupling to muons (electrons) which are constrained to $\hat{m}_\phi > 1.7(1.8)$ at 95% C.L., with minimal dependence on the coupled quark flavour [99]; see also [100].

5 Primary observables: anomalies and constraints

In this section, we first present analytic estimates that help to identify the most relevant LQ couplings for each of the primary observables in section 5.1. Then, we turn to a numerical study for scenario B in section 5.2.

LIST OF PRIMARY OBSERVABLES				
Observable	Experiment			
	Current constraint/measurement		Future reach	
$R(D)$	$0.339 \pm 0.026 \pm 0.014$	at 1σ level	[19]	± 0.016 (0.008) for 5 (50) ab^{-1} [102]
$R(D^*)$	$0.295 \pm 0.010 \pm 0.010$	at 1σ level	[19]	± 0.009 (0.0045) for 5 (50) ab^{-1} [102]
Δa_μ	$(2.51 \pm 0.59) \times 10^{-9}$	at 1σ level	[21; 57]	$\pm 0.4 \times 10^{-9}$ [103]
$\text{BR}(\tau \rightarrow \mu\gamma)$	4.2×10^{-8}	at 90% C.L.	[104]	6.9×10^{-9} [105]
$\text{BR}(\mu \rightarrow e\gamma)$	4.2×10^{-13}	at 90% C.L.	[106]	6×10^{-14} [107]
$\text{BR}(\tau \rightarrow 3\mu)$	2.1×10^{-8}	at 90% C.L.	[108]	3.6×10^{-10} [105]
$\text{BR}(\tau \rightarrow \mu e \bar{e})$	1.8×10^{-8}	at 90% C.L.	[108]	2.9×10^{-10} [105]
$\text{BR}(\mu \rightarrow 3e)$	1.0×10^{-12}	at 90% C.L.	[109]	$20(1) \times 10^{-16}$ [110]
$\text{CR}(\mu - e; \text{Al})$				$2.6(2.9) \times 10^{-17}$ [111; 112]
$R_{K^*}^\nu$	2.7	at 90% C.L.	[113]	$1.0 \pm 0.25(0.1)$ for 5 (50) ab^{-1} [114]
$g_{\tau_A}/g_A^{\text{SM}}$	1.00154 ± 0.00128	at 1σ level	[115; 116]	$\pm 7.5(0.75) \times 10^{-5}$ [116–118]
$\tau_{B_c}^{\text{SM}}$	$0.52^{+0.18}_{-0.12}$ ps	at 1σ level	[119]	
$c\bar{c} \rightarrow \tau\bar{\tau}$	$ b_{32} < 2.6$ ($\hat{m}_\phi = 2$)		[120; 121]	

Table 4: **List of primary observables.** We list the observables that dominantly constrain this model together with the current experimental constraint/measurement and the future reach. The values for $R(D)$ and $R(D^*)$ reflect the 2021 averages from the HFLAV collaboration. The future reach for $\text{BR}(\mu \rightarrow 3e)$ (in parentheses) is for Phase 1 (2) of the Mu3e experiment. For $\text{CR}(\mu - e; \text{Al})$, the first (second) value is the future reach of COMET (Mu2e). The future reach for $R_{K^*}^\nu$ assumes a result which is consistent with the SM expectation [114]. For the future projections of $g_{\tau_A}/g_A^{\text{SM}}$, we have assumed that the measurements of g_{τ_A} are improved by the same factor as $\sin^2 \theta_{\text{eff}}$ [116]; the unbracketed projection is that for the International Linear Collider (ILC) [117], and the bracketed value is for the Future Circular Collider (FCC) [118]. The current experimental constraint on the B_c lifetime is $\tau_{B_c}^{\text{exp}} = (0.510 \pm 0.009)$ ps [19; 93]. Note that the constraint arising from high- p_T lepton searches differs from the other constraints, since it is directly imposed in the primary scan via an adequate restriction of the range for $|b_{32}|$ as indicated.

5.1 Analytic estimates

The analytic estimates, derived in the following, are expressed in terms of the effective parameters in the charged fermion mass basis. The underlying complete formulae can be found in appendix C. Note, in particular, that the low-energy effective theory (LEFT) Wilson coefficients are given in the Jenkins-Manohar-Stoffer (JMS) basis [101].

5.1.1 $R(D)$ and $R(D^*)$

The LFU ratios $R(D)$ and $R(D^*)$ are observables of high importance for this study. Taking into account only tree-level corrections induced by the LQ ϕ , schematically depicted in the left of figure 1, we find the following terms in the relevant effective semi-leptonic charged-current Lagrangian

$$\begin{aligned}
\mathcal{L} \supset & C_{vedu,ij32}^{VLL} (\bar{\nu}_i \gamma^\mu P_L e_j) (\bar{b} \gamma_\mu P_L c) + C_{vedu,ij32}^{SRR} (\bar{\nu}_i P_R e_j) (\bar{b} P_R c) \\
& + C_{vedu,ij32}^{TRR} (\bar{\nu}_i \sigma^{\mu\nu} P_R e_j) (\bar{b} \sigma_{\mu\nu} P_R c) + \text{h.c.} .
\end{aligned} \tag{65}$$

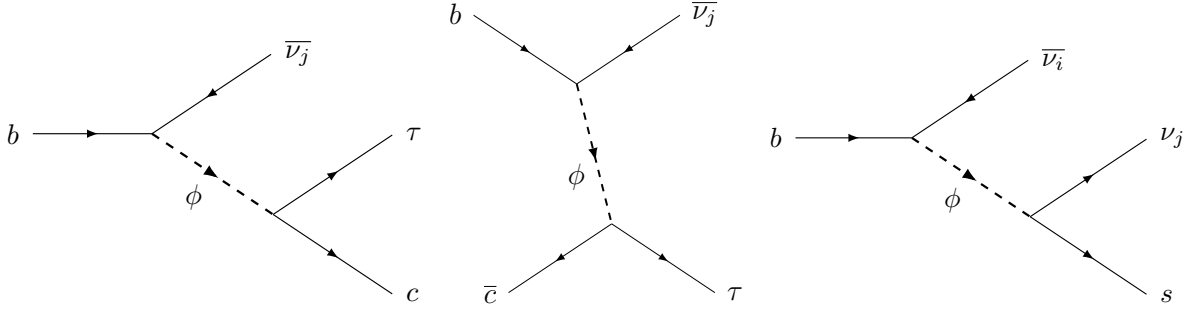


Figure 1: Feynman diagrams for tree-level contributions to charged-current $b \rightarrow c$ processes (left, centre) and neutral-current $b \rightarrow s$ processes (right) via an intermediate LQ, ϕ .

The relation between the scalar and tensor Wilson coefficients, $C_{\nu edu,ij32}^{SRR}(m_\phi) = -4 C_{\nu edu,ij32}^{TRR}(m_\phi)$, which becomes $C_{\nu edu,ij32}^{SRR}(\mu_B) \approx -8 C_{\nu edu,ij32}^{TRR}(\mu_B)$ at the hadronic scale $\mu = \mu_B = 4.8$ GeV due to RG running, indicates that contributions from the tensor operator only play a role, if they are enhanced via form factors or the phase-space configuration.

We derive analytic expressions for $R(D)$ and $R(D^*)$ from the requirement of (approximate) agreement with the results obtained from `flavio` [62; 63], v2.3, that is, we also use the values $R(D)_{\text{SM}} = 0.297 \pm 0.008$ and $R(D^*)_{\text{SM}} = 0.245 \pm 0.008$ given by `flavio`. In particular, the latter exhibits a tension with experimental data at the $\sim 3\sigma$ level, see table 1 and section 5.2.2.¹⁷

The LQ ϕ modifies $R(D)$ and $R(D^*)$ dominantly via contributions to the tau lepton channel, that is $j = 3$ in the above formulae. As expected, the largest correction occurs for a tau neutrino ν_τ in the final state which allows for interference with the SM contribution. Nonetheless, we generically also account for the lepton flavour violating (LFV) contribution with a muon neutrino ν_μ in the estimates of the relevant observables in this section (see e.g. in eq. (66) and eq. (67) the rightmost terms), as this may have an appreciable impact. On the contrary, the channel with an electron neutrino ν_e can always be neglected, since the involved couplings are very small as a result of the residual symmetry Z_{17}^{diag} , that is, $x_{11}, x_{13} \sim \lambda^9$ and $x_{12} \sim \lambda^{11}$, see eq. (54).

Corrections to $R(D)$ are mainly due to the interference between the scalar-operator contribution and the SM one

$$\begin{aligned} \frac{R(D)}{R(D)_{\text{SM}}} &\approx 1 - 1.17 \text{Re} \left(\hat{C}_{\nu edu,3332}^{SRR}(\mu_B) \right) + 0.63 \left(\left| \hat{C}_{\nu edu,3332}^{SRR}(\mu_B) \right|^2 + \left| \hat{C}_{\nu edu,2332}^{SRR}(\mu_B) \right|^2 \right) \\ &\quad + 0.72 \text{Re} \left(\hat{C}_{\nu edu,3332}^{TRR}(\mu_B) \right) + 0.37 \left(\left| \hat{C}_{\nu edu,3332}^{TRR}(\mu_B) \right|^2 + \left| \hat{C}_{\nu edu,2332}^{TRR}(\mu_B) \right|^2 \right) \\ &\approx 1 + 1.07 \frac{|a_{33} b_{32}|}{\hat{m}_\phi^2} \cos(\text{Arg}(a_{33}) - \text{Arg}(b_{32})) + 0.46 \frac{|a_{33} b_{32}|^2}{\hat{m}_\phi^4} + 0.02 \frac{|a_{23} b_{32}|^2}{\hat{m}_\phi^4}. \end{aligned} \quad (66)$$

Here, we have introduced dimensionless Wilson coefficients $\hat{C} = C \times \text{TeV}^2$ for convenience. The dominant corrections to $R(D^*)$ are sourced by the interference between the tensor operator and the SM in this model

$$\begin{aligned} \frac{R(D^*)}{R(D^*)_{\text{SM}}} &\approx 1 + 0.10 \text{Re} \left(\hat{C}_{\nu edu,3332}^{SRR}(\mu_B) \right) + 0.03 \left(\left| \hat{C}_{\nu edu,3332}^{SRR}(\mu_B) \right|^2 + \left| \hat{C}_{\nu edu,2332}^{SRR}(\mu_B) \right|^2 \right) \\ &\quad + 4.21 \text{Re} \left(\hat{C}_{\nu edu,3332}^{TRR}(\mu_B) \right) + 8.60 \left(\left| \hat{C}_{\nu edu,3332}^{TRR}(\mu_B) \right|^2 + \left| \hat{C}_{\nu edu,2332}^{TRR}(\mu_B) \right|^2 \right) \\ &\approx 1 + 0.36 \frac{|a_{33} b_{32}|}{\hat{m}_\phi^2} \cos(\text{Arg}(a_{33}) - \text{Arg}(b_{32})) + 0.12 \frac{|a_{33} b_{32}|^2}{\hat{m}_\phi^4} + 0.01 \frac{|a_{23} b_{32}|^2}{\hat{m}_\phi^4}. \end{aligned} \quad (67)$$

¹⁷Since v2.0, `flavio` uses the form factors of reference [64] which are determined via Heavy-Quark Effective Theory. Furthermore, the implementation is based on the helicity formalism [122] which has been extensively tested as a general framework.

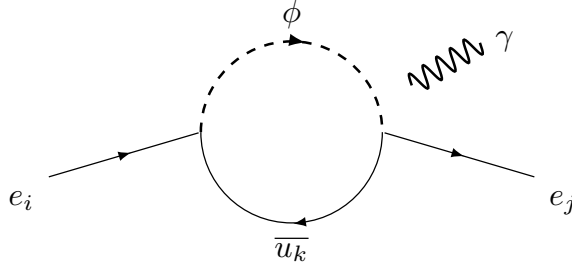


Figure 2: Feynman diagram for the one-loop contribution to the process $e_i \rightarrow e_j \gamma$ via an intermediate LQ (ϕ) and an up-type quark (u_k).

Note that contributions from the vector operator to $R(D^{(*)})$ are suppressed because of the hierarchy $z_{32}/y_{32} \sim \lambda^2$, see eq. (58) and eq. (60).

5.1.2 Anomalous magnetic moment of muon and muon mass correction

Given that the deviation from the SM prediction for the AMM of the muon, Δa_μ , is of 4.2σ significance [21; 57], we discuss the viability of this model in explaining this anomaly. The leading-order LQ contribution is generated by the one-loop diagram shown in figure 2. In particular, it is dominated by the contribution in which the chirality flip occurs via a mass insertion on the internal quark leg – and can therefore be enhanced by the mass of this quark (here denoted m_{u_k} , consistent with figure 2). For the full calculation of the leptonic AMM, we refer to appendix C.2.

Taking the dominant contribution to be the one with the top quark in the loop, and $m_\phi \gg m_{u_k}$, eq. (131) and eq. (144) in appendix C.2 reduce to the following

$$\Delta a_\mu \approx -\frac{2 \operatorname{Re}(b_{23}c_{23}^*)}{\hat{m}_\phi^2} \times 10^{-9} = -\frac{2|b_{23}c_{23}|}{\hat{m}_\phi^2} \cos(\operatorname{Arg}(b_{23}) - \operatorname{Arg}(c_{23})) \times 10^{-9}. \quad (68)$$

Contrasting this with table 4, the order of magnitude of the AMM of the muon generated by this model can be consistent with the present experimental average.

Requiring that this anomaly is addressed tightly constrains the parameter space of the order-one coefficients c_{23} and b_{23} . To satisfy the current experimental value at the n -sigma level requires them to obey the following relations

$$\left| \begin{cases} 0.890 \operatorname{Re}(b_{23}c_{23}^*) + 2.51, & \hat{m}_\phi = 2 \\ 0.307 \operatorname{Re}(b_{23}c_{23}^*) + 2.51, & \hat{m}_\phi = 4 \\ 0.159 \operatorname{Re}(b_{23}c_{23}^*) + 2.51, & \hat{m}_\phi = 6 \end{cases} \right| \lesssim n \times 0.59 [0.4]. \quad (69)$$

Here, the current experimental bound is shown with the prospective sensitivity given in square brackets. The latter assumes that the best-fit value remains fixed but with the target precision listed in table 4. Results for the AMM of the electron and of the tau lepton are discussed in section 6.7.

Given that we generally consider complex LQ couplings, there is scope to generate both an AMM and an electric dipole moment (EDM) for charged leptons, as discussed in appendix C.2. The leptonic EDMs do not presently provide competitive constraints on the parameter space of this model and, therefore, we defer the discussion of these to section 6.

Through a diagram similar to that shown in figure 2, the LQ also introduces a correction to the muon mass. Adapting the result from reference [116], the full expression for this correction can be found in appendix C.1. At LO this contribution reduces to

$$m_\mu \approx \left| m_\mu^{\text{tree}} - \frac{3}{16\pi^2} m_t b_{23} c_{23}^* \lambda^4 (1 + t_t \ln t_t) \right| \lesssim \left| m_\mu^{\text{tree}} \right| + \left| \frac{3}{16\pi^2} m_t b_{23} c_{23}^* \lambda^4 (1 + t_t \ln t_t) \right|, \quad (70)$$

where m_μ^{tree} denotes the tree-level muon mass, the upper bound follows from the triangle inequality, and t_X denotes the mass squared of particle X normalised to the LQ mass squared, i.e.

$$t_X = \frac{m_X^2}{m_\phi^2}. \quad (71)$$

In the region of parameter space consistent with explaining the AMM of the muon, we observe numerically that the correction can be significant at the order of 80 percent, with this value being extracted from the data output of the comprehensive scan discussed in section 6. However, as stated in section 3.2, it is always possible to absorb this correction by redefining the effective parameter e_{22} .¹⁸

5.1.3 Radiative charged lepton flavour violating decays $e_i \rightarrow e_j \gamma$

Similarly to the AMM of the muon, cLFV decays of the form $e_i \rightarrow e_j \gamma$ proceed at LO via the one-loop diagram given in figure 2. Notably, the diagram for the contribution to the AMM of the muon shares a common vertex with both the ones for the cLFV decays $\tau \rightarrow \mu \gamma$ and $\mu \rightarrow e \gamma$. Therefore, we expect these two decays to provide competitive constraints on the explanation of the former anomaly. From table 4, we see that the present experimental bound on $\text{BR}(\mu \rightarrow e \gamma)$ is five orders of magnitude more stringent than $\text{BR}(\tau \rightarrow \mu \gamma)$. However, the former provides a weaker constraint due to the efficient suppression of the LQ coupling y_{13} , $y_{13} = b_{13} \lambda^9$, thanks to the residual symmetry Z_{17}^{diag} , see eq. (58).

Following from eq. (131) and eq. (142) in appendix C.2, we arrive at the following expressions for the LO contributions to these BRs, parametrising the contributions from loops containing the top quark

$$\text{BR}(\mu \rightarrow e \gamma) \sim \frac{|b_{13} c_{23}|^2}{\hat{m}_\phi^4} \times 10^{-11}, \quad (72)$$

and

$$\text{BR}(\tau \rightarrow \mu \gamma) \sim \frac{|b_{23} c_{33}|^2}{\hat{m}_\phi^4} \times 10^{-5}. \quad (73)$$

Comparing these with the constraints quoted in table 4, these estimates show that significant rates for both decay modes can be generated. We, thus, use these to constrain the relevant couplings as follows, where the current experimental bound is shown with the prospective sensitivity mentioned in square brackets. For $\mu \rightarrow e \gamma$, we have

$$|b_{13} c_{23}| \lesssim \left\{ \begin{array}{l} 0.444 [0.168], \quad \hat{m}_\phi = 2 \\ 1.264 [0.477], \quad \hat{m}_\phi = 4 \\ 5.915 [0.845], \quad \hat{m}_\phi = 6 \end{array} \right\}. \quad (74)$$

This shows that this constraint is especially strong for smaller LQ masses. As indicated above, the parameter c_{23} appears in the expressions for both $\text{BR}(\mu \rightarrow e \gamma)$ and the AMM of the muon, which makes the constraint from $\text{BR}(\mu \rightarrow e \gamma)$ important for refining the parameter space which could explain the measured value of the AMM of the muon. Similarly, for $\tau \rightarrow \mu \gamma$ we find

$$|b_{23} c_{33}| \lesssim \left\{ \begin{array}{l} 0.259 [0.105], \quad \hat{m}_\phi = 2 \\ 1.037 [0.420], \quad \hat{m}_\phi = 4 \\ 2.333 [0.946], \quad \hat{m}_\phi = 6 \end{array} \right\}. \quad (75)$$

¹⁸An alternative approach to addressing the correction of the muon mass would be to implement a constraint based on its size, as is done for example in references [123; 124].

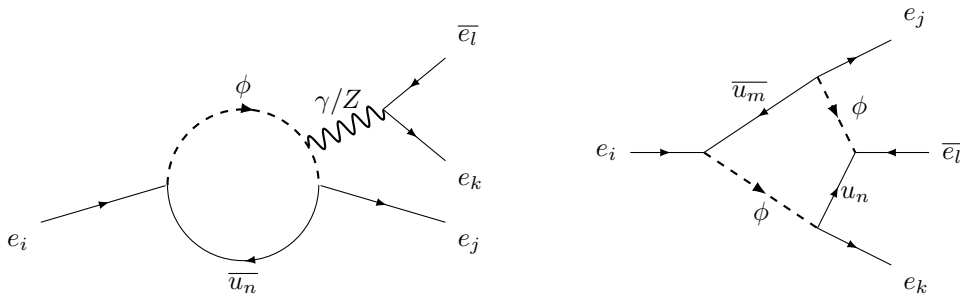


Figure 3: Representative Feynman diagrams for the process $e_i \rightarrow e_j e_k \bar{e}_l$ mediated by the LQ ϕ at one-loop order, where the up-type quarks u_n and u_m run in the loop.

Here, the effective parameter b_{23} appears, but also the parameter $c_{33} \approx a_{33}$. The latter plays an important role in the generation of the corrections to $R(D)$ and $R(D^*)$ in this model, as discussed in section 5.1.1.

5.1.4 Trilepton decays $e_i \rightarrow e_j e_l \bar{e}_l$

Trilepton cLFV decays provide another sensitive probe for new physics, particularly in light of several relevant future sensitivities. Representative Feynman diagrams are shown in figure 3. The dominant contributions to the three most sensitive processes are

$$\text{BR}(\mu \rightarrow 3e) \sim \frac{|b_{13}c_{23}|^2}{\hat{m}_\phi^4} \times 10^{-14}, \quad (76)$$

$$\text{BR}(\tau \rightarrow 3\mu) \sim \frac{|b_{23}c_{33}|^2 + 0.07 |c_{23}c_{33}|^2}{\hat{m}_\phi^4} \times 10^{-7}, \quad (77)$$

$$\text{BR}(\tau \rightarrow \mu e \bar{e}) \sim \frac{|b_{23}c_{33}|^2 + 0.05 |c_{23}c_{33}|^2}{\hat{m}_\phi^4} \times 10^{-7}. \quad (78)$$

Besides the respective long-distance γ -penguin contribution with the chirality flip due to an internal top quark, for tau lepton decays we also take into account the Z -penguin contribution with two internal top quark mass insertions which, although suppressed, becomes relevant for some regions of the parameter space. The full expressions for the BRs can be retrieved from eq. (145) and eq. (147) in appendix C.2.4 for the relevant flavour combinations. For γ -penguin dominance, one finds [125; 126]

$$\frac{\text{BR}(\tau \rightarrow 3\mu)}{\text{BR}(\tau \rightarrow \mu\gamma)} \approx \frac{\alpha_{\text{em}}}{3\pi} \left(\ln \left(\frac{m_\tau^2}{m_\mu^2} \right) - \frac{11}{4} \right) \approx \frac{1}{400}, \quad (79)$$

and thus the existing experimental bound on $\text{BR}(\tau \rightarrow \mu\gamma)$ implies that no signal of $\tau \rightarrow 3\mu$ can be expected at Belle II. Still, sufficiently large Z -penguin contributions can render the decays $\tau \rightarrow \mu e_i \bar{e}_i$ potentially observable at Belle II.

The upper bounds on the BRs can be translated into constraints on the effective parameters. While the experimental limit on the BR of $\mu \rightarrow 3e$ is currently less sensitive compared to the one on $\mu \rightarrow e\gamma$, the Mu3e experiment [110] is expected to provide a competitive sensitivity, i.e.

$$|b_{13}c_{23}| \lesssim \begin{cases} 0.298, & \hat{m}_\phi = 2 \\ 0.840, & \hat{m}_\phi = 4 \\ 1.61, & \hat{m}_\phi = 6 \end{cases} \quad (80)$$

using the value given for Phase 2, see table 4. The decays $\tau \rightarrow 3\mu$ and $\tau \rightarrow \mu e \bar{e}$ are both mainly sensitive to $|b_{23}c_{33}|$ and lead to similar constraints on the combination. In the regime of γ -penguin

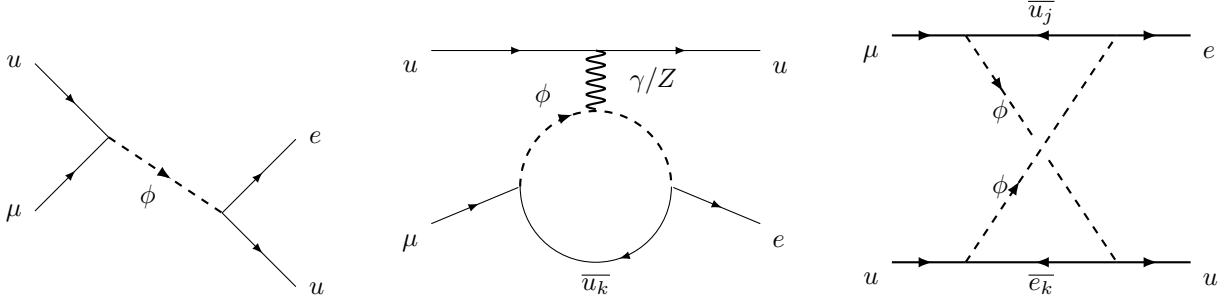


Figure 4: Representative Feynman diagrams for $\mu - e$ conversion in nuclei mediated by the LQ ϕ at tree level and one-loop order with up-type quarks u_k and u_j and the charged lepton e_k running in the loop.

dominance the BRs are closely related which results in

$$\frac{\text{BR}(\tau \rightarrow 3\mu)}{\text{BR}(\tau \rightarrow \mu e \bar{e})} \approx \frac{2 \ln(m_\tau/m_\mu) - 11/4}{2 \ln(m_\tau/m_\mu) - 3} \approx 1.09. \quad (81)$$

As the decays are mainly sensitive to small LQ masses, we only present the constraints for $\hat{m}_\phi = 2$. Currently, $\tau \rightarrow \mu e \bar{e}$ imposes [108]

$$|b_{23}c_{33}|^2 + 0.0561 |c_{23}c_{33}|^2 \lesssim 4.30 \quad \text{for } \hat{m}_\phi = 2, \quad (82)$$

while in the future the sensitivity of Belle II [114] allows to probe

$$|b_{23}c_{33}|^2 + 0.0806 |c_{23}c_{33}|^2 \lesssim 0.0655 \quad \text{for } \hat{m}_\phi = 2, \quad (83)$$

assuming the absence of a signal. Due to suppressed LQ couplings, other cLFV trilepton decays do not provide any strong constraints and neither achieve a competitive sensitivity at Belle II.

5.1.5 $\mu - e$ conversion in nuclei

There are relevant contributions to $\mu - e$ conversion in nuclei mediated by the LQ ϕ both at tree level and one-loop order. Representative Feynman diagrams are displayed in figure 4. The dominant contribution to $\mu - e$ conversion in nuclei originates from the long-range γ -penguin. We find that also tree-level scalar contributions become relevant in some part of the parameter space. Using this approximation the conversion rate (CR) can be written as, see reference [127] and also appendix C.3.8,

$$\omega_{\text{conv}} = \left| -\frac{C_{e\gamma}^{12}}{2m_\mu} D \right|^2 + \left| -\frac{C_{e\gamma}^{21*}}{2m_\mu} D + \tilde{g}_{RS}^{(p)} S^{(p)} + \tilde{g}_{RS}^{(n)} S^{(n)} \right|^2 \quad (84)$$

which is expressed in terms of the relevant dipole-operator Wilson coefficients in the JMS basis [101] and the effective scalar contribution

$$\begin{aligned} C_{e\gamma}^{21} &\approx \frac{e m_t}{64\pi^2 m_\phi^2} (7 + 4 \ln t_t) c_{23}^* b_{13} \lambda^{10}, & \tilde{g}_{RS}^{(N)} &\approx G_S^{u,N} \frac{c_{21} b_{11}^*}{2m_\phi^2} \lambda^{13}, \\ C_{e\gamma}^{12} &\approx \frac{e m_t}{64\pi^2 m_\phi^2} (7 + 4 \ln t_t) c_{13}^* b_{23} \lambda^{12} \end{aligned} \quad (85)$$

with $G_S^{u,p} = 5.1$, $G_S^{u,n} = 4.3$ [128] and $N = p, n$. Nuclear physics effects are parametrised by D and $S^{(N)}$ and the numerical values for aluminium are [127] $D = 0.0362 m_\mu^{5/2}$, $S^{(p)} = 0.0155 m_\mu^{5/2}$ and

$S^{(n)} = 0.0167 m_\mu^{5/2}$. Experiments generally report the CR normalised to the muon capture rate, $\text{CR} = \omega_{\text{conv}}/\omega_{\text{capt}}$, with the latter being $\omega_{\text{capt}} = 0.7054 \times 10^6 \text{ s}^{-1}$ for aluminium [127].

Although $\text{BR}(\mu \rightarrow e\gamma)$ currently leads to stronger constraints, $\mu - e$ conversion in aluminium can provide an excellent probe for the $\mu - e$ transition. From the expected future reach of COMET to $\text{CR}(\mu - e; \text{Al})$ in table 4, we derive

$$\left| c_{23} b_{13}^* + \begin{Bmatrix} 0.00486 \\ 0.00344 \\ 0.00293 \end{Bmatrix} c_{21} b_{11}^* \right|^2 + 0.00263 |c_{13}^* b_{23}|^2 \lesssim \begin{Bmatrix} 0.00373, & \hat{m}_\phi = 2 \\ 0.0300, & \hat{m}_\phi = 4 \\ 0.110, & \hat{m}_\phi = 6 \end{Bmatrix} \quad (86)$$

under the assumption of no signal. The dominant contribution is constituted by the combination $c_{23} b_{13}^*$ which is also constrained by the non-observation of $\mu \rightarrow e\gamma$. In fact, if all other contributions are neglected, the CR exhibits the strict correlation $\text{CR}(\mu - e; \text{Al}) \approx 0.0027 \text{BR}(\mu \rightarrow e\gamma)$.

5.1.6 $B_c \rightarrow \tau\nu$

In this model, the LQ ϕ contributes to the leptonic decay $B_c \rightarrow \tau\nu$ and therefore modifies the lifetime of the B_c meson via the process illustrated in the centre of figure 1, see reference [129]. In line with this approach, we employ a constraint on the B_c lifetime in the SM in this work. We equate the measured decay width with the sum of the contributions of the SM and from the LQ ϕ , i.e.

$$\Gamma_{B_c}^{\text{exp}} = \Gamma_{B_c}^{\text{SM}} + \Gamma_{B_c}^\phi. \quad (87)$$

Here, we fix $\tau_{B_c}^{\text{exp}} = 1/\Gamma_{B_c}^{\text{exp}} = 0.510 \pm 0.009 \text{ ps}$ [93] to the best-fit value while $\Gamma_{B_c}^\phi$ accounts for the tree-level process $bc \rightarrow \tau\nu$ induced by ϕ . The decay width $\Gamma_{B_c}^\phi$ can be calculated by subtracting the SM contribution to $\Gamma(B_c \rightarrow \tau\nu)$, see eq. (162) and eq. (164). Hence, it also captures interference effects. $\Gamma_{B_c}^{\text{SM}}$ takes into account all SM contributions to the B_c decay width.

We do not attempt a calculation of $\Gamma_{B_c}^{\text{SM}} = 1/\tau_{B_c}^{\text{SM}}$, but instead indirectly infer it from eq. (87) and confront this inferred value with the result $\tau_{B_c}^{\text{SM}} \in [0.4, 0.7] \text{ ps}$ [119], see also table 4 and eq. (165) for the complete expression.¹⁹ The LQ ϕ mainly sources the channel with a tau neutrino ν_τ in the final state. Upon rearranging eq. (87), one approximately finds

$$\frac{\tau_{B_c}^{\text{SM}}}{\tau_{B_c}^{\text{exp}}} = \left[1 - \frac{\Gamma_{B_c}^\phi}{\Gamma_{B_c}^{\text{exp}}} \right]^{-1} \approx 1 + \frac{\Gamma_{B_c}^\phi}{\Gamma_{B_c}^{\text{exp}}} \quad (88)$$

$$\approx 1 - 0.13 \frac{\text{Re}(a_{33} b_{32})}{\hat{m}_\phi^2} + 0.19 \frac{|a_{33} b_{32}|^2}{\hat{m}_\phi^4} + 0.01 \frac{|a_{23} b_{32}|^2}{\hat{m}_\phi^4} \quad (89)$$

$$= 1 - 0.13 \frac{|a_{33} b_{32}|}{\hat{m}_\phi^2} \cos(\text{Arg}(a_{33}) - \text{Arg}(b_{32})) + 0.19 \frac{|a_{33} b_{32}|^2}{\hat{m}_\phi^4} + 0.01 \frac{|a_{23} b_{32}|^2}{\hat{m}_\phi^4} \quad (90)$$

where the rightmost term in eq. (89) and eq. (90) represents the LFV contribution with a muon neutrino ν_μ in the final state. Eq. (87) is also equivalent to the following relation

$$\text{BR}(B_c \rightarrow \tau\nu) = \text{BR}(B_c \rightarrow \tau\nu)_{\text{SM}} - \left(\frac{\tau_{B_c}^{\text{exp}}}{\tau_{B_c}^{\text{SM}}} - 1 \right). \quad (91)$$

Thereby, imposing an upper bound on the BR, say $\text{BR}(B_c \rightarrow \tau\nu) \lesssim 0.3$ [129] or $\text{BR}(B_c \rightarrow \tau\nu) \lesssim 0.1$ [132], which takes into account the (semi)tauonic contributions in the SM and from new physics, is equivalent to $\tau_{B_c}^{\text{SM}} \lesssim 0.70 \text{ ps}$ or $\tau_{B_c}^{\text{SM}} \lesssim 0.55 \text{ ps}$, respectively.

¹⁹For more recent calculations of the B_c lifetime in the SM, see references [130; 131].

5.1.7 $R_{K^{(*)}}^\nu$

We consider the decay $B \rightarrow K^{(*)}\nu\bar{\nu}$ and normalise it to the respective SM prediction in the ratio $R_{K^{(*)}}^\nu$. Eq. (166) contains the full expression for this contribution, which is derived following reference [133]. The dominant contributions arise via the process illustrated in figure 1, and give

$$\begin{aligned}
R_{K^{(*)}}^\nu \approx & 1 + 1.69 \frac{|a_{33}a_{32}|}{\hat{m}_\phi^2} \cos(\text{Arg}(a_{33}) - \text{Arg}(a_{32})) + 2.15 \frac{|a_{33}a_{32}|^2}{\hat{m}_\phi^4} \\
& + 0.09 \frac{|a_{23}a_{22}|}{\hat{m}_\phi^2} \cos(\text{Arg}(a_{23}) - \text{Arg}(a_{22})) + 0.01 \frac{|a_{23}a_{22}|^2}{\hat{m}_\phi^4} \\
& + 0.11 \left(\frac{|a_{23}a_{32}|^2}{\hat{m}_\phi^4} + \frac{|a_{33}a_{22}|^2}{\hat{m}_\phi^4} \right).
\end{aligned} \tag{92}$$

The first line of eq. (92) represents the contribution from the tau neutrino-antineutrino pair $\nu_\tau\bar{\nu}_\tau$ in the final state, while the second line encodes the contribution from the combination $\nu_\mu\bar{\nu}_\mu$, and the last line contains the LFV contribution from the combinations $\nu_\tau\bar{\nu}_\mu$ and $\nu_\mu\bar{\nu}_\tau$, respectively. As the contributions to RH vector currents are negligible in this model, we have $R_K^\nu = R_{K^*}^\nu$ and thus the more stringent experimental bound, $R_{K^*}^\nu < 2.7$ at 90% C.L. [113], acts as a primary constraint.

5.1.8 $Z \rightarrow \tau\tau$

Inducing contributions to $b \rightarrow c\tau\nu$ in this model, as discussed in section 5.1.1, requires that the LQ coupling to the bottom quark and (in particular) the tau neutrino, encoded in a_{33} , is enhanced. This effective parameter is related via the CKM mixing matrix to c_{33} which describes the coupling between the top quark and the tau lepton. Therefore, an explanation of the flavour anomalies in $R(D)$ and $R(D^*)$ may be associated with large corrections via a top-quark loop to $Z \rightarrow \tau\tau$. These contributions are illustrated in figure 5.

Following from reference [134], we parametrise these contributions by considering the effective axial-vector couplings of the Z boson to fermions, where the full expressions for these contributions can be found in appendix C.4. At LO for the effective $\tau\tau$ coupling, eq. (191) in appendix C.4 reduces to

$$\delta g_{\tau_A} \approx \left\{ \begin{array}{l} 2.28, \quad \hat{m}_\phi = 2 \\ 0.75, \quad \hat{m}_\phi = 4 \\ 0.38, \quad \hat{m}_\phi = 6 \end{array} \right\} |c_{33}|^2 \times 10^{-4}. \tag{93}$$

Following from appendix C.4 for the definition of $g_A^{\text{SM}} (< 0)$, taking lepton flavour to be conserved for SM couplings (i.e. g_A^{SM} is the same for all lepton flavours) this yields

$$g_{\tau_A}/g_A^{\text{SM}} \approx 1 - \left[\left\{ \begin{array}{l} 4.54, \quad \hat{m}_\phi = 2 \\ 1.50, \quad \hat{m}_\phi = 4 \\ 0.75, \quad \hat{m}_\phi = 6 \end{array} \right\} |c_{33}|^2 \times 10^{-4} \right]. \tag{94}$$

Therefore, allowing for a 3σ margin about the best-fit value quoted in table 4, we obtain the following constraints on $|c_{33}|$

$$|c_{33}| \lesssim \left\{ \begin{array}{l} 2.25, \quad \hat{m}_\phi = 2 \\ 3.92, \quad \hat{m}_\phi = 4 \\ 5.50, \quad \hat{m}_\phi = 6 \end{array} \right\}. \tag{95}$$

Note that if the present best-fit value for $g_{\tau_A}/g_A^{\text{SM}}$ remains the same, but if either of the projected sensitivities to this observable mentioned in table 4 are reached, then this model would not be

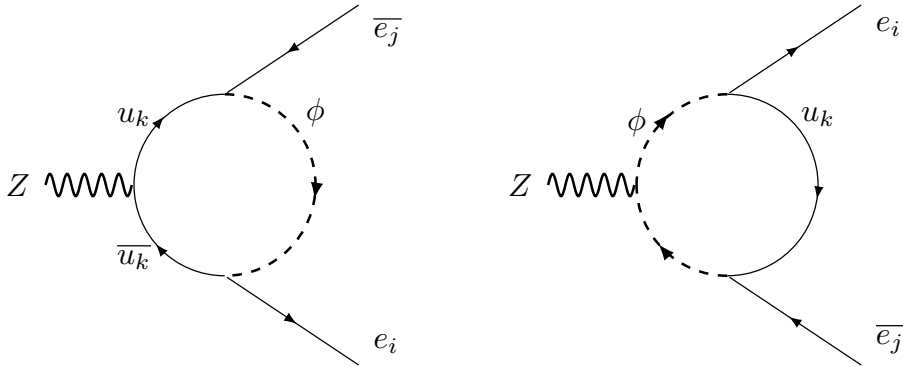


Figure 5: Dominant LQ, ϕ , contribution to the process $Z \rightarrow e_i \bar{e}_j$, arising at one-loop order with the up-type quark u_k running in the loop.

capable of addressing this deviation from the SM value. Thus, we do not give a future reach for the bound on $|c_{33}|$ in eq. (95). This is seen explicitly from the results presented in section 5.2.5 and in section 6.

5.1.9 High- p_T dilepton searches

Several recent studies [121; 135–137] have placed constraints on effective operators using LHC data. In reference [121], the process $q\bar{q} \rightarrow \tau\bar{\tau}$ has been considered for the LQ ϕ , among other ones, and the ATLAS analysis in reference [120] has been reinterpreted in order to put a constraint on the LQ couplings for masses $1 \leq \hat{m}_\phi \leq 3$. Reading off from the top-right of figure 4 in reference [121] and using the fact that the LHC does not distinguish between chiralities, we find an upper bound for the LQ coupling involving a RH tau lepton and a charm quark

$$|y_{32}| = |b_{32}| < \hat{m}_\phi + 0.6. \quad (96)$$

Similarly, in reference [137] the process $b + c \rightarrow \tau + \nu$ has been considered and two analyses [138; 139] by ATLAS and CMS have been recast to place a constraint on the charged-current effective operators. The resulting constraints, under the assumption of the dominance of a single operator, are found in table II of reference [137]. In terms of the effective couplings at the LQ mass scale, they read

$$\sqrt{|a_{33}c_{32}|} < 3.5 \hat{m}_\phi \quad \text{and} \quad \sqrt{|a_{33}b_{32}|} < 0.70 \hat{m}_\phi, \quad (97)$$

where we have included RG corrections due to QCD using `RunDec` [140; 141]. Still, these constraints are automatically respected in the model, if the experimental bounds on other primary observables are imposed.

5.2 Numerical study

In this section, we present and discuss the results of a numerical scan taking into account the primary observables. The focus rests on studying the way in which the imposed current experimental bounds shape the parameter space compatible with the model, and how this affects the possibility to explain the observed flavour anomalies in $R(D^{(*)})$ and in the AMM of the muon, see table 4. Furthermore, the results help to establish biases for the comprehensive scan discussed in section 6.

Observable	Effective parameters	Observable	Effective parameters
$R(D)$	$a_{33}, b_{32}, (a_{23})$	$\text{BR}(\mu \rightarrow 3e)$	b_{13}, c_{23}
$R(D^*)$	$a_{33}, b_{32}, (a_{23})$	$\text{CR}(\mu - e; \text{Al})$	$b_{13}, c_{23}, (b_{11}, b_{23}, c_{13}, c_{21})$
Δa_μ	b_{23}, c_{23}	$R_{K^*}^\nu$	$a_{32}, a_{33}, (a_{22}, a_{23})$
$\text{BR}(\tau \rightarrow \mu\gamma)$	b_{23}, c_{33}	$g_{\tau A}/g_A^{\text{SM}}$	c_{33}
$\text{BR}(\mu \rightarrow e\gamma)$	b_{13}, c_{23}	$\tau_{B_c}^{\text{SM}}$	$a_{33}, b_{32}, (a_{23})$
$\text{BR}(\tau \rightarrow 3\mu)$	$b_{23}, c_{33}, (c_{23})$	$c\bar{c} \rightarrow \tau\bar{\tau}$	b_{32}
$\text{BR}(\tau \rightarrow \mu e\bar{e})$	$b_{23}, c_{33}, (c_{23})$	$bc \rightarrow \tau\nu$	$a_{33}, b_{32}, (c_{32})$

Table 5: **List of primary observables and relevant effective parameters.** We list the observables that dominantly constrain this model together with the effective parameters of LQ couplings in the charged fermion mass basis, see section 3.3.2, which capture the most relevant contributions, respectively, in line with the analytic estimates performed in section 5.1. The parameters listed in round brackets refer to subdominant contributions.

5.2.1 Preliminaries

According to the strategy outlined in section 4, the following discussion refers to scenario B only. The effective parameters²⁰ a_{ij} , b_{ij} and c_{ij}^B (except for c_{12}^B , see below) of the LQ couplings \mathbf{x} , \mathbf{y} and \mathbf{z} are independently varied within the ranges given in eqs. (62) and (63). Note that we make a different choice in the case of $|b_{32}|$ for $\hat{m}_\phi = 2$, see table 4. Furthermore, combining eqs. (57), (61) and the first line in eq. (124) with the structure of the CKM mixing matrix in scenario B, see eqs. (38) and (40), one finds

$$|V_{us}| \approx \left| \frac{c_{12}^B}{a_{11}} \right| \lambda, \quad |V_{cb}| \approx |\tilde{c}| \lambda^2 \quad \text{and} \quad |V_{td}| \approx |\bar{c}| \lambda^3 \quad (98)$$

up to corrections of higher order in λ . Comparing these predictions to the best-fit values of the experimentally inferred CKM mixing matrix elements, $|V_{us}| = \lambda = 0.22650_{-0.00048}^{+0.00048}$, $|V_{cb}| = 0.04053_{-0.00061}^{+0.00083}$, and $|V_{td}| = 0.00854_{-0.00016}^{+0.00023}$ [93], we conclude that the relation between the LQ couplings \mathbf{x} and \mathbf{z} is, indeed, to a good approximation given by the CKM mixing matrix, if we constrain the parameters c_{12}^B , \tilde{c} and \bar{c} as follows

$$c_{12}^B = a_{11} \alpha e^{i\omega_1}, \quad \tilde{c} = \beta e^{i\omega_2}, \quad \bar{c} = \gamma e^{i\omega_3} \quad (99)$$

with

$$0.5 \leq \alpha, \beta, \gamma \leq 1.5. \quad (100)$$

The phases are varied in the full range

$$0 \leq \omega_i < 2\pi \quad \text{for } i = 1, 2, 3. \quad (101)$$

Here, no information about CP phases, captured by the Jarlskog invariant, has been taken into account.

The subsequent discussion including the figures is based on a sample comprising $4(3)[2] \times 10^6$ points for $\hat{m}_\phi = 2(4)[6]$. The hadronic observables $R(D)$, $R(D^*)$ and $\tau_{B_c}^{\text{SM}}$ exhibit RG running under QCD and so we evaluate them at the scale $\mu = \mu_B = 4.8 \text{ GeV}$, as detailed in appendix C.3.2. On the contrary, the remaining leptonic observables are evaluated at $\mu = m_\phi$, that is, we neglect

²⁰We remind that c_{ij} and c_{ij}^B are in general two inequivalent sets of effective parameters, see section 3.3.2.

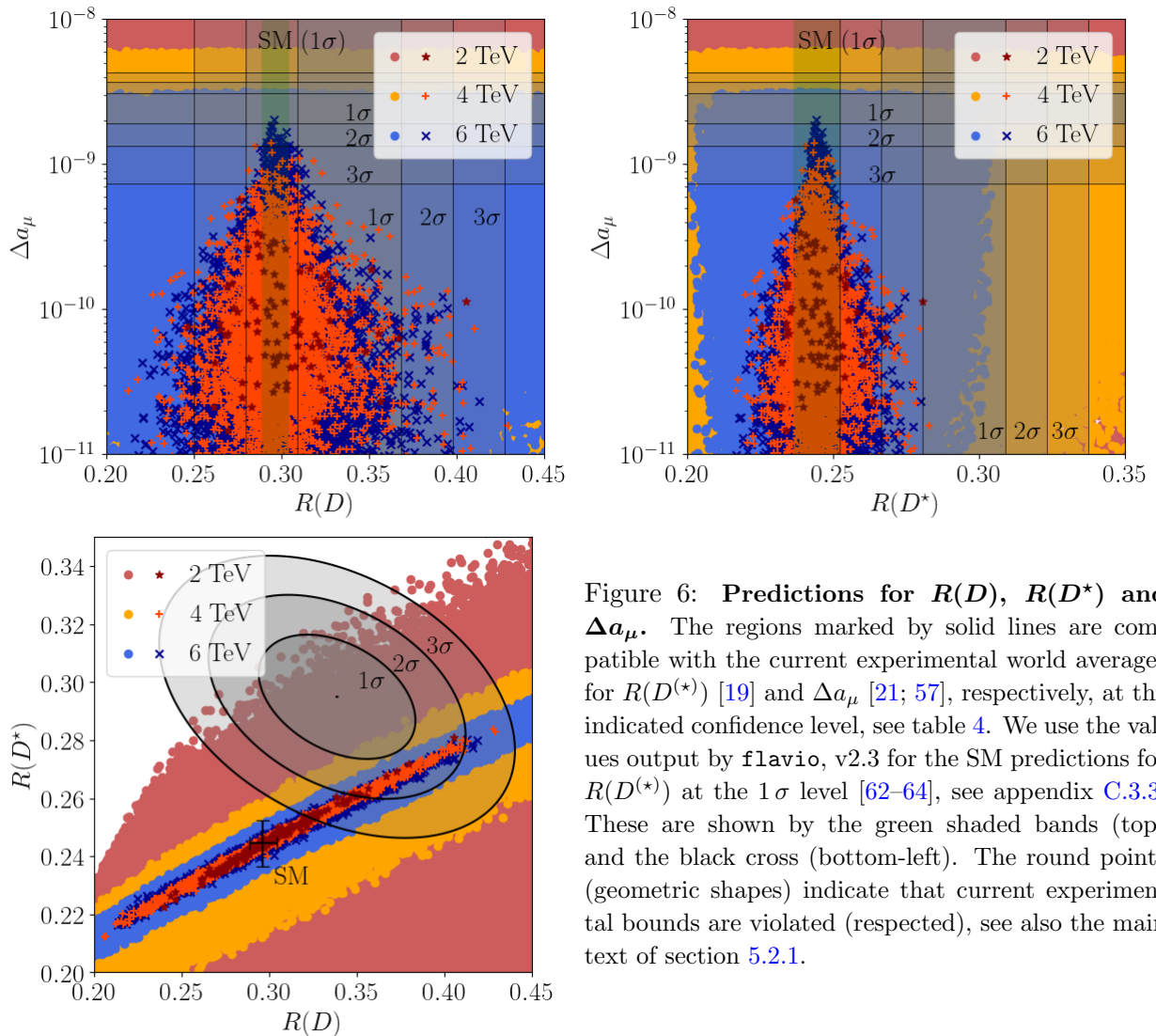


Figure 6: **Predictions for $R(D)$, $R(D^*)$ and Δa_μ .** The regions marked by solid lines are compatible with the current experimental world averages for $R(D^*)$ [19] and Δa_μ [21; 57], respectively, at the indicated confidence level, see table 4. We use the values output by `flavio`, v2.3 for the SM predictions for $R(D^*)$ at the 1σ level [62–64], see appendix C.3.3. These are shown by the green shaded bands (top) and the black cross (bottom-left). The round points (geometric shapes) indicate that current experimental bounds are violated (respected), see also the main text of section 5.2.1.

the smaller contributions from QED running in this section. We impose the current experimental bounds on $\text{BR}(\tau \rightarrow \mu\gamma)$, $\text{BR}(\mu \rightarrow e\gamma)$, $\text{BR}(\tau \rightarrow 3\mu)$, $\text{BR}(\tau \rightarrow \mu e\bar{e})$, $\text{BR}(\mu \rightarrow 3e)$, $R_{K^{(*)}}^\nu$, $\tau_{B_c}^{\text{SM}}$ and $g_{\tau_A}/g_A^{\text{SM}}$, see table 4. For completeness, we also track the contributions to the scalar charged-current Wilson coefficient $C_{vedu,3332}^{SRR}$ and provide a brief discussion in appendix D.

In general, for the scatter plots in this section we use round sample points to indicate the violation of at least one of the imposed experimental bounds, and the ones with a specific shape (star, plus, cross) show that all considered current bounds are respected. The employed colours as well as shapes allow to distinguish well between the results for the different LQ masses, $\hat{m}_\phi = 2, 4, 6$, as displayed in the plot legends. Furthermore, solid lines generally refer to current experimental data at a given confidence level, whereas a dashed line indicates a prospective bound or a future sensitivity. Gray shadings are used in order to better distinguish the regions in parameter space compatible with current data at different confidence levels. Besides, the green shaded regions, as well as the black cross in the bottom-left plot of figure 6, indicate the SM prediction for $R(D)$ and $R(D^*)$ at the 1σ level, respectively.

5.2.2 $R(D)$, $R(D^*)$ and anomalous magnetic moment of muon

Addressing the anomalies. The capability of this model to explain the anomalies in $R(D)$, $R(D^*)$ and in the AMM of the muon, as found in the primary scan, is illustrated in figure 6. A

priori, a value up to $\Delta a_\mu \approx 3 \times 10^{-9}$ or larger can be achieved, depending on the LQ mass, in accordance with the analytic estimate in eq. (68) in the case of large LQ couplings. Still, after imposing the experimental bounds of all primary observables, a result of the order $\Delta a_\mu \sim 10^{-9}$ is not generic, but instead we find a suppression by one or two orders of magnitude for about 90 percent of the viable sample points with positive Δa_μ generated in the primary scan, irrespective of the LQ mass. We remark that imposing these experimental bounds does not lead to a preference for either sign of Δa_μ , as is expected, since none of the primary observables exhibits a particular sensitivity to the phase of b_{23} or $c_{23} \approx a_{23}$.²¹ Nevertheless, the results hint towards the possibility of explaining Δa_μ at the 2σ level or better in this model, see the top in figure 6.

Furthermore, as expected from eq. (68), i.e. $\Delta a_\mu \propto |b_{23}c_{23}|$, and $R(D^{(*)})$ mainly controlled by $|a_{33}b_{32}|$, see eqs. (66, 67), these observables are a priori not (strongly) correlated in this model. The distribution of viable sample points in figure 6 is due to the experimental constraint on $\text{BR}(\tau \rightarrow \mu\gamma)$, see section 5.2.3 for more details. In particular, this entails a tension between explaining the flavour anomaly in $R(D^{(*)})$ at the 3σ level or better and generating $\Delta a_\mu \sim 10^{-9}$.

Using `flavio` [62–64] (since v2.0), one finds that the SM prediction $R(D)_{\text{SM}} = 0.297 \pm 0.008$ is compatible with the current experimental world average at the 2σ level, that is, the anomaly is primarily constituted by the discrepancy between $R(D^{(*)})_{\text{SM}} = 0.245 \pm 0.008$ and the corresponding experimental value [19] which overlap only at the 3σ level.²² Thus, a combined explanation of the anomalies in $R(D)$, $R(D^{(*)})$ and in the AMM of the muon at a confidence level of 3σ or better is challenging in the primary scan, in particular due to the correlation between the latter two observables. We refer to section 6.4 for a revision of these trends.

The observables $R(D)$ and $R(D^{(*)})$ are linearly correlated in the model by construction. As is visible in the bottom-left plot in figure 6, only in the case $\hat{m}_\phi = 6$ a combined explanation of the anomalies in $R(D^{(*)})$ at the 1σ level is a priori impossible. Imposing the experimental bounds results in a quite pronounced correlation, namely $R(D^{(*)}) \approx 0.30 R(D) + 0.15$, and a combined explanation of $R(D)$ and $R(D^{(*)})$ is possible at the 2σ level for all considered LQ masses.

Correlations between parameters. In order to substantiate these results, we have checked for all LQ couplings whether they display some non-trivial correlation, if the flavour anomalies in $R(D)$ and $R(D^{(*)})$ are explained, or in the case the measured value of the AMM of the muon is explained, assuming a certain confidence level in each case. For that purpose, we make use of an algorithm to calculate Spearman’s rank correlation coefficient, as provided by the library `seaborn` [142].

The correlation plots in figure 7 show the effective parameters, separated in magnitude and argument, which display a non-zero correlation, if $R(D^{(*)})$ (left) and Δa_μ (right) are explained, respectively. Here, all sample points for which the respective anomaly is explained are taken into account, regardless of whether all experimental bounds on the primary observables are respected or not. The effective parameter b_{13} is included as well for the sake of comparison, because it is sensitive to the experimental bounds. Its effects are detailed in sections 5.2.3 and 5.2.4. We have chosen $\hat{m}_\phi = 4$ and the confidence level of 2σ as illustrative example. Nevertheless, the results are not appreciably different for the other considered LQ masses and confidence levels. A negative (positive) correlation is shown in blueish (reddish) colour. The points entering the correlation plot for $R(D^{(*)})$ and Δa_μ comprise roughly 10 and 15 percent of the entire sample for $\hat{m}_\phi = 4$,

²¹As can be seen in eq. (60), the effective parameters c_{23} and a_{23} as well as c_{33} and a_{33} agree up to $\mathcal{O}(\lambda^4)$, respectively. Since c_{23} and c_{33} are not varied directly in the primary scan, the implications for these are mainly discussed in terms of a_{23} and a_{33} in this section.

²²Since the values for $R(D)_{\text{SM}}$ and $R(D^{(*)})_{\text{SM}}$ that are generated by `flavio` differ from those quoted in reference [19], the significances are not in exact correspondence with the ones in table 1.

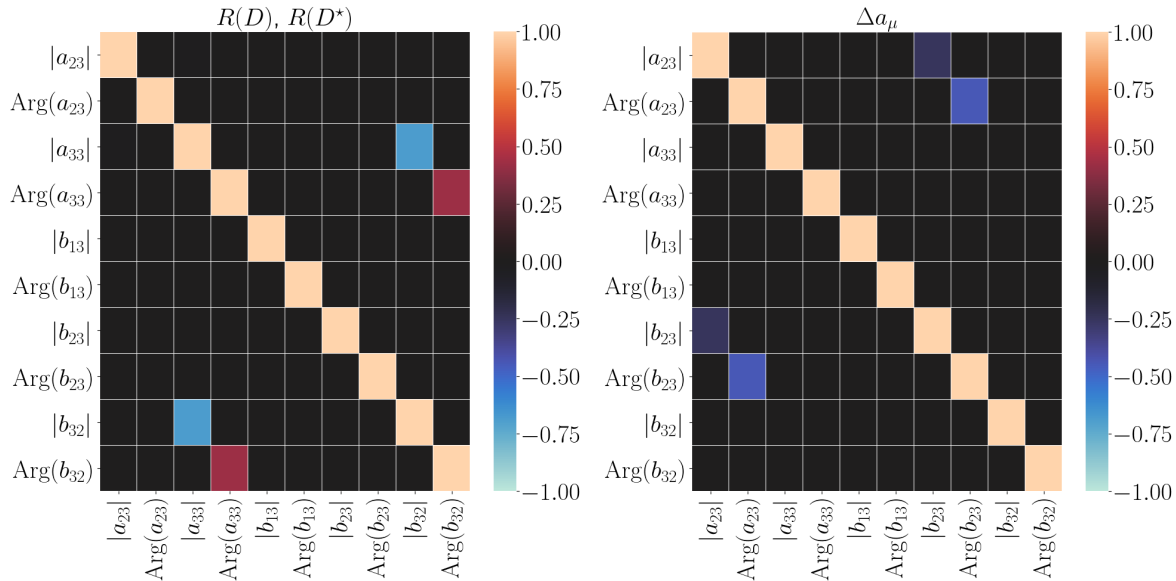


Figure 7: Correlation plots for $\hat{m}_\phi = 4$ based on the sample points which explain $R(D^{(*)})$ (left) and Δa_μ (right) at 2σ and 1σ level, respectively. The plots visualise Spearman's rank correlation coefficient, calculated via the library `seaborn` [142]. A negative (positive) correlation among, e.g., the magnitudes of two effective parameters indicates that if one of them increases, the other one tends to decrease (also increase). Note that sample points not respecting all experimental bounds on the primary observables are taken into account here as well.

respectively.

As evidenced by the analytic estimates for $R(D)$ and $R(D^*)$ in eqs. (66) and (67), the result for either observable is largely controlled by the product $|a_{33}b_{32}|$ which has to fall in an appropriate range to explain the anomalies. Furthermore, the arguments of the (complex) effective parameters a_{33} and b_{32} have to be positively correlated, implying that their difference should be close to zero and thus the cosines appearing in eqs. (66) and (67) take values close to one. This shows that explaining the flavour anomalies in $R(D)$ and $R(D^*)$ requires the contribution linear in $|a_{33}b_{32}|$ to be positive, that is, the contribution quadratic in $|a_{33}b_{32}|$ is generically too small to yield a dominant effect.

Similarly, as explaining the anomaly in the AMM of the muon needs positive Δa_μ , the difference of $\text{Arg}(c_{23}) \approx \text{Arg}(a_{23})$ and $\text{Arg}(b_{23})$ is necessarily close to π so that the sign of the cosine appearing in eq. (68) can cancel the negative overall sign. Thus, the right plot in figure 7 indicates a (moderate) negative correlation, both in the case of $|a_{23}|$ and $|b_{23}|$ as well as for the arguments. Note that the negative correlation of the magnitudes is less pronounced than in the case of $|a_{33}|$ and $|b_{32}|$, see left plot in figure 7. We interpret this as being due to the fact that the product $|a_{33}b_{32}|$ more directly determines the result for $R(D^{(*)})$, since there is not only the contribution arising from the interference with the SM, but also the (smaller) contribution proportional to $|a_{33}b_{32}|^2$, which is unaffected by $\text{Arg}(a_{33}) - \text{Arg}(b_{32})$, cf. eqs. (66) and (67). For the dominant contribution to the AMM of the muon instead, a too large value of $|a_{23}b_{23}|$ can be easily compensated by an appropriate value of $\text{Arg}(a_{23}) - \text{Arg}(b_{23})$. Thus, in the case of the AMM of the muon the sensitivities to the magnitudes and arguments of a_{23} and b_{23} are more similar.

5.2.3 Radiative charged lepton flavour violating decays $\tau \rightarrow \mu\gamma$ and $\mu \rightarrow e\gamma$

Shaping the parameter space. We move on to the discussion of the primary observables acting as constraints on the model, starting with the radiative cLFV decays $\tau \rightarrow \mu\gamma$ and $\mu \rightarrow e\gamma$. The

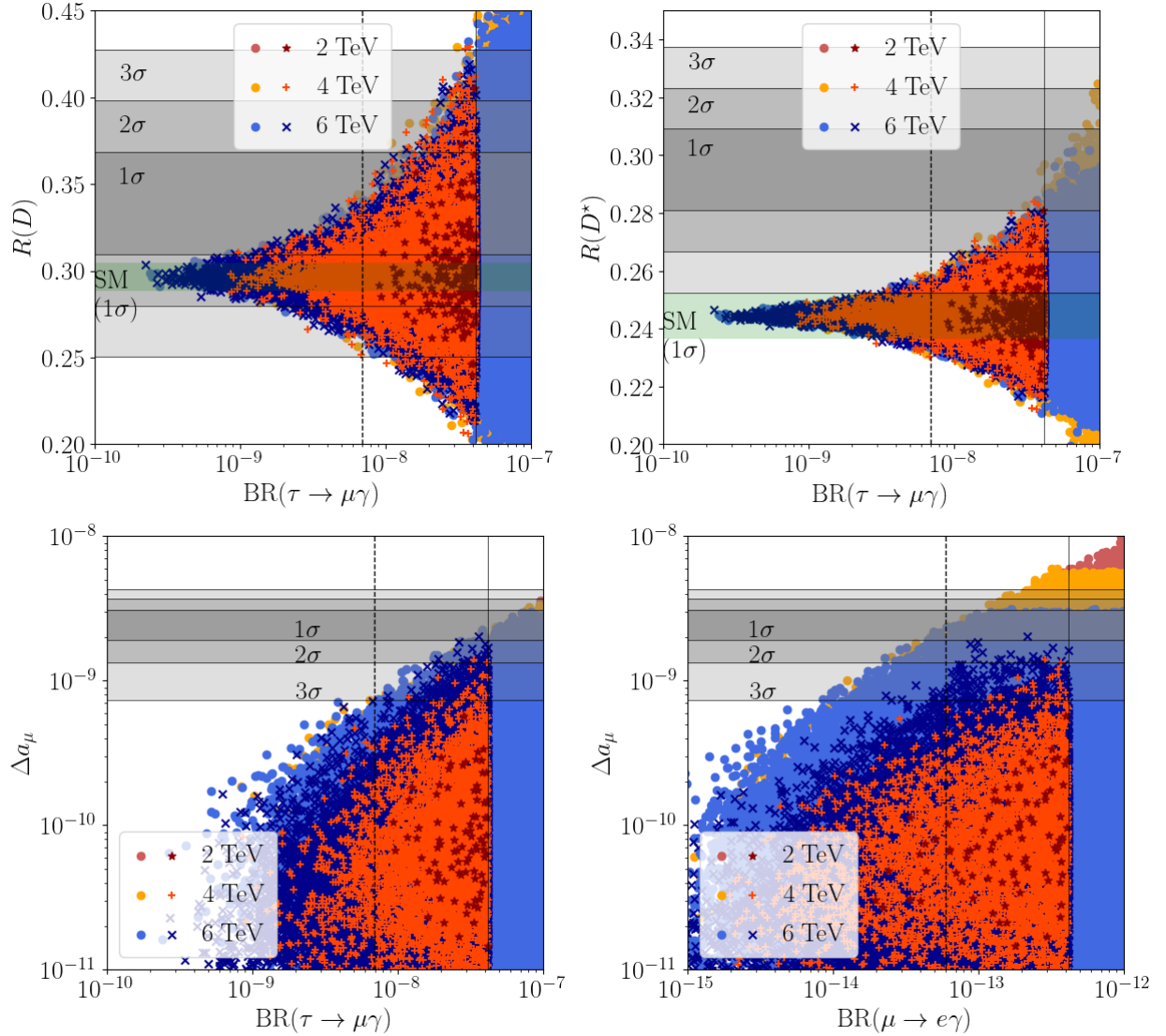


Figure 8: **Constraining power and future reach of $\tau \rightarrow \mu\gamma$ and $\mu \rightarrow e\gamma$.** The vertical solid (dashed) lines indicate the current bound on (future sensitivity of) $\text{BR}(\tau \rightarrow \mu\gamma)$ [104; 114] in the upper plots and the bottom-left one, and the current bound on (future sensitivity of) $\text{BR}(\mu \rightarrow e\gamma)$ [106; 107] in the bottom-right plot, see table 4. The round points (geometric shapes) indicate that current experimental bounds are violated (respected), see also the main text of section 5.2.1.

interplay between the corresponding BRs, $R(D^{(*)})$ and Δa_μ is shown in figure 8. As is expected from the analytic estimates, there are correlations between these observables: $\text{BR}(\tau \rightarrow \mu\gamma)$ is intertwined with $R(D)$ and $R(D^*)$ via the effective parameter $|c_{33}| \approx |a_{33}|$, and with Δa_μ through $|b_{23}|$, while the latter observable also largely depends on $|c_{23}| \approx |a_{23}|$, which is, on the other hand, constrained by the experimental bound on $\text{BR}(\mu \rightarrow e\gamma)$, see sections 5.1.1, 5.1.2 and 5.1.3. One typically generates large contributions to $\text{BR}(\tau \rightarrow \mu\gamma)$, also depending on the LQ mass. Thus, this observable represents a strong constraint on the parameter space of this model. Still, the experimental bound on $\text{BR}(\mu \rightarrow e\gamma)$ can be easily saturated as well.

This implies that both the flavour anomalies in $R(D)$ and $R(D^*)$ can individually be explained at least at the 2σ level for all considered LQ masses, while passing the current experimental bound on $\text{BR}(\tau \rightarrow \mu\gamma)$, see figure 8. Still, the result for $R(D^*)$ turns out to be always smaller than the experimental best-fit value. Note, though, that even in the case of a non-observation of $\tau \rightarrow \mu\gamma$ at Belle II [114], an explanation of $R(D)$ within the 1σ level would still be possible, whereas an

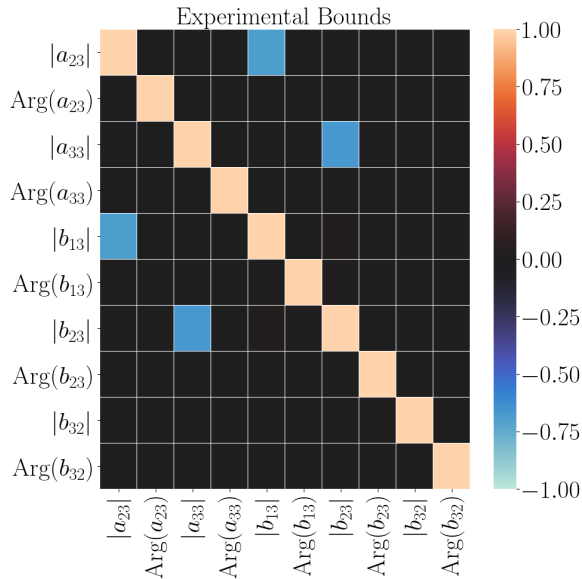


Figure 9: **Correlation plot for $\hat{m}_\phi = 4$ based on the sample points which respect the experimental bounds of all primary constraints.** The plot visualises Spearman's rank correlation coefficient, calculated via the library `seaborn` [142], see caption of figure 7 for more details. We remind that the LO contributions to $\text{BR}(\tau \rightarrow \mu\gamma)$ and $\text{BR}(\mu \rightarrow e\gamma)$ are proportional to $|a_{33}b_{23}|^2$ and $|a_{23}b_{13}|^2$, respectively, see section 5.1.3.

accommodation of the anomaly in $R(D^*)$ would be disfavoured in that case.

Furthermore, the shape of the viable parameter space in figure 6 can be understood by noticing the role of the experimental bound on $\text{BR}(\tau \rightarrow \mu\gamma)$. As indicated in section 5.1, the deviation of $R(D)/R(D)_{\text{SM}}$ and $R(D^*)/R(D^*)_{\text{SM}}$ from one can be approximated as a quadratic function in $|a_{33}|$, respectively, see eqs. (66) and (67). Together with $\Delta a_\mu \propto |b_{23}|$, see eq. (68), and the experimental bound on $\text{BR}(\tau \rightarrow \mu\gamma)$ constraining the product $|b_{23}c_{33}| \approx |b_{23}a_{33}|$ according to eq. (73), this bounds $R(D)/R(D)_{\text{SM}}$ and $R(D^*)/R(D^*)_{\text{SM}}$ from above as a function of Δa_μ .

The upcoming searches for $\tau \rightarrow \mu\gamma$ and $\mu \rightarrow e\gamma$ [107] will both probe large parts of the currently viable parameter space. In particular, for $\hat{m}_\phi = 2$ the search for $\tau \rightarrow \mu\gamma$ is expected to provide a relevant test for this model. The bottom-left plot in figure 8 also indicates that current data on $\tau \rightarrow \mu\gamma$ implies an upper limit on the AMM of the muon, $\Delta a_\mu \lesssim 3 \times 10^{-9}$, in this model. This can readily be recovered from combining the estimates in eq. (68) and (73) with the current experimental bound on $\text{BR}(\tau \rightarrow \mu\gamma)$, $\text{BR}(\tau \rightarrow \mu\gamma)_{\text{exp}} < 4.2 \times 10^{-8}$ [104]. In addition, both the future search for $\tau \rightarrow \mu\gamma$ at Belle II and the one for $\mu \rightarrow e\gamma$ at MEG II will test the capability of the model to explain the measured value of Δa_μ and potentially render an explanation of this flavour anomaly unlikely, see also the discussion in section 6.4.

Correlations between parameters. We, thus, find that the available parameter space of this model is dominantly constrained by the experimental bounds on the radiative cLFV decays $\tau \rightarrow \mu\gamma$ and $\mu \rightarrow e\gamma$. This is further evidenced by the correlation plot in figure 9 which shows the effective parameters that display non-zero correlations, if the experimental bounds of all primary constraints are imposed. As for the correlation plots discussed in section 5.2.2, the mass $\hat{m}_\phi = 4$ is chosen as illustrative example and the results are not appreciably different for the other considered LQ masses. We also include the effective parameter b_{32} in order to contrast the findings to the case of explaining the experimental anomalies in figure 7. Note that only 0.35 percent of the generated sample points respect all imposed bounds for $\hat{m}_\phi = 4$ and thus constitute the plot in figure 9.

Imposing an adequate negative correlation between the magnitudes $|a_{23}|$ and $|b_{13}|$ as well as $|a_{33}|$ and $|b_{23}|$, respectively, is sufficient in the primary scan to render a sample point compatible with every experimental constraint taken into account. This is in very good agreement with the findings of section 5.1.3. Generally, at least one of the two BRs, $\text{BR}(\tau \rightarrow \mu\gamma)$ and $\text{BR}(\mu \rightarrow e\gamma)$, is larger than its corresponding current experimental bound in the primary scan, if a bound on one of the other primary constraints is violated. Thus, the latter appear to be considerably less

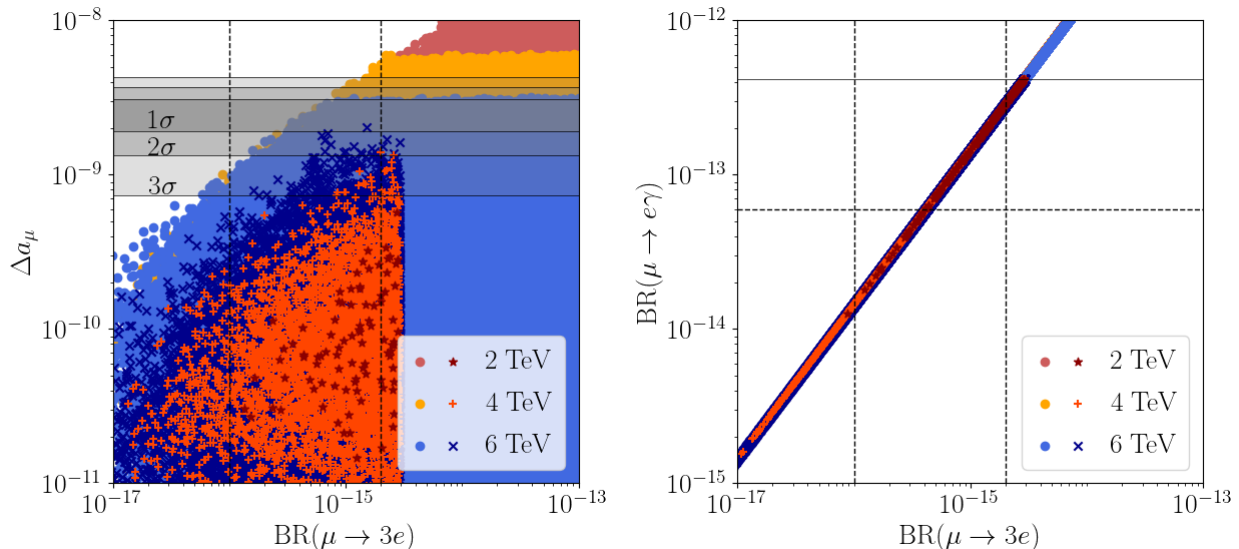


Figure 10: **Constraining power and future reach of $\mu \rightarrow 3e$.** The vertical dashed lines indicate the respective projected reach of Phase 1 and Phase 2 of the Mu3e experiment [110], see table 4. The round points (geometric shapes) indicate that current experimental bounds are violated (respected), see also the main text of section 5.2.1.

competitive. Still, this observation is partly revised in section 6.4.

5.2.4 Trilepton decays $\mu \rightarrow 3e$, $\tau \rightarrow 3\mu$, $\tau \rightarrow \mu e \bar{e}$ and $\mu - e$ conversion in aluminium

In this section, we discuss the findings of the primary scan for several cLFV trilepton decays and $\mu - e$ conversion in aluminium.²³

The results, shown in the left plot in figure 10, indicate that the reach of Phase 2 of the Mu3e experiment [110] may render an explanation of the anomaly in the AMM of the muon in this model unlikely. The right plot in figure 10 verifies that $\mu \rightarrow 3e$ is entirely dominated by long-range contributions from γ -penguin diagrams. Thus, one can effectively establish a one-to-one correspondence with the BR of $\mu \rightarrow e\gamma$ in the model, as stated in section 5.1.4.

If $\mu - e$ conversion in nuclei was similarly dominated by long-range γ -penguins, the plots in the top in figure 11 would also just feature a straight line in the centre of the coloured region. Due to subdominant contributions, see section 5.1.5, the result can generically deviate from the γ -penguin approximation by a factor two or three. Still, the future search for $\mu - e$ conversion in aluminium can be expected to complement the one for $\mu \rightarrow 3e$, as can be seen in the top-right plot in figure 11. The experiments COMET [111] and Mu2e [112] are both projected to efficiently probe the possibility of explaining the measured value of Δa_μ in this model, see the bottom-left plot in figure 11.

In the following, we only discuss plots involving $\tau \rightarrow 3\mu$. However, the obtained BRs for $\tau \rightarrow 3\mu$ and $\tau \rightarrow \mu e \bar{e}$ are almost identical in the primary scan and thus the inferred statements also apply to $\text{BR}(\tau \rightarrow \mu e \bar{e})$. There can be, nevertheless, appreciable differences between the two in

²³We note that, relatively independently of the target nucleus, the model can generate contributions of $\mathcal{O}(10^{-13})$ to the respective CRs for $\hat{m}_\phi = 4$ and 6, and contributions of $\mathcal{O}(10^{-12})$ for $\hat{m}_\phi = 2$. These are, however, ruled out due to the stringent bound on and the strong correlation with $\text{BR}(\mu \rightarrow e\gamma)$ in this regime. Thus, the current experimental bounds, $\text{CR}(\mu - e; \text{Ti}[\text{Au}]\{\text{Pb}\})_{\text{exp}} < 0.061[0.070]\{4.6\} \times 10^{-11}$, [143–145] do not impose relevant constraints on the model. In addition, the reach of future searches for $\mu - e$ conversion in aluminium [111; 112] is projected to be three to four orders of magnitude better than for carbon targets [146].

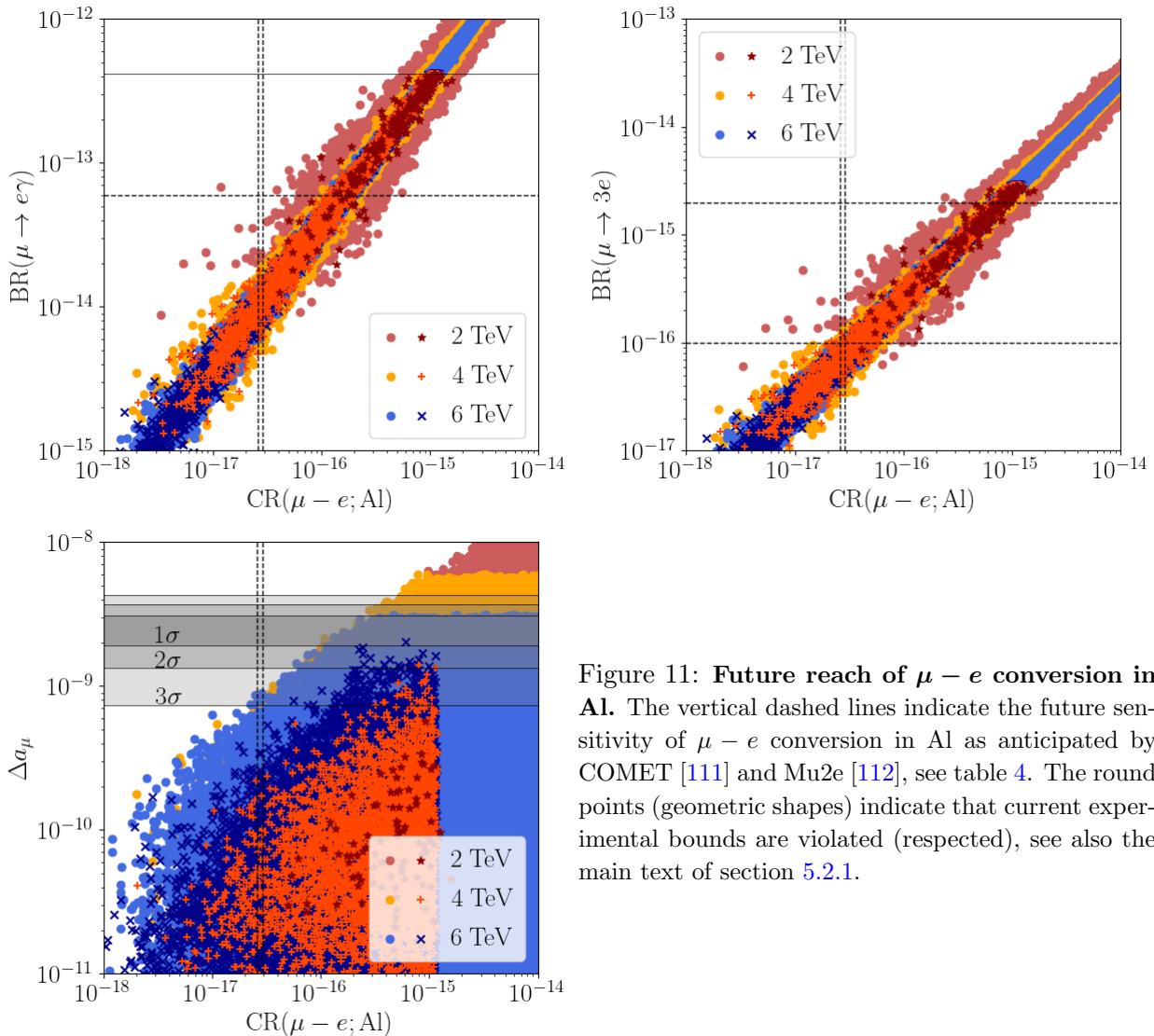


Figure 11: **Future reach of $\mu - e$ conversion in Al.** The vertical dashed lines indicate the future sensitivity of $\mu - e$ conversion in Al as anticipated by COMET [111] and Mu2e [112], see table 4. The round points (geometric shapes) indicate that current experimental bounds are violated (respected), see also the main text of section 5.2.1.

the comprehensive scan, see section 6.4.3. Figure 12 confirms that the upcoming search for $\tau \rightarrow 3\mu$ at Belle II [114] can be expected to probe a region of the parameter space which is compatible with current constraints. As demonstrated in section 5.1.4, this region corresponds to sufficiently large Z -penguin contributions. Indeed, if only long-range γ -penguins were present, the top-left plot involving $\text{BR}(\tau \rightarrow \mu\gamma)$ would display a straight line located at the upper edge of the coloured region.

The hierarchy $|c_{23}| \approx |a_{23}| \gg |b_{23}|$ required for large Z -penguin contributions also suppresses the product of the magnitudes of the two effective parameters and thus the contribution to the AMM of the muon, see eqs. (68) and (77). As a consequence, observing $\tau \rightarrow 3\mu$ at Belle II would indicate that an explanation of the measured value of Δa_μ is very unlikely for $\hat{m}_\phi = 4, 6$. For these LQ masses, conversely, the largest contributions to Δa_μ are generated, if $\text{BR}(\tau \rightarrow 3\mu)$ remains below the prospective sensitivity. This upper bound on Δa_μ , $\Delta a_\mu \propto |b_{23}|$, as a function of $\text{BR}(\tau \rightarrow 3\mu)$, $\text{BR}(\tau \rightarrow 3\mu) \propto |c_{33}|^2$, is again mainly due to the experimental constraint on $\text{BR}(\tau \rightarrow \mu\gamma)$, $\text{BR}(\tau \rightarrow \mu\gamma) \propto |b_{23}c_{33}|^2$.

In the model, a signal in $\tau \rightarrow 3\mu$ effectively enforces a signal in $\tau \rightarrow \mu\gamma$, but the reverse is not true in general. Furthermore, the plots in the bottom of figure 12 suggest that a result $\text{BR}(\tau \rightarrow 3\mu) \gtrsim \mathcal{O}(10^{-10})$ becomes increasingly disfavoured, if the contributions to cLFV $\mu \rightarrow e$ transitions shrink. Since $|b_{13}| \gtrsim \lambda$ in the primary scan, this shrinkage mostly relies on small values

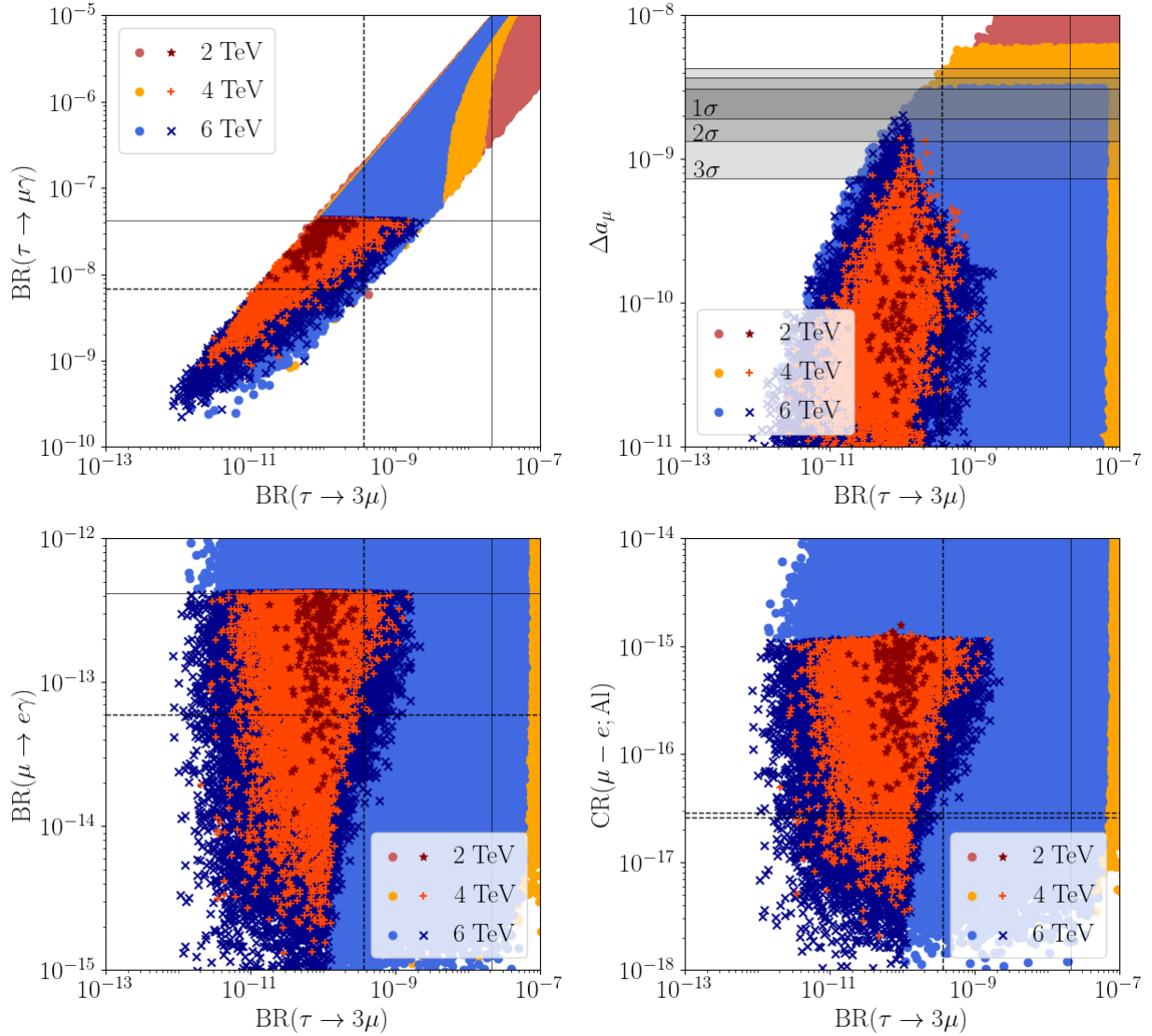


Figure 12: **Constraining power and future reach of $\tau \rightarrow 3\mu$.** The vertical solid (dashed) lines indicate the current bound on (future sensitivity of) $\tau \rightarrow 3\mu$ [108; 114], see table 4. The round points (geometric shapes) indicate that current experimental bounds are violated (respected), see also the main text of section 5.2.1.

for $|c_{23}| \approx |a_{23}|$, see sections 5.1.3 and 5.1.5, and so the Z -penguin contributions to $\tau \rightarrow 3\mu$ become more suppressed. Hence, $\text{BR}(\tau \rightarrow 3\mu)$ is more tightly correlated with $\text{BR}(\tau \rightarrow \mu\gamma)$ in this case, and it is more difficult to respect the stringent experimental bound on the latter. In turn, if $\tau \rightarrow 3\mu$ is observable at Belle II, $|c_{23}| \approx |a_{23}|$ must be rather large and therefore one generates an enhancement of $\text{BR}(\mu \rightarrow e\gamma)$ and $\text{CR}(\mu - e; \text{Al})$. Note that this interplay is far less pronounced in the comprehensive scan, see section 6.4.

5.2.5 $B_c \rightarrow \tau\nu$, $R_{K^{(*)}}^\nu$ and $Z \rightarrow \tau\tau$

We proceed with a discussion of further hadronic observables as well as the axial-vector coupling of Z bosons to tau leptons. As illustrated in figure 13, a large contribution from the LQ to the

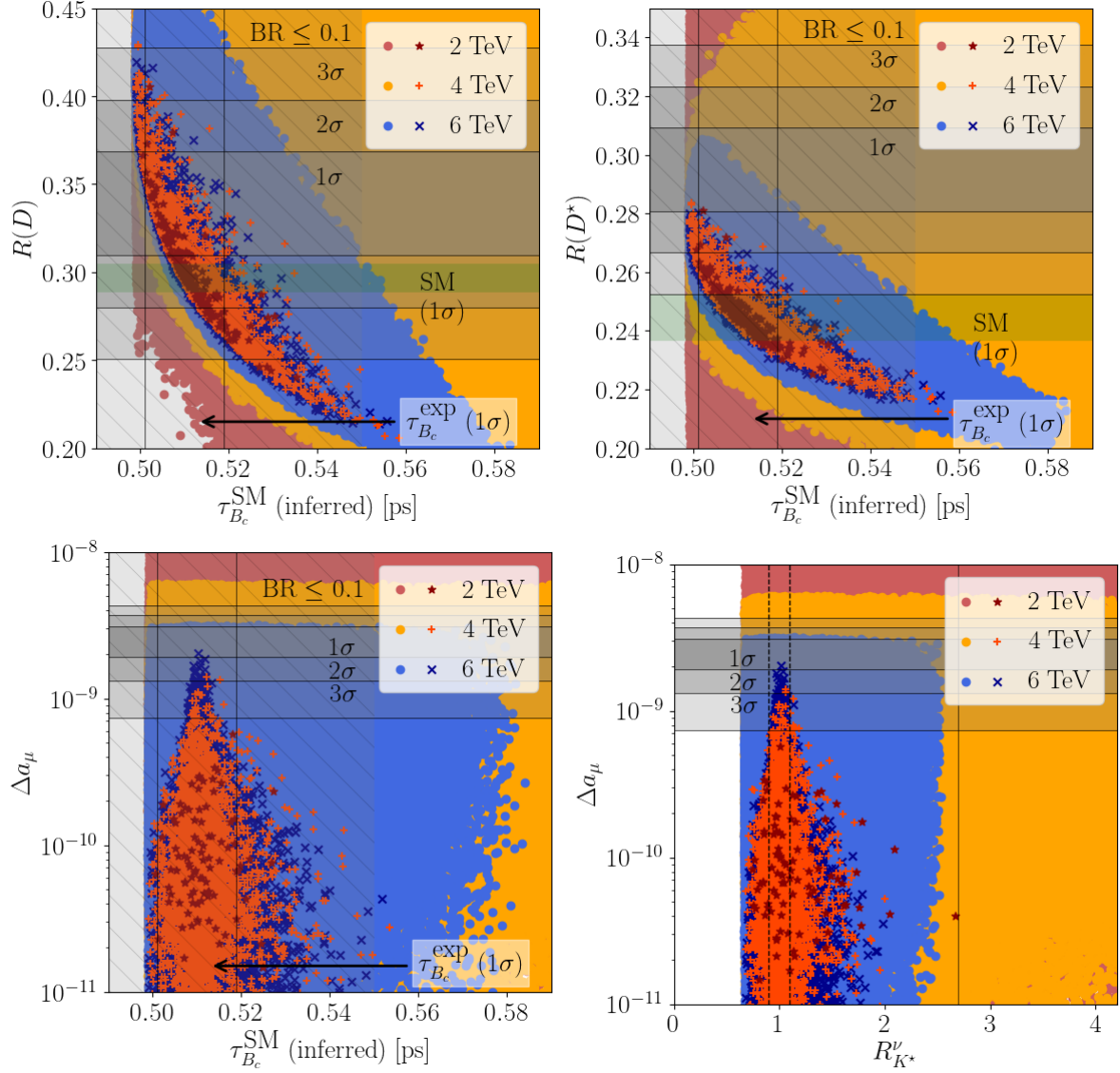


Figure 13: **Constraining power and future reach of $\tau_{B_c}^{\text{SM}}$ and $R_{K^*}^\nu$.** In the top and the bottom-left plot, the vertical solid lines indicate the region in which the inferred SM contribution to the B_c lifetime agrees with the experimental best-fit value at the 1σ level [93], and the hatched area marks the region in which $\text{BR}(B_c \rightarrow \tau\nu)$ remains smaller than 0.1, as given via eq. (91). In the bottom-right plot, the vertical solid line shows (dashed lines show) the region compatible with the current experimental bound on (future reach of) $R_{K^*}^\nu$ [113; 114], see also table 4. For the future reach, an SM-like value and an uncertainty of ten percent are assumed. The round points (geometric shapes) indicate that current experimental bounds are violated (respected), see also the main text of section 5.2.1.

lifetime of the B_c meson is incompatible with the imposed experimental bounds.²⁴ In particular, the model can accommodate the current best-fit value of $R(D)_{\text{exp}} = 0.339 \pm 0.026 \pm 0.014$, even if that contribution vanished. Besides, the results suggest that $\tau_{B_c}^{\text{SM}}$ would still be close to agreeing with the measured lifetime $\tau_{B_c}^{\text{exp}} = (0.510 \pm 0.009)$ ps [93] at the 1σ level for the largest value of $R(D^*)$ achievable in this model (which would also be closest to the best-fit value). In case of larger LQ masses, a substantial contribution to the lifetime of the B_c meson from the LQ only arises, if $R(D)$ and $R(D^*)$ become smaller than in the SM, respectively, which is in agreement

²⁴We stress again that we have not attempted to perform a calculation of the SM contribution to the B_c lifetime, but have indirectly inferred it from the requirement that the combined contribution from the SM and the LQ agrees with the experimentally determined lifetime.

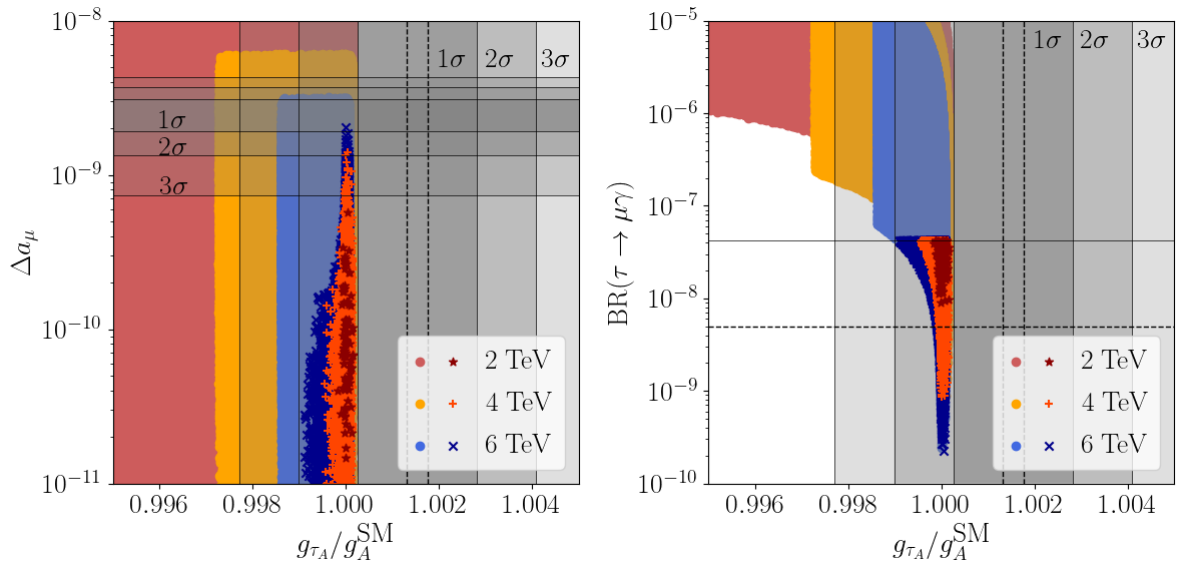


Figure 14: **Constraining power and future reach of $g_{\tau_A}/g_A^{\text{SM}}$.** The regions indicated by vertical solid (dashed) lines are compatible with the current experimental world averages for (future sensitivity of) $g_{\tau_A}/g_A^{\text{SM}}$ [21; 57] at the shown confidence level [115; 116] (at the 3σ level [116–118]), see table 4. The round points (geometric shapes) indicate that current experimental bounds are violated (respected), see also the main text of section 5.2.1.

with the opposite signs of the respective contributions linear in $|a_{33}b_{32}|$ in the analytic estimates in eqs. (66), (67) and (90). This interdependence can get (partly) lifted, if the channel with a muon neutrino ν_μ in the final state becomes more relevant, see section 6.4 for details.

Nevertheless, a deviation of $\tau_{B_c}^{\text{SM}}$ from the best-fit value of $\tau_{B_c}^{\text{exp}}$ by more than ten percent is incompatible with the considered constraints. This implies that the BR for $B_c \rightarrow \tau\nu$ remains below 0.1 in most cases, and can potentially exceed this limit only to a very small degree. In line with eq. (91), imposing the upper bound $\text{BR}(B_c \rightarrow \tau\nu) \lesssim 0.1$ constrains the SM contribution to the lifetime to fulfil $\tau_{B_c}^{\text{SM}} \lesssim 0.55$ ps, indicated by the hatched region in the top and the bottom-left plot in figure 13. Therein, the vertical solid lines indicate the region in which the SM prediction agrees with the measured lifetime of the B_c meson at the 1σ level. Furthermore, we recall that $\text{BR}(B_c \rightarrow \tau\nu) \lesssim 0.3$ corresponds to $\tau_{B_c}^{\text{SM}} \lesssim 0.7$ ps.

If the measured value of Δa_μ is explained at the 3σ level or better in this model, we find that a substantial deviation of $\tau_{B_c}^{\text{SM}}$ from the measured B_c lifetime is very unlikely for $\hat{n}_\phi = 4, 6$. This reflects the fact that an explanation of $R(D)$ and $R(D^*)$ competes with an explanation of Δa_μ , see sections 5.2.2 and 5.2.3. The results of the primary scan also suggest that $R_{K^{(*)}}^\nu$ is close to one in that case. We refer to section 6.4 for a discussion of the results of the comprehensive scan. Thus, the prospective measurement of $B \rightarrow K^{(*)} + \text{invisible}$ at Belle II [114] provides a promising avenue to test this model, since the primary scan prompts the expectation that the non-appearance of a substantial excess on top of the SM expectation implies the best chances for an explanation of the observed anomaly in the AMM of the muon. As is the case for $R(D)/R(D)_{\text{SM}}$ and $R(D^*)/R(D^*)_{\text{SM}}$, the observables $R_{K^{(*)}}^\nu$ and $\tau_{B_c}^{\text{SM}}/\tau_{B_c}^{\text{exp}}$ can also be approximated as quadratic functions in $|a_{33}|$, respectively, and are therefore correlated with Δa_μ , $\Delta a_\mu \propto |b_{23}|$, via the experimental bound on $\text{BR}(\tau \rightarrow \mu\gamma)$, $\text{BR}(\tau \rightarrow \mu\gamma) \propto |a_{33}b_{23}|^2$, see the relevant estimates in section 5.1.

As evidenced in figure 14, the contributions to the AMM of the muon, $\Delta a_\mu \propto |a_{23}b_{23}|$, and $g_{\tau_A}/g_A^{\text{SM}}$ are not per se correlated, as is expected from eq. (94) according to which the difference of $g_{\tau_A}/g_A^{\text{SM}}$ from one is essentially only controlled by $|c_{33}| \approx |a_{33}|$. Still, if the experimental constraints

of all primary observables are imposed, the axial-vector coupling of Z bosons to tau leptons is necessarily SM-like, if the measured value of Δa_μ is explained at the 3σ level. In particular, the deviation from LFU would be constrained to be much smaller than 0.1 percent. This correlation is established through the bound on $\text{BR}(\tau \rightarrow \mu\gamma)$, $\text{BR}(\tau \rightarrow \mu\gamma) \propto |a_{33}b_{23}|^2$, which is illustrated by the plot on the right in figure 14. It is clearly visible that a deviation of $g_{\tau A}/g_A^{\text{SM}}$ from the current experimental world average [115; 116] by more than 2σ is incompatible with the constraint on $\text{BR}(\tau \rightarrow \mu\gamma)$. Furthermore, the future search for $\tau \rightarrow \mu\gamma$ at Belle II [114] can conclusively test the capability of the model to induce a significant deviation from LFU in axial-vector couplings.

6 Comprehensive study

In this section, we conduct a comprehensive scan over the parameter space of this model, only considering the phenomenology of scenario B. In order to do so, we first perform a chi-squared fit to the charged fermion masses and quark mixing, as detailed in section 6.1. This fixes (a subset of) the effective parameters d_{ij} , e_{ij} and f_{ij} . Furthermore, we obtain the unitary matrices necessary in order to transform the LQ couplings $\hat{\mathbf{x}}$ and $\hat{\mathbf{y}}$ to the charged fermion mass basis. Then, we bias this numerical study to account for the parameter space, preferred by the primary observables, as has been revealed by the analysis in section 5.2. We can thereby focus on important regions of parameter space and extract the most useful information from this multi-dimensional parameter scan. The details of the biasing can be found in section 6.2. Otherwise we vary all parameters with flat priors, and in the ranges specified in eqs. (62) and (63). For more information about the scan procedure, we refer to appendix E.1.

To perform this numerical study, we use a combination of different computational software. We encode this model in SARAH [96; 97]. The program SARAH generates an output module for use with SPheno [97], which can calculate the Wilson coefficients, decay rates and a set of flavour observables, defined by FlavorKit [96].²⁵ We also make use of flavio [62] to process analytically defined sets of Wilson coefficients, where appropriate, and use these to calculate a broader class of flavour observables. The running of Wilson coefficients in flavio is implemented using the Wilson package [95]. In this way, it is possible to construct an efficient multi-dimensional parameter scan, the results of which are discussed in the following. Information regarding the conventions of the shown plots is given in section 6.3.

We consider not only the primary observables in section 6.4 and appendix E.2, as explored in section 5, but also secondary and tertiary observables. Secondary observables are outlined and analytic estimates are provided for these in section 6.5. We discuss the numerical results for the secondary observables in section 6.6 and tertiary observables are commented in section 6.7 as well as in appendix E.3.

6.1 Fit of charged fermion masses and quark mixing

In order to fix the effective parameters d_{ij} , e_{ij} and f_{ij} , contained in the charged fermion mass matrices M_d , M_e and M_u , respectively, we perform a chi-squared fit of the charged fermion masses and quark mixing. As discussed in section 3, accommodating quark mixing correctly requires to consider scenario B, i.e. the up-type quark mass matrix has to be of the form given in eq. (28). As the mass of the LQ is selected to be maximally a few TeV, see eq. (64), we fit the charged fermion masses at a scale of $\mu = 1$ TeV, taken from reference [94]. Quark mixing is fitted to the best-fit values given by the PDG (Particle Data Group) [93], because RG running effects are small.

²⁵A comprehensive discussion of this can be found in reference [147].

\hat{m}_ϕ	$ a_{33} $	$ b_{32} $	$\cos(\text{Arg}(a_{33}) - \text{Arg}(b_{32}))$	$ a_{23} $	$\cos(\text{Arg}(a_{23}) - \text{Arg}(b_{23}))$
2	[0.2, 0.7]	[1.1, 2.6]	[0.4, 1.0]	–	[−1.0, 0.0]
4	[0.2, 1.9]	[1.0, 4.5]	[0.1, 1.0]	[1.6, 4.4]	[−1.0, −0.5]
6	[0.2, 3.6]	[0.8, 4.5]	[0.0, 1.0]	[1.4, 4.4]	[−1.0, −0.3]

Table 6: **Inputs for biasing in comprehensive scan, derived from primary scan.** These intervals have been identified in the primary scan as satisfying all primary constraints and explaining at least one of the flavour anomalies in $R(D^{(*)})$ or in the AMM of the muon at the 3σ level or better. The fact that there is no entry for $|a_{23}|$ in the case of $\hat{m}_\phi = 2$ means that no points have been identified in the primary scan that allow the presented conditions to be met. Therefore, we take $[\lambda, 1/\lambda]$ to be the imposed range for biasing the magnitude of the effective parameter a_{23} . Then, we manually input the restricted range for $\cos(\text{Arg}(a_{23}) - \text{Arg}(b_{23}))$ for $\hat{m}_\phi = 2$ to ensure that the contribution to the AMM of the muon is positive, compare eq. (68). Note that these values are taken together with the inequalities found in eqs. (102) and (103) to also bias the values of the effective parameters $|b_{13}|$ and $|b_{23}|$. All shown numbers are rounded to one decimal place.

This model contains two Higgs doublets, H_u giving masses to up-type quarks, and H_d giving masses to down-type quarks as well as charged leptons. The suppression of the down-type quark and charged lepton masses with respect to those of the up-type quarks (in particular, the top quark) is achieved by taking the VEV of H_d to be much smaller than that of H_u – recall eq. (15). Thus, in the chi-squared fit we have (mainly) varied the size of the VEV of H_d such that $\langle H_d^0 \rangle$ takes a minimum value of 1.22 GeV and a maximum value of 4.86 GeV, generating several viable data sets. Each of these leads to an excellent fit to the charged fermion masses taken at $\mu = 1$ TeV [94] and to quark mixing [93]. From these data sets, we do not only extract the values of masses and mixing, but more importantly the unitary matrices L_d, R_d, L_e, R_e, L_u and R_u , necessary in order to compute the form of the LQ couplings $\hat{\mathbf{x}}$ and $\hat{\mathbf{y}}$ in the charged fermion mass basis, i.e. the LQ couplings \mathbf{x}, \mathbf{y} and \mathbf{z} , according to eqs. (54), (55) and (58). For further details about the implementation of the chi-squared fit in the scan, see appendix E.1.

6.2 Biases from primary scan

We remind that the study of primary observables involves samples of $4(3)[2] \times 10^6$ data points for $\hat{m}_\phi = 2(4)[6]$, sampled as described in section 5.2.1. These points have been filtered to select only those that pass the primary constraints in table 4, including $g_{\tau A}/g_A^{\text{SM}}$ at the 3σ level and $\tau_{B_c}^{\text{SM}}$ at the 1σ level.

In an unbiased scan, it turns out to be difficult to extract points capable of addressing the three flavour anomalies, while passing the constraints arising from the experimental bounds on the radiative cLFV decays $\tau \rightarrow \mu\gamma$ and $\mu \rightarrow e\gamma$. From table 5 it becomes evident why, since common effective parameters drive these observables, recalling that a_{ij} and c_{ij} are related via the CKM mixing matrix. For this reason, the biases in table 6 are presented for points satisfying all primary constraints, together with two further numerical restrictions, see eqs. (102) and (103). The latter intent to address the constraints from $\tau \rightarrow \mu\gamma$ and $\mu \rightarrow e\gamma$ by biasing the values of the magnitudes of the effective parameters b_{23} and b_{13} , respectively.

For a value of the magnitude of the effective parameter a_{23} chosen according to table 6, we also impose a restriction on the magnitude of b_{13} in order to pass the experimental bound on the

BR of $\mu \rightarrow e\gamma$, see eq. (72),

$$|b_{13}| \lesssim \frac{1}{|a_{23}|} \left\{ \begin{array}{l} 0.41, \hat{m}_\phi = 2 \\ 1.16, \hat{m}_\phi = 4 \\ 2.22, \hat{m}_\phi = 6 \end{array} \right\}. \quad (102)$$

Furthermore, respecting the experimental constraint on the BR of $\tau \rightarrow \mu\gamma$ enforces that, once a value for the magnitude of a_{33} is chosen according to table 6, the magnitude of b_{23} is restricted such that

$$|b_{23}| \lesssim \frac{1}{|a_{33}|} \left\{ \begin{array}{l} 0.16, \hat{m}_\phi = 2 \\ 0.45, \hat{m}_\phi = 4 \\ 0.86, \hat{m}_\phi = 6 \end{array} \right\}, \quad (103)$$

compare eq. (73). This means that determining whether a sample point can rather explain the flavour anomalies in $R(D^{(*)})$, for which $|a_{33}|$ needs to be quite large, or in the AMM of the muon, for which $|b_{23}|$ must be quite large, is tightly controlled by the bound on the BR of $\tau \rightarrow \mu\gamma$. The ranges for $|a_{33}|$ indicated in table 6 are the union of the ranges separately extracted using the 3σ ranges of $R(D^{(*)})$ and of the AMM of the muon.

Note that these constraints are imposed on the effective parameters in the charged fermion mass basis, while scanning over effective parameters in the interaction basis in the comprehensive scan. Therefore, we have two related, but distinctly defined, regions of parameter space. The transformations between them are given by the unitary matrices, generated by the chi-squared fit to charged fermion masses and quark mixing, as described in section 6.1. As addressed in section 4, varying the effective parameters in the interaction basis in the range found in eq. (62) ensures the preservation of the expansion in orders of λ used to construct the underlying model. In doing so, the corresponding effective parameters in the charged fermion mass basis, calculated from this scan, may fall outside the range $[\lambda, 1/\lambda]$, compare table 10 in appendix E.1.

For practicality in implementing the biases, we assume that the LO relations listed in appendix B can be used to translate between bases. In particular, we first assume that

$$|a_{33}| = |\hat{a}_{33}|, \quad |b_{32}| = |\hat{b}_{32}|, \quad \text{and} \quad |b_{23}| = |\hat{b}_{23}|, \quad (104)$$

which allows us to directly bias the input values for $|\hat{a}_{33}|$, $|\hat{b}_{32}|$, and $|\hat{b}_{23}|$. All other effective parameters in the interaction basis are varied in the ranges, specified by eqs. (62) and (63). We then bias the magnitudes of a_{23} and b_{13} by first extracting their values from the effective parameters in the interaction basis, using the aforementioned unitary matrices, and afterwards enforcing the bounds shown in table 6 and eq. (102), respectively. For further details regarding the implementation of the scan, see appendix E.1.

We do not claim to have extensively explored the entire multi-dimensional parameter space of this model, but implement the biases from the primary scan to better identify regions capable of explaining the three flavour anomalies and respecting all considered present constraints.

6.3 Conventions for plots presented in this section

Before discussing the results of this comprehensive scan, we first outline the conventions for displaying data in this section. In all plots the displayed coloured points pass all considered constraints – red stars for $\hat{m}_\phi = 2$, yellow plus signs for $\hat{m}_\phi = 4$, and blue crosses for $\hat{m}_\phi = 6$, as shown in the plot legends. Black dotted lines indicate the central values for SM predictions, black solid lines show present experimental constraints and black dashed lines show prospective bounds. Where

SPREAD OF RESULTS FOR PRIMARY OBSERVABLES IN COMPREHENSIVE SCAN						
Observable	$\hat{m}_\phi = 2, P = 5955$		$\hat{m}_\phi = 4, P = 12570$		$\hat{m}_\phi = 6, P = 39807$	
	[min., max.]	Average	[min., max.]	Average	[min., max.]	Average
$R(D)$	[0.302, 0.452]	0.333	[0.297, 0.442]	0.321	[0.291, 0.436]	0.316
$R(D^*)$	[0.245, 0.293]	0.256	[0.243, 0.288]	0.252	[0.238, 0.285]	0.250
$\Delta a_\mu \times 10^{10}$	[-0.350, 18.26]	1.658	[0.320, 22.40]	2.363	[0.013, 20.21]	1.252
$\text{BR}(\tau \rightarrow \mu\gamma) \times 10^8$	[0.234, 4.200]	3.123	[0.099, 4.200]	2.997	[0.040, 4.200]	2.834
$\text{BR}(\mu \rightarrow e\gamma) \times 10^{14}$	[0.014, 42.00]	19.96	[0.008, 42.00]	20.65	[0.002, 42.00]	20.10
$\text{BR}(\tau \rightarrow 3\mu) \times 10^{10}$	[0.149, 30.92]	1.895	[0.078, 31.42]	3.754	[0.030, 31.86]	3.479
$\text{BR}(\tau \rightarrow \mu e\bar{e}) \times 10^{10}$	[0.103, 59.72]	1.948	[0.036, 28.83]	2.465	[0.016, 18.20]	1.891
$\text{BR}(\mu \rightarrow 3e) \times 10^{16}$	[0.010, 29.54]	14.04	[0.005, 29.53]	14.52	[0.001, 29.54]	14.13
$\text{CR}(\mu - e; \text{Al}) \times 10^{16}$	[0.009, 14.40]	6.341	[0.002, 13.56]	6.480	[0.002, 13.37]	6.298
$R_{K^*}^\nu$	[0.672, 2.695]	1.171	[0.672, 2.694]	1.096	[0.668, 2.698]	1.071
$(1 - g_{\tau_A}/g_A^{\text{SM}}) \times 10^4$	[-1.646, 1.963]	-0.203	[-1.593, 4.791]	0.742	[-0.777, 9.193]	1.986
$\tau_{B_c}^{\text{SM}}$ (inferred) [ps]	[0.499, 0.540]	0.506	[0.500, 0.524]	0.507	[0.499, 0.527]	0.507

Table 7: **Overview of spread of results for primary observables in comprehensive scan.** We present a summary of the statistics reflecting the distribution of primary observables: the minimum, maximum and average values generated for a sample of P points passing the primary constraints.

we display a physical observable on an axis, grey shaded regions indicate the 1, 2 and 3 σ contours about the present experimental best-fit values. If relevant for that observable, a red-brown shaded region indicates a prospective reach, as labelled, with a best-fit value denoted with a solid red-brown line. Where we show an effective parameter (or combination of them) on an axis, the grey shaded band indicates the region of parameter space probed by the primary scan. Overlaid white crosses in each of the displayed plots, labelled ‘Anomalies’ in the legends, are points that can simultaneously address the anomalies in $R(D)$, $R(D^*)$ and in the AMM of the muon within the 3 σ range of their present best-fit values. Each of these features can be seen in figure 15. Additional features in plots are defined in the captions.

6.4 Numerical results for primary observables

For the comprehensive scan, we sample 1.5×10^5 points for each of the three LQ masses. In the primary scan, approximately 0.005 (0.35) [2.4] percent of sample points have passed the primary constraints for $\hat{m}_\phi = 2(4)[6]$. In contrast, for the comprehensive scan we find that approximately 4(8)[27] percent of sample points pass the primary constraints for $\hat{m}_\phi = 2(4)[6]$. Therefore, in the comprehensive scan the percentage of viable points has particularly increased for $\hat{m}_\phi = 2$. Below we discuss the efficacy of this biased scan for addressing the flavour anomalies and evading constraints. Once we have imposed all constraints, we identify 58(1)[0] points for $\hat{m}_\phi = 2(4)[6]$ that can generate $R(D)$, $R(D^*)$ and the AMM of the muon within the 3 σ range of the present best-fit values. These points are illustrated by white crosses in the plots, as mentioned in section 6.3.²⁶

²⁶As most of these points correspond to $\hat{m}_\phi = 2$, we do not distinguish between LQ masses for the white crosses.

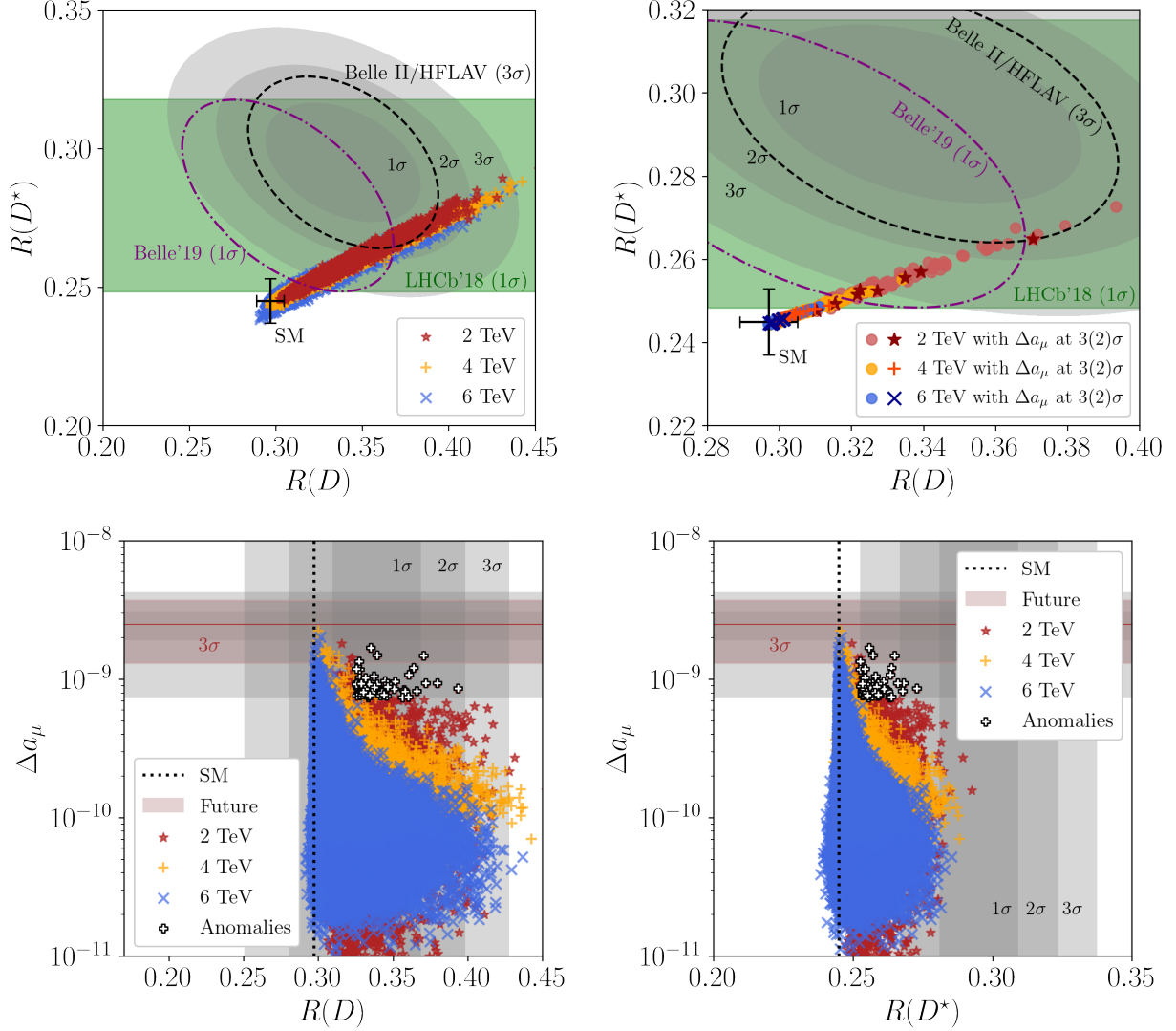


Figure 15: **Results of the comprehensive scan for the flavour anomalies in $R(D)$, $R(D^*)$ and in the AMM of the muon.** The top-left plot shows points that pass all considered constraints, while the top-right plot shows points that not only pass these constraints but also satisfy Δa_μ within 3σ (light-coloured circles) or 2σ (dark-coloured other shapes) of the present best-fit value. The scale in the top-right plot is magnified in order to highlight the region populated by the data. In both plots, the purple dot-dashed ellipse shows the 1σ contour about the most recent Belle results for $R(D)$ and $R(D^*)$ [13], and a green band shows the 1σ region about the most recent LHCb result for $R(D^*)$ [17; 18]. The black dashed ellipse indicates the prospective 3σ reach for 5 ab^{-1} of data at Belle II [102], assuming the best-fit value from 2021 and the correlation coefficient from the HFLAV collaboration [19]. The SM values for $R(D)$ and $R(D^*)$ (with associated uncertainties) are illustrated by a black barred cross in the top plots, and the SM central values are given as black dotted lines in the bottom plots. These SM values are extracted from flavio [62; 63], v2.3. The bottom plots show the AMM of the muon plotted against $R(D)$ (left) and $R(D^*)$ (right), with the red-brown band showing the 3σ projected sensitivity from the Muon $g-2$ experiment [103]. This (roughly) overlays the present 2σ region, assuming the best-fit value remains the same as the current experimental average (see red-brown solid line). For further information on how to read this figure, see section 6.3.

The difference in the parameter space probed by the primary and comprehensive scan, in turn, impacts the resultant ranges of the observables. This may occur due to modifying the sampled region for a particular effective parameter that enters in a dominant contribution according to section 5.1 (e.g. smaller accessible values of the magnitude of b_{13} , discussed in section 6.4.2), or

through an enhancement of the effective parameters appearing as subdominant in the primary scan (e.g. enhancement of LFV contributions in processes with neutrinos in the final state, see section 6.4.4). Each of these may be a result of biasing and/or the use of a different basis. We emphasise that for the plots contained in this section, used to contrast the two scans, the coloured points always represent those for which all primary constraints are satisfied. Constraints from secondary and tertiary observables are automatically fulfilled after imposing all primary constraints. Table 7 contains a summary of the spread of the numerical results for the primary observables.

Regarding the computation of the primary observables, we directly employ the analytic expressions for the trilepton decays, i.e. for $\text{BR}(\tau \rightarrow 3\mu)$, $\text{BR}(\tau \rightarrow \mu e \bar{e})$ and $\text{BR}(\mu \rightarrow 3e)$, from appendix C.2.4, and for $Z \rightarrow \tau\tau$ from appendix C.4. So, for these observables the calculation method is the same as in the primary scan in section 5. For the other primary observables, the method is different compared to the scan in section 5, since we numerically calculate $R(D)$, $R(D^*)$ and $R_{K^*}^\nu$ using the Wilson coefficients in appendix C.3, the `Wilson` package [95] and `flavio` [62; 63]. Furthermore, we compute Δa_μ , $\text{BR}(\tau \rightarrow \mu\gamma)$, $\text{BR}(\mu \rightarrow e\gamma)$ and $\text{CR}(\mu - e; \text{Al})$ using `SARAH` and `SPheno` [96; 97].

For $Z \rightarrow \tau\tau$, we do not find a discernible difference between the distributions of data from the primary and comprehensive scans. We thus refer to section 5.2.5 for a discussion of the results. We, however, display the output for $Z \rightarrow \tau\tau$, when discussing the secondary observable $g_{\mu_A}/g_A^{\text{SM}}$ in section 6.6.

6.4.1 Differences between data sets

Before comparing the results of the primary and comprehensive scans, we first comment on some important differences between the outputs of the primary scan, discussed in section 5, and the comprehensive one, discussed in this section. In table 10 in appendix E.1 we list the distributions of the unhatted LQ couplings extracted from the comprehensive scan. In this way, we can identify the effective parameters whose magnitude can be (much) smaller than λ , e.g. $|b_{13}|$, or (much) larger than $1/\lambda$, e.g. $|a_{22}|$, i.e. the region sampled in the primary scan. This difference impacts the distribution of the observables influenced by these parameters.

We look at the effective parameters that dominantly drive the analytic estimates for the primary observables, listed in table 5. We note that there is complementary influence of the effective parameters b_{13} and a_{23} via the constraints from $\mu \rightarrow e$ processes, especially $\text{BR}(\mu \rightarrow e\gamma)$. We also see from table 5 that the effective parameter b_{23} is responsible for the dominant contributions to both the AMM of the muon and to cLFV tau decays, especially $\text{BR}(\tau \rightarrow \mu\gamma)$. Therefore, as discussed in section 5, the magnitude of b_{23} should not be too large. Table 10 shows that b_{13} can take particularly small values in the comprehensive scan, which means that sampled points with larger values of $c_{23} \approx a_{23}$ are capable of avoiding constraints from $\mu \rightarrow e$ processes, see eq. (102). These larger values of the magnitude of a_{23} then require smaller b_{23} in order to generate large Δa_μ compatible with the experimental indication. At the same time, large contributions to the BR of $\tau \rightarrow \mu\gamma$ are avoided. This makes the comprehensive scan more likely to identify a larger sample of viable points consistent with reconciling the anomaly in the AMM of the muon – which is a challenge for the primary scan.

Furthermore, we note several instances in which the differences in the two scans result in an amplification of a contribution to a primary observable, identified as subdominant in section 5. Interestingly, this is relevant for the case of LFV contributions to decays with neutrinos in the final state, including $R(D)$, $R(D^*)$, τ_{B_c} and $R_{K^*}^\nu$. As we have seen, cLFV can be considerable in this model, and it is thus reasonable to expect similar violation in decays involving neutrinos.

We discuss the features mentioned above and other differences between the results of these two scans in the following. Throughout this section, we use the term ‘viable’ to denote points that are capable of passing all constraints, but not necessarily addressing the three flavour anomalies. For instance, all data points displayed in plots in this section are *viable* points.

6.4.2 Addressing the anomalies

In the comprehensive scan, we are able to identify valid points that can explain the anomalies in all three observables, $R(D)$, $R(D^*)$ and Δa_μ , at the 3σ level (see light-coloured circles in the top-right plot in figure 15). Indeed, the data reveals that, with the correlation between $R(D)$ and $R(D^*)$ accommodated, the anomalies in these two observables and the measured value of Δa_μ can be explained at the 2σ level for $\hat{m}_\phi = 2$ (see dark-coloured points in the top-right plot in figure 15). Note that the latter cannot be explicitly seen in the bottom in figure 15, because the σ -regions about the best-fit values of $R(D)$ and $R(D^*)$ do not consider the correlation between these two observables.

If we only look at the flavour anomalies in $R(D)$ and $R(D^*)$, all three considered LQ masses are compatible with viable solutions at the 2σ level (see the top-left plot in figure 15). This is also found in the primary scan in section 5. In case the best-fit values remain the same and the Belle II collaboration increases the precision with which they can probe these observables [102], the prospective 3σ contour assuming 5 ab^{-1} of data is shown in the top in figure 15 as black dashed ellipse.²⁷ We, therefore, expect that future measurements of $R(D)$ and $R(D^*)$ at Belle II will provide an important test of this model, and also recognise that the LQ masses we have shown to be viable to explain the anomalies are likely within the reach of upcoming LQ direct-production searches at the LHC.

Furthermore, we indicate the prospects for future measurements of the AMM of the muon. In the bottom in figure 15, the 3σ projected sensitivity from the Muon $g-2$ experiment [103] is seen to (roughly) overlay the present 2σ region for this observable. If, as we have illustrated here, the best-fit value remains the same and the sensitivity is improved, this will challenge the model as an explanation of the three anomalies, but not entirely rule out the viable parameter space. This is consistent with the preceding discussion, and is evident from the distribution of white crosses in the plots in figure 15.

Simultaneously addressing all three anomalies. In the primary scan, it is found to be difficult to identify points that can address all three flavour anomalies simultaneously. A key limiting factor is the interplay between large contributions to the AMM of the muon and large contributions to the radiative cLFV processes $\tau \rightarrow \mu\gamma$ and $\mu \rightarrow e\gamma$. Here we discuss how this limitation is relaxed in the comprehensive scan.

We first analytically show that the maximum value of the AMM of the muon compatible with the primary constraints is (roughly) inversely proportional to the magnitude of the effective parameter b_{13} . Recall from the estimate in eq. (68) that

$$|\Delta a_\mu| \lesssim \frac{|b_{23}c_{23}|}{\hat{m}_\phi^2} \times 10^{-9}. \quad (105)$$

The present bound on the combination $|b_{13}c_{23}|$ from $\text{BR}(\mu \rightarrow e\gamma)$, see eq. (74), can be used to parametrise the dependence on $|b_{13}|$ for a viable point. We can also bound the magnitude of b_{23} (roughly) from above by considering the dominant contribution to $\text{BR}(\tau \rightarrow \mu\gamma)$, see eq. (75), which

²⁷In generating this projected Belle II chi-squared ellipse, we have assumed the same correlation coefficient and best-fit value as have been reported for the HFLAV averages in 2021 [19].

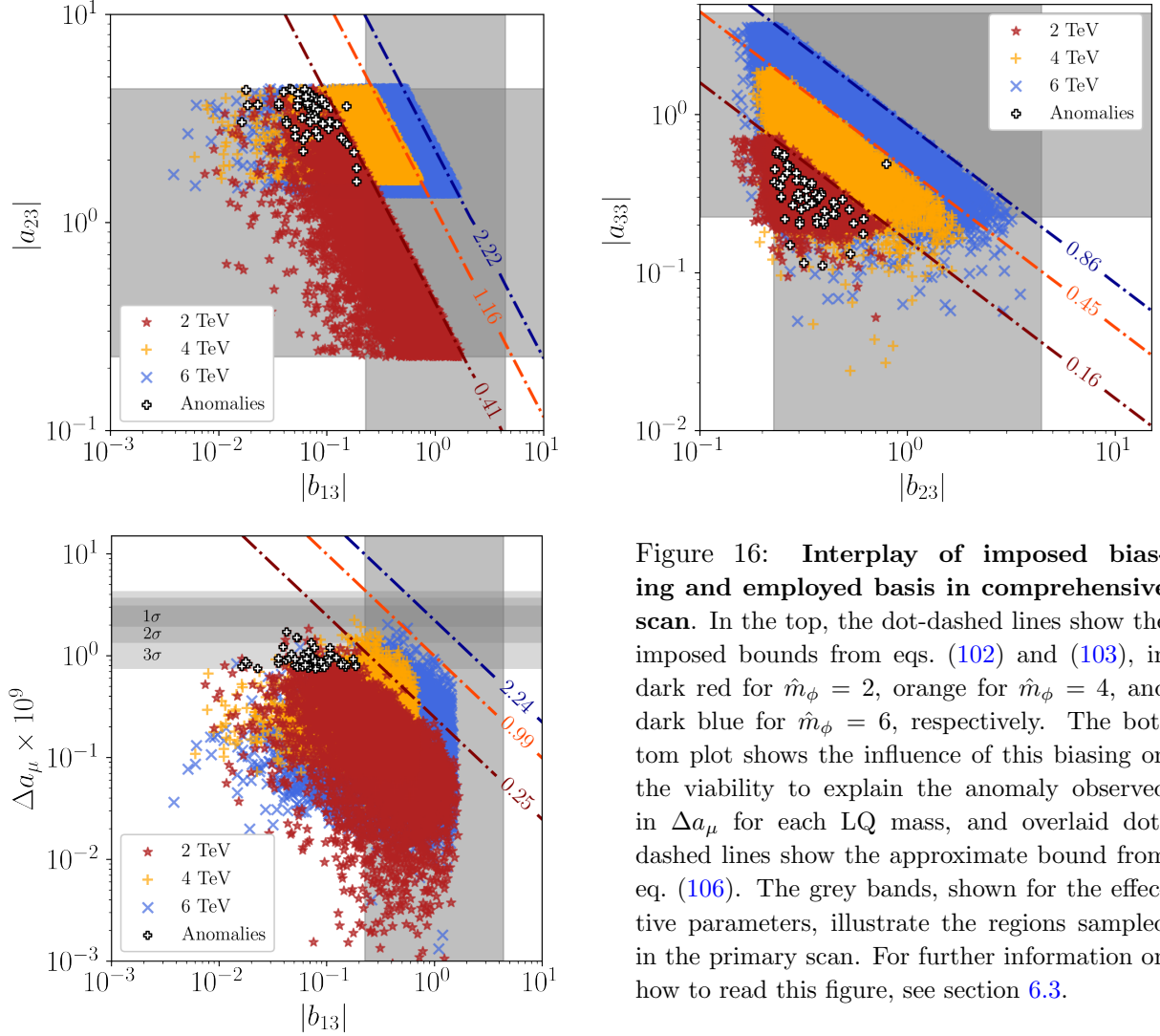


Figure 16: **Interplay of imposed biasing and employed basis in comprehensive scan.** In the top, the dot-dashed lines show the imposed bounds from eqs. (102) and (103), in dark red for $\hat{m}_\phi = 2$, orange for $\hat{m}_\phi = 4$, and dark blue for $\hat{m}_\phi = 6$, respectively. The bottom plot shows the influence of this biasing on the viability to explain the anomaly observed in Δa_μ for each LQ mass, and overlaid dot-dashed lines show the approximate bound from eq. (106). The grey bands, shown for the effective parameters, illustrate the regions sampled in the primary scan. For further information on how to read this figure, see section 6.3.

is proportional to $|b_{23}c_{33}|$, and using the minimum sampled value of the magnitude of $c_{33} \approx a_{33}$ from table 6. Therefore, an approximate upper bound for the maximally accessible value of $|\Delta a_\mu|$ for each LQ mass can be expressed as

$$|\Delta a_\mu| \lesssim \frac{1}{|b_{13}|} \left\{ \begin{array}{l} 0.249, \quad \hat{m}_\phi = 2 \\ 0.993, \quad \hat{m}_\phi = 4 \\ 2.236, \quad \hat{m}_\phi = 6 \end{array} \right\} \times 10^{-9}. \quad (106)$$

This inverse correlation between the maximum value of $|\Delta a_\mu|$ and the magnitude of the effective parameter b_{13} is also influenced by the biasing procedure, which aims to target points that avoid constraints from the two radiative cLFV decays $\mu \rightarrow e\gamma$ and $\tau \rightarrow \mu\gamma$ using eqs. (102) and (103).

The influence of biasing the effective parameters and the distribution of those dominating the contributions to radiative cLFV decays are illustrated in the top in figure 16. The top-left plot shows the distribution of values of the magnitude of b_{13} accessible in the primary and comprehensive scans. Whereas the minimum value for $|b_{13}|$ is seen to be as small as $\mathcal{O}(10^{-3})$ in the comprehensive scan, the primary scan only employs values larger than $\lambda \approx 0.22$. From eq. (106), we therefore expect larger accessible values of the AMM of the muon, while, at the same time, evading the primary constraints. This is, indeed, the case as shown in the bottom in figure 16, where we show the distribution of Δa_μ plotted against the value of $|b_{13}|$. This effect is especially striking for $\hat{m}_\phi = 2$, for which the only points that explain the observed anomaly in Δa_μ within the 3σ

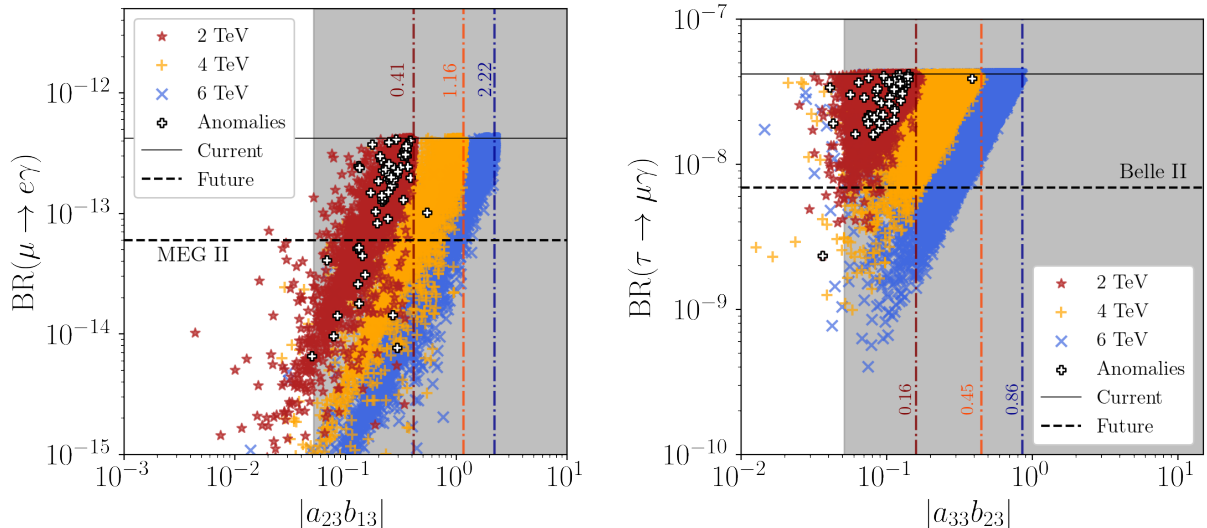


Figure 17: **Impact of sampling on radiative cLFV decays in comprehensive scan.** The vertical dot-dashed lines show the upper bounds on the respective product of effective parameters taken from eqs. (102) and (103), in dark red for $\hat{m}_\phi = 2$, orange for $\hat{m}_\phi = 4$, and dark blue for $\hat{m}_\phi = 6$, respectively. For further information on how to read this figure, see section 6.3.

range are found outside the grey-shaded region, i.e the sampled region of the magnitude of b_{13} in the primary scan. We note that in the bottom in figure 16 we also overlay as dot-dashed lines the upper bound for each LQ mass, as shown eq. (106). We see reasonable agreement with the data, given that this upper bound has been derived under the assumption that the magnitudes of both a_{33} and b_{23} lie in the interval $[\lambda, 1/\lambda]$, which is, however, not always fulfilled in the comprehensive scan, compare top-right plot in figure 16.

Contributions from lepton flavour violating channels to $R(D)$ and $R(D^*)$. We comment on the impact of the LFV contribution from $b \rightarrow c\tau\nu_\mu$ to $R(D)$ and $R(D^*)$ in the comprehensive scan. Appealing to the analytic formulae in eqs. (66) and (67), we see that the contribution from the LFV final state with a muon neutrino is proportional to $|a_{23}b_{32}|$. We recall that the magnitude of a_{23} is biased towards larger values, see table 6, and we thus expect non-negligible contributions from this decay channel to $R(D)$ and $R(D^*)$ in the comprehensive scan. Even though this LFV channel does not interfere with the SM contribution, for $\hat{m}_\phi = 2$ it can generate an enhancement above the SM value as large as 40 percent for $R(D)$ and 30 percent for $R(D^*)$, respectively, using all viable points. For $\hat{m}_\phi = 4, 6$ there is at most a 10 percent enhancement in either observable above the SM value, which is roughly consistent with the present 1σ margin about the best-fit values. Therefore, we emphasise that this effect cannot be neglected, when considering these observables in this model, particularly as future experiments will reach increased sensitivity.

6.4.3 Leptonic primary constraints

In section 5.2.3 it is shown that the strongest present experimental constraints on this model arise from the radiative cLFV decays $\tau \rightarrow \mu\gamma$ and $\mu \rightarrow e\gamma$. In the following, we discuss the differences between the results of the primary and comprehensive scans for these and other leptonic primary constraints as well as the prospects that these processes offer as signals of this model at future experiments.

Radiative charged lepton flavour violating decays. In figure 17, we show the impact of biasing on the parameter space in the case of the radiative cLFV decays $\mu \rightarrow e\gamma$ and $\tau \rightarrow \mu\gamma$. The upper bounds from eqs. (102) and (103) are shown as vertical dot-dashed lines.

Since in the comprehensive scan the magnitude of the effective parameter b_{13} can be significantly lower than λ , also the attained values of the product $|a_{23}b_{13}|$ can be smaller than naively expected, compare coloured points and grey-shaded region in the left plot in figure 17. This product being smaller generally corresponds to a suppressed value of $\text{BR}(\mu \rightarrow e\gamma)$, consistent with the analytic estimate in eq. (72). We see that a signal of $\mu \rightarrow e\gamma$ is predicted to be observed at MEG II [107] for a large number of viable points, in agreement with the findings of the primary scan, see section 5.2.3. Nevertheless, there are points capable of addressing all three flavour anomalies that remain unconstrained by this observable even with this increased sensitivity.

Similarly, we note that the magnitude of the effective parameter a_{33} can be smaller than λ , see top-right plot in figure 16, though to a lesser extent than in the case of b_{13} . We, thus, expect points in the right plot in figure 17 to fall below the grey region for the product $|a_{33}b_{23}|$. Smaller accessible values of a_{33} imply viable points with larger magnitude of b_{23} , although we see that the present bound from $\text{BR}(\tau \rightarrow \mu\gamma)$ is already very constraining on this product. Furthermore, we note that the majority of points able to address the three anomalies, i.e. the white crosses, lead to a value for $\text{BR}(\tau \rightarrow \mu\gamma)$ in the region that can be probed by the future sensitivity of Belle II [105].

Finally, we mention that the distributions for these radiative cLFV decays with respect to $R(D)$, $R(D^*)$ and the AMM of the muon can be found in figure 26 in appendix E.2. These can be compared with figure 8 in section 5.2.3.

Trilepton tau decays. We discuss the results for the primary constraints $\text{BR}(\tau \rightarrow 3\mu)$ and $\text{BR}(\tau \rightarrow \mu e\bar{e})$ in the comprehensive scan. The relationship between these two observables is displayed in the top-left plot in figure 18. Unlike in the primary scan in section 5, we in general do not find that $\text{BR}(\tau \rightarrow 3\mu) \approx \text{BR}(\tau \rightarrow \mu e\bar{e})$, i.e. eq. (81) does not hold for the shown data. This is due to the impact of subdominant contributions to both processes, including the Z -penguin contributions explicitly detailed in eqs. (77) and (78), as well as subleading contributions to both processes, e.g. contributions due to box diagrams as discussed in appendix C.2. We show the relation given in eq. (81), reflecting γ -penguin dominance, as an overlaid purple dot-dashed line. We note that there is a strong positive correlation between the observables, but a spread influenced non-trivially by these subdominant contributions. Therefore, both observables should be separately considered with respect to the future prospects for signals at Belle II [105].

Next, we would like to contrast the results for $\text{BR}(\tau \rightarrow 3\mu)$ with those of the primary scan. In the top-right plot in figure 18 we show $\text{BR}(\tau \rightarrow 3\mu)$ plotted against $\text{BR}(\tau \rightarrow \mu\gamma)$. The overlaid purple dot-dashed line shows the estimate from eq. (79), i.e. the linear correlation between $\text{BR}(\tau \rightarrow 3\mu)$ and $\text{BR}(\tau \rightarrow \mu\gamma)$ in the case of γ -penguin dominance. Comparing this plot with the corresponding one in figure 12, we notice a large number of points, particularly for $\hat{n}_\phi = 2$, that result in a value for $\text{BR}(\tau \rightarrow 3\mu)$ which can be probed at Belle II unlike in the case of the primary scan. This includes a sizeable number of the white crosses, points capable of addressing all three anomalies, which motivates further examination of this difference.

The explanation for this difference lies in the relevance of Z - and γ -penguin contributions to $\text{BR}(\tau \rightarrow 3\mu)$. Eq. (77) reveals that both contributions are proportional to $|c_{33}| \approx |a_{33}|$, and also to $|c_{23}| \approx |a_{23}|$ (Z -penguin) or $|b_{23}|$ (γ -penguin), respectively. Smaller γ -penguin contributions correspond to smaller values of $\text{BR}(\tau \rightarrow \mu\gamma)$, see eq. (73), and are thus preferred in the comprehensive scan due to biasing, compare eq. (103). Therefore, in order to generate a significant contribution to the AMM of the muon larger values of the magnitude of the effective parameter $a_{23} \approx c_{23}$ are needed, see eq. (68) and table 6. This, in turn, typically enhances the Z -penguin contributions to

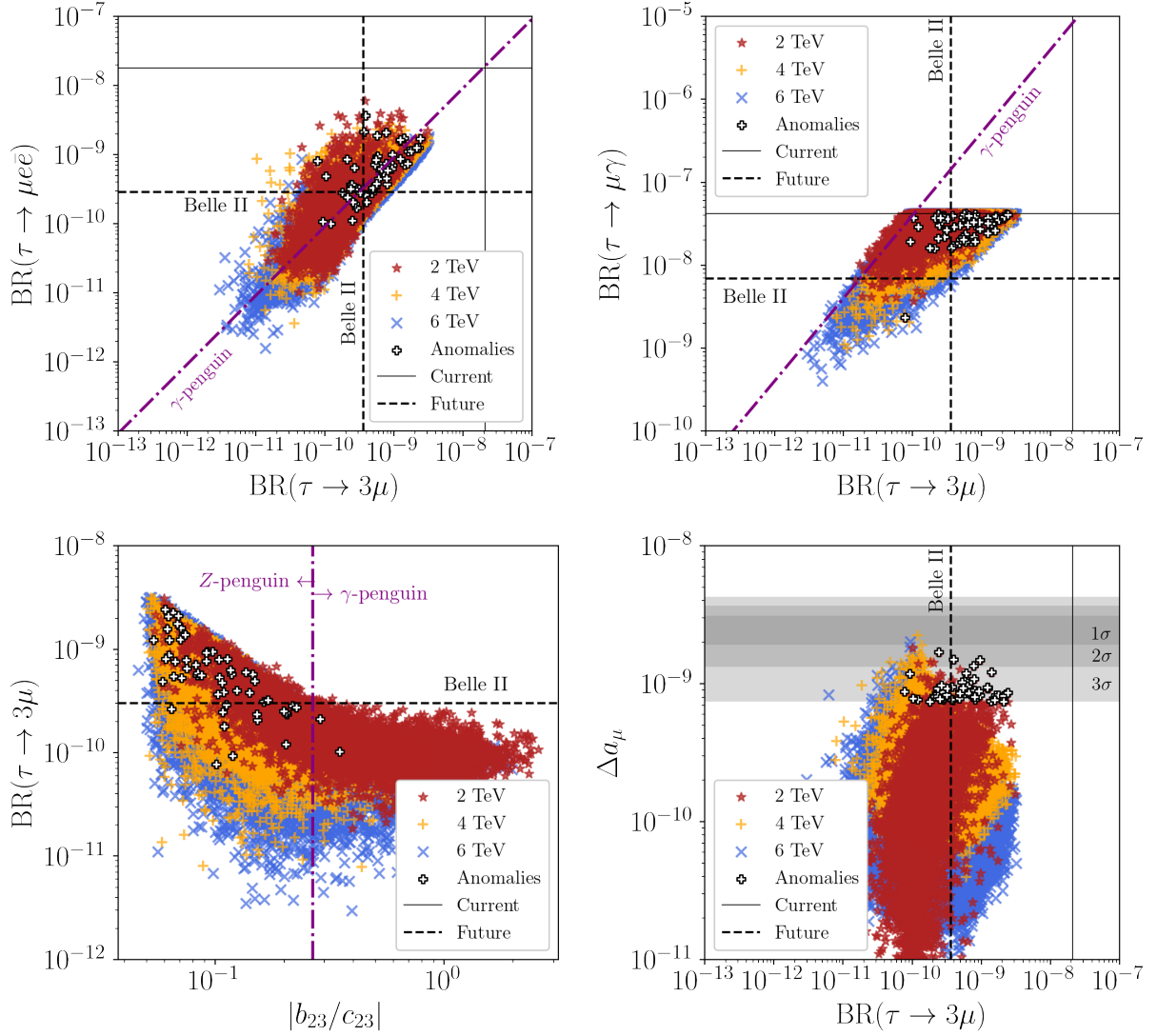


Figure 18: **Impact of sampling on trilepton tau decays in comprehensive scan.** In the two plots in the top, the purple dot-dashed line, labelled ‘ γ -penguin’, indicates the approximate relation between these observables in the case of γ -penguin dominance, see eqs. (81) (left) and (79) (right). In the bottom-left plot the purple dot-dashed line shows the borderline between Z- and γ -penguin dominance, as labelled. For further information on how to read this figure, see section 6.3.

$\text{BR}(\tau \rightarrow 3\mu)$. From eq. (77) we can derive the value of the ratio $|b_{23}/c_{23}|$ at which the dominant contribution changes. This is illustrated as a purple dot-dashed line in the bottom-left plot in figure 18. Consistent with the preceding discussion we see that points preferred by explaining the flavour anomalies overwhelmingly correspond to those which have values of $|b_{23}/c_{23}|$ in the range of Z-penguin dominance. In the bottom-right plot in figure 18, we also see that, indeed, these same points correspond to significant contributions to Δa_μ .

Furthermore, we notice in the bottom-right plot in figure 18 a prominent feature, namely a diagonal cutoff towards the top-right corner of the plot for $\hat{m}_\phi = 4, 6$, which is not present for $\hat{m}_\phi = 2$. In section 5.2.4, this feature has been associated with the inverse proportionality of the maximum contributions to $\text{BR}(\tau \rightarrow \mu\gamma)$ and Δa_μ , at LO. In the top-right plot in figure 12, we observe this cutoff for all three sampled LQ masses, although less clearly for $\hat{m}_\phi = 2$. For larger LQ masses, subdominant contributions, particularly to $\text{BR}(\tau \rightarrow \mu\gamma)$ and $\text{BR}(\tau \rightarrow 3\mu)$, are more suppressed by the LQ mass, and consequently this cutoff is more pronounced. For $\hat{m}_\phi = 2$, such

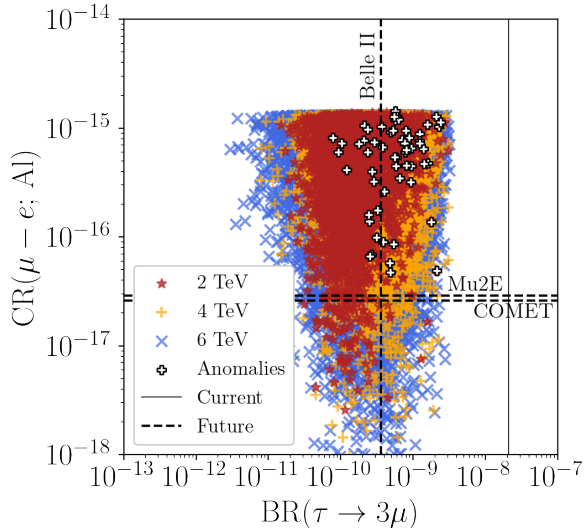


Figure 19: **Example of interplay between $\text{BR}(\tau \rightarrow 3\mu)$ and $\mu \rightarrow e$ processes in comprehensive scan.** We plot $\text{CR}(\mu \rightarrow e; \text{Al})$ against $\text{BR}(\tau \rightarrow 3\mu)$ in order to illustrate the spread of points that correspond to large $\text{BR}(\tau \rightarrow 3\mu)$, but a small signal in $\mu \rightarrow e$ processes. We show for $\text{CR}(\mu \rightarrow e; \text{Al})$ two prospective limits as black dashed lines, from COMET [111] and Mu2e [112]. For further information on how to read this figure, see section 6.3.

contributions enter and weaken the mentioned inverse proportionality – leading to the observed spread of points towards the top-right corner of the plot.

In summary, the flavour anomaly in the AMM of the muon can be explained, while potentially large signals for both $\tau \rightarrow 3\mu$ and $\tau \rightarrow \mu e \bar{e}$ can be observed at Belle II. These signals are driven by largish Z -penguin contributions that, unlike contributions due to γ -penguins, are not constrained by correspondingly large contributions to $\text{BR}(\tau \rightarrow \mu\gamma)$. The correlation between larger BRs for trilepton tau decays and sizeable values of the AMM of the muon is enhanced by the biasing, and particularly by the increase in sampled viable points with a large magnitude of the effective parameter a_{23} , as discussed in section 6.4.2.

Further $\mu \rightarrow e$ processes. With smaller values of the magnitude of the effective parameter b_{13} , see top-left plot in figure 16, in particular the white crosses, we can also access smaller values of the observables dominantly driven by this parameter. These include, as we can see from table 5, $\text{BR}(\mu \rightarrow e\gamma)$, $\text{CR}(\mu \rightarrow e; \text{Al})$ and $\text{BR}(\mu \rightarrow 3e)$. Although smaller b_{13} allows to evade present constraints, it does not exclude these channels as means to test this model at future experiments. As the prospects for $\text{BR}(\mu \rightarrow e\gamma)$ are already discussed, we focus in the following on the other two processes. From table 7 we see that on average $\text{BR}(\mu \rightarrow 3e) \sim \mathcal{O}(10^{-15})$ which is an order of magnitude larger than the projected sensitivity of Phase 2 of the Mu3e experiment [110]. Still, we find points that can evade this constraint, even with this future sensitivity, including the ones that are capable of addressing the three flavour anomalies. Similarly, we have on average $\text{CR}(\mu \rightarrow e; \text{Al}) \sim \mathcal{O}(10^{-16})$ which is an order of magnitude larger than the future projections for COMET [111] and Mu2e [112]. Compellingly, in figure 19 we see that all white crosses, associated with points that explain the three flavour anomalies at the 3σ level or better, are within the region of parameter space probed by either future search for $\mu \rightarrow e$ conversion in aluminium. Therefore, we predict a signal to be observed for this process. Note that the same proportionality between $\text{CR}(\mu \rightarrow e; \text{Al})$ and $\text{BR}(\mu \rightarrow e\gamma)$ is found in the comprehensive scan as in the primary scan, illustrated in figure 11. So, the upper bound on $\text{CR}(\mu \rightarrow e; \text{Al})$, seen in figure 19, stems from respecting the present constraint on $\text{BR}(\mu \rightarrow e\gamma)$.

Furthermore, we comment on the relation between $\mu \rightarrow e$ processes and $\text{BR}(\tau \rightarrow 3\mu)$ in this model. This is a continuation of the discussion found in section 5.2.4, in which it is noted that large $\text{BR}(\tau \rightarrow 3\mu)$, observable at Belle II, is much less likely, if contributions to $\mu \rightarrow e$ processes are beyond the reach of future experiments. This relation is found to be less pronounced in the

comprehensive scan, because smaller values of the rates of $\mu \rightarrow e$ processes can be generally reached, given that their dominant contributions are proportional to the magnitude of b_{13} . As this effective parameter can take much smaller values in the comprehensive scan, larger values of the magnitude of $a_{23} \approx c_{23}$ become allowed that can enhance Z -penguin contributions to $\text{BR}(\tau \rightarrow 3\mu)$. This explains the existence of viable points towards the bottom-right corner in figure 19, not observed in the corresponding plot of the primary scan, see figure 12. We notice that the plots for $\text{BR}(\mu \rightarrow 3e)$ and $\text{BR}(\mu \rightarrow e\gamma)$ reveal a very similar behaviour to the one for $\text{CR}(\mu - e; \text{Al})$ shown in figure 19.

6.4.4 Hadronic primary constraints

In the primary scan in section 5 the behaviour of the hadronic observables $R_{K^*}^\nu$ and τ_{B_c} , the B_c lifetime, is explored. Notably, both of these observables involve neutrinos in the final state. Naively, one may be tempted to consider only contributions for which lepton flavour is conserved, and therefore lead to interference with the corresponding SM contributions. However, as pointed out for $R(D)$ and $R(D^*)$ in section 6.4.2, the contributions from LFV channels are found to be non-negligible in the comprehensive scan. We discuss these and other differences between the primary and comprehensive scan for $R_{K^*}^\nu$ and τ_{B_c} in the following.

Contributions to observable $R_{K^*}^\nu$. From section 5.2.5 we expect the constraint on $\text{BR}(\tau \rightarrow \mu\gamma)$, whose dominant contribution is driven by the product $|b_{23}c_{33}|$, to impact the size of the main contributions to $R_{K^*}^\nu$, driven by the magnitude of $a_{33} \approx c_{33}$, and to the AMM of the muon, depending dominantly on the magnitude of b_{23} , see table 5. This correlation is visible to a certain extent in the primary scan, see bottom-right plot in figure 13. In the comprehensive scan, the relation between the effective parameters a_{33} and b_{23} is further enhanced by the biasing, see eq. (103). Thus, the observed correlation is apparent in the top-left plot in figure 20, in particular for $\hat{m}_\phi = 4$ and $\hat{m}_\phi = 6$. As can be seen, the majority of points that imply values for $R_{K^*}^\nu$ close to its present bound corresponds to smaller values of Δa_μ . This trend seems absent for $\hat{m}_\phi = 2$, as we discuss in the following.

In order to understand the distribution of values for $R_{K^*}^\nu$ in the comprehensive scan, we first recall that the dominant contribution in the model has $\nu_\tau \bar{\nu}_\tau$ in the final state, see eq. (92), and is determined by the product $|a_{33}a_{32}|$. In the top-right plot in figure 20, we see that there is, indeed, a strong correlation between larger values of the magnitude of a_{32} and large values for $R_{K^*}^\nu$. Numerically we find that $|a_{32}|$ can be as large as $\mathcal{O}(10)$, see table 10 in appendix E.1. This can be traced back to a potentially large additional contribution to the effective parameter a_{32} , originating from the transformation from the interaction to the charged fermion mass basis, compare eq. (124). At the same time, we see in the bottom-left plot in figure 20 that the biasing prefers smaller values of $|a_{33}| \approx |c_{33}|$ for smaller LQ masses, see also table 6, and that most white crosses also correspond to smaller $|a_{33}|$. For these smaller values, larger values of the magnitude of b_{23} are likely to be compatible with the present bound from $\text{BR}(\tau \rightarrow \mu\gamma)$, compare eq. (73). These larger values of $|b_{23}|$ tend to increase Δa_μ , see eq. (68), and can push it closer to the present best-fit value. Altogether, we can generally expect larger contributions to $R_{K^*}^\nu$ to be accessible for $\nu_\tau \bar{\nu}_\tau$ in the final state than in the primary scan, see section 5.2.5. However, for $\hat{m}_\phi = 2$ smaller values of $|a_{33}|$ are usually attained, as we see from the bottom-left plot in figure 20. Nevertheless, large values for $R_{K^*}^\nu$ can be obtained.

From eq. (92), we note that there can be sizeable contributions from the channel with $\nu_\mu \bar{\nu}_\mu$ in the final state which are proportional to the product $|a_{23}a_{22}|$ as well as LFV contributions having $\nu_\mu \bar{\nu}_\tau$ and $\nu_\tau \bar{\nu}_\mu$ in the final state that are driven by $|a_{23}a_{32}|$ and $|a_{33}a_{22}|$, respectively. In the

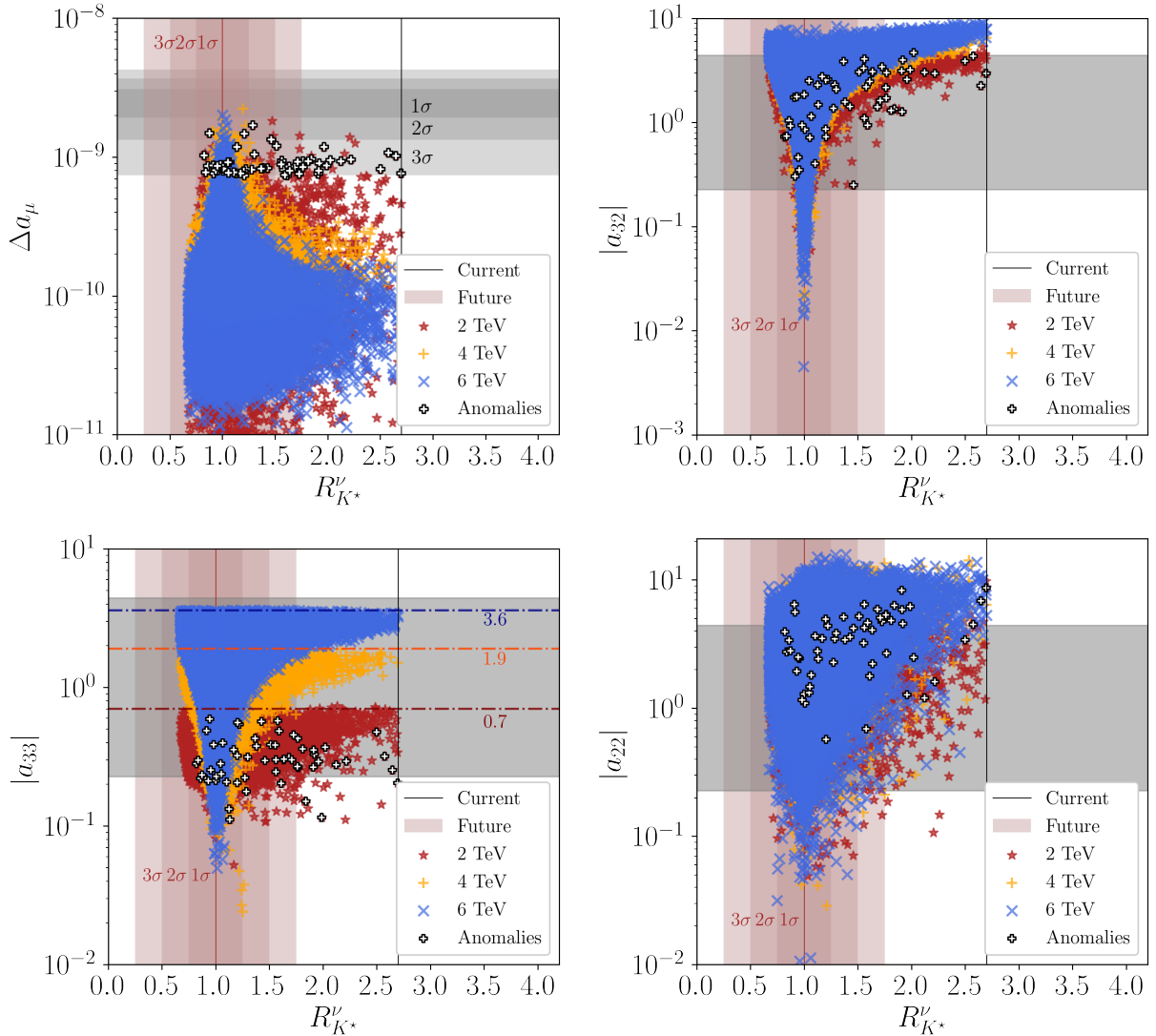


Figure 20: **Impact of sampling on $R_{K^*}^\nu$ in comprehensive scan.** The red-brown shaded regions show the projected reach for $R_{K^*}^\nu$ at Belle II for 5 ab^{-1} of data, assuming the best-fit value is SM-like. The top-left plot shows the parameter space for $R_{K^*}^\nu$ plotted together with Δa_μ . The remaining plots show $R_{K^*}^\nu$ plotted together with one of the relevant effective parameters, as identified in the analytic estimate in eq. (92). For the bottom-left plot, the dot-dashed lines show the upper limit on the magnitude of a_{33} for each LQ mass, taken from table 6, in dark red for $\hat{m}_\phi = 2$, orange for $\hat{m}_\phi = 4$, and dark blue for $\hat{m}_\phi = 6$, respectively. For further information on how to read this figure, see section 6.3.

comprehensive scan, we find that the magnitude of a_{22} can be as large as $\mathcal{O}(10)$, see bottom-right plot in figure 20 and table 10 in appendix E.1. At the same time, larger values of the magnitude of a_{23} are preferred by the biasing, see table 6. Therefore, the contribution with $\nu_\mu \bar{\nu}_\mu$ in the final state becomes more significant for $R_{K^*}^\nu$ in comparison to the primary scan. This argument is supported by the positive correlation in the data between large $|a_{22}|$ and larger $R_{K^*}^\nu$, shown in the bottom-right plot in figure 20. Additionally, the LFV contributions with $\nu_\mu \bar{\nu}_\tau$ and $\nu_\tau \bar{\nu}_\mu$ in the final state can also generate relevant contributions, particularly driven by larger values of the product $|a_{23} a_{32}|$. For the other contribution proportional to the product $|a_{33} a_{22}|$, the biasing prefers smaller values of $|a_{33}|$, see table 6 and bottom-left plot in figure 20, in particular for smaller LQ masses, so that we do not expect it to be equally important.

In summary, the current constraint on $R_{K^*}^\nu$ is found to genuinely shape the viable parameter

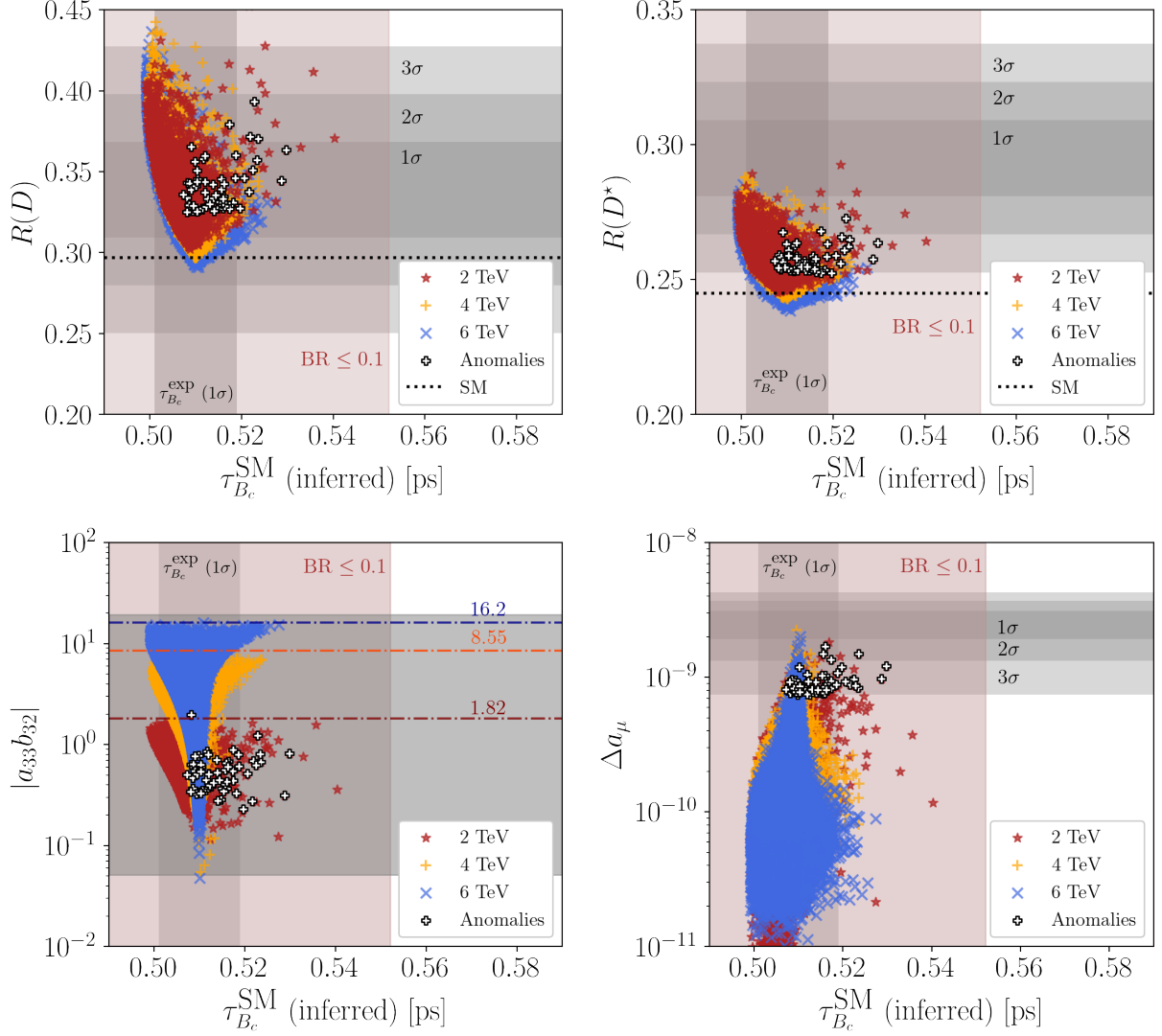


Figure 21: **Impact of sampling on inferred SM contribution to B_c lifetime in comprehensive scan.** For the B_c lifetime, the grey shaded region represents the 1σ region about the present experimental best-fit value of τ_{B_c} , and the red-brown shaded region shows the area that corresponds to $\text{BR}(B_c \rightarrow \tau\nu) \leq 0.1$. For the bottom-left plot, the grey-shaded region represents the sampled parameter range in the primary scan and the dot-dashed lines show the upper limit on the product $|a_{33}b_{32}|$ for each LQ mass, calculated from table 6, in dark red for $\hat{m}_\phi = 2$, orange for $\hat{m}_\phi = 4$, and dark blue for $\hat{m}_\phi = 6$, respectively. Further information on how to read this figure can be found in section 6.3.

space, and the prospective measurement of $B \rightarrow K^{(*)} + \text{invisible}$ at Belle II [114] provides a promising avenue to test this model.

Lifetime of B_c meson. For this observable, we similarly find differences between the values obtained in the comprehensive and the primary scan. While a substantial contribution to the B_c lifetime is associated with values of $R(D)$ and $R(D^*)$ below their SM predictions in the primary scan, see top in figure 13 in section 5 and discussion in section 5.2.5, in the comprehensive scan, especially for $\hat{m}_\phi = 2$, points are observed that are in disagreement with this statement and therefore hint at the influence of subdominant contributions. This can be explicitly seen in the top in figure 21.

Eq. (90) shows that the dominant term for the inferred SM contribution to the B_c lifetime,

LIST OF SECONDARY OBSERVABLES				
Observable	Experiment			
	Current constraint/measurement		Future reach	
$ d_\mu $	$< 1.5 \times 10^{-19} e \text{ cm}$	at 90% C.L. [148]	1000 (60) [1] $\times 10^{-24} e \text{ cm}$	[149–153]
$g_{\mu_A}/g_A^{\text{SM}}$	0.99986 ± 0.00108	at 1σ level [115; 116]	$\pm 6.3 (0.63) \times 10^{-5}$	[116–118]
$R_D^{\mu/e}$	0.995 ± 0.090	at 1σ level [154]	± 0.00995	[155]
$R_{D^*}^{e/\mu}$	1.01 ± 0.032	at 1σ level [156]	± 0.0101	[155]
$\text{BR}(B \rightarrow \tau\nu)$	$(1.09 \pm 0.24) \times 10^{-4}$	at 1σ level [93]	$\pm 9 (4)\%$ at 5 (50) ab^{-1}	[102]

Table 8: **List of secondary observables.** We list the observables that can potentially be used to further constrain and test this model, together with their current experimental constraint/measurement and future sensitivity. In the case of the EDM of the muon, d_μ , the future projection without brackets refers to the reach expected from the Muon $g-2$ experiment at Fermilab [149], and a similar experimental effort [150] undertaken at J-PARC. The values in brackets are estimates given for experimental proposals using the frozen-spin technique [151–153]. In the case of the future projections for g_{μ_A} , we assume that the measurements of g_{μ_A} are improved by the same factor as $\sin^2 \theta_{\text{eff}}$ [116]; the unbracketed projection is for the ILC [117], and the bracketed value is for the FCC [118].

inferred $\tau_{B_c}^{\text{SM}}$, is driven by the product $|a_{33}b_{32}|$, which corresponds to the tau neutrino being in the final state and which interferes with the SM contribution. From the bottom-left plot in figure 21, we see that this product is sampled over a much smaller range for $\hat{m}_\phi = 2$ than for the other LQ masses, due to the biasing imposed, see table 6. However, for small values of this product, larger values of the inferred $\tau_{B_c}^{\text{SM}}$ are nevertheless accessible. This indicates the relevance of subdominant contributions. The other contribution, mentioned in eq. (90), is proportional to the product $|a_{23}b_{32}|$, and corresponds to the muon neutrino in the final state. One should recall that the magnitude of $a_{23} \approx c_{23}$ needs to be quite large to explain the observed anomaly in Δa_μ and that we sample more viable points with such larger values due to the biasing, see table 6. We, thus, can expect an enhancement of the LFV contribution, with the muon neutrino in the final state, to the inferred $\tau_{B_c}^{\text{SM}}$ – similarly to the effect found for $R(D)$ and $R(D^*)$, see section 6.4.2. For $\hat{m}_\phi = 2$, we see from the bottom in figure 21 that a sizeable fraction of the points that correspond to small values of the product $|a_{33}b_{32}|$ and larger inferred $\tau_{B_c}^{\text{SM}}$ also leads to a larger value for the AMM of the muon, compare especially the white crosses.

Despite the differences found in the results of the primary and comprehensive scan, this model still predicts $\text{BR}(B_c \rightarrow \tau\nu)$ to be below 0.1. More precise measurements of $B_c \rightarrow \tau\nu$ could provide a further test of this model, in particular when considering the complementarity with measurements of $R(D)$ and $R(D^*)$.

6.5 Analytic estimates for secondary observables

As in section 5, we first discuss analytic estimates for the secondary observables. Present constraints/measurements and future reach for these are summarised in table 8.

6.5.1 Electric dipole moment of muon

The contributions to leptonic AMMs and EDMs arise both from the one-loop diagram, shown in figure 2 in section 5.1.2. In fact, they correspond to the real and imaginary part of the same effective vertex, as can be seen from eq. (144) in appendix C.2. As we generate large contributions

to the AMM of the muon and we allow for complex values for the LQ couplings, we expect that this model can lead to sizeable values for the EDM of the muon.

Similar to the AMM of the muon, most relevant is the contribution in which a chirality flip occurs via a mass insertion on the internal quark line, and which is thus enhanced by the mass of the top quark. The following expression for d_μ can be derived, assuming $m_\phi \gg m_t$,

$$|d_\mu| \approx \frac{2|\text{Im}(c_{23}b_{23}^*)|}{\hat{m}_\phi^2} \times 10^{-22} e \text{ cm}. \quad (107)$$

This predicts the value of d_μ below the current bound, but well within the reach of future experiments, as quoted in table 8. This is consistent with the literature for expected correlations between d_μ and solutions to the present flavour anomaly in the AMM of the muon, particularly for the LQ ϕ , see e.g. [124; 157].

6.5.2 $Z \rightarrow \mu\mu$

In order to achieve sizeable contributions to the AMM of the muon through loops with a top quark, an associated enhanced contribution to the process $Z \rightarrow \mu\mu$ is expected, see diagrams in figure 5. Similarly to section 5.1.8, we use eq. (191) in appendix C.4 to parametrise the contribution to the effective axial-vector coupling of Z to muons in this model. Following appendix C.4 for the definition of g_A^{SM} , $g_A^{\text{SM}} < 0$, and taking lepton flavour to be conserved for SM couplings, i.e. g_A^{SM} is the same for all lepton flavours, we find

$$g_{\mu_A}/g_A^{\text{SM}} \approx 1 - \left[\left\{ \begin{array}{ll} 2.31, & \hat{m}_\phi = 2 \\ 0.76, & \hat{m}_\phi = 4 \\ 0.39, & \hat{m}_\phi = 6 \end{array} \right\} |c_{23}|^2 \times 10^{-5} \right]. \quad (108)$$

If we allow for a 3σ margin about the best-fit value, given in table 8, we obtain upper bounds on the magnitude of c_{23} , namely the unbracketed values below

$$|c_{23}| \lesssim \left\{ \begin{array}{ll} 12.1 [3.8], & \hat{m}_\phi = 2 \\ 21.1 [6.6], & \hat{m}_\phi = 4 \\ 29.5 [9.2], & \hat{m}_\phi = 6 \end{array} \right\}. \quad (109)$$

In the comprehensive scan, the values of $c_{23} \approx a_{23}$ typically do not become larger than $1/\lambda$, see table 10 in appendix E.1, and so the present constraints from this process are not competitive. However, future experiments are projected to be much more sensitive, as can be seen from the values in square brackets in eq. (109). These are extracted using the projected sensitivity for the ILC [117], see table 8. A further reduction of the error by a factor of ten is expected from the FCC [118], allowing to probe more viable parameter space. Therefore, this observable will be relevant in the future, particularly for $\hat{m}_\phi = 2$.

6.5.3 Lepton flavour universality ratios $R_D^{\mu/e}$ and $R_{D^*}^{e/\mu}$

The observed anomalies in $R(D)$ and $R(D^*)$ raise the question whether the effects of LFU violation may be evident in other ratios of $b \rightarrow ce_i\nu_j$ processes. Two of particular interest are the ratios $R_D^{\mu/e}$ and $R_{D^*}^{e/\mu}$

$$R_D^{\mu/e} = \frac{\Gamma(B \rightarrow D\mu\nu)}{\Gamma(B \rightarrow De\nu)} \quad \text{and} \quad R_{D^*}^{e/\mu} = \frac{\Gamma(B \rightarrow D^*e\nu)}{\Gamma(B \rightarrow D^*\mu\nu)}. \quad (110)$$

Using the expressions from appendix C.3.4 we arrive at the following estimates at LO

$$\frac{R_D^{\mu/e}}{[R_D^{\mu/e}]_{\text{SM}}} \approx 1 + \left(\frac{2.25 \operatorname{Re}(b_{22}^* a_{23}) + 19.7 \operatorname{Re}(a_{23}^* c_{22})}{\hat{m}_\phi^2} \right) \times 10^{-4} \quad (111)$$

and

$$\frac{R_{D^*}^{e/\mu}}{[R_{D^*}^{e/\mu}]_{\text{SM}}} \approx 1 - \left(\frac{0.68 \operatorname{Re}(b_{22}^* a_{23}) + 19.6 \operatorname{Re}(a_{23}^* c_{22})}{\hat{m}_\phi^2} \right) \times 10^{-4} . \quad (112)$$

The terms proportional to $\operatorname{Re}(b_{22}^* a_{23})$ come from the scalar-operator contribution, while the vector-operator contribution is responsible for the dominant terms proportional to $\operatorname{Re}(a_{23}^* c_{22})$. Both contributions arise at the same order in λ . As shown in sections 3.3.1 and 3.3.2, in this model the LQ coupling y_{22} turns out to be larger than expected, $y_{22} = b_{22} \lambda^3$. This coupling enters the estimates for these observables. We also note that both observables depend on the effective parameter $a_{23} \approx c_{23}$, which plays an important role for addressing the flavour anomaly in the AMM of the muon. Eventually, note that the SM value for both observables is approximately one, with the exact value used in the comprehensive scan being extracted from `flavio`, v2.3.

6.5.4 Leptonic decay $B \rightarrow \tau \nu$

In this model, the LQ ϕ contributes to the leptonic decay $B \rightarrow \tau \nu$, which is CKM-suppressed due to $|V_{ub}| \sim \lambda^3$ in the SM, see eq. (162) in appendix C.3.5 with $u_k = u$ for the full decay width including the contributions from ϕ . We focus on the case of a tau neutrino in the final state, since its contribution interferes with the SM one. The largest contribution arises for the Wilson coefficient $C_{\nu edu,3331}^{VLL}$, while the Wilson coefficient $C_{\nu edu,3331}^{SRR}$ is suppressed at the scale $\mu = m_\phi$ due to the hierarchy $y_{31}/z_{31} \sim \lambda^2$, see eqs. (58) and (55). This suppression is only partly compensated by the RG running down to the hadronic scale $\mu = \mu_B = 4.8$ GeV and the chirality enhancement of the scalar-operator contribution. This together results in an enhancement factor of roughly 6.5. We, thus, find

$$\frac{\operatorname{BR}(B \rightarrow \tau \nu)}{\operatorname{BR}(B \rightarrow \tau \nu)_{\text{SM}}} \approx 1 - \frac{0.1}{\hat{m}_\phi^2} \operatorname{Re}(a_{33} c_{31}^*) = 1 - \frac{0.1}{\hat{m}_\phi^2} |a_{33} c_{31}| \cos(\operatorname{Arg}(a_{33}) - \operatorname{Arg}(c_{31})) . \quad (113)$$

All contributions which are quadratic in Wilson coefficients, induced by the LQ ϕ , can be neglected. Note that the currently viable parameter space of the model will only be probed by future searches for $B \rightarrow \tau \nu$ to an appreciable extent, despite its dependence on the LQ couplings y_{31} and z_{31} which involve quarks of the first generation.

6.6 Numerical results for secondary observables

In this section, we analyse the numerical results for the secondary observables from the comprehensive scan. We first comment on the leptonic observables, illustrated in figure 22, before moving onto the hadronic observables, shown in figure 23. A summary of the spread of the numerical results for the secondary observables is given in table 9.

Leptonic secondary observables. Regarding the EDM of the muon, we see that viable points are capable of generating a maximum of $|d_\mu| \sim \mathcal{O}(10^{-22}) e \text{ cm}$ and that points, associated with explaining the anomaly observed in the AMM of the muon at the 3σ level or better, predict the EDM of the muon to lie in the interval $[10^{-25}, 10^{-22}] e \text{ cm}$, see top-left plot in figure 22. While this signal could not be seen at the Muon $g-2$ experiment at Fermilab, some parameter space

SPREAD OF SECONDARY OBSERVABLES IN COMPREHENSIVE SCAN						
Observable	$\hat{m}_\phi = 2, P = 5955$		$\hat{m}_\phi = 4, P = 12570$		$\hat{m}_\phi = 6, P = 39807$	
	[min., max.]	Average	[min., max.]	Average	[min., max.]	Average
$ d_\mu \times 10^{25} [e \text{ cm}]$	[0.067, 2144]	153.4	[0.033, 1449]	128.1	[0.003, 1417]	86.51
$R_D^{\mu/e}$	[0.983, 1.015]	1.000	[0.994, 1.004]	1.000	[0.996, 1.002]	1.000
$R_{D^*}^{e/\mu}$	[0.989, 1.020]	1.003	[0.999, 1.009]	1.003	[1.001, 1.007]	1.003
$\text{BR}(B \rightarrow \tau\nu) \times 10^5$	[8.201, 9.505]	8.862	[8.278, 9.341]	8.853	[8.216, 9.396]	8.845
$(1 - g_{\mu_A}/g_A^{\text{SM}}) \times 10^4$	[0.008, 4.223]	0.292	[0.178, 1.383]	0.427	[0.069, 0.704]	0.214

Table 9: **Overview of spread of secondary observables in comprehensive scan.** We present a summary of the statistics reflecting the distribution of secondary observables: the minimum, maximum and average values generated for a sample of P points passing the primary constraints.

is expected to be probed at the muEDM experiment at the Paul Scherrer Institute (PSI) and similar experiments using the frozen-spin technique, as indicated by the black dashed lines in the top-left plot in figure 22. We remind that a bias for the difference of the arguments of the effective parameters $a_{23} \approx c_{23}$ and b_{23} is employed, see table 6, such that more sizeable contributions to the AMM of the muon, and thus a larger real part of the relevant Wilson coefficient, are generated. Therefore, we expect the comprehensive scan to prefer smaller values of the imaginary part of the product of the same effective parameters, see eq. (107). This, in turn, leads to a distribution of values of d_μ below the analytic estimate of $\mathcal{O}(10^{-22}) e \text{ cm}$. Still, enhanced contributions to both observables are seen to be compatible, and so this effect is limited. Furthermore, note that we do not observe any preference for the sign of the EDM of the muon. Given that the contributions to it turn out to be suppressed relative to present constraints, there is no need for an additional CP symmetry to restrict its size.

Turning to the effective coupling of Z to muons, we first repeat that according to the analytic estimate the dominant contribution to the ratio $g_{\mu_A}/g_A^{\text{SM}}$ is proportional to $|c_{23}|^2$ and negative such that the resulting value of $g_{\mu_A}/g_A^{\text{SM}}$ should always be smaller than one in this model, see eq. (108). This is consistent with the data, illustrated in the top-right plot in figure 22. Then, we remind that the comprehensive scan prefers larger values of the magnitude of $a_{23} \approx c_{23}$, since this increases the chances to satisfactorily address the flavour anomalies. Such larger values correspond to points with a smaller ratio $g_{\mu_A}/g_A^{\text{SM}}$, as observed in the distribution of white crosses in the top-right plot in figure 22. Present constraints are not competitive enough to be illustrated in this plot, although the present best-fit value may hint at contributions beyond the SM that generate a ratio $g_{\mu_A}/g_A^{\text{SM}}$ smaller than one. From the top-right plot in figure 22, we see that increased precision will allow to probe parts of the viable parameter space of this model. Note that we use the projected ILC bounds [117], but a further reduction of the error by a factor of ten is expected from the FCC [118]. For completeness, a plot showing the EDM of the muon and the ratio $g_{\mu_A}/g_A^{\text{SM}}$ can be found in the left plot in figure 27 in appendix E.2.

Lastly, we observe no correlation between $g_{\mu_A}/g_A^{\text{SM}}$ and $g_{\tau_A}/g_A^{\text{SM}}$. This is expected from the analytic estimates, see eqs. (94) and (108), since these ratios dominantly depend on distinct effective parameters. The regions of the two ratios in the comprehensive scan are displayed in the bottom plot in figure 22 for the three different LQ masses and result from the biasing imposed on the

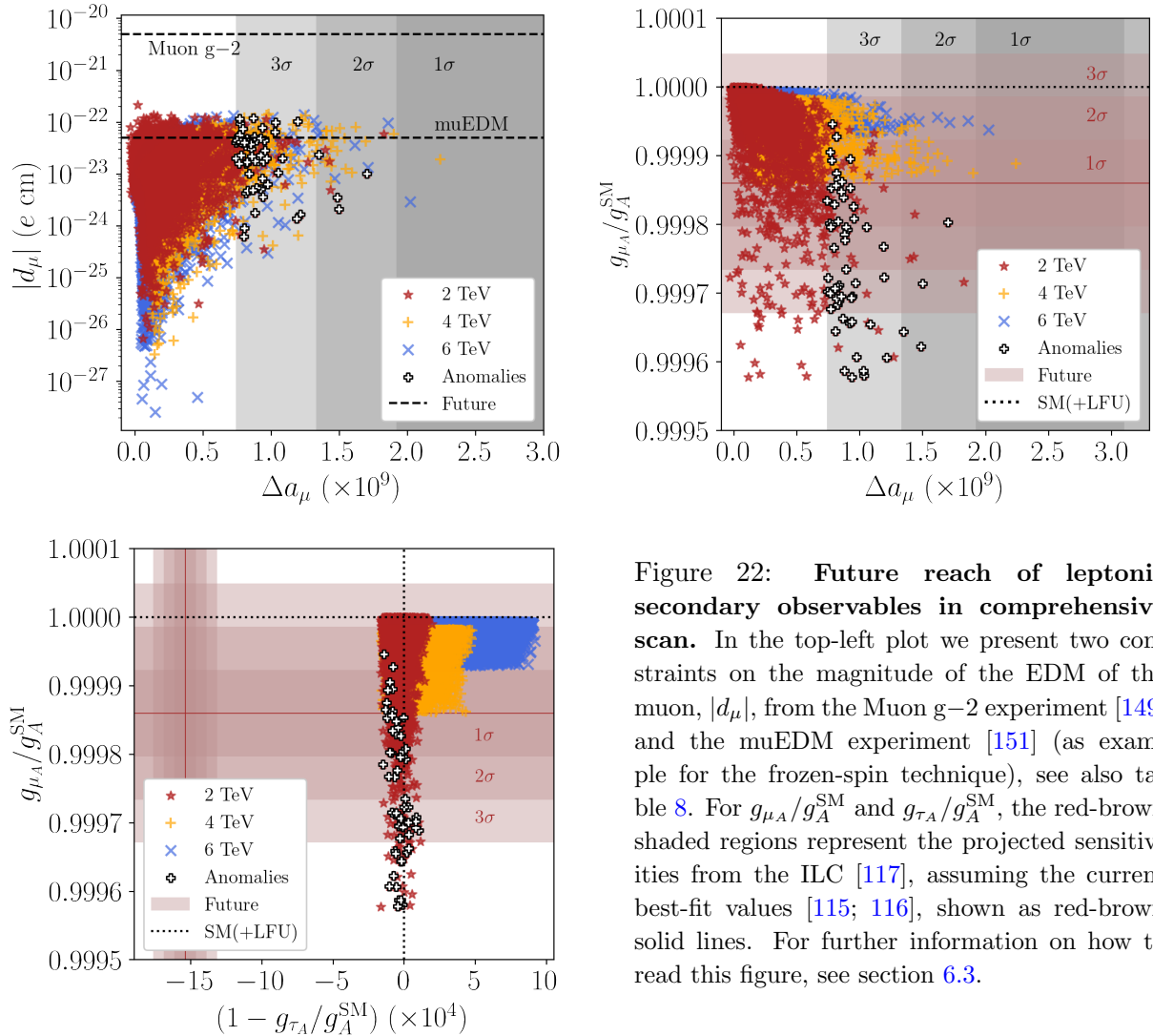


Figure 22: **Future reach of leptonic secondary observables in comprehensive scan.** In the top-left plot we present two constraints on the magnitude of the EDM of the muon, $|d_\mu|$, from the Muon $g-2$ experiment [149] and the muEDM experiment [151] (as example for the frozen-spin technique), see also table 8. For $g_{\mu A}/g_A^{\text{SM}}$ and $g_{\tau A}/g_A^{\text{SM}}$, the red-brown shaded regions represent the projected sensitivities from the ILC [117], assuming the current best-fit values [115; 116], shown as red-brown solid lines. For further information on how to read this figure, see section 6.3.

effective parameters $a_{23} \approx c_{23}$ and $a_{33} \approx c_{33}$, respectively, see table 6.

Hadronic secondary observables. The LFU ratios $R_D^{\mu/e}$ and $R_{D^*}^{e/\mu}$ are useful probes for $b \rightarrow ce_i\nu_j$ processes that do not involve the tau lepton. The results of the comprehensive scan reveal an anti-correlation in the deviations of these two ratios from the SM values. This is consistent with the analytic estimates in eqs. (111) and (112). We note that the effective parameters b_{22} and $c_{22} \approx a_{22}$ which enter the estimates for these observables can be $\mathcal{O}(10)$ in the comprehensive scan, see table 10 in appendix E.1, while a_{23} is biased towards larger values, see table 6. This enhancement explains the extent of the distribution of points in the left plot in figure 23. Presently, all predictions are consistent with the measurements, although the experimental sensitivity is expected to considerably improve at Belle II [155].

On the other hand, $\text{BR}(B \rightarrow \tau\nu)$ is interesting as observable, since it probes the process $bu \rightarrow \tau\nu$, which is sensitive to the LQ coupling between the bottom quark and tau neutrino common with $b \rightarrow c\tau\nu$, but is suppressed by the small coupling between the up quark and tau lepton in this model, $z_{31} = c_{31}\lambda^3$, see eq. (55). For this BR, we predict a value consistent within 2 to 3 σ of the projected sensitivity, assuming that the best-fit value of this measurement remains the current one. In the right plot in figure 23 we illustrate this observable plotted against $R(D)$. As one can see, we find no correlation between these two observables. A plot for $R(D^*)$ shows

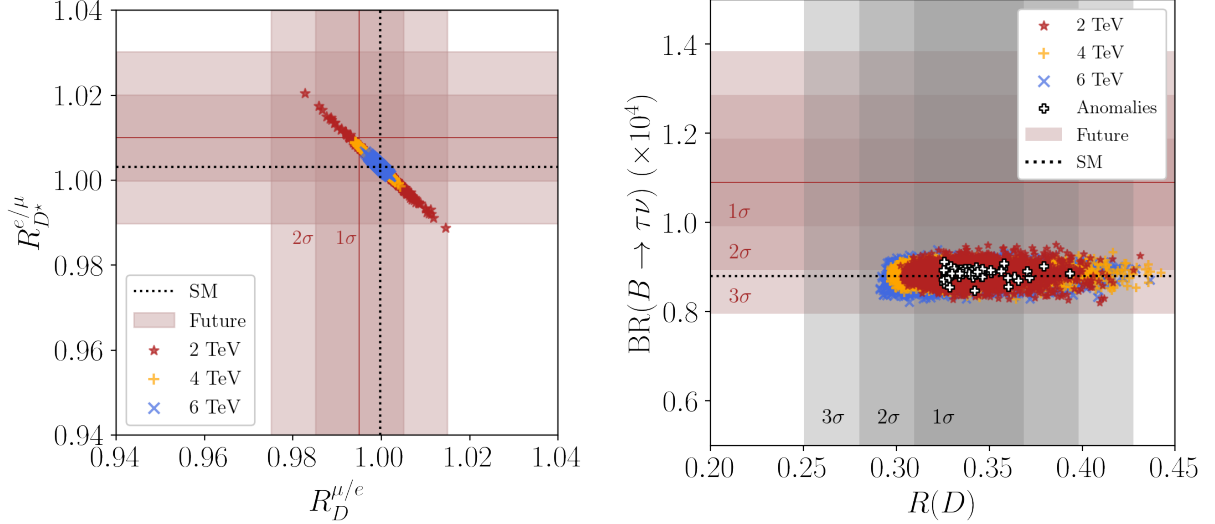


Figure 23: **Future reach of hadronic secondary observables in comprehensive scan.** In both plots, we present the projected sensitivities from Belle II for $R_D^{\mu/e}$, $R_{D^*}^{e/\mu}$ [155] and $\text{BR}(B \rightarrow \tau\nu)$, at 5 ab^{-1} , [102]. Note that we do not show the white crosses in the left plot, because they would uniformly lie across the entire allowed range. A complementary plot showing $\text{BR}(B \rightarrow \tau\nu)$ against $R(D^*)$ can be found in the right plot in figure 27 in appendix E.2. For further information on how to read this figure, see section 6.3.

a similar result, and can be found in the right plot in figure 27 in appendix E.2. We note that the scalar-operator contribution to this observable remains suppressed by the size of the coupling $y_{31} = b_{31} \lambda^5$, see eq. (58), consistent with the analytic estimate in section 6.5.4. For the effective parameter b_{31} , an enhancement only slightly above $1/\lambda$ is found in the comprehensive scan, see table 10 in appendix E.1, which is not sufficient to make this contribution competitive with the one from the vector operator. Furthermore, we note that, indeed, the effective parameter $c_{31} \approx a_{31}$ can take rather large values.

6.7 Comment on tertiary observables

In the following, we briefly comment on the results for the tertiary observables extracted from the comprehensive scan. We find that none of these observables, listed in table 11 in appendix E.3, provides a signal within the reach of current and planned experiments. Thus, any observation of new physics in these allows to falsify this model. We relegate detailed ranges for these observables for each LQ mass to table 12 in appendix E.3 and only make a few comments below. Note that in table 11 also the present experimental constraints and calculation method employed in the comprehensive scan are found, while table 12 also displays the prospective future reach for these observables.

For processes involving electrons, we first observe that the effective coupling of Z to electrons is suppressed by small LQ couplings of $\mathcal{O}(\lambda^9)$, see eqs. (55) and (58). Thus, we do not expect large LQ contributions to $Z \rightarrow ee$ in this model, as reflected in the data in table 12. We see that these contributions are up to eleven orders of magnitude below future sensitivities. Similarly, the contribution to the AMM of the electron generated in this model for each LQ mass is $\mathcal{O}(10^{-21})$. Present measurements of Δa_e hint at a preference for $|\Delta a_e| \sim 10^{-12}$ [158; 159], although these two measurements indicate deviations from the SM value with opposite sign and comparable magnitude. We, therefore, note that this model would be incapable of addressing this anomaly, but could be revisited in case the present discrepancy in the experimental results is resolved. Likewise, the results for the EDM of the electron show that a detection in future experiments [160]

should not be expected.

We predict the BRs for $B_s \rightarrow \tau\tau$, $D_s \rightarrow \tau\nu$ and $D_s \rightarrow \mu\nu$ to be only slightly beyond the projected sensitivity to these observables. Furthermore, the future sensitivities for tau decays to a muon and light mesons, i.e. $\text{BR}(\tau \rightarrow [\rho, \phi, \pi]\mu)$, are only one or two orders of magnitude above the maximum value generated for these observables in the comprehensive scan. These decays can, thus, be of interest when considering a next generation of experiments, beyond what is currently found in the literature.

7 Summary and outlook

We have considered an extension of the SM with two Higgs doublets H_u and H_d (in the decoupling limit) and one scalar LQ ϕ that transforms as $(3, 1, -\frac{1}{3})$ under the SM gauge group. The main purpose of the LQ ϕ is to explain the flavour anomalies in $R(D)$, $R(D^*)$ and in the AMM of the muon. The flavour structure of this model is constrained by the flavour group $G_f = D_{17} \times Z_{17}$. The three scalars H_u , H_d and ϕ are singlets under the dihedral group, whereas the three generations of all SM fermion species transform as doublet and singlet, apart from the three RH up-type quarks that are all singlets. In this way, the masses of the charged fermions of the third generation arise without breaking the dihedral group.

The flavour symmetry G_f is (mainly) broken by the VEVs of four different spurions, called S , T , U and W , that are assigned to doublets of the dihedral group. While the role of S is to (mainly) generate the LQ couplings $\hat{\mathbf{x}}$ and $\hat{\mathbf{y}}$, T and U are responsible for the mass of the second and first generation of both down-type quarks and charged leptons, respectively. The spurion W , eventually, is necessary in order to give mass to the charm quark and to generate the correct size of the Cabibbo angle. The smaller quark mixing angles as well as the up quark mass arise automatically due to the spurions S as well as T and U , respectively. According to their roles, the VEVs of these spurions are of different order of magnitude in the expansion parameter λ , $\lambda \approx 0.2$, i.e. $\langle S \rangle \sim \lambda$, $\langle T \rangle \sim \lambda^2$, $\langle U \rangle \sim \lambda^4$ and $\langle W \rangle \sim (\lambda^5, \lambda^4)^t$. In order to achieve suitable textures for the LQ couplings $\hat{\mathbf{x}}$ and $\hat{\mathbf{y}}$ and, at the same time, avoid too large effects related to quarks and/or leptons of the first generation, a residual symmetry Z_{17}^{diag} , being the diagonal subgroup of a Z_{17} group, contained in D_{17} , and the external Z_{17} symmetry, is preserved by both $\hat{\mathbf{x}}$ and $\hat{\mathbf{y}}$ at LO.

We have performed analytical and numerical studies of the phenomenology of this model. In doing so, all considered observables have been classified as primary, secondary or tertiary. The primary observables include the flavour anomalies in $R(D)$, $R(D^*)$ and in the AMM of the muon as well as observables for which the present experimental measurements can (significantly) constrain the viable parameter space of this model. Secondary observables instead do not currently provide competitive constraints, but mid-term future experiments offer an opportunity to probe them and thus this model. For primary as well as secondary observables analytical estimates are given. Lastly, tertiary observables are not expected to allow to probe the model in the mid-term future, but are discussed lest future measurements bring these into disagreement with the SM.

In the primary scan, we have focussed on the primary observables and varied the effective parameters of the LQ couplings in the charged fermion mass basis as (mostly) independent complex order-one numbers. In this way, we have identified the two radiative cLFV decays $\mu \rightarrow e\gamma$ and $\tau \rightarrow \mu\gamma$ as the most stringent constraints on the parameter space of the model. Furthermore, we have extracted biases on the effective parameters of the LQ couplings which have been used to guide the more thorough comprehensive scan. A simultaneous reconciliation of all three flavour anomalies has proven to be very challenging in the primary scan.

The comprehensive scan has involved primary, secondary and tertiary observables. In contrast

to the primary scan, it has been performed over effective parameters in the interaction basis. Thus, a subset of these has been fixed by a chi-squared fit to the charged fermion masses and quark mixing, achieving excellent agreement with the measured values (for scenario B). The remaining parameters, taken to be complex order-one numbers and parametrising the LQ couplings, have been biased using the input from the primary scan. In the comprehensive scan, we have found that this model is compatible with all constraints, while being capable of explaining the observed deviations in $R(D)$, $R(D^*)$ and Δa_μ from the SM predictions within the 3σ ranges of their present best-fit values for LQ masses of 2 and 4 TeV. Furthermore, an LQ with a mass of 2 TeV allows for compatibility with all considered constraints, while reconciling the three flavour anomalies at the 2σ level. The secondary observables studied in the comprehensive scan are the EDM of the muon, the effective coupling of Z to muons, the LFU ratios $R_D^{\mu/e}$ and $R_{D^*}^{e/\mu}$ as well as $\text{BR}(B \rightarrow \tau\nu)$.

The differences between the parameter space probed by the primary and the comprehensive scan have been discussed in detail. The use of the interaction basis is the main reason for the comprehensive scan being able to reconcile all three flavour anomalies. At the same time, this has shown a considerable preference for one of the effective parameters, namely b_{13} , being slightly smaller than expected from the construction of the model. This indicates that an improved version of this model should further suppress this particular LQ coupling by λ or λ^2 . Contributions beyond the ones from γ -penguins can play an important role in several decays such that e.g. not only the tau decay $\tau \rightarrow \mu\gamma$ can be accessible at Belle II, but, at the same time, $\tau \rightarrow 3\mu$ and $\tau \rightarrow \mu e \bar{e}$ can be measured. For the primary observables with neutrinos in the final state, i.e. $R(D)$, $R(D^*)$, $R_{K^*}^\nu$ and the lifetime of the B_c meson, LFV contributions are found to be relevant, generating effects up to 40 percent in some instances.

There are several interesting directions to expand the current study. On the phenomenological side, it is highly interesting to study the observables $R(J/\psi)$ and $R(\Lambda_c)$ that are (tightly) related to the analysed $b \rightarrow c$ transitions as well as the angular distributions of $B \rightarrow D^* e_i \nu$ [161] and the longitudinal polarisation of the tau lepton in $B \rightarrow D^* \tau \nu$ [129]. Some of these also reveal a (slight) disagreement between the current measured value and the SM expectation, e.g. $R(J/\psi)$ [162]. Other flavour anomalies, such as those observed in $b \rightarrow s$ transitions, e.g. in $R(K)$, $R(K^*)$ and in the process $B_s \rightarrow \mu\mu$, may also be relevant to address, see e.g. reference [163] for a recent concise overview. For this purpose, an additional LQ, for example transforming as $(3, 3, -\frac{1}{3})$ under the SM gauge group, has to be added to the model, see e.g. references [70; 74; 78; 164]. This may have the added effect of simultaneously generating neutrino masses. A neutrino mass mechanism could be incorporated in many different ways. It could be either one type of seesaw mechanism, e.g. by adding RH neutrinos to the existing model [165], or some radiative generation mechanism, see reference [166] for a review. In the current analysis, it has been assumed, for simplicity, that possible diquark couplings of the LQ ϕ are forbidden by a baryon number symmetry. However, it may also be interesting to study the efficacy of G_f to suppress these couplings beyond the strong existing bounds from searches for proton decay [93], see e.g. references [85; 167] for studies about also controlling them with the help of a flavour symmetry.

With non-vanishing neutrino masses, lepton mixing becomes physical and its appropriate description, i.e. two large mixing angles and one small one [168], may require a change in the assignment of the LH lepton doublets to representations of G_f or even the extension or change of G_f itself. The observed lepton mixing angles are often interpreted as sign of unification of the three generations of LH lepton doublets into an irreducible three-dimensional representation of the flavour symmetry, for reviews see references [6–9]. Prime candidates for such a flavour symmetry are the groups belonging to the series $\Delta(6n^2)$ with n integer and at least two [169]. As has been shown, they lead to an adequate description of lepton as well as quark mixing, see e.g. references [170–174], and also of the charged fermion mass hierarchies, if accompanied by an

appropriate external symmetry, see e.g. the supersymmetric model in reference [175]. Furthermore, it is interesting to consider adding a CP symmetry to G_f , given that this can also constrain the two Majorana phases in the lepton sector [176] (see also references [3; 177–183]) and might, at the same time, be beneficial for controlling the amount of CP violation in the LQ couplings.

Eventually, an extension of the SM gauge group similar to the Pati-Salam theory has proven to be useful, since in this way the vector LQ transforming as $(3, 1, \frac{2}{3})$ under the SM gauge group arises automatically, when breaking to the SM, see e.g. references [184–188]. This vector LQ is capable of addressing all aforementioned flavour anomalies, assuming an appropriate structure of its couplings to the SM fermions can be achieved. While in the case of a vector LQ the flavour structure is determined by the gauge group of the model, for scalar LQs, explaining (some of) the observed flavour anomalies, it is also worth considering a possible embedding of the model into a (partially) unified theory endowed with a flavour (and CP) symmetry.

Acknowledgements

M.S. and C.H. thank John Gargalionis for providing us with data from the scans found in reference [66]. I.B. and C.H. thank Mark Goodsell, Werner Porod and Avelino Vicente for help with SARAH and SPheno. T.F. and M.S. acknowledge helpful correspondence with Thorsten Feldmann. We also thank Peter Stangl for information on flavio. In addition to the software packages cited in the text, this research has made extensive use of matplotlib [189; 190]. C.H. has been partly supported by the European Union’s Horizon 2020 research and innovation programme under the Marie Skłodowska-Curie grant agreement No. 754496 (FELLINI programme) as well as is supported by Spanish MINECO through the Ramón y Cajal programme RYC2018-024529-I, by the national grant PID2020-113644GB-I00 and by the Generalitat Valenciana through PROMETEO/2021/083. C.H. has also received support from the European Union’s Horizon 2020 research and innovation programme under the Marie Skłodowska-Curie grant agreement No. 860881 (HIDDe ν network). I.B. is supported in part by the Australian Research Council and the Australian Government Research Training Program Scholarship initiative. T.F. and M.S. acknowledge support by the Australian Research Council. C.H. would like to thank the Instituto de Fisica Teorica (IFT UAM-CSIC) in Madrid for support via the Centro de Excelencia Severo Ochoa Program under Grant CEX2020-001007-S, during the Extended Workshop “Neutrino Theories”, where this work developed.

Note added on $R(D)$ and $R(D^*)$

After the completion of this work, the LHCb collaboration has published a combined analysis of $R(D)$ and $R(D^*)$ [191] using muonic tau reconstruction, resulting in $R(D) = 0.441 \pm 0.060 \pm 0.066$ and $R(D^*) = 0.281 \pm 0.018 \pm 0.024$, as well as an updated measurement [192] utilising hadronic τ^+ decays, $R(D^*) = 0.257 \pm 0.012 \pm 0.018$. These results are consistent with the SM predictions in table 1, for $R(D^*)$ within the 1σ and for $R(D)$ within the 2σ range, but with relatively large experimental uncertainties. Consequently, the HFLAV averages for $R(D)$ and $R(D^*)$ have been updated to include the new measurements [193], giving $R(D) = 0.356 \pm 0.029$ and $R(D^*) = 0.284 \pm 0.013$ (with a correlation of $\rho = -0.37$). Compared with the previous averages, quoted in table 1, this is closer to the SM prediction for $R(D^*)$, but further away from the SM value of $R(D)$. Nevertheless, both averages remain in agreement at the 1σ level with the previous ones. The discrepancy with the SM predictions now amounts to 3.2σ which is only slightly reduced from 3.4σ , see table 1. Thus, the results have not changed significantly and remain qualitatively the

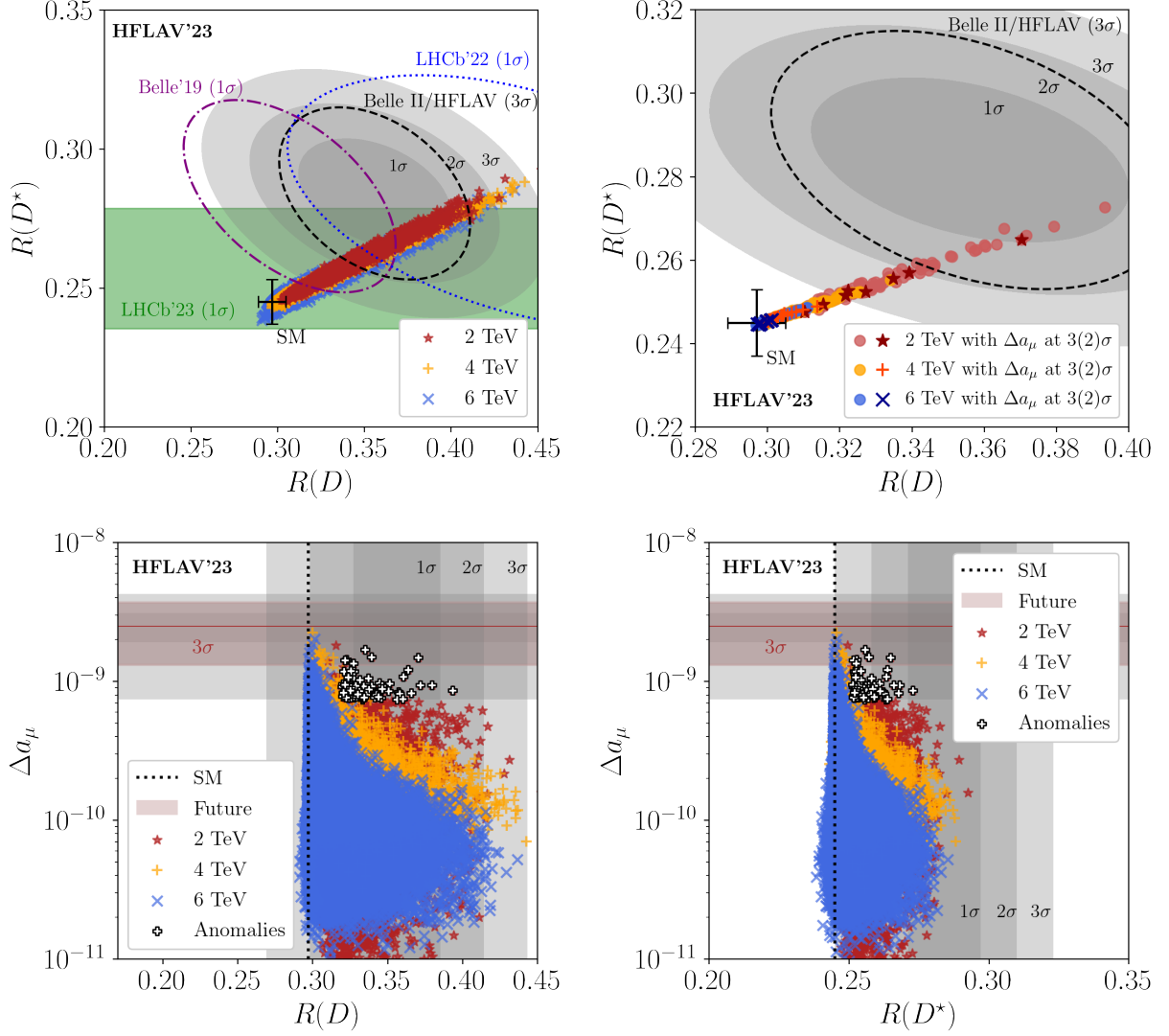


Figure 24: **Results of comprehensive scan for the flavour anomalies in $R(D)$, $R(D^*)$ and in the AMM of the muon using updated HFLAV averages for $R(D)$ and $R(D^*)$.** This figure is an updated version of figure 15, taking into account the new LHCb combined analysis of $R(D)$ and $R(D^*)$ [191] and the latest LHCb measurement of $R(D^*)$ using hadronic τ^+ decays [192], which have led to new HFLAV averages for these. In the top-left plot, the blue dotted ellipse represents the 1σ contour of the new LHCb combined analysis, while the green band now shows the 1σ region about the most recent LHCb result for $R(D^*)$. The black dashed ellipse indicates the prospective 3σ reach for 5 ab^{-1} of data at Belle II [102], assuming the best-fit value from 2023 and the correlation coefficient from the HFLAV collaboration [193]. In the top-right plot which shows points that not only pass all considered constraints but also satisfy Δa_μ within 3σ (light-coloured circles) or 2σ (dark-coloured other shapes) of the present best-fit value we have magnified the scale and, at the same time, removed the results by single experiments for better readability. For further information on how to read this figure, see section 6.3, in particular figure 15.

same.

In any case, it is interesting to confront the outcome of the comprehensive scan with these new averages. In order to do so, we employ the same data set as shown in section 6 and present figure 24 as updated version of figure 15. Once the primary constraints, see table 4, are enforced in the comprehensive scan, we find $75(5)[0]$ points for $\hat{m}_\phi = 2(4)[6]$ that can now generate $R(D)$, $R(D^*)$ and the AMM of the muon within the respective 3σ ranges. In fact, this is a slight quantitative improvement over the $58(1)[0]$ points identified and discussed in section 6.4.

A Group theory of D_{17}

In this appendix, we briefly summarise the main features of the non-abelian discrete group D_{17} [81]. It is a member of the series of dihedral groups D_n that are non-abelian for $n \geq 3$. It has 34 distinct elements and contains ten real irreducible representations: two singlets, the trivial singlet $\mathbf{1}_1$ as well as $\mathbf{1}_2$, and eight doublets, called $\mathbf{2}_i$ with $i = 1, \dots, 8$. All these eight doublets are faithful. The group D_{17} can be described, like the other dihedral groups, with the help of two generators a and b which fulfil the following relations

$$a^{17} = e, \quad b^2 = e, \quad a b a = b \quad (114)$$

with e denoting the neutral element of the group. The representation matrices $a(\mathbf{r})$ and $b(\mathbf{r})$ of the two generators a and b read in the different representations \mathbf{r}

$$a(\mathbf{1}_1) = b(\mathbf{1}_1) = 1 \quad \text{and} \quad a(\mathbf{1}_2) = 1, \quad b(\mathbf{1}_2) = -1 \quad (115)$$

as well as

$$a(\mathbf{2}_i) = \begin{pmatrix} \omega_{17}^i & 0 \\ 0 & \omega_{17}^{17-i} \end{pmatrix} \quad \text{and} \quad b(\mathbf{2}_i) = \begin{pmatrix} 0 & 1 \\ 1 & 0 \end{pmatrix}, \quad (116)$$

where ω_{17} is the 17th root of unity, $\omega_{17} = e^{\frac{2\pi i}{17}}$. In this model, we only make use of the doublets $\mathbf{2}_1, \mathbf{2}_2, \mathbf{2}_3$ and $\mathbf{2}_4$. The most relevant Kronecker products and Clebsch-Gordan coefficients are presented in the following. The latter have a particularly simple form in the chosen basis. Assume a and b are singlets, $\begin{pmatrix} c_1 \\ c_2 \end{pmatrix}, \begin{pmatrix} d_1 \\ d_2 \end{pmatrix}$ are doublets, then we have [81]

$$\mathbf{1}_1 \times \mathbf{1}_1 : a b \sim \mathbf{1}_1, \quad (117a)$$

$$\mathbf{1}_1 \times \mathbf{1}_2 : a b \sim \mathbf{1}_2, \quad (117b)$$

$$\mathbf{1}_2 \times \mathbf{1}_2 : a b \sim \mathbf{1}_1, \quad (117c)$$

$$\mathbf{1}_1 \times \mathbf{2}_i : \begin{pmatrix} a c_1 \\ a c_2 \end{pmatrix} \sim \mathbf{2}_i, \quad (117d)$$

$$\mathbf{1}_2 \times \mathbf{2}_i : \begin{pmatrix} a c_1 \\ -a c_2 \end{pmatrix} \sim \mathbf{2}_i, \quad (117e)$$

$$\mathbf{2}_1 \times \mathbf{2}_1 : c_1 d_2 + c_2 d_1 \sim \mathbf{1}_1, \quad c_1 d_2 - c_2 d_1 \sim \mathbf{1}_2, \quad \begin{pmatrix} c_1 d_1 \\ c_2 d_2 \end{pmatrix} \sim \mathbf{2}_2, \quad (117f)$$

$$\mathbf{2}_1 \times \mathbf{2}_2 : \begin{pmatrix} c_2 d_1 \\ c_1 d_2 \end{pmatrix} \sim \mathbf{2}_1, \quad \begin{pmatrix} c_1 d_1 \\ c_2 d_2 \end{pmatrix} \sim \mathbf{2}_3, \quad (117g)$$

$$\mathbf{2}_2 \times \mathbf{2}_2 : c_1 d_2 + c_2 d_1 \sim \mathbf{1}_1, \quad c_1 d_2 - c_2 d_1 \sim \mathbf{1}_2, \quad \begin{pmatrix} c_1 d_1 \\ c_2 d_2 \end{pmatrix} \sim \mathbf{2}_4, \quad (117h)$$

$$\mathbf{2}_1 \times \mathbf{2}_3 : \begin{pmatrix} c_2 d_1 \\ c_1 d_2 \end{pmatrix} \sim \mathbf{2}_2, \quad \begin{pmatrix} c_1 d_1 \\ c_2 d_2 \end{pmatrix} \sim \mathbf{2}_4, \quad (117i)$$

$$\mathbf{2}_2 \times \mathbf{2}_3 : \begin{pmatrix} c_2 d_1 \\ c_1 d_2 \end{pmatrix} \sim \mathbf{2}_1, \quad \begin{pmatrix} c_1 d_1 \\ c_2 d_2 \end{pmatrix} \sim \mathbf{2}_5, \quad (117j)$$

$$\mathbf{2}_3 \times \mathbf{2}_3 : c_1 d_2 + c_2 d_1 \sim \mathbf{1}_1, \quad c_1 d_2 - c_2 d_1 \sim \mathbf{1}_2, \quad \begin{pmatrix} c_1 d_1 \\ c_2 d_2 \end{pmatrix} \sim \mathbf{2}_6, \quad (117k)$$

$$\mathbf{2}_1 \times \mathbf{2}_4 : \begin{pmatrix} c_2 d_1 \\ c_1 d_2 \end{pmatrix} \sim \mathbf{2}_3, \quad \begin{pmatrix} c_1 d_1 \\ c_2 d_2 \end{pmatrix} \sim \mathbf{2}_5, \quad (117l)$$

$$\mathbf{2}_2 \times \mathbf{2}_4 : \begin{pmatrix} c_2 d_1 \\ c_1 d_2 \end{pmatrix} \sim \mathbf{2}_2, \quad \begin{pmatrix} c_1 d_1 \\ c_2 d_2 \end{pmatrix} \sim \mathbf{2}_6, \quad (117m)$$

$$\mathbf{2}_3 \times \mathbf{2}_4 : \begin{pmatrix} c_2 d_1 \\ c_1 d_2 \end{pmatrix} \sim \mathbf{2}_1, \quad \begin{pmatrix} c_1 d_1 \\ c_2 d_2 \end{pmatrix} \sim \mathbf{2}_7, \quad (117n)$$

$$\mathbf{2}_4 \times \mathbf{2}_4 : c_1 d_2 + c_2 d_1 \sim \mathbf{1}_1, \quad c_1 d_2 - c_2 d_1 \sim \mathbf{1}_2, \quad \begin{pmatrix} c_1 d_1 \\ c_2 d_2 \end{pmatrix} \sim \mathbf{2}_8. \quad (117o)$$

We note, furthermore, that the Clebsch-Gordan coefficients for combinations, involving conjugated fields, look slightly different, since the generator a is chosen as complex matrix in the two-dimensional representations $\mathbf{2}_i$, although all these representations are real. For a being a singlet and $\begin{pmatrix} c_1 \\ c_2 \end{pmatrix}, \begin{pmatrix} d_1 \\ d_2 \end{pmatrix}$ being doublets, the combinations involving $c_{1,2}^*$ read e.g.

$$\mathbf{2}_i \times \mathbf{1}_1 : \begin{pmatrix} c_2^* a \\ c_1^* a \end{pmatrix} \sim \mathbf{2}_i, \quad (118a)$$

$$\mathbf{2}_i \times \mathbf{1}_2 : \begin{pmatrix} c_2^* a \\ -c_1^* a \end{pmatrix} \sim \mathbf{2}_i, \quad (118b)$$

$$\mathbf{2}_1 \times \mathbf{2}_1 : c_1^* d_1 + c_2^* d_2 \sim \mathbf{1}_1, \quad c_1^* d_1 - c_2^* d_2 \sim \mathbf{1}_2, \quad \begin{pmatrix} c_2^* d_1 \\ c_1^* d_2 \end{pmatrix} \sim \mathbf{2}_2, \quad (118c)$$

$$\mathbf{2}_1 \times \mathbf{2}_2 : \begin{pmatrix} c_1^* d_1 \\ c_2^* d_2 \end{pmatrix} \sim \mathbf{2}_1, \quad \begin{pmatrix} c_2^* d_1 \\ c_1^* d_2 \end{pmatrix} \sim \mathbf{2}_3. \quad (118d)$$

The general form of the Kronecker products and Clebsch-Gordan coefficients can be found in [81].

B Relations between Lagrangian and effective parameters

Here, we collect the relations between the Lagrangian parameters and the effective ones, appearing in the charged fermion mass matrices and LQ couplings assuming real parameters.

The effective parameters f_{ij} , appearing in the up-type quark mass matrix in eq. (23), are related as follows to the Lagrangian parameters α_i^u

$$\begin{aligned} f_{11} &= \alpha_4^u, & (119) \\ f_{12} &= \alpha_2^u + \alpha_5^u \lambda^2 + (\alpha_5^u)' \lambda^2 + \alpha_{13}^u \lambda^5 + \alpha_{18}^u \lambda^3 + \alpha_{19}^u \lambda^6 + \alpha_{20}^u \lambda^5 + \alpha_{27}^u \lambda^7 + \alpha_{29}^u \lambda^5, \\ f_{13} &= \alpha_{14}^u \lambda^2 + \alpha_{15}^u + \alpha_{16}^u \lambda + \alpha_{17}^u \lambda^2 + \alpha_{21}^u \lambda^3 + \alpha_{28}^u \lambda^4, \\ f_{21} &= \alpha_{10}^u, \\ f_{22} &= \alpha_2^u + \alpha_5^u \lambda^2 - (\alpha_5^u)' \lambda^2 + \alpha_6^u \lambda^2 + \alpha_9^u \lambda^8 + \alpha_{12}^u \lambda^7 + (\alpha_{18}^u)' \lambda^5 + (\alpha_{20}^u)' \lambda^7, \\ f_{23} &= \alpha_3^u + (\alpha_{14}^u)' \lambda^9 + (\alpha_{16}^u)' \lambda^6 + \alpha_{30}^u \lambda^{10}, \\ f_{31} &= \alpha_{22}^u + \alpha_{23}^u, \\ f_{32} &= \alpha_7^u + \alpha_8^u \lambda^5 + \alpha_{11}^u \lambda^2 + \alpha_{26}^u \lambda^7, \\ f_{33} &= \alpha_1^u + \alpha_{24}^u \lambda^{10} + \alpha_{25}^u \lambda^{10}. \end{aligned}$$

For the effective parameters d_{ij} , used in the down-type quark mass matrix in eq. (33), we have as relations to the Lagrangian parameters α_i^d

$$d_{11} = \alpha_3^d + \alpha_9^d \lambda^7 + \alpha_{13}^d \lambda^8, \quad (120)$$

$$\begin{aligned}
d_{12} &= \alpha_7^d + (\alpha_9^d)' \lambda^3 + (\alpha_{13}^d)' \lambda^2 + \alpha_{16}^d \lambda + \alpha_{24}^d \lambda^4 + \alpha_{25}^d \lambda^3, \\
d_{13} &= \alpha_8^d \lambda^2 + \alpha_{10}^d + \alpha_{11}^d \lambda + \alpha_{12}^d \lambda^2 + \alpha_{14}^d \lambda^3 + \alpha_{22}^d \lambda^4, \\
d_{21} &= \alpha_6^d, \\
d_{22} &= \alpha_2^d + (\alpha_{13}^d)'' \lambda^9 + (\alpha_{16}^d)' \lambda^6 + \alpha_{21}^d \lambda^{10}, \\
d_{23} &= \alpha_4^d + (\alpha_8^d)' \lambda^9 + (\alpha_{11}^d)' \lambda^6 + \alpha_{23}^d \lambda^{10}, \\
d_{31} &= \alpha_{15}^d, \\
d_{32} &= \alpha_5^d + \alpha_{17}^d \lambda^6 + \alpha_{20}^d \lambda^6, \\
d_{33} &= \alpha_1^d + \alpha_{18}^d \lambda^{10} + \alpha_{19}^d \lambda^{10}.
\end{aligned}$$

Likewise, we find for e_{ij} , the effective parameters contained in the charged lepton mass matrix M_e , see eq. (44), that they are expressed in terms of α_i^e , appearing in the Lagrangians in eqs. (42,43), as follows

$$\begin{aligned}
e_{11} &= \alpha_3^e + \alpha_6^e \lambda^7 + \alpha_9^e \lambda^8, \\
e_{12} &= \alpha_{12}^e, \\
e_{21} &= \alpha_{11}^e + \alpha_{17}^e \lambda^2 + \alpha_{22}^e \lambda^3 + \alpha_{23}^e \lambda^4, \\
e_{22} &= \alpha_2^e + (\alpha_9^e)' \lambda^9 + \alpha_{13}^e \lambda^6 + \alpha_{27}^e \lambda^{10}, \\
e_{23} &= \alpha_4^e + \alpha_{10}^e \lambda^{11} + \alpha_{14}^e \lambda^8 + \alpha_{26}^e \lambda^{10}, \\
e_{31} &= \alpha_7^e + \alpha_8^e \lambda^3 + \alpha_{15}^e \lambda + \alpha_{16}^e \lambda^2 + \alpha_{19}^e, \\
e_{32} &= \alpha_5^e + \alpha_{18}^e \lambda^9 + \alpha_{20}^e \lambda^6 + \alpha_{25}^e \lambda^8, \\
e_{33} &= \alpha_1^e + \alpha_{21}^e \lambda^{10} + \alpha_{24}^e \lambda^{10}.
\end{aligned} \tag{121}$$

We continue with the relations between the effective parameters \hat{a}_{ij} , appearing in the LQ coupling $\hat{\mathbf{x}}$, see eq. (50), and the coefficients β_i^L

$$\begin{aligned}
\hat{a}_{11} &= \beta_9^L \lambda + \beta_{10}^L \lambda^2 + \beta_{18}^L \lambda^2 + \beta_{20}^L, \\
\hat{a}_{12} &= (\beta_{10}^L)', \\
\hat{a}_{21} &= \beta_6^L + \beta_7^L \lambda + \beta_{11}^L \lambda^3 + \beta_{16}^L \lambda + \beta_{19}^L \lambda^4 + \beta_{21}^L \lambda^3, \\
\hat{a}_{22} &= \beta_4^L + (\beta_6^L)' \lambda^4 + (\beta_{11}^L)' \lambda^9 + (\beta_{21}^L)' \lambda^9, \\
\hat{a}_{23} &= \beta_2^L + \beta_{12}^L \lambda^{11} + \beta_{17}^L \lambda^8 + \beta_{25}^L \lambda^{10}, \\
\hat{a}_{31} &= \beta_5^L \lambda^2 + \beta_8^L + \beta_{13}^L \lambda + \beta_{14}^L \lambda^2 + \beta_{15}^L \lambda^3 + \beta_{24}^L \lambda^4, \\
\hat{a}_{32} &= \beta_3^L + (\beta_5^L)' \lambda^9 + (\beta_{13}^L)' \lambda^6 + \beta_{26}^L \lambda^{10}, \\
\hat{a}_{33} &= \beta_1^L + \beta_{22}^L \lambda^{10} + \beta_{23}^L \lambda^{10}.
\end{aligned} \tag{122}$$

For the LQ coupling $\hat{\mathbf{y}}$, found in eq. (53), we define the effective parameters \hat{b}_{ij} in terms of the coefficients β_i^R as

$$\begin{aligned}
\hat{b}_{11} &= \beta_7^R + \beta_{15}^R, \\
\hat{b}_{12} &= \beta_{13}^R + \beta_{14}^R \lambda^3 + \beta_{17}^R \lambda + \beta_{18}^R \lambda^2 + \beta_{21}^R, \\
\hat{b}_{13} &= \beta_{10}^R \lambda + \beta_{11}^R \lambda^2 + \beta_{19}^R \lambda^2 + \beta_{23}^R, \\
\hat{b}_{21} &= \beta_6^R, \\
\hat{b}_{22} &= \beta_3^R + \beta_{20}^R \lambda^9 + \beta_{24}^R \lambda^6 + \beta_{29}^R \lambda^8, \\
\hat{b}_{23} &= \beta_2^R + \beta_9^R \lambda^4 + \beta_{12}^R \lambda^9 + \beta_{26}^R \lambda^9, \\
\hat{b}_{31} &= \beta_{16}^R + \beta_{22}^R,
\end{aligned} \tag{123}$$

$$\begin{aligned}\hat{b}_{32} &= \beta_1^R + \beta_{27}^R \lambda^{10} + \beta_{28}^R \lambda^{10}, \\ \hat{b}_{33} &= \beta_4^R + \beta_5^R \lambda^5 + \beta_8^R \lambda^2 + \beta_{25}^R \lambda^7.\end{aligned}$$

The effective parameters a_{ij} in the LQ coupling \mathbf{x} , given in eq. (54), read in terms of the effective parameters \hat{a}_{ij} , d_{ij} and e_{ij} , as follows

$$\begin{aligned}a_{11} &= \hat{a}_{11} + \mathcal{O}(\lambda^3), \\ a_{12} &= -\frac{\hat{a}_{22}e_{11}e_{21}}{e_{22}^2} + \frac{\hat{a}_{23}d_{23}e_{11}e_{21}}{d_{33}e_{22}^2} + \frac{\hat{a}_{32}e_{11}e_{21}e_{23}}{e_{22}^2e_{33}} - \frac{\hat{a}_{33}d_{23}e_{11}e_{21}e_{23}}{d_{33}e_{22}^2e_{33}} + \mathcal{O}(\lambda), \\ a_{13} &= -\frac{\hat{a}_{23}e_{11}e_{21}}{e_{22}^2} + \frac{\hat{a}_{33}e_{11}e_{21}e_{23}}{e_{22}^2e_{33}} + \mathcal{O}(\lambda^2), \\ a_{21} &= \hat{a}_{21} + \mathcal{O}(\lambda), \\ a_{22} &= \hat{a}_{22} - \frac{d_{23}}{d_{33}} \left(\hat{a}_{23} - \frac{\hat{a}_{33}e_{23}}{e_{33}} \right) - \frac{\hat{a}_{32}e_{23}}{e_{33}} + \mathcal{O}(\lambda^2), \\ a_{23} &= \hat{a}_{23} - \frac{\hat{a}_{33}e_{23}}{e_{33}} + \mathcal{O}(\lambda^2), \\ a_{31} &= \hat{a}_{31} - \frac{\hat{a}_{32}d_{12}}{d_{22}} - \frac{\hat{a}_{33}d_{13}}{d_{33}} + \frac{\hat{a}_{33}d_{12}d_{23}}{d_{22}d_{33}} + \mathcal{O}(\lambda), \\ a_{32} &= \hat{a}_{32} - \frac{\hat{a}_{33}d_{23}}{d_{33}} + \mathcal{O}(\lambda^2), \\ a_{33} &= \hat{a}_{33} + \mathcal{O}(\lambda^2).\end{aligned}\tag{124}$$

Similarly, we can express the effective parameters c_{ij} in the LQ coupling \mathbf{z} in eq. (55) in terms of \hat{a}_{ij} , e_{ij} and f_{ij} and find for scenario A

$$\begin{aligned}c_{11} &= \hat{a}_{11} + \mathcal{O}(\lambda^2), \\ c_{12} &= \frac{\hat{a}_{11}f_{12}}{f_{22}} + \mathcal{O}(\lambda), \\ c_{13} &= -\frac{\hat{a}_{23}e_{11}e_{21}}{e_{22}^2} + \frac{\hat{a}_{33}e_{11}e_{21}e_{23}}{e_{22}^2e_{33}} + \mathcal{O}(\lambda^2), \\ c_{21} &= -\frac{f_{12}}{e_{33}f_{22}f_{33}} (\hat{a}_{33}e_{23}f_{23} - \hat{a}_{23}e_{33}f_{23} - \hat{a}_{32}e_{23}f_{33} + \hat{a}_{22}e_{33}f_{33}) + \mathcal{O}(\lambda^2), \\ c_{22} &= \hat{a}_{22} - \frac{\hat{a}_{32}e_{23}}{e_{33}} - \left(\hat{a}_{23} - \frac{\hat{a}_{33}e_{23}}{e_{33}} \right) \frac{f_{23}}{f_{33}} + \mathcal{O}(\lambda^2), \\ c_{23} &= \hat{a}_{23} - \frac{\hat{a}_{33}e_{23}}{e_{33}} + \mathcal{O}(\lambda^2), \\ c_{31} &= \frac{f_{12}(\hat{a}_{33}f_{23} - \hat{a}_{32}f_{33})}{f_{22}f_{33}} + \mathcal{O}(\lambda^2), \\ c_{32} &= \hat{a}_{32} - \frac{\hat{a}_{33}f_{23}}{f_{33}} + \mathcal{O}(\lambda^2), \\ c_{33} &= \hat{a}_{33} + \mathcal{O}(\lambda^2).\end{aligned}\tag{125}$$

The effective parameters b_{ij} in the LQ coupling \mathbf{y} , found in eq. (58), read for scenario A in terms of \hat{b}_{ij} , e_{ij} and f_{ij}

$$\begin{aligned}b_{11} &= \hat{b}_{11} + \mathcal{O}(\lambda^3), \\ b_{12} &= \hat{b}_{12} - \frac{\hat{b}_{22}e_{21}}{e_{22}} - \frac{\hat{b}_{32}e_{31}}{e_{33}} + \frac{\hat{b}_{32}e_{21}e_{32}}{e_{22}e_{33}} + \mathcal{O}(\lambda^2), \\ b_{13} &= \hat{b}_{13} - \frac{\hat{b}_{23}e_{21}}{e_{22}} + \mathcal{O}(\lambda^2),\end{aligned}\tag{126}$$

$$\begin{aligned}
b_{21} &= -\frac{\hat{b}_{22}f_{11}f_{12}}{f_{22}^2} + \frac{\hat{b}_{32}e_{22}e_{23}f_{11}f_{12}}{e_{33}^2f_{22}^2} + \frac{\hat{b}_{32}e_{32}f_{11}f_{12}}{e_{33}f_{22}^2} + \mathcal{O}(\lambda), \\
b_{22} &= \hat{b}_{22} - \frac{\hat{b}_{32}(e_{22}e_{23} + e_{32}e_{33})}{e_{33}^2} + \mathcal{O}(\lambda^2), \\
b_{23} &= \hat{b}_{23} + \mathcal{O}(\lambda^4), \\
b_{31} &= -\frac{\hat{b}_{32}f_{11}f_{12}}{f_{22}^2} + \mathcal{O}(\lambda), \\
b_{32} &= \hat{b}_{32} + \mathcal{O}(\lambda^6), \\
b_{33} &= \hat{b}_{33} + \frac{\hat{b}_{32}f_{32}}{f_{33}} + \mathcal{O}(\lambda^2).
\end{aligned}$$

C Formulae for phenomenology

We use the Warsaw basis [194] for SM Effective Field Theory (SMEFT) and the JMS basis [101] below the electroweak scale for low-energy EFT.

C.1 Correction to charged lepton masses

The LQ contributes via its couplings to the charged lepton self-energies. This results in a correction to the charged lepton masses which is approximately given by [116]

$$m_{e_i} = m_{e_i}^{\text{tree}} \left(1 + \frac{1}{2}\Sigma_{ii}^{LL} + \frac{1}{2}\Sigma_{ii}^{RR} \right) + \Sigma_{ii}^{LR} \quad (127)$$

in terms of the self-energies Σ_{ij}^{XY} , where $X, Y \in \{L, R\}$ label the chiralities of the charged leptons and i, j the lepton flavour. It can be compactly rewritten as

$$m_{e_i} = \left| m_{e_i}^{\text{tree}} - \frac{3}{16\pi^2} \sum_{j=1}^3 \left(m_{u_j} y_{ij} z_{ij}^* \mathcal{J}_0(1, t_{u_j}) + \frac{1}{4} m_{e_i}^{\text{tree}} (|z_{ij}|^2 + |y_{ij}|^2) \mathcal{J}_1(1, t_{u_j}) \right) \right|, \quad (128)$$

where t_X is defined in eq. (71). After removing the UV divergences using minimal subtraction, the loop functions take the simple form

$$\mathcal{J}_0(x, y) = 1 + \ln x + y \ln y, \quad \mathcal{J}_1(x, y) = \frac{1}{2} + \ln x - y. \quad (129)$$

The last terms of the loop functions \mathcal{J}_0 and \mathcal{J}_1 are only numerically relevant for the top quark and can be neglected otherwise.

C.2 Leptonic processes

C.2.1 Effective interactions at one-loop order

The relevant effective Lagrangian using the JMS basis [101] reads

$$\begin{aligned}
\mathcal{L} \supset & C_{ee,ijkl}^{VLL} (\bar{e}_i \gamma^\mu P_L e_j) (\bar{e}_k \gamma_\mu P_L e_l) + C_{ee,ijkl}^{VRR} (\bar{e}_i \gamma^\mu P_R e_j) (\bar{e}_k \gamma_\mu P_R e_l) + C_{ee,ijkl}^{VLR} (\bar{e}_i \gamma^\mu P_L e_j) (\bar{e}_k \gamma_\mu P_R e_l) \\
& + [C_{ee,ijkl}^{SRR} (\bar{e}_i P_R e_j) (\bar{e}_k P_R e_l) + \text{h.c.}] + [C_{e\gamma}^{ij} (\bar{e}_i \sigma^{\mu\nu} P_R e_j) F_{\mu\nu} + \text{h.c.}].
\end{aligned} \quad (130)$$

Note that some of the Wilson coefficients contain redundant indices. We define the covariant derivative in QED as $D_\mu = \partial_\mu + iQeA_\mu$ following the convention in [101]. We use `FeynRules` [195], `FeynArts` [196], `FormCalc` [197; 198], `Package-X` [199], and `ANT` [200] to evaluate the amplitudes

and match the result to the operator basis. The Wilson coefficient of the dipole operator is given by

$$C_{e\gamma}^{ij} = -\frac{e}{32\pi^2 m_\phi^2} \sum_m \left((m_{e_i} y_{im}^* y_{jm} + m_{e_j} z_{im}^* z_{jm}) [f_S(t_{u_m}) - 3f_F(t_{u_m})] \right. \\ \left. - m_{u_m} z_{im}^* y_{jm} [g_S(t_{u_m}) - 3g_F(t_{u_m})] \right) \quad (131)$$

$$\approx \frac{e}{128\pi^2 m_\phi^2} \sum_m (m_{e_i} y_{im}^* y_{jm} + m_{e_j} z_{im}^* z_{jm} + 2m_{u_m} z_{im}^* y_{jm} (7 + 4 \ln t_{u_m})) ,$$

where $e = |e|$ is the unit electric charge. The relevant loop functions are given by

$$f_S(x) = \frac{x+1}{4(x-1)^2} - \frac{x \ln x}{2(x-1)^3}, \quad f_F(x) = \frac{x^2 - 5x - 2}{12(x-1)^3} + \frac{x \ln x}{2(x-1)^4}, \quad (132)$$

$$g_S(x) = \frac{1}{x-1} - \frac{\ln x}{(x-1)^2}, \quad g_F(x) = \frac{x-3}{2(x-1)^2} + \frac{\ln x}{(x-1)^3}.$$

The contributions to the four-lepton interactions can be split in different parts. The Higgs-penguin contributions are suppressed by the small charged lepton masses and thus negligible. The Z -penguin contributions are given by

$$C_{ee,ijkl}^{VLL,Z} = \frac{3\sqrt{2}G_F(1-2s_W^2)}{64\pi^2} \sum_m t_{u_m} (1 + \ln t_{u_m}) (\delta_{il} z_{km}^* z_{jm} + \delta_{ij} z_{km}^* z_{lm} + \delta_{kl} z_{im}^* z_{jm} + \delta_{jk} z_{im}^* z_{lm}) , \quad (133)$$

$$C_{ee,ijkl}^{VRR,Z} = \frac{3\sqrt{2}G_F s_W^2}{32\pi^2} \sum_m t_{u_m} (1 + \ln t_{u_m}) (\delta_{il} y_{km}^* y_{jm} + \delta_{ij} y_{km}^* y_{lm} + \delta_{kl} y_{im}^* y_{jm} + \delta_{jk} y_{im}^* y_{lm}) , \quad (134)$$

$$C_{ee,ijkl}^{VLR,Z} = -\frac{3\sqrt{2}G_F}{16\pi^2} \sum_m t_{u_m} (1 + \ln t_{u_m}) ((1-2s_W^2) \delta_{ij} y_{km}^* y_{lm} + 2s_W^2 \delta_{kl} z_{im}^* z_{jm}) , \quad (135)$$

where G_F denotes the Fermi constant and $s_W = \sin \theta_W$ the sine of the weak mixing angle, θ_W .

The short-distance γ -penguin contributions are given by

$$C_{ee,ijkl}^{VLL,\gamma} = \frac{\alpha_{em}}{96\pi m_\phi^2} \sum_m (5 + 4 \ln t_{u_m}) (\delta_{il} z_{km}^* z_{jm} + \delta_{kl} z_{im}^* z_{jm} + \delta_{ij} z_{km}^* z_{lm} + \delta_{jk} z_{im}^* z_{lm}) , \quad (136)$$

$$C_{ee,ijkl}^{VRR,\gamma} = \frac{\alpha_{em}}{96\pi m_\phi^2} \sum_m (5 + 4 \ln t_{u_m}) (\delta_{il} y_{km}^* y_{jm} + \delta_{kl} y_{im}^* y_{jm} + \delta_{ij} y_{km}^* y_{lm} + \delta_{jk} y_{im}^* y_{lm}) , \quad (137)$$

$$C_{ee,ijkl}^{VLR,\gamma} = \frac{\alpha_{em}}{24\pi m_\phi^2} \sum_m (5 + 4 \ln t_{u_m}) (\delta_{ij} y_{km}^* y_{lm} + \delta_{kl} z_{im}^* z_{jm}) , \quad (138)$$

where α_{em} denotes the fine structure constant. Finally, the box diagrams also contribute to the four-lepton operators

$$C_{ee,ijkl}^{VLL,\text{box}} = \frac{3}{256\pi^2 m_\phi^2} \sum_{m,n} z_{jm} z_{ln} (z_{in}^* z_{km}^* + z_{im}^* z_{kn}^*) , \quad (139)$$

$$C_{ee,ijkl}^{VRR,\text{box}} = \frac{3}{256\pi^2 m_\phi^2} \sum_{m,n} y_{jm} y_{ln} (y_{in}^* y_{km}^* + y_{im}^* y_{kn}^*) , \quad (140)$$

$$C_{ee,ijkl}^{VLR,\text{box}} = \frac{3}{64\pi^2 m_\phi^2} \sum_{m,n} y_{ln} z_{jm} y_{kn}^* z_{im}^* . \quad (141)$$

C.2.2 Radiative charged lepton flavour violating decays $e_i \rightarrow e_j \gamma$

The BR for $e_i \rightarrow e_j \gamma$ can be expressed in terms of the dipole Wilson coefficients

$$\text{BR}(e_i \rightarrow e_j \gamma) = \frac{m_{e_i}^3}{4\pi\Gamma_{e_i}} (|C_{e\gamma}^{ji}|^2 + |C_{e\gamma}^{ij}|^2), \quad (142)$$

where Γ_{e_i} denotes the full decay width of the charged lepton e_i .

C.2.3 Dipole moments

The electromagnetic current of a particle of mass m coupling to a real on-shell photon can be parametrised in terms of three form factors F_i , see e.g. [201; 202],

$$\langle p_1 | j^\mu(0) | p_2 \rangle = \bar{u}(\mathbf{p}_1) \left[F_1(q^2) \gamma^\mu + F_2(q^2) \frac{i\sigma^{\mu\nu}}{2m} q_\nu + F_3(q^2) \frac{\sigma^{\mu\nu}}{2m} \gamma_5 q_\nu \right] u(\mathbf{p}_2), \quad (143)$$

where $q^\mu = p_1^\mu - p_2^\mu$. At zero squared momentum transfer, $q^2 = 0$, the form factors can be identified with the electric charge $eF_1(0)$, the AMM $a = F_2(0)$, and the EDM $d = -eF_3(0)/2m$. Taking into account the definition of the covariant derivative, we find for the contributions of the dipole operator to the AMM and the EDM of the charged lepton e_i with $F_1(0) = -1$

$$a_{e_i} = \frac{4m_{e_i}}{e} \text{Re}(C_{e\gamma}^{ii}), \quad d_{e_i} = 2 \text{Im}(C_{e\gamma}^{ii}), \quad (144)$$

respectively.

C.2.4 Trilepton decays $e_i \rightarrow e_j e_k \bar{e}_m$

We have recalculated trilepton decays due to discrepancies in the literature [200; 203] and make use of the recent calculation in terms of EFT [204] and earlier references [125; 205]. Note there are no redundant indices in reference [204], and thus there are additional symmetry factors. The BR for $e_i \rightarrow e_j e_j \bar{e}_j$ is

$$\begin{aligned} \text{BR}(e_i \rightarrow e_j e_j \bar{e}_j) = \frac{m_{e_i}^5}{3(16\pi)^3 \Gamma_{e_i}} & \left[16|C^{VLL}|^2 + 16|C^{VRR}|^2 + 8|C^{VLR}|^2 + 8|C^{VRL}|^2 \right. \\ & + \frac{256e^2}{m_{e_i}^2} \left(\ln \frac{m_{e_i}^2}{m_{e_j}^2} - \frac{11}{4} \right) (|C_{e\gamma}^{ji}|^2 + |C_{e\gamma}^{ij}|^2) \\ & \left. - \frac{64e}{m_{e_i}} \text{Re} [(2C^{VLL} + C^{VLR})C_{e\gamma}^{ji*} + (2C^{VRR} + C^{VRL})C_{e\gamma}^{ij}] \right], \quad (145) \end{aligned}$$

where the coefficients in the decay rate are given in terms of the Wilson coefficients

$$C^{VLL} = 2C_{ee,jijj}^{VLL}, \quad C^{VRR} = 2C_{ee,jijj}^{VRR}, \quad C^{VLR} = C_{ee,jijj}^{VLR}, \quad C^{VRL} = C_{ee,jjji}^{VRL}. \quad (146)$$

The BR for $e_i \rightarrow e_j e_k \bar{e}_k$ is

$$\begin{aligned} \text{BR}(e_i \rightarrow e_j e_k \bar{e}_k) = \frac{m_{e_i}^5}{3(16\pi)^3 \Gamma_{e_i}} & \left[8|C^{VLL}|^2 + 8|C^{VRR}|^2 + 8|C^{VLR}|^2 + 8|C^{VRL}|^2 \right. \\ & \left. + \frac{256e^2}{m_{e_i}^2} \left(\ln \frac{m_{e_i}^2}{m_{e_j}^2} - 3 \right) (|C_{e\gamma}^{ji}|^2 + |C_{e\gamma}^{ij}|^2) \right] \quad (147) \end{aligned}$$

$$- \frac{64e}{m_{e_i}} \text{Re} \left[(C^{VLL} + C^{VLR}) C_{e\gamma}^{ji*} + (C^{VRR} + C^{VRL}) C_{e\gamma}^{ij} \right],$$

where the coefficients in the decay rate are given in terms of the Wilson coefficients

$$C^{VLL} = 4 C_{ee,jikk}^{VLL}, \quad C^{VRR} = 4 C_{ee,jikk}^{VRR}, \quad C^{VLR} = C_{ee,jikk}^{VLR}, \quad C^{VRL} = C_{ee,kkji}^{VLR}. \quad (148)$$

The BR for $e_i \rightarrow e_k e_k \bar{e}_j$ is

$$\text{BR}(e_i \rightarrow e_k e_k \bar{e}_j) = \frac{m_{e_i}^5}{3(16\pi)^3 \Gamma_{e_i}} \left[16|C^{VLL}|^2 + 16|C^{VRR}|^2 + 8|C^{VLR}|^2 + 8|C^{VRL}|^2 \right], \quad (149)$$

where the coefficients in the decay rate are given in terms of the Wilson coefficients

$$C^{VLL} = 2 C_{ee,kikj}^{VLL}, \quad C^{VRR} = 2 C_{ee,kikj}^{VRR}, \quad C^{VLR} = C_{ee,kikj}^{VLR}, \quad C^{VRL} = C_{ee,kkji}^{VLR}. \quad (150)$$

The Higgs-penguin contribution is neglected, because it is suppressed by small charged lepton Yukawa couplings and thus no scalar operators are induced at leading order.

C.3 Semi-leptonic processes

C.3.1 Effective Lagrangian

The effective Lagrangian relevant for semi-leptonic interactions is

$$\begin{aligned} \mathcal{L} \supset & C_{eq}^{VLL} (\bar{e}\gamma^\mu P_L e) (\bar{q}\gamma_\mu P_L q) + C_{eq}^{VRR} (\bar{e}\gamma^\mu P_R e) (\bar{q}\gamma_\mu P_R q) \\ & + C_{eq}^{VLR} (\bar{e}\gamma^\mu P_L e) (\bar{q}\gamma_\mu P_R q) + C_{qe}^{VLR} (\bar{q}\gamma_\mu P_L q) (\bar{e}\gamma^\mu P_R e) \\ & + [C_{eq}^{SRR} (\bar{e} P_R e) (\bar{q} P_R q) + C_{eq}^{SRL} (\bar{e} P_R e) (\bar{q} P_L q) + C_{eq}^{TRR} (\bar{e} \sigma^{\mu\nu} P_R e) (\bar{q} \sigma_{\mu\nu} P_R q) + \text{h.c.}] \\ & + C_{\nu q}^{VLL} (\bar{\nu}\gamma^\mu P_L \nu) (\bar{q}\gamma_\mu P_L q) + C_{\nu q}^{VLR} (\bar{\nu}\gamma^\mu P_L \nu) (\bar{q}\gamma_\mu P_R q) \\ & + [C_{\nu ed}^{VLL} (\bar{\nu}\gamma^\mu P_L e) (\bar{d}\gamma_\mu P_L u) + C_{\nu ed}^{VLR} (\bar{\nu}\gamma^\mu P_L e) (\bar{d}\gamma_\mu P_R u) \\ & + C_{\nu ed}^{SRR} (\bar{\nu} P_R e) (\bar{d} P_R u) + C_{\nu ed}^{SRL} (\bar{\nu} P_R e) (\bar{d} P_L u) + C_{\nu ed}^{TRR} (\bar{\nu} \sigma^{\mu\nu} P_R e) (\bar{d} \sigma_{\mu\nu} P_R u) + \text{h.c.}], \end{aligned} \quad (151)$$

where the first three lines describe neutral-current interactions between charged leptons and quarks, the fourth line describes neutral-current interactions between neutrinos and quarks, and the last two lines describe charged-current interactions. The flavour indices are suppressed in the above equation. In the following discussion, they are indicated as subscripts, e.g. $C_{eq,i,jkl}^{VLL} (\bar{e}_i \gamma^\mu P_L e_j) (\bar{q}_k \gamma_\mu P_L q_l)$.

The dominant RG corrections are due to QCD. Their correction at one-loop order to the Wilson coefficients of operators with two quarks and two leptons is described by

$$\begin{aligned} C^{VXY}(\mu = m_b) &= C^{VXY}(\mu = m_\phi), \\ C^{SXY}(\mu = m_b) &= \left[\frac{\alpha_s(m_t)}{\alpha_s(m_b)} \right]^{-\frac{3C_F}{\beta_0^{(5)}}} \left[\frac{\alpha_s(m_\phi)}{\alpha_s(m_t)} \right]^{-\frac{3C_F}{\beta_0^{(6)}}} C^{SXY}(\mu = m_\phi), \\ C^{TXY}(\mu = m_b) &= \left[\frac{\alpha_s(m_t)}{\alpha_s(m_b)} \right]^{\frac{C_F}{\beta_0^{(5)}}} \left[\frac{\alpha_s(m_\phi)}{\alpha_s(m_t)} \right]^{\frac{C_F}{\beta_0^{(6)}}} C^{TXY}(\mu = m_\phi), \end{aligned} \quad (152)$$

where $X, Y \in \{L, R\}$ denote the chiralities of the fermion bilinears. The Casimir invariant C_F and $\beta_0^{(n_f)}$ which parametrises the one-loop RG equation of the strong coupling are

$$C_F = (N_c^2 - 1)/(2N_c) = 4/3, \quad \beta_0^{(n_f)} = 11 - 2n_f/3 \quad (153)$$

with $N_c = 3$ colours and n_f flavours.

C.3.2 Tree-level matching

Here, we provide the matching to relevant operators in the low-energy EFT at tree level. At this level, the interactions of the LQ ϕ induce Wilson coefficients with two quarks and two leptons. The non-zero Wilson coefficients for neutral-current interactions are given by

$$\begin{aligned} C_{\nu d,ijkl}^{VLL} &= \frac{x_{jl}x_{ik}^*}{2m_\phi^2}, & C_{eu,ijkl}^{VLL} &= \frac{z_{jl}z_{ik}^*}{2m_\phi^2}, & C_{eu,ijkl}^{VRR} &= \frac{y_{ik}y_{jl}^*}{2m_\phi^2}, \\ C_{eu,ijkl}^{SRR} &= \frac{z_{ik}^*y_{jl}}{2m_\phi^2}, & C_{eu,ijkl}^{TRR} &= -\frac{1}{4} \frac{z_{ik}^*y_{jl}}{2m_\phi^2} \end{aligned} \quad (154)$$

and the ones for charged-current interactions are

$$C_{\nu du,ijkl}^{VLL} = -\frac{x_{ik}^*z_{jl}}{2m_\phi^2}, \quad C_{\nu du,ijkl}^{SRR} = -\frac{x_{ik}^*y_{jl}}{2m_\phi^2}, \quad C_{\nu du,ijkl}^{TRR} = \frac{1}{4} \frac{x_{ik}^*y_{jl}}{2m_\phi^2}. \quad (155)$$

For the charged-current observables, involving the quark flavour transition $b \rightarrow c$ and defined in the following, the RG running of the contributions to the Wilson coefficients due to the LQ ϕ between the scale, set by the LQ mass, and the hadronic scale, $\mu = \mu_B = 4.8$ GeV, is accounted for as

$$\begin{aligned} \frac{C_{\nu du,\beta\alpha 32}^{VLL}(\mu_B)}{C_{\nu du,\beta\alpha 32}^{VLL}} &\approx \begin{Bmatrix} 1.016, & \hat{m}_\phi = 2 \\ 1.018, & \hat{m}_\phi = 4 \\ 1.019, & \hat{m}_\phi = 6 \end{Bmatrix}, & \frac{C_{\nu du,\beta\alpha 32}^{SRR}(\mu_B)}{C_{\nu du,\beta\alpha 32}^{SRR}} &\approx \begin{Bmatrix} 1.675, & \hat{m}_\phi = 2 \\ 1.736, & \hat{m}_\phi = 4 \\ 1.770, & \hat{m}_\phi = 6 \end{Bmatrix}, \\ \frac{C_{\nu du,\beta\alpha 32}^{TRR}(\mu_B)}{C_{\nu du,\beta\alpha 32}^{TRR}} &\approx \begin{Bmatrix} 0.860, & \hat{m}_\phi = 2 \\ 0.852, & \hat{m}_\phi = 4 \\ 0.848, & \hat{m}_\phi = 6 \end{Bmatrix}, \end{aligned} \quad (156)$$

where the numerical values in brackets have been extracted using the `Wilson` package [95].

C.3.3 $R(D^{(*)})$

We define

$$\begin{aligned} G_\alpha^D &\approx \sum_{\beta=1}^3 \left(\begin{Bmatrix} 0.500, & \alpha = 1 \\ 0.500, & \alpha = 2 \\ 1.000, & \alpha = 3 \end{Bmatrix} \left| (1+\delta) \cdot 2\sqrt{2}G_F V_{cb} \delta_{\alpha\beta} - C_{\nu du,\beta\alpha 32}^{VLL}(\mu_B) \right|^2 \right. \\ &\quad + \begin{Bmatrix} 0.596 \\ 0.593 \\ 1.120 \end{Bmatrix} \left| C_{\nu du,\beta\alpha 32}^{SRR}(\mu_B) \right|^2 + \begin{Bmatrix} 0.272 \\ 0.272 \\ 0.662 \end{Bmatrix} \left| C_{\nu du,\beta\alpha 32}^{TRR}(\mu_B) \right|^2 \\ &\quad - \begin{Bmatrix} 0.000 \\ 0.079 \\ 1.563 \end{Bmatrix} \operatorname{Re} \left(\left((1+\delta) \cdot 2\sqrt{2}G_F V_{cb} \delta_{\alpha\beta} - C_{\nu du,\beta\alpha 32}^{VLL}(\mu_B) \right) C_{\nu du,\beta\alpha 32}^{SRR*}(\mu_B) \right) \\ &\quad \left. - \begin{Bmatrix} 0.000 \\ 0.084 \\ 0.959 \end{Bmatrix} \operatorname{Re} \left(\left((1+\delta) \cdot 2\sqrt{2}G_F V_{cb} \delta_{\alpha\beta} - C_{\nu du,\beta\alpha 32}^{VLL}(\mu_B) \right) C_{\nu du,\beta\alpha 32}^{TRR*}(\mu_B) \right) \right) \end{aligned} \quad (157)$$

and

$$G_\alpha^{D^*} \approx \sum_{\beta=1}^3 \left(\begin{Bmatrix} 0.501, & \alpha = 1 \\ 0.499, & \alpha = 2 \\ 1.000, & \alpha = 3 \end{Bmatrix} \left| (1+\delta) \cdot 2\sqrt{2}G_F V_{cb} \delta_{\alpha\beta} - C_{\nu du,\beta\alpha 32}^{VLL}(\mu_B) \right|^2 \right) \quad (158)$$

$$\begin{aligned}
& + \begin{Bmatrix} 0.039 \\ 0.039 \\ 0.053 \end{Bmatrix} |C_{\nu edu, \beta\alpha 32}^{SRR}(\mu_B)|^2 + \begin{Bmatrix} 6.372 \\ 6.364 \\ 15.347 \end{Bmatrix} |C_{\nu edu, \beta\alpha 32}^{TRR}(\mu_B)|^2 \\
& - \begin{Bmatrix} 0.000 \\ -0.012 \\ -0.139 \end{Bmatrix} \operatorname{Re} \left(\left((1 + \delta) \cdot 2\sqrt{2}G_F V_{cb} \delta_{\alpha\beta} - C_{\nu edu, \beta\alpha 32}^{VLL}(\mu_B) \right) C_{\nu edu, \beta\alpha 32}^{SRR*}(\mu_B) \right) \\
& - \begin{Bmatrix} -0.001 \\ -0.261 \\ -5.620 \end{Bmatrix} \operatorname{Re} \left(\left((1 + \delta) \cdot 2\sqrt{2}G_F V_{cb} \delta_{\alpha\beta} - C_{\nu edu, \beta\alpha 32}^{VLL}(\mu_B) \right) C_{\nu edu, \beta\alpha 32}^{TRR*}(\mu_B) \right).
\end{aligned}$$

Here, α (β) denotes the flavour of the charged lepton (neutrino) in the final state. The numbers in the first (second) [third] entry of the vectors in curly brackets encode the hadronic form factors employed by `flavio` [62–64] (since v2.0), and the integrated-out phase space for $\alpha = 1$ (2) [3]. These numbers can be compared to the ones that are found in reference [206]. The correction δ , $\delta = 0.007$, accounts for QED running of the SM contribution to $C_{\nu edu}^{VLL}$ from the Z -boson mass scale down to the hadronic scale, $\mu = \mu_B = 4.8$ GeV. We employ the best-fit value for V_{cb} from the PDG, $V_{cb} \approx 0.0405$ [93]. These general formulae then constitute $R(D)$ and $R(D^*)$

$$\frac{R(D)}{R(D)_{\text{SM}}} = \frac{G_3^D}{G_2^D + G_1^D}, \quad \frac{R(D^*)}{R(D^*)_{\text{SM}}} = \frac{G_3^{D^*}}{G_2^{D^*} + G_1^{D^*}}. \quad (159)$$

Using the values $R(D)_{\text{SM}} = 0.297 \pm 0.008$ and $R(D^*)_{\text{SM}} = 0.245 \pm 0.008$ given by `flavio`, v2.3, we find that the results obtained from the expressions above deviate from those obtained from `flavio` only by up to 0.5 percent in the ranges of $R(D^{(*)})$ displayed in the plots.

C.3.4 $R_D^{\mu/e}$ and $R_{D^*}^{e/\mu}$

Similarly to $R(D^{(*)})$ in appendix C.3.3, these observables can be calculated using eqs. (157) and (158), such that

$$R_D^{\mu/e} = \frac{\Gamma(B \rightarrow D\mu\nu)}{\Gamma(B \rightarrow De\nu)} = \frac{G_2^D}{G_1^D}, \quad (160)$$

and

$$R_{D^*}^{e/\mu} = \frac{\Gamma(B \rightarrow D^*e\nu)}{\Gamma(B \rightarrow D^*\mu\nu)} = \frac{G_1^{D^*}}{G_2^{D^*}}. \quad (161)$$

C.3.5 Leptonic pseudoscalar meson decays $B_k \rightarrow \tau\nu$

A pseudoscalar meson B_k , constituted by a bottom quark b and an up-type quark u_k , decays into a tau lepton and a neutrino with a rate [93; 207]

$$\Gamma_{B_k \rightarrow \tau\nu} = \frac{G_F^2}{8\pi} m_{B_k} f_{B_k}^2 |V_{u_k b}|^2 m_\tau^2 \left(1 - \frac{m_\tau^2}{m_{B_k}^2}\right)^2 \sum_{\beta=1}^3 \left| (1 + \delta) \cdot \delta_{3\beta} - \frac{1}{2\sqrt{2}G_F V_{u_k b}} C_{\nu edu, \beta 33k}^\phi(\mu_B) \right|^2 \quad (162)$$

where

$$C_{\nu edu, \beta 33k}^\phi(\mu_B) = C_{\nu edu, \beta 33k}^{VLL}(\mu_B) - \frac{m_{B_k}^2}{m_\tau (m_{u_k}(\mu_B) + m_b(\mu_B))} C_{\nu edu, \beta 33k}^{SRR}(\mu_B). \quad (163)$$

Here, m_{B_k} and f_{B_k} are the mass and decay constant of the meson, respectively. The correction $\delta = 0.007$ accounts for QED running of the SM contribution to $C_{\nu edu}^{VLL}$ from the Z -boson mass scale down to the hadronic scale, $\mu = \mu_B = 4.8$ GeV.

From eq. (162), one may define

$$\Gamma_{B_c}^\phi = \frac{G_F^2 m_{B_c} f_{B_c}^2 V_{cb}^2 m_\tau^2}{8\pi} \left(1 - \frac{m_\tau^2}{m_{B_c}^2}\right)^2 \times \left(\sum_{\beta=1}^3 \left| (1+\delta) \cdot \delta_{3\beta} - \frac{1}{2\sqrt{2}G_F V_{cb}} C_{\nu edu, \beta 332}^\phi(\mu_B) \right|^2 - (1+\delta)^2 \right) \quad (164)$$

which vanishes in the absence of contributions to $B_c \rightarrow \tau\nu$ from the LQ ϕ . Then, rearranging eq. (87) yields the following inferred SM contribution to the B_c lifetime

$$\tau_{B_c}^{\text{SM}} = \left[\frac{1}{\tau_{B_c}^{\text{exp}}} - \frac{G_F^2 m_{B_c} f_{B_c}^2 V_{cb}^2 m_\tau^2}{8\pi} \left(1 - \frac{m_\tau^2}{m_{B_c}^2}\right)^2 \times \left(\sum_{\beta=1}^3 \left| (1+\delta) \cdot \delta_{3\beta} - \frac{1}{2\sqrt{2}G_F V_{cb}} C_{\nu edu, \beta 332}^\phi(\mu_B) \right|^2 - (1+\delta)^2 \right) \right]^{-1}. \quad (165)$$

We require that the result for $\tau_{B_c}^{\text{SM}}$ lies in the interval [0.4, 0.7] ps, following the estimate in reference [119], at the 1σ level, and neglect all other uncertainties against the broadness of this range. Furthermore, we use the PDG values $\tau_{B_c}^{\text{exp}} = 0.510$ ps, $m_{B_c} = 6.2745$ GeV, $m_\tau = 1.7769$ GeV, $V_{cb} \approx 0.0405$ [93] as well as $f_{B_c} = 434$ MeV [208] and the quark masses $m_c(\mu_B) = 0.9023$ GeV and $m_b(\mu_B) = 4.0945$ GeV, as output by `flavio`, v2.3.

C.3.6 $B \rightarrow K^{(*)}\nu\bar{\nu}$

The BR of the decay $B \rightarrow K^{(*)}$ plus missing energy is normalised to the SM prediction in the ratio $R_{K^{(*)}}^\nu$. As $C_{\nu d}^{VLR}$ is not generated at one-loop order in the SM, the decay $B \rightarrow K^{(*)}\nu\bar{\nu}$ is dominated by $C_{\nu d, \alpha\beta 23}^{VLL}$. In contrast to the SM case, the flavours of the neutrinos do not have to coincide for the contribution due to the LQ ϕ . Following reference [133], we obtain

$$R_{K^{(*)}}^\nu = \frac{1}{3} \sum_{\alpha, \beta=1}^3 \left| \delta_{\alpha\beta} + \frac{C_{\nu d, \alpha\beta 23}^{VLL}}{C_{\nu d, 23, \text{SM}}^{VLL}} \right|^2. \quad (166)$$

We use $C_{\nu d, 23, \text{SM}}^{VLL} \approx (1.01 - 0.02i) \times (10 \text{ TeV})^{-2}$ which is the value given by `flavio`, v2.3, see also [209], converted to the JMS basis and evaluated at the hadronic scale, $\mu = \mu_B = 4.8$ GeV.

C.3.7 Relevant Wilson coefficients for $b \rightarrow se_i\bar{e}_j$

The relevant Wilson coefficients for $b \rightarrow se_i\bar{e}_j$ at one-loop order can be obtained from eq. (A.6) in [75]

$$C_{ed, ij 23}^{VLL} = -\frac{1}{64\pi^2 m_\phi^2} \sum_{m, n} x_{m2}^* x_{m3} z_{jn} z_{in}^* + \frac{\sqrt{2}G_F}{16\pi^2} V_{ts}^* V_{tb} z_{j3} z_{i3}^* t_t, \quad (167)$$

$$C_{de, 23ij}^{VLR} = -\frac{1}{64\pi^2 m_\phi^2} \sum_{m, n} x_{m2}^* x_{m3} y_{jn} y_{in}^* - \frac{\sqrt{2}G_F}{32\pi^2} V_{ts}^* V_{tb} y_{j3} y_{i3}^* t_t \left(\ln t_t + \frac{3}{2} \right). \quad (168)$$

Note that the contributions from the up and the charm quark have been neglected.

For lepton flavour conserving interactions, we have to additionally consider the down-type quark dipole operator

$$\mathcal{L} \supset C_{d\gamma}^{ij} (\bar{d}_i \sigma_{\alpha\beta} P_R d_j) F^{\alpha\beta} + \text{h.c.} \quad (169)$$

with the Wilson coefficients

$$C_{d\gamma}^{23} = -\frac{e m_b}{576\pi^2} \sum_m \frac{x_{m2}^* x_{m3}}{m_\phi^2}, \quad C_{d\gamma}^{32} = -\frac{e m_s}{576\pi^2} \sum_m \frac{x_{m2} x_{m3}^*}{m_\phi^2}. \quad (170)$$

These calculated contributions are used in the numerical evaluation of the tertiary constraints in the comprehensive scan.

C.3.8 $\mu - e$ conversion rate

Not taking into account next-to-leading-order corrections (in the loop expansion), we obtain at one-loop order the following contributions in the limit of vanishing external masses and momenta in addition to the tree-level contributions discussed above. The short-distance γ -penguin contributions result in

$$C_{eq,ijkk}^{VLL,\gamma} = C_{eq,ijkk}^{VLR,\gamma} = -\frac{Q^q e^2}{96\pi^2 m_\phi^2} \sum_m z_{im}^* z_{jm} (5 + 4 \ln t_{u_m}), \quad (171)$$

$$C_{eq,ijkk}^{VRR,\gamma} = C_{qe,kkij}^{VLR,\gamma} = -\frac{Q^q e^2}{96\pi^2 m_\phi^2} \sum_m y_{im}^* y_{jm} (5 + 4 \ln t_{u_m}), \quad (172)$$

where Q^q denotes the electric charge of the quark. The Z -penguin diagrams generate the Wilson coefficients

$$C_{eq,ijkk}^{VLL,Z} = -\frac{6\sqrt{2}G_F(T_3 - Q^q s_W^2)}{16\pi^2} \sum_m z_{im}^* z_{jm} t_{u_m} (1 + \ln t_{u_m}), \quad (173)$$

$$C_{eq,ijkk}^{VLR,Z} = \frac{6\sqrt{2}G_F Q^q s_W^2}{16\pi^2} \sum_m z_{im}^* z_{jm} t_{u_m} (1 + \ln t_{u_m}), \quad (174)$$

$$C_{qe,kkij}^{VLR,Z} = \frac{6\sqrt{2}G_F(T_3 - Q^q s_W^2)}{16\pi^2} \sum_m y_{im}^* y_{jm} t_{u_m} (1 + \ln t_{u_m}), \quad (175)$$

$$C_{eq,ijkk}^{VRR,Z} = -\frac{6\sqrt{2}G_F Q^q s_W^2}{16\pi^2} \sum_m y_{im}^* y_{jm} t_{u_m} (1 + \ln t_{u_m}). \quad (176)$$

For up-type quarks, there are no contributions from box diagrams. For down-type quarks, there are only box contributions to vector operators. Thus for $\mu - e$ conversion the only relevant contribution is to vector operators with down quarks which, neglecting all Yukawa couplings apart from the one of the top quark, y_t , are given by

$$C_{ed,ijkk}^{VLL,\text{box}} = \sum_{m,n} \frac{|x_{nk}|^2 z_{im}^* z_{jm}}{64\pi^2 m_\phi^2} + \frac{\sqrt{2}G_F x_{ik}^* x_{jk}}{16\pi^2} t_W \ln t_W - \frac{|V_{td_k}|^2 y_t^2 z_{j3} z_{i3}^*}{32\pi^2 m_\phi^2} \left[\frac{1}{t_t - t_W} + \frac{t_W \ln \frac{t_W}{t_t}}{(t_t - t_W)^2} \right] \quad (177)$$

$$\begin{aligned} & - \frac{\sqrt{2}G_F}{16\pi^2} \sum_m (z_{im}^* x_{jk} V_{u_m d_k}^* + x_{ik}^* z_{jm} V_{u_m d_k}) \frac{t_W (t_W \ln t_W - t_{u_m} \ln t_{u_m})}{t_W - t_{u_m}} \\ & + \frac{\sqrt{2}G_F}{16\pi^2} \sum_{m,n} z_{in}^* z_{jm} V_{u_m d_k} V_{u_n d_k} \\ & \quad \times \left[\frac{t_W^3 \ln t_W}{(t_{u_m} - t_W)(t_{u_n} - t_W)} + \frac{t_W t_{u_m}^2 \ln t_{u_m}}{(t_W - t_{u_m})(t_{u_n} - t_{u_m})} + \frac{t_W t_{u_n}^2 \ln t_{u_n}}{(t_W - t_{u_n})(t_{u_m} - t_{u_n})} \right] \end{aligned}$$

$$C_{de,kkij}^{VLR,\text{box}} = \sum_{m,n} \frac{|x_{nk}|^2 y_{im}^* y_{jm}}{64\pi^2 m_\phi^2} - \frac{|V_{td_k}|^2 y_t^2 y_{j3} y_{i3}^*}{64\pi^2 m_\phi^2} \left[\frac{t_t}{t_W - t_t} - \frac{t_W^2 \ln t_W}{(t_W - t_t)^2} + \frac{(2t_W - t_t)t_t \ln t_t}{(t_W - t_t)^2} \right] \quad (178)$$

$$-\sum_{m,n} \frac{\sqrt{2}G_F V_{u_m d_k} V_{u_n d_k}^* y_{in}^* y_{jm} t_W t_{u_m}^{1/2} t_{u_n}^{1/2}}{8\pi^2} \times \left[\frac{t_W \ln t_W}{(t_W - t_{u_m})(t_W - t_{u_n})} + \frac{t_{u_m} \ln t_{u_m}}{(t_W - t_{u_m})(t_{u_n} - t_{u_m})} + \frac{t_{u_n} \ln t_{u_n}}{(t_W - t_{u_n})(t_{u_m} - t_{u_n})} \right].$$

The $\mu - e$ CR can be obtained from the effective Lagrangian following reference [127]

$$\omega_{\text{conv}} = \left| -\frac{C_{e\gamma,12}}{2m_\mu} D + \tilde{g}_{LS}^{(p)} S^{(p)} + \tilde{g}_{LV}^{(p)} V^{(p)} + (p \rightarrow n) \right|^2 + \left| -\frac{C_{e\gamma,21}^*}{2m_\mu} D + \tilde{g}_{RS}^{(p)} S^{(p)} + \tilde{g}_{RV}^{(p)} V^{(p)} + (p \rightarrow n) \right|^2 \quad (179)$$

with the effective coupling constants

$$\tilde{g}_{LS}^{(N)} = \sum_i G_S^{q_i, N} (C_{eq,12ii}^{SRR} + C_{eq,12ii}^{SRL}) \quad (180)$$

$$\tilde{g}_{RS}^{(N)} = \sum_i G_S^{q_i, N} (C_{eq,21ii}^{SRR^*} + C_{eq,21ii}^{SRL^*}) \quad (181)$$

$$\tilde{g}_{LV}^{(p)} = 2 (C_{eu,1211}^{VLL} + C_{eu,1211}^{VLR}) + (C_{ed,1211}^{VLL} + C_{ed,1211}^{VLR}) \quad (182)$$

$$\tilde{g}_{RV}^{(p)} = 2 (C_{eu,1211}^{VRR} + C_{ue,1112}^{VLR}) + (C_{ed,1211}^{VRR} + C_{de,1112}^{VLR}) \quad (183)$$

$$\tilde{g}_{LV}^{(n)} = (C_{eu,1211}^{VLL} + C_{eu,1211}^{VLR}) + 2 (C_{ed,1211}^{VLL} + C_{ed,1211}^{VLR}) \quad (184)$$

$$\tilde{g}_{RV}^{(n)} = (C_{eu,1211}^{VRR} + C_{ue,1112}^{VLR}) + 2 (C_{ed,1211}^{VRR} + C_{de,1112}^{VLR}) \quad (185)$$

with $N = p, n$. In the numerical analysis we use the nuclear form factors $G_S^{q_i, N}$ given in reference [128] and the overlap integrals D , $S^{(N)}$ and $V^{(N)}$ and capture rates ω_{capt} presented in reference [127].

C.4 Z decays to fermions

For calculating the contributions to leptonic Z decays due to the LQ ϕ , we follow the procedure of reference [134]. To parametrise these effects, we consider the effective Lagrangian for the Z boson interaction with an SM fermion f_i

$$\mathcal{L}_{\text{eff}}^Z = \frac{g}{\cos \theta_W} \sum_{i,j} \bar{f}_i \gamma^\mu \left[g_{f_L}^{ij} P_L + g_{f_R}^{ij} P_R \right] f_j Z_\mu, \quad (186)$$

where g is the $SU(2)$ gauge coupling, and

$$g_{f_{L(R)}}^{ij} = g_{f_{L(R)}}^{\text{SM}} \delta^{ij} + \delta g_{f_{L(R)}}^{ij}. \quad (187)$$

At tree level, the SM effective couplings are given by

$$g_{f_L}^0 = T_3^f - Q^f \sin^2 \theta_W, \quad g_{f_R}^0 = -Q^f \sin^2 \theta_W, \quad (188)$$

where Q^f is the electric charge of the fermion f , and T_3^f is its third component of weak isospin.

For the remainder of this appendix, we focus on the interactions with charged leptons, i.e. $f_i = e_i$. At higher loop order in the SM, these couplings are modified by factors $\rho_f = 1.00937$ and $\sin^2 \theta_{\text{eff}} = 0.231533$ [93],

$$g_{f_L}^{\text{SM}} = \sqrt{\rho_f} (T_3^f - Q^f \sin^2 \theta_{\text{eff}}), \quad g_{f_R}^{\text{SM}} = -\sqrt{\rho_f} Q^f \sin^2 \theta_{\text{eff}}. \quad (189)$$

The contributions to the effective couplings for $Z \rightarrow f\bar{f}$ are calculated in general for scalar LQ models in reference [134]. We refrain from detailing these results here, but instead recast the dominant contributions in the context of this model.

For charged leptons, to contrast with existing constraints, we note the relation of the effective couplings $g_{f_{L(R)}}^{ij}$ to those for vector and axial-vector interactions

$$g_{e_{V(A)}}^{ij} = g_{e_L}^{ij} \pm g_{e_R}^{ij}. \quad (190)$$

In this model, charged leptons couple solely to up-type quarks and an enhancement via the top quark mass yields the following dominant contribution

$$\delta g_{e_{A(V)}}^{ii} = \delta g_{e_{iA(V)}} \approx \frac{N_c}{32\pi^2} \frac{t_t(t_t - 1 - \ln t_t)}{(t_t - 1)^2} (|z_{i3}|^2 \pm |y_{i3}|^2). \quad (191)$$

Note that the dependence of the SM value on $\sin^2 \theta_{\text{eff}}$ motivates the consideration of the future sensitivity of collider experiments, as listed in table 8. Prospective sensitivities are quoted from reference [116], where they have assumed that the measurements of $g_{e_{iA}}$ are improved by the same factor as $\sin^2 \theta_{\text{eff}}$, and $g_{e_{iA}}$ provides the more sensitive probe to new physics than $g_{e_{iV}}$.

D Supplementary information for section 5

In the following, we briefly discuss current constraints on and the projected sensitivity of future experiments to contributions to the magnitude of the Wilson coefficient $C_{\nu_{\text{edu}},3332}^{SRR}$. It constitutes the dominant contribution to the observables $R(D)$, $R(D^*)$ and $\tau_{B_c}^{\text{SM}}$ in this model. According to eqs. (155) and (156), we find $C_{\nu_{\text{edu}},3332}^{SRR} \approx -1.7 x_{33} y_{32}/(2 m_\phi^2) \approx -1.7 a_{33} b_{32}/(2 m_\phi^2)$ at the hadronic scale, $\mu = \mu_B = 4.8$ GeV. Note the following statements are directly inferred from the primary scan which is discussed in section 5. A comparison with the comprehensive scan, see section 6, only reveals small deviations from the results described below for $\hat{m}_\phi = 2$.

As can be seen in the top in figure 25, the achievable deviation of $R(D)$ and $R(D^*)$ from their respective SM values grows linearly with an increase of the magnitude of $C_{\nu_{\text{edu}},3332}^{SRR}$. Only for $|C_{\nu_{\text{edu}},3332}^{SRR}| \gtrsim 0.2/\text{TeV}^2$, a slight deviation from this trend becomes visible. This confirms that the contributions to $R(D)$ and $R(D^*)$ which are linear in the Wilson coefficient, since they arise from the interference with the SM contribution, see eqs. (66) and (67), dominate for smaller values of the LQ couplings. These plots also conveniently illustrate that the anomaly is mainly driven by the experimental data for $R(D^*)$, that is, explaining $R(D^*)$ at the 2σ (1σ) level requires $|C_{\nu_{\text{edu}},3332}^{SRR}| \gtrsim 0.2$ (0.3)/ TeV^2 .

The centre-left plot in figure 25 evidences that a correlation between the AMM of the muon, $\Delta a_\mu \propto |b_{23}c_{23}|$, and the Wilson coefficient, $|C_{\nu_{\text{edu}},3332}^{SRR}| \propto |a_{33}b_{32}|$, only arises after imposing the bound on $\text{BR}(\tau \rightarrow \mu\gamma)$, $\text{BR}(\tau \rightarrow \mu\gamma) \propto |b_{23}c_{33}|^2 \approx |b_{23}a_{33}|^2$. Indeed, the current constraint requires that $|C_{\nu_{\text{edu}},3332}^{SRR}| \lesssim 0.4/\text{TeV}^2$, and the upcoming search for this process at Belle II [104] can strengthen this to $|C_{\nu_{\text{edu}},3332}^{SRR}| \lesssim 0.15/\text{TeV}^2$, see centre-right plot. Note that an efficient test of the capability of the model to explain the AMM of the muon still requires a further refinement of that bound, as is visible in the centre-left plot.

Lastly, one can see that the inferred value of $\tau_{B_c}^{\text{SM}}$ is slightly less sensitive to $|C_{\nu_{\text{edu}},3332}^{SRR}|$ than $R(D)$ or $R(D^*)$ are. The distribution of generated sample points for $\hat{m}_\phi = 2$ features a kink which is localised at the upper boundary of the coloured region at $|C_{\nu_{\text{edu}},3332}^{SRR}| \approx 0.13/\text{TeV}^2$, due to the experimental constraint on b_{32} , $|b_{32}| < 2.6$, see table 4. Note that $|C_{\nu_{\text{edu}},3332}^{SRR}| \gtrsim 0.3/\text{TeV}^2$ is necessary to have $\text{BR}(B_c \rightarrow \tau\nu)$ exceed approximately 0.1.

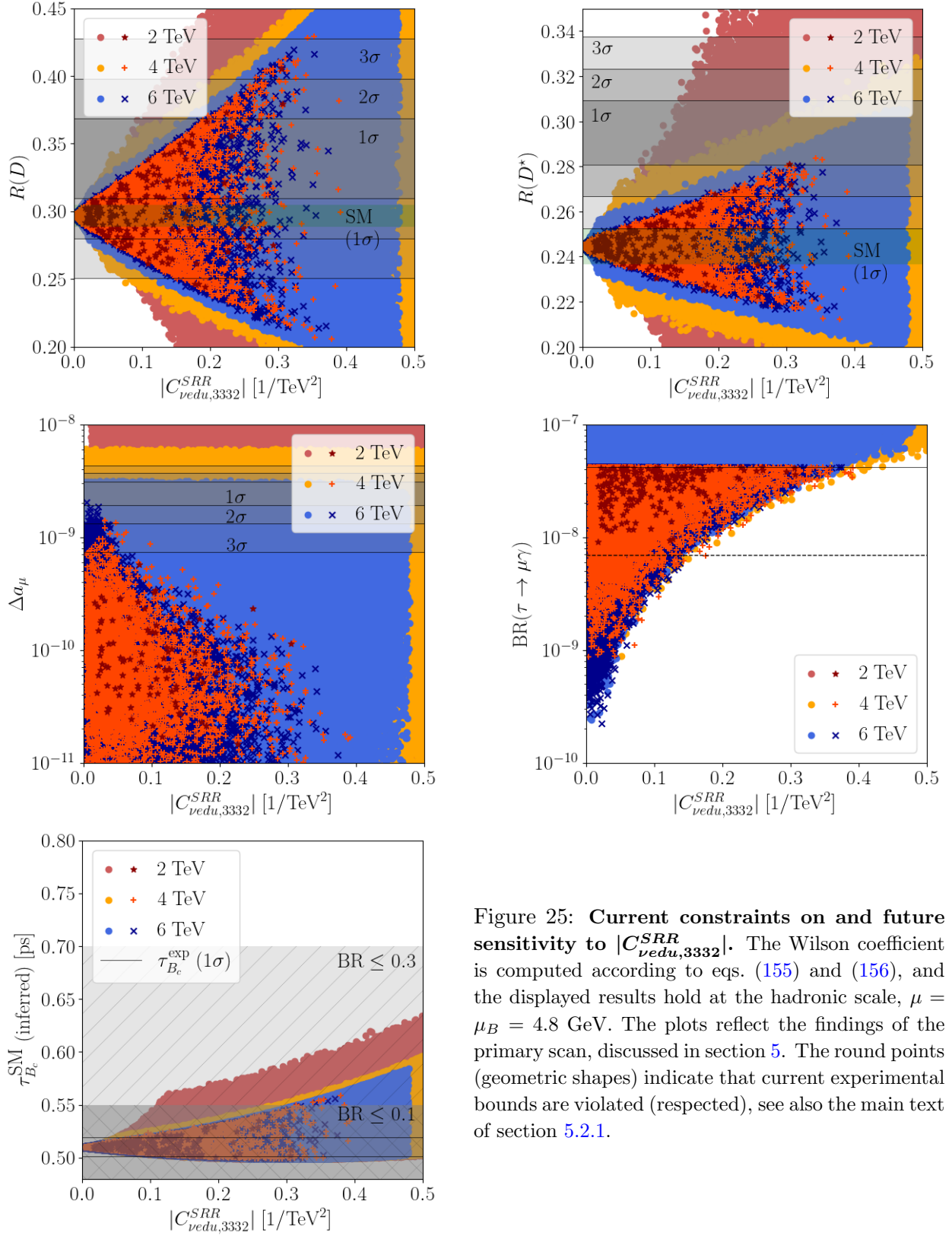


Figure 25: **Current constraints on and future sensitivity to $|C_{vedu,3332}^{SRR}|$.** The Wilson coefficient is computed according to eqs. (155) and (156), and the displayed results hold at the hadronic scale, $\mu = \mu_B = 4.8$ GeV. The plots reflect the findings of the primary scan, discussed in section 5. The round points (geometric shapes) indicate that current experimental bounds are violated (respected), see also the main text of section 5.2.1.

E Supplementary information for section 6

E.1 Details of method of comprehensive scan

In the following, we present details of how the comprehensive scan has been implemented. First note that, although the LQ couplings are sampled in the interaction basis, they are input to `SPheno` in the charged fermion mass basis, which avoids modifying the hard-coded fermion masses in `SPheno`. As such, we use the unitary matrices L_d , R_d , L_e , R_e , L_u and R_u , extracted from the chi-squared fit discussed in section 6.1, to perform this basis transformation. As mentioned in section 5.1.2, the correction to the muon mass arising from LQ contributions could be corrected for by appropriately redefining the effective parameter e_{22} in the charged lepton mass matrix M_e , see eqs. (44) and (45). Nevertheless, since this redefinition has hardly any effect on the form of the unitary matrices L_e and R_e , see analytic expressions in eqs. (46) and (47), it is neglected throughout the scan.

Furthermore, we notice that we implement the model in the comprehensive scan in a simplified version, considering only one SM-like Higgs doublet that gives masses to all charged fermions. As explained in section 2, the main reason for having two Higgs doublets, H_u and H_d , is to facilitate the search for a suitable flavour symmetry. The existence of these two Higgs doublets is, however, not relevant for the explanation of the flavour anomalies, observed in $R(D)$, $R(D^*)$ and in the AMM of the muon. As a consequence, the suppression of the down-type quark masses and of the charged lepton masses is no longer due to the VEV of H_d being much smaller than that of H_u , compare eq. (15), but becomes encoded in the effective parameters d_{ij} and e_{ij} , that must be appropriately rescaled. Such a rescaling only changes the magnitudes of these parameters, but not the results for the unitary matrices L_d , R_d , L_e , R_e , L_u and R_u , since the latter contain ratios of d_{ij} , e_{ij} and f_{ij} , respectively. Therefore, this simplification has no impact on the calculated LQ couplings \mathbf{x} , \mathbf{y} and \mathbf{z} . In addition, considering only one SM-like Higgs doublet allows us to simplify the implementation of this model with the computational tools employed.

We proceed as follows with sampling over the parameter space consistently with the biasing, discussed in section 6.2

1. Sample \hat{a}_{33} , \hat{b}_{32} and \hat{b}_{23} using the biases for the effective parameters in the charged fermion mass basis, see table 6 and eq. (103). Sample all other effective parameters in the interaction basis, including \hat{a}_{23} and \hat{b}_{13} , with flat priors within the ranges specified in eqs. (62) and (63);
2. Transform these parameters into the ones in the charged fermion mass basis using the unitary matrices L_d , R_d , L_e , R_e , L_u and R_u , extracted from the chi-squared fit discussed in section 6.1;
3. Check that the generated values of the effective parameters a_{23} and b_{13} satisfy eq. (102), and that a_{23} and the cosine of the arguments of the latter and the effective parameter b_{23} are within the prescribed regions in table 6;
4. If any of the checks in step 3 fails, return to step 1; otherwise, a valid set of effective parameters is found.

The distribution of the magnitudes of the effective parameters in the charged fermion mass basis, output from the comprehensive scan, is summarised in table 10.

E.2 Additional plots

In this appendix, we present some supplementary plots showing the distributions of different primary and secondary observables in the comprehensive scan. Figure 26 illustrates the correlation

SPREAD OF UNHATTED LQ COUPLINGS IN COMPREHENSIVE SCAN						
Parameter	$\hat{m}_\phi = 2$		$\hat{m}_\phi = 4$		$\hat{m}_\phi = 6$	
	[min., max.]	Average	[min., max.]	Average	[min., max.]	Average
$ a_{11} $	[0.23, 4.41]	2.32	[0.23, 4.41]	2.33	[0.23, 4.41]	2.33
$ a_{12} $	[0.01, 5.70]	0.75	[0.003, 7.59]	1.09	[0.001, 8.62]	1.03
$ a_{13} $	[0.001, 2.01]	0.19	[0.001, 2.63]	0.53	[0.002, 2.73]	0.51
$ a_{21} $	[0.08, 17.1]	3.12	[0.03, 23.9]	4.27	[0.03, 23.1]	4.10
$ a_{22} $	[0.05, 10.6]	2.12	[0.03, 14.2]	3.27	[0.01, 15.8]	3.21
$ a_{23} $	[0.23, 4.40]	0.91	[1.60, 4.40]	2.34	[1.40, 4.40]	2.30
$ a_{31} $	[0.11, 38.3]	8.92	[0.07, 45.8]	10.2	[0.02, 59.8]	11.5
$ a_{32} $	[0.06, 5.31]	2.20	[0.02, 6.55]	2.41	[0.005, 8.94]	2.61
$ a_{33} $	[0.05, 0.73]	0.37	[0.02, 1.90]	0.85	[0.05, 3.62]	1.58
$ b_{11} $	[0.22, 4.43]	2.33	[0.22, 4.43]	2.31	[0.21, 4.44]	2.32
$ b_{12} $	[0.07, 48.1]	10.8	[0.12, 65.0]	13.1	[0.09, 69.2]	13.2
$ b_{13} $	[0.007, 1.67]	0.43	[0.006, 0.70]	0.33	[0.004, 1.57]	0.65
$ b_{21} $	[0.02, 13.3]	3.58	[0.02, 19.9]	3.70	[0.03, 19.6]	4.06
$ b_{22} $	[0.01, 11.2]	3.63	[0.02, 15.5]	3.97	[0.01, 15.5]	4.20
$ b_{23} $	[0.15, 0.80]	0.31	[0.18, 1.84]	0.38	[0.15, 3.48]	0.43
$ b_{31} $	[0.21, 4.07]	1.63	[0.17, 6.08]	1.99	[0.15, 6.34]	2.10
$ b_{32} $	[1.10, 2.60]	1.70	[1.00, 4.50]	2.23	[0.80, 4.50]	2.27
$ b_{33} $	[0.03, 12.9]	2.68	[0.01, 11.1]	2.25	[0.02, 13.5]	3.02

Table 10: **Spread of magnitudes of unhatted LQ couplings for viable points in comprehensive scan.** Recall that the effective parameters c_{ij} are related to a_{ij} via the CKM mixing matrix.

between $\text{BR}(\tau \rightarrow \mu\gamma)$ and the three different flavour anomalies as well as between $\text{BR}(\mu \rightarrow e\gamma)$ and the AMM of the muon. These plots should be compared with the corresponding ones, obtained in the primary scan, see figure 8 in the main text. Observe the effects of biasing in refining the sampled parameter space. Other features and discussion of these observables can be found in section 6.4.3. In figure 27 we show two additional plots for secondary observables, which complement the discussion in section 6.6.

E.3 Tertiary observables

Table 11 details the present experimental constraints on the tertiary observables and the calculation method employed for each observable in the comprehensive scan. Table 12 displays a summary of the results for the tertiary observables, mentioning the range for each of them obtained for the sample of P points passing the primary constraints as well as listing the future reach for these observables.

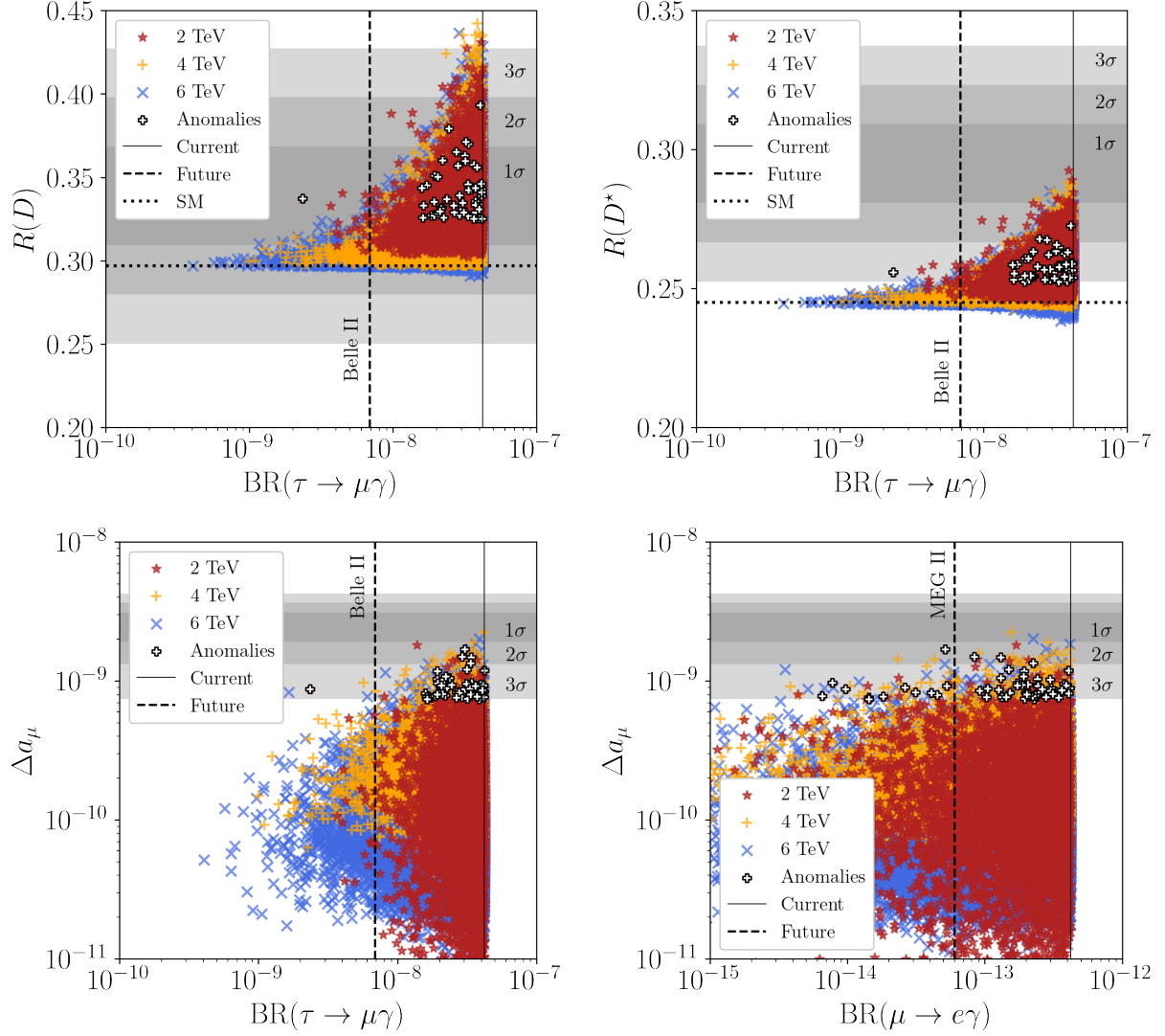


Figure 26: **Constraining power and future reach of radiative cLFV decays in comprehensive scan.** These plots show the results for the BRs of the radiative cLFV decays $\tau \rightarrow \mu\gamma$ and $\mu \rightarrow e\gamma$, plotted against the anomalous observables $R(D)$, $R(D^*)$ and the AMM of the muon. They can be compared with the corresponding plots for the primary scan, displayed in figure 8 in the main text. For further information on how to read this figure, see section 6.3.

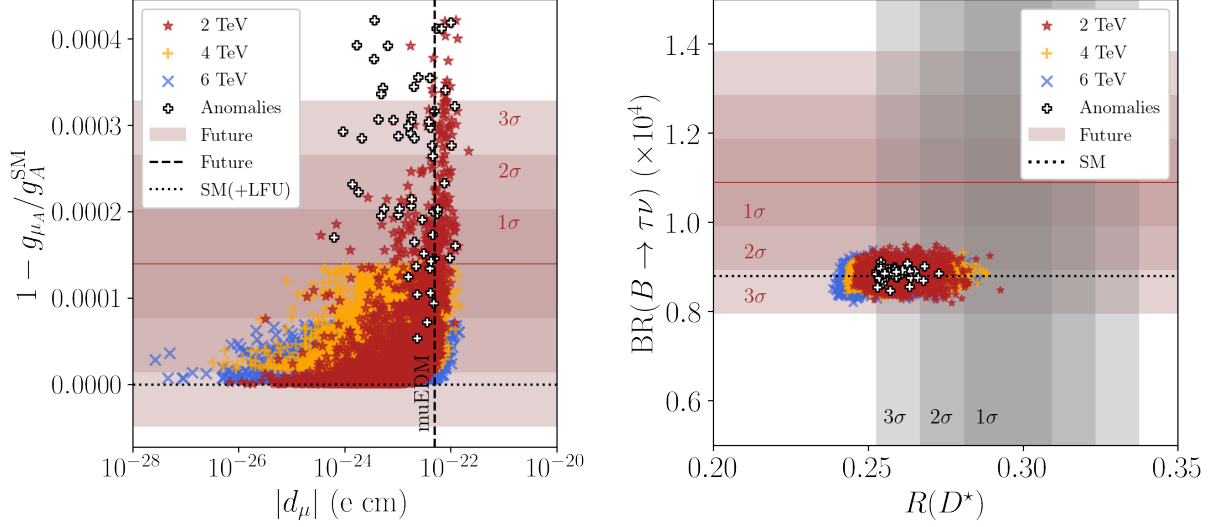


Figure 27: **Additional plots for secondary observables in comprehensive scan.** In the left plot, for $g_{\mu_A}/g_A^{\text{SM}}$ the red-brown shaded regions represent the projected sensitivities from the ILC [117], assuming the present best-fit value [115; 116] shown as red-brown solid line. Furthermore, we show as future constraint on the EDM of the muon the one expected from the muEDM experiment [151] (as example for the frozen-spin technique). In the right plot, we present the projected sensitivity from Belle II for 5 ab^{-1} for $\text{BR}(B \rightarrow \tau\nu)$ [102] as red-brown shaded regions about the current best-fit value [93]. For further information on how to read this figure, see section 6.3.

Observable	Present constraint	Calculation method	Observable	Present constraint	Calculation method
$\text{BR}(B_s \rightarrow \tau\tau)$	6.8×10^{-3}	C.3.7 & flavio	$\Delta M_{B_s}/\Delta M_{B_s}^{\text{SM}}$	1.11 ± 0.09 [210]	SPheno
$\text{BR}(D_s \rightarrow \tau\nu)$	$(5.32 \pm 0.11) \times 10^{-2}$	SPheno	$\text{BR}(D_s \rightarrow \mu\nu)$	$(5.43 \pm 0.15) \times 10^{-3}$	SPheno
$\text{BR}(K^+ \rightarrow \pi^+\nu\nu)$	$(1.7 \pm 1.1) \times 10^{-10}$	flavio	$\text{BR}(K_L \rightarrow \pi^0\nu\nu)$	2.6×10^{-8}	flavio
Δa_e	- †	SPheno	Δa_τ	$\lesssim \mathcal{O}(0.01)$	SPheno
$ d_e $ [e cm]	$< 1.1 \times 10^{-29}$	SPheno	$ d_\tau $ [e cm]	$\lesssim \mathcal{O}(10^{-16})$	SPheno
$\text{BR}(B \rightarrow X_s\gamma)$	$(3.32 \pm 0.15) \times 10^{-4}$	SPheno	$\text{BR}(\tau \rightarrow e\gamma)$	3.3×10^{-8}	SPheno
$\text{BR}(\tau \rightarrow 3e)$	2.7×10^{-8}	SPheno	$\text{BR}(\tau \rightarrow \bar{\mu}\mu e)$	2.7×10^{-8}	SPheno
$\text{BR}(\tau \rightarrow \bar{e}\mu\mu)$	1.7×10^{-8}	SPheno	$\text{BR}(\tau \rightarrow \bar{\mu}ee)$	1.5×10^{-8}	SPheno
$\text{BR}(\tau \rightarrow \pi e)$	8.8×10^{-8}	SPheno	$\text{BR}(\tau \rightarrow \pi\mu)$	1.1×10^{-7}	[203]
$\text{BR}(\tau \rightarrow \phi e)$	3.1×10^{-8}	SPheno	$\text{BR}(\tau \rightarrow \rho e)$	1.8×10^{-8}	SPheno
$\text{BR}(\tau \rightarrow \phi\mu)$	8.4×10^{-8}	SPheno	$\text{BR}(\tau \rightarrow \rho\mu)$	1.2×10^{-8}	SPheno
$g_{e_A}/g_A^{\text{SM}} - 1$	$(-3.19 \pm 6.98) \times 10^{-4}$ [116]	C.4			

Table 11: **List of tertiary observables and their present experimental bounds and calculation method in comprehensive scan.** Constraints quoted without explicit reference are taken from reference [93]. †: presently, anomalies in Δa_e indicate a preference for $|\Delta a_e| \sim 10^{-12}$ [158; 159]. However, as the status of these anomalies is unresolved (two separate measurements show deviations from the SM with opposite sign), we take this value to be a future reach rather than a present constraint.

SPREAD OF TERTIARY OBSERVABLES IN COMPREHENSIVE SCAN				
Observable	Future reach	$\hat{m}_\phi = 2, P = 5955$ [min., max.]	$\hat{m}_\phi = 4, P = 12570$ [min., max.]	$\hat{m}_\phi = 6, P = 39807$ [min., max.]
$\text{BR}(B_s \rightarrow \tau\tau)$	$\sim 10^{-6}$ [211]	$[7.21, 8.49] \times 10^{-7}$	$[6.22, 9.36] \times 10^{-7}$	$[6.02, 9.61] \times 10^{-7}$
$\Delta M_{B_s}/\Delta M_{B_s}^{\text{SM}}$	-	[0.96, 1.05]	[0.85, 1.11]	[0.66, 1.36]
$\text{BR}(D_s \rightarrow \mu\nu)$	$(5.49 \pm 0.05) \times 10^{-3}$ [114]	$[5.45, 5.46] \times 10^{-3}$	$[5.45, 5.46] \times 10^{-3}$	$[5.45, 5.46] \times 10^{-3}$
$\text{BR}(D_s \rightarrow \tau\nu)$	$(5.48 \pm 0.12) \times 10^{-2}$ [114]	$[5.28, 5.36] \times 10^{-2}$	$[5.30, 5.34] \times 10^{-2}$	$[5.30, 5.33] \times 10^{-2}$
$\frac{\text{BR}(K_L \rightarrow \pi^0\nu\nu)}{\text{BR}(K_L \rightarrow \pi^0\nu\nu)_{\text{SM}}}$	1 ± 0.09 [212]	[0.99, 1.02]	[0.99, 1.02]	[0.99, 1.02]
$\frac{\text{BR}(K^+ \rightarrow \pi^+\nu\nu)}{\text{BR}(K^+ \rightarrow \pi^+\nu\nu)_{\text{SM}}}$	-	[0.96, 1.03]	[0.98, 1.01]	[0.99, 1.01]
$\text{BR}(B \rightarrow X_s\gamma)$	-	$[3.290, 3.292] \times 10^{-4}$	$[3.290, 3.292] \times 10^{-4}$	$[3.290, 3.292] \times 10^{-4}$
$1 - g_{eA}/g_A^{\text{SM}}$	$(3.19 \pm 0.041) \times 10^{-4}$ [116]	$[-1.53 \times 10^{-13}, 1.55 \times 10^{-15}]$	$[-8.46 \times 10^{-14}, 7.77 \times 10^{-16}]$	$[-4.62 \times 10^{-14}, 7.77 \times 10^{-16}]$
Δa_e	$\mathcal{O}(10^{-12})$ [158; 159]	$[-5.39, 7.33] \times 10^{-21}$	$[-3.46, 3.25] \times 10^{-21}$	$[-1.68, 2.10] \times 10^{-21}$
Δa_τ	$< \mathcal{O}(10^{-3})$ [213; 214]	$[-1.28, 1.82] \times 10^{-7}$	$[-6.50, 9.87] \times 10^{-8}$	$[-7.29, 8.76] \times 10^{-8}$
$ d_e $ [e cm]	$\lesssim 5 \times 10^{-30}$ [160]	$[3.66 \times 10^{-36}, 1.18 \times 10^{-31}]$	$[1.81 \times 10^{-37}, 6.28 \times 10^{-32}]$	$[1.31 \times 10^{-38}, 3.30 \times 10^{-32}]$
$ d_\tau $ [e cm]	$\lesssim 10^{-19}$ [215]	$[4.30 \times 10^{-26}, 1.12 \times 10^{-21}]$	$[3.25 \times 10^{-27}, 5.10 \times 10^{-22}]$	$[2.77 \times 10^{-27}, 5.70 \times 10^{-22}]$
$\text{BR}(\tau \rightarrow e\gamma)$	$< 9 \times 10^{-9}$ [105]	$[9.73 \times 10^{-19}, 3.31 \times 10^{-14}]$	$[2.08 \times 10^{-19}, 6.24 \times 10^{-15}]$	$[8.44 \times 10^{-20}, 3.33 \times 10^{-14}]$
$\text{BR}(\tau \rightarrow 3e)$	$< 4.7 \times 10^{-10}$ [105]	$[3.51 \times 10^{-20}, 4.47 \times 10^{-16}]$	$[1.03 \times 10^{-20}, 7.66 \times 10^{-17}]$	$[4.74 \times 10^{-21}, 4.01 \times 10^{-16}]$
$\text{BR}(\tau \rightarrow \bar{\mu}\mu e)$	$< 4.5 \times 10^{-10}$ [105]	$[7.63 \times 10^{-21}, 1.10 \times 10^{-16}]$	$[3.34 \times 10^{-21}, 2.15 \times 10^{-17}]$	$[1.38 \times 10^{-21}, 7.79 \times 10^{-17}]$
$\text{BR}(\tau \rightarrow \bar{e}\mu\mu)$	$< 2.6 \times 10^{-10}$ [105]	$[1.74 \times 10^{-30}, 2.71 \times 10^{-21}]$	$[1.96 \times 10^{-28}, 4.46 \times 10^{-21}]$	$[8.11 \times 10^{-29}, 3.20 \times 10^{-21}]$
$\text{BR}(\tau \rightarrow \bar{\mu}ee)$	$< 2.3 \times 10^{-10}$ [105]	$[2.45 \times 10^{-39}, 1.01 \times 10^{-27}]$	$[8.78 \times 10^{-39}, 9.98 \times 10^{-28}]$	$[5.32 \times 10^{-40}, 2.47 \times 10^{-28}]$
$\text{BR}(\tau \rightarrow \pi e)$	$< 7.3 \times 10^{-10}$ [105]	$[1.71 \times 10^{-23}, 5.11 \times 10^{-19}]$	$[1.08 \times 10^{-24}, 1.00 \times 10^{-19}]$	$[5.55 \times 10^{-25}, 8.78 \times 10^{-20}]$
$\text{BR}(\tau \rightarrow \pi\mu)$	$< 7.1 \times 10^{-10}$ [105]	$[4.70 \times 10^{-19}, 1.09 \times 10^{-12}]$	$[2.87 \times 10^{-20}, 2.29 \times 10^{-13}]$	$[4.83 \times 10^{-21}, 7.77 \times 10^{-14}]$
$\text{BR}(\tau \rightarrow \phi e)$	$< 7.4 \times 10^{-10}$ [105]	$[1.26 \times 10^{-22}, 1.08 \times 10^{-17}]$	$[5.49 \times 10^{-24}, 3.80 \times 10^{-18}]$	$[4.63 \times 10^{-25}, 1.07 \times 10^{-18}]$
$\text{BR}(\tau \rightarrow \rho e)$	$< 3.8 \times 10^{-10}$ [105]	$[1.41 \times 10^{-21}, 5.13 \times 10^{-17}]$	$[1.57 \times 10^{-22}, 1.74 \times 10^{-17}]$	$[1.33 \times 10^{-23}, 4.94 \times 10^{-18}]$
$\text{BR}(\tau \rightarrow \phi\mu)$	$< 8.4 \times 10^{-10}$ [105]	$[1.28 \times 10^{-14}, 3.52 \times 10^{-11}]$	$[6.77 \times 10^{-16}, 1.58 \times 10^{-11}]$	$[1.38 \times 10^{-16}, 4.97 \times 10^{-12}]$
$\text{BR}(\tau \rightarrow \rho\mu)$	$< 5.5 \times 10^{-10}$ [105]	$[6.55 \times 10^{-14}, 2.61 \times 10^{-10}]$	$[4.67 \times 10^{-15}, 1.14 \times 10^{-10}]$	$[8.44 \times 10^{-16}, 3.81 \times 10^{-11}]$

Table 12: **Overview of spread of tertiary observables in comprehensive scan.** We present a summary of the statistics reflecting the distribution of tertiary observables: the minimum and maximum generated value for a sample of P points passing the primary constraints together with the future reach. For values quoted from Belle II [105], these represent projections for 50 ab^{-1} of data. Prospective reach intervals illustrate the assumption that the best-fit value of the measurement stays the same. The future projection for $\text{BR}(K_L \rightarrow \pi^0\nu\nu)$ is interpreted assuming a future measurement centred at the SM prediction. Note that we quote an extended number of decimal points for $\text{BR}(B \rightarrow X_s\gamma)$ to show that a variation occurs at the third decimal point. A dash (-) is used to indicate where a future reach could not be identified in the literature.

References

- [1] C.D. Froggatt and H.B. Nielsen, *Hierarchy of Quark Masses, Cabibbo Angles and CP Violation*, *Nucl. Phys. B* **147** (1979) 277.
- [2] P.F. Harrison, D.H. Perkins and W.G. Scott, *Tri-bimaximal mixing and the neutrino oscillation data*, *Phys. Lett. B* **530** (2002) 167 [[hep-ph/0202074](#)].
- [3] P.F. Harrison and W.G. Scott, *Symmetries and generalizations of tri-bimaximal neutrino mixing*, *Phys. Lett. B* **535** (2002) 163 [[hep-ph/0203209](#)].
- [4] Z.-z. Xing, *Nearly tri bimaximal neutrino mixing and CP violation*, *Phys. Lett. B* **533** (2002) 85 [[hep-ph/0204049](#)].
- [5] P.F. Harrison and W.G. Scott, *Permutation symmetry, tri-bimaximal neutrino mixing and the S_3 group characters*, *Phys. Lett. B* **557** (2003) 76 [[hep-ph/0302025](#)].
- [6] H. Ishimori, T. Kobayashi, H. Ohki, Y. Shimizu, H. Okada and M. Tanimoto, *Non-Abelian Discrete Symmetries in Particle Physics*, *Prog. Theor. Phys. Suppl.* **183** (2010) 1 [[1003.3552](#)].
- [7] S.F. King and C. Luhn, *Neutrino Mass and Mixing with Discrete Symmetry*, *Rept. Prog. Phys.* **76** (2013) 056201 [[1301.1340](#)].
- [8] F. Feruglio and A. Romanino, *Lepton flavor symmetries*, *Rev. Mod. Phys.* **93** (2021) 015007 [[1912.06028](#)].
- [9] W. Grimus and P.O. Ludl, *Finite flavour groups of fermions*, *J. Phys. A* **45** (2012) 233001 [[1110.6376](#)].
- [10] BABAR collaboration, *Evidence for an excess of $\bar{B} \rightarrow D^{(*)}\tau^-\bar{\nu}_\tau$ decays*, *Phys. Rev. Lett.* **109** (2012) 101802 [[1205.5442](#)].
- [11] BABAR collaboration, *Measurement of an Excess of $\bar{B} \rightarrow D^{(*)}\tau^-\bar{\nu}_\tau$ Decays and Implications for Charged Higgs Bosons*, *Phys. Rev. D* **88** (2013) 072012 [[1303.0571](#)].
- [12] BELLE collaboration, *Measurement of the branching ratio of $\bar{B} \rightarrow D^{(*)}\tau^-\bar{\nu}_\tau$ relative to $\bar{B} \rightarrow D^{(*)}\ell^-\bar{\nu}_\ell$ decays with hadronic tagging at Belle*, *Phys. Rev. D* **92** (2015) 072014 [[1507.03233](#)].
- [13] BELLE collaboration, *Measurement of $\mathcal{R}(D)$ and $\mathcal{R}(D^*)$ with a semileptonic tagging method*, *Phys. Rev. Lett.* **124** (2020) 161803 [[1910.05864](#)].
- [14] BELLE collaboration, *Measurement of the τ lepton polarization and $R(D^*)$ in the decay $\bar{B} \rightarrow D^*\tau^-\bar{\nu}_\tau$* , *Phys. Rev. Lett.* **118** (2017) 211801 [[1612.00529](#)].
- [15] BELLE collaboration, *Measurement of the τ lepton polarization and $R(D^*)$ in the decay $\bar{B} \rightarrow D^*\tau^-\bar{\nu}_\tau$ with one-prong hadronic τ decays at Belle*, *Phys. Rev. D* **97** (2018) 012004 [[1709.00129](#)].
- [16] LHCb collaboration, *Measurement of the ratio of branching fractions $\mathcal{B}(\bar{B}^0 \rightarrow D^{*+}\tau^-\bar{\nu}_\tau)/\mathcal{B}(\bar{B}^0 \rightarrow D^{*+}\mu^-\bar{\nu}_\mu)$* , *Phys. Rev. Lett.* **115** (2015) 111803 [[1506.08614](#)].
- [17] LHCb collaboration, *Measurement of the ratio of the $B^0 \rightarrow D^{*-}\tau^+\nu_\tau$ and $B^0 \rightarrow D^{*-}\mu^+\nu_\mu$ branching fractions using three-prong τ -lepton decays*, *Phys. Rev. Lett.* **120** (2018) 171802 [[1708.08856](#)].
- [18] LHCb collaboration, *Test of Lepton Flavor Universality by the measurement of the $B^0 \rightarrow D^{*-}\tau^+\nu_\tau$ branching fraction using three-prong τ decays*, *Phys. Rev. D* **97** (2018) 072013 [[1711.02505](#)].
- [19] HFLAV collaboration, *Averages of b-hadron, c-hadron, and τ -lepton properties as of 2018*, *Eur. Phys. J. C* **81** (2021) 226 [[1909.12524](#)].

- [20] MUON G-2 collaboration, *Final Report of the Muon E821 Anomalous Magnetic Moment Measurement at BNL*, *Phys. Rev. D* **73** (2006) 072003 [[hep-ex/0602035](#)].
- [21] MUON G-2 collaboration, *Measurement of the Positive Muon Anomalous Magnetic Moment to 0.46 ppm*, *Phys. Rev. Lett.* **126** (2021) 141801 [[2104.03281](#)].
- [22] M. Davier, A. Hoecker, B. Malaescu and Z. Zhang, *Reevaluation of the hadronic vacuum polarisation contributions to the Standard Model predictions of the muon $g - 2$ and $\alpha(m_Z^2)$ using newest hadronic cross-section data*, *Eur. Phys. J. C* **77** (2017) 827 [[1706.09436](#)].
- [23] A. Keshavarzi, D. Nomura and T. Teubner, *Muon $g - 2$ and $\alpha(M_Z^2)$: a new data-based analysis*, *Phys. Rev. D* **97** (2018) 114025 [[1802.02995](#)].
- [24] G. Colangelo, M. Hoferichter and P. Stoffer, *Two-pion contribution to hadronic vacuum polarization*, *JHEP* **02** (2019) 006 [[1810.00007](#)].
- [25] M. Hoferichter, B.-L. Hoid and B. Kubis, *Three-pion contribution to hadronic vacuum polarization*, *JHEP* **08** (2019) 137 [[1907.01556](#)].
- [26] M. Davier, A. Hoecker, B. Malaescu and Z. Zhang, *A new evaluation of the hadronic vacuum polarisation contributions to the muon anomalous magnetic moment and to $\alpha(m_Z^2)$* , *Eur. Phys. J. C* **80** (2020) 241 [[1908.00921](#)].
- [27] A. Keshavarzi, D. Nomura and T. Teubner, *$g - 2$ of charged leptons, $\alpha(M_Z^2)$, and the hyperfine splitting of muonium*, *Phys. Rev. D* **101** (2020) 014029 [[1911.00367](#)].
- [28] A. Kurz, T. Liu, P. Marquard and M. Steinhauser, *Hadronic contribution to the muon anomalous magnetic moment to next-to-next-to-leading order*, *Phys. Lett. B* **734** (2014) 144 [[1403.6400](#)].
- [29] FERMILAB LATTICE, LATTICE-HPQCD, MILC collaboration, *Strong-Isospin-Breaking Correction to the Muon Anomalous Magnetic Moment from Lattice QCD at the Physical Point*, *Phys. Rev. Lett.* **120** (2018) 152001 [[1710.11212](#)].
- [30] BUDAPEST-MARSEILLE-WUPPERTAL collaboration, *Hadronic vacuum polarization contribution to the anomalous magnetic moments of leptons from first principles*, *Phys. Rev. Lett.* **121** (2018) 022002 [[1711.04980](#)].
- [31] RBC, UKQCD collaboration, *Calculation of the hadronic vacuum polarization contribution to the muon anomalous magnetic moment*, *Phys. Rev. Lett.* **121** (2018) 022003 [[1801.07224](#)].
- [32] D. Giusti, V. Lubicz, G. Martinelli, F. Sanfilippo and S. Simula, *Electromagnetic and strong isospin-breaking corrections to the muon $g - 2$ from Lattice QCD+QED*, *Phys. Rev. D* **99** (2019) 114502 [[1901.10462](#)].
- [33] PACS collaboration, *Hadronic vacuum polarization contribution to the muon $g - 2$ with $2+1$ flavor lattice QCD on a larger than $(10 \text{ fm})^4$ lattice at the physical point*, *Phys. Rev. D* **100** (2019) 034517 [[1902.00885](#)].
- [34] FERMILAB LATTICE, LATTICE-HPQCD, MILC collaboration, *Hadronic-vacuum-polarization contribution to the muon's anomalous magnetic moment from four-flavor lattice QCD*, *Phys. Rev. D* **101** (2020) 034512 [[1902.04223](#)].
- [35] A. Gérardin, M. Cè, G. von Hippel, B. Hörz, H.B. Meyer, D. Mohler et al., *The leading hadronic contribution to $(g - 2)_\mu$ from lattice QCD with $N_f = 2 + 1$ flavours of $O(a)$ improved Wilson quarks*, *Phys. Rev. D* **100** (2019) 014510 [[1904.03120](#)].
- [36] C. Aubin, T. Blum, C. Tu, M. Golterman, C. Jung and S. Peris, *Light quark vacuum polarization at the physical point and contribution to the muon $g - 2$* , *Phys. Rev. D* **101** (2020) 014503 [[1905.09307](#)].

- [37] D. Giusti and S. Simula, *Lepton anomalous magnetic moments in Lattice QCD+QED*, *PoS LATTICE2019* (2019) 104 [[1910.03874](#)].
- [38] K. Melnikov and A. Vainshtein, *Hadronic light-by-light scattering contribution to the muon anomalous magnetic moment revisited*, *Phys. Rev. D* **70** (2004) 113006 [[hep-ph/0312226](#)].
- [39] P. Masjuan and P. Sanchez-Puertas, *Pseudoscalar-pole contribution to the $(g_\mu - 2)$: a rational approach*, *Phys. Rev. D* **95** (2017) 054026 [[1701.05829](#)].
- [40] G. Colangelo, M. Hoferichter, M. Procura and P. Stoffer, *Dispersion relation for hadronic light-by-light scattering: two-pion contributions*, *JHEP* **04** (2017) 161 [[1702.07347](#)].
- [41] M. Hoferichter, B.-L. Hoid, B. Kubis, S. Leupold and S.P. Schneider, *Dispersion relation for hadronic light-by-light scattering: pion pole*, *JHEP* **10** (2018) 141 [[1808.04823](#)].
- [42] A. Gérardin, H.B. Meyer and A. Nyffeler, *Lattice calculation of the pion transition form factor with $N_f = 2 + 1$ Wilson quarks*, *Phys. Rev. D* **100** (2019) 034520 [[1903.09471](#)].
- [43] J. Bijnens, N. Hermansson-Truedsson and A. Rodríguez-Sánchez, *Short-distance constraints for the $HLbL$ contribution to the muon anomalous magnetic moment*, *Phys. Lett. B* **798** (2019) 134994 [[1908.03331](#)].
- [44] G. Colangelo, F. Hagelstein, M. Hoferichter, L. Laub and P. Stoffer, *Longitudinal short-distance constraints for the hadronic light-by-light contribution to $(g - 2)_\mu$ with large- N_c Regge models*, *JHEP* **03** (2020) 101 [[1910.13432](#)].
- [45] V. Pauk and M. Vanderhaeghen, *Single meson contributions to the muon's anomalous magnetic moment*, *Eur. Phys. J. C* **74** (2014) 3008 [[1401.0832](#)].
- [46] I. Danilkin and M. Vanderhaeghen, *Light-by-light scattering sum rules in light of new data*, *Phys. Rev. D* **95** (2017) 014019 [[1611.04646](#)].
- [47] F. Jegerlehner, *The Anomalous Magnetic Moment of the Muon*, vol. 274, Springer, Cham (2017), [10.1007/978-3-319-63577-4](#).
- [48] M. Knecht, S. Narison, A. Rabemananjara and D. Rabetiarivony, *Scalar meson contributions to a μ from hadronic light-by-light scattering*, *Phys. Lett. B* **787** (2018) 111 [[1808.03848](#)].
- [49] G. Eichmann, C.S. Fischer and R. Williams, *Kaon-box contribution to the anomalous magnetic moment of the muon*, *Phys. Rev. D* **101** (2020) 054015 [[1910.06795](#)].
- [50] P. Roig and P. Sanchez-Puertas, *Axial-vector exchange contribution to the hadronic light-by-light piece of the muon anomalous magnetic moment*, *Phys. Rev. D* **101** (2020) 074019 [[1910.02881](#)].
- [51] G. Colangelo, M. Hoferichter, A. Nyffeler, M. Passera and P. Stoffer, *Remarks on higher-order hadronic corrections to the muon $g-2$* , *Phys. Lett. B* **735** (2014) 90 [[1403.7512](#)].
- [52] T. Blum, N. Christ, M. Hayakawa, T. Izubuchi, L. Jin, C. Jung et al., *Hadronic Light-by-Light Scattering Contribution to the Muon Anomalous Magnetic Moment from Lattice QCD*, *Phys. Rev. Lett.* **124** (2020) 132002 [[1911.08123](#)].
- [53] T. Aoyama, M. Hayakawa, T. Kinoshita and M. Nio, *Complete Tenth-Order QED Contribution to the Muon $g-2$* , *Phys. Rev. Lett.* **109** (2012) 111808 [[1205.5370](#)].
- [54] T. Aoyama, T. Kinoshita and M. Nio, *Theory of the Anomalous Magnetic Moment of the Electron*, *Atoms* **7** (2019) 28.
- [55] A. Czarnecki, W.J. Marciano and A. Vainshtein, *Refinements in electroweak contributions to the muon anomalous magnetic moment*, *Phys. Rev. D* **67** (2003) 073006 [[hep-ph/0212229](#)].

- [56] C. Grendiger, D. Stöckinger and H. Stöckinger-Kim, *The electroweak contributions to $(g - 2)_\mu$ after the Higgs boson mass measurement*, *Phys. Rev. D* **88** (2013) 053005 [[1306.5546](#)].
- [57] T. Aoyama et al., *The anomalous magnetic moment of the muon in the Standard Model*, *Phys. Rept.* **887** (2020) 1 [[2006.04822](#)].
- [58] S. Borsanyi et al., *Leading hadronic contribution to the muon magnetic moment from lattice QCD*, *Nature* **593** (2021) 51 [[2002.12347](#)].
- [59] M. Cè et al., *Window observable for the hadronic vacuum polarization contribution to the muon $g-2$ from lattice QCD*, *Phys. Rev. D* **106** (2022) 114502 [[2206.06582](#)].
- [60] C. Alexandrou et al., *Lattice calculation of the short and intermediate time-distance hadronic vacuum polarization contributions to the muon magnetic moment using twisted-mass fermions*, 6, 2022.
- [61] FERMILAB LATTICE, MILC, HPQCD collaboration, *Windows on the hadronic vacuum polarisation contribution to the muon anomalous magnetic moment*, *Phys. Rev. D* **106** (2022) 074509 [[2207.04765](#)].
- [62] D.M. Straub, *flavio: a Python package for flavour and precision phenomenology in the Standard Model and beyond*, 10, 2018.
- [63] D. Straub, P. Stangl, M. Kirk, J. Kumar, C. Niehoff, E. Gurler et al., *flav-io/flavio: v2.3.1*, Oct., 2021. [10.5281/zenodo.5543714](#).
- [64] M. Bordone, M. Jung and D. van Dyk, *Theory determination of $\bar{B} \rightarrow D^{(*)} \ell^- \bar{\nu}$ form factors at $\mathcal{O}(1/m_c^2)$* , *Eur. Phys. J. C* **80** (2020) 74 [[1908.09398](#)].
- [65] M. Bauer and M. Neubert, *Minimal Leptoquark Explanation for the $R_{D^{(*)}}$, R_K , and $(g - 2)_\mu$ Anomalies*, *Phys. Rev. Lett.* **116** (2016) 141802 [[1511.01900](#)].
- [66] Y. Cai, J. Gargalionis, M.A. Schmidt and R.R. Volkas, *Reconsidering the One Leptoquark solution: flavor anomalies and neutrino mass*, *JHEP* **10** (2017) 047 [[1704.05849](#)].
- [67] A. Crivellin, D. Müller and T. Ota, *Simultaneous explanation of $R(D^{(*)})$ and $b \rightarrow s \mu^+ \mu^-$: the last scalar leptoquarks standing*, *JHEP* **09** (2017) 040 [[1703.09226](#)].
- [68] D. Buttazzo, A. Greljo, G. Isidori and D. Marzocca, *B-physics anomalies: a guide to combined explanations*, *JHEP* **11** (2017) 044 [[1706.07808](#)].
- [69] D. Marzocca, *Addressing the B-physics anomalies in a fundamental Composite Higgs Model*, *JHEP* **07** (2018) 121 [[1803.10972](#)].
- [70] I. Bigaran, J. Gargalionis and R.R. Volkas, *A near-minimal leptoquark model for reconciling flavour anomalies and generating radiative neutrino masses*, *JHEP* **10** (2019) 106 [[1906.01870](#)].
- [71] S. Balaji and M.A. Schmidt, *Unified $SU(4)$ theory for the $R_{D^{(*)}}$ and $R_{K^{(*)}}$ anomalies*, *Phys. Rev. D* **101** (2020) 015026 [[1911.08873](#)].
- [72] A. Crivellin, D. Müller and F. Saturnino, *Flavor Phenomenology of the Leptoquark Singlet-Triplet Model*, *JHEP* **06** (2020) 020 [[1912.04224](#)].
- [73] S. Saad and A. Thapa, *Common origin of neutrino masses and $R_{D^{(*)}}$, $R_{K^{(*)}}$ anomalies*, *Phys. Rev. D* **102** (2020) 015014 [[2004.07880](#)].
- [74] S. Saad, *Combined explanations of $(g - 2)_\mu$, $R_{D^{(*)}}$, $R_{K^{(*)}}$ anomalies in a two-loop radiative neutrino mass model*, *Phys. Rev. D* **102** (2020) 015019 [[2005.04352](#)].
- [75] V. Gherardi, D. Marzocca and E. Venturini, *Low-energy phenomenology of scalar leptoquarks at one-loop accuracy*, *JHEP* **01** (2021) 138 [[2008.09548](#)].

- [76] M. Bordone, O. Catà, T. Feldmann and R. Mandal, *Constraining flavour patterns of scalar leptoquarks in the effective field theory*, *JHEP* **03** (2021) 122 [[2010.03297](#)].
- [77] J. Julio, S. Saad and A. Thapa, *Marriage between neutrino mass and flavor anomalies*, *Phys. Rev. D* **106** (2022) 055003 [[2203.15499](#)].
- [78] S.-L. Chen, W.-w. Jiang and Z.-K. Liu, *Combined explanations of B-physics anomalies, $(g - 2)_{e,\mu}$ and neutrino masses by scalar leptoquarks*, *Eur. Phys. J. C* **82** (2022) 959 [[2205.15794](#)].
- [79] W. Grimus and L. Lavoura, *A Discrete symmetry group for maximal atmospheric neutrino mixing*, *Phys. Lett. B* **572** (2003) 189 [[hep-ph/0305046](#)].
- [80] W. Grimus and L. Lavoura, *$S_3 \times Z_2$ model for neutrino mass matrices*, *JHEP* **08** (2005) 013 [[hep-ph/0504153](#)].
- [81] A. Blum, C. Hagedorn and M. Lindner, *Fermion Masses and Mixings from Dihedral Flavor Symmetries with Preserved Subgroups*, *Phys. Rev. D* **77** (2008) 076004 [[0709.3450](#)].
- [82] C.S. Lam, *Symmetry of Lepton Mixing*, *Phys. Lett. B* **656** (2007) 193 [[0708.3665](#)].
- [83] I. de Medeiros Varzielas and G. Hiller, *Clues for flavor from rare lepton and quark decays*, *JHEP* **06** (2015) 072 [[1503.01084](#)].
- [84] I. de Medeiros Varzielas and S.F. King, *$R_{K^{(*)}}$ with leptoquarks and the origin of Yukawa couplings*, *JHEP* **11** (2018) 100 [[1807.06023](#)].
- [85] I. de Medeiros Varzielas and J. Talbert, *Simplified Models of Flavourful Leptoquarks*, *Eur. Phys. J. C* **79** (2019) 536 [[1901.10484](#)].
- [86] L.J. Hall and M.B. Wise, *Flavor Changing Higgs - Boson Couplings*, *Nucl. Phys. B* **187** (1981) 397.
- [87] J.F. Donoghue and L.F. Li, *Properties of Charged Higgs Bosons*, *Phys. Rev. D* **19** (1979) 945.
- [88] H.E. Haber and Y. Nir, *Multiscalar Models With a High-energy Scale*, *Nucl. Phys. B* **335** (1990) 363.
- [89] I. Doršner, S. Fajfer, A. Greljo, J.F. Kamenik and N. Košnik, *Physics of leptoquarks in precision experiments and at particle colliders*, *Phys. Rept.* **641** (2016) 1 [[1603.04993](#)].
- [90] C. Hagedorn and M. Serone, *Leptons in Holographic Composite Higgs Models with Non-Abelian Discrete Symmetries*, *JHEP* **10** (2011) 083 [[1106.4021](#)].
- [91] C. Hagedorn and M. Serone, *General Lepton Mixing in Holographic Composite Higgs Models*, *JHEP* **02** (2012) 077 [[1110.4612](#)].
- [92] C. Jarlskog, *Commutator of the Quark Mass Matrices in the Standard Electroweak Model and a Measure of Maximal CP Nonconservation*, *Phys. Rev. Lett.* **55** (1985) 1039.
- [93] PARTICLE DATA GROUP collaboration, *Review of Particle Physics*, *PTEP* **2020** (2020) 083C01.
- [94] Z.-z. Xing, H. Zhang and S. Zhou, *Updated Values of Running Quark and Lepton Masses*, *Phys. Rev. D* **77** (2008) 113016 [[0712.1419](#)].
- [95] J. Aebischer, J. Kumar and D.M. Straub, *Wilson: a Python package for the running and matching of Wilson coefficients above and below the electroweak scale*, *Eur. Phys. J. C* **78** (2018) 1026 [[1804.05033](#)].
- [96] W. Porod, F. Staub and A. Vicente, *A Flavor Kit for BSM models*, *Eur. Phys. J. C* **74** (2014) 2992 [[1405.1434](#)].
- [97] W. Porod and F. Staub, *SPheno 3.1: Extensions including flavour, CP-phases and models beyond the MSSM*, *Comput. Phys. Commun.* **183** (2012) 2458 [[1104.1573](#)].

- [98] ATLAS collaboration, *Search for new phenomena in pp collisions in final states with tau leptons, b-jets, and missing transverse momentum with the ATLAS detector*, *Phys. Rev. D* **104** (2021) 112005 [[2108.07665](#)].
- [99] ATLAS collaboration, *Search for pairs of scalar leptoquarks decaying into quarks and electrons or muons in $\sqrt{s} = 13$ TeV pp collisions with the ATLAS detector*, *JHEP* **10** (2020) 112 [[2006.05872](#)].
- [100] CMS collaboration, *Search for new particles in events with energetic jets and large missing transverse momentum in proton-proton collisions at $\sqrt{s} = 13$ TeV*, *JHEP* **11** (2021) 153 [[2107.13021](#)].
- [101] E.E. Jenkins, A.V. Manohar and P. Stoffer, *Low-Energy Effective Field Theory below the Electroweak Scale: Operators and Matching*, *JHEP* **03** (2018) 016 [[1709.04486](#)].
- [102] BELLE-II collaboration, *Snowmass Whitepaper: The Belle II Detector Upgrade Program*, in *2022 Snowmass Summer Study*, 3, 2022 [[2203.11349](#)].
- [103] MUON G-2 collaboration, J. Grange et al., *Muon (g-2) Technical Design Report*, 1, 2015.
- [104] BELLE collaboration, *Search for lepton-flavor-violating tau-lepton decays to $\ell\gamma$ at Belle*, *JHEP* **10** (2021) 19 [[2103.12994](#)].
- [105] S. Banerjee et al., *Snowmass 2021 White Paper: Charged lepton flavor violation in the tau sector*, in *2022 Snowmass Summer Study*, 3, 2022 [[2203.14919](#)].
- [106] MEG collaboration, *Search for the lepton flavour violating decay $\mu^+ \rightarrow e^+\gamma$ with the full dataset of the MEG experiment*, *Eur. Phys. J. C* **76** (2016) 434 [[1605.05081](#)].
- [107] MEG II collaboration, *The Search for $\mu^+ \rightarrow e^+\gamma$ with 10^{-14} Sensitivity: the Upgrade of the MEG Experiment*, *Symmetry* **13** (2021) 1591 [[2107.10767](#)].
- [108] K. Hayasaka et al., *Search for Lepton Flavor Violating Tau Decays into Three Leptons with 719 Million Produced Tau+Tau- Pairs*, *Phys. Lett. B* **687** (2010) 139 [[1001.3221](#)].
- [109] SINDRUM collaboration, *Search for the Decay $\mu^+ \rightarrow e^+e^+e^-$* , *Nucl. Phys. B* **299** (1988) 1.
- [110] A. Blondel et al., *Research Proposal for an Experiment to Search for the Decay $\mu \rightarrow eee$* , 1, 2013.
- [111] COMET collaboration, *COMET Phase-I Technical Design Report*, *PTEP* **2020** (2020) 033C01 [[1812.09018](#)].
- [112] MU2E collaboration, L. Bartoszek et al., *Mu2e Technical Design Report*, 10, 2014. 10.2172/1172555.
- [113] BELLE collaboration, *Search for $B \rightarrow h\nu\bar{\nu}$ decays with semileptonic tagging at Belle*, *Phys. Rev. D* **96** (2017) 091101 [[1702.03224](#)].
- [114] BELLE-II collaboration, *The Belle II Physics Book*, *PTEP* **2019** (2019) 123C01 [[1808.10567](#)].
- [115] ALEPH, DELPHI, L3, OPAL, SLD, LEP ELECTROWEAK WORKING GROUP, SLD ELECTROWEAK GROUP, SLD HEAVY FLAVOUR GROUP collaboration, *Precision electroweak measurements on the Z resonance*, *Phys. Rept.* **427** (2006) 257 [[hep-ex/0509008](#)].
- [116] A. Crivellin, C. Greub, D. Müller and F. Saturnino, *Scalar Leptoquarks in Leptonic Processes*, *JHEP* **02** (2021) 182 [[2010.06593](#)].
- [117] *The International Linear Collider Technical Design Report - Volume 2: Physics*, 6, 2013.
- [118] FCC collaboration, *FCC-ee: The Lepton Collider: Future Circular Collider Conceptual Design Report Volume 2*, *Eur. Phys. J. ST* **228** (2019) 261.

- [119] M. Beneke and G. Buchalla, *The B_c Meson Lifetime*, *Phys. Rev. D* **53** (1996) 4991 [[hep-ph/9601249](#)].
- [120] ATLAS collaboration, *Search for additional heavy neutral Higgs and gauge bosons in the ditau final state produced in 36 fb^{-1} of pp collisions at $\sqrt{s} = 13 \text{ TeV}$ with the ATLAS detector*, *JHEP* **01** (2018) 055 [[1709.07242](#)].
- [121] A. Angelescu, D. Bećirević, D. Faroughy and O. Sumensari, *Closing the window on single leptoquark solutions to the B -physics anomalies*, *JHEP* **10** (2018) 183 [[1808.08179](#)].
- [122] J. Gratex, M. Hopfer and R. Zwicky, *Generalised helicity formalism, higher moments and the $B \rightarrow K_{J_K}(\rightarrow K\pi)\bar{\ell}_1\ell_2$ angular distributions*, *Phys. Rev. D* **93** (2016) 054008 [[1506.03970](#)].
- [123] P. Athron, C. Balázs, D.H.J. Jacob, W. Kotlarski, D. Stöckinger and H. Stöckinger-Kim, *New physics explanations of a_μ in light of the FNAL muon $g - 2$ measurement*, *JHEP* **09** (2021) 080 [[2104.03691](#)].
- [124] I. Bigaran and R.R. Volkas, *Reflecting on chirality: CP-violating extensions of the single scalar-leptoquark solutions for the $(g-2)_{e,\mu}$ puzzles and their implications for lepton EDMs*, *Phys. Rev. D* **105** (2022) 015002 [[2110.03707](#)].
- [125] Y. Kuno and Y. Okada, *Muon decay and physics beyond the standard model*, *Rev. Mod. Phys.* **73** (2001) 151 [[hep-ph/9909265](#)].
- [126] A. Crivellin, S. Najjari and J. Rosiek, *Lepton Flavor Violation in the Standard Model with general Dimension-Six Operators*, *JHEP* **04** (2014) 167 [[1312.0634](#)].
- [127] R. Kitano, M. Koike and Y. Okada, *Detailed calculation of lepton flavor violating muon electron conversion rate for various nuclei*, *Phys. Rev. D* **66** (2002) 096002 [[hep-ph/0203110](#)].
- [128] T.S. Kosmas, S. Kovalenko and I. Schmidt, *Nuclear muon-e-conversion in strange quark sea*, *Phys. Lett. B* **511** (2001) 203 [[hep-ph/0102101](#)].
- [129] R. Alonso, B. Grinstein and J. Martin Camalich, *Lifetime of B_c^- Constrains Explanations for Anomalies in $B \rightarrow D^{(*)}\tau\nu$* , *Phys. Rev. Lett.* **118** (2017) 081802 [[1611.06676](#)].
- [130] J. Aebischer and B. Grinstein, *Standard Model prediction of the B_c lifetime*, *JHEP* **07** (2021) 130 [[2105.02988](#)].
- [131] J. Aebischer and B. Grinstein, *A novel determination of the B_c lifetime*, *Phys. Lett. B* **834** (2022) 137435 [[2108.10285](#)].
- [132] A.G. Akeroyd and C.-H. Chen, *Constraint on the branching ratio of $B_c \rightarrow \tau\bar{\nu}$ from LEP1 and consequences for $R(D^{(*)})$ anomaly*, *Phys. Rev. D* **96** (2017) 075011 [[1708.04072](#)].
- [133] A.J. Buras, J. Girrbach-Noe, C. Niehoff and D.M. Straub, *$B \rightarrow K^{(*)}\nu\bar{\nu}$ decays in the Standard Model and beyond*, *JHEP* **02** (2015) 184 [[1409.4557](#)].
- [134] P. Arnan, D. Bećirevic, F. Mescia and O. Sumensari, *Probing low energy scalar leptoquarks by the leptonic W and Z couplings*, *JHEP* **02** (2019) 109 [[1901.06315](#)].
- [135] J. Fuentes-Martin, A. Greljo, J. Martin Camalich and J.D. Ruiz-Alvarez, *Charm physics confronts high- p_T lepton tails*, *JHEP* **11** (2020) 080 [[2003.12421](#)].
- [136] A. Angelescu, D.A. Faroughy and O. Sumensari, *Lepton Flavor Violation and Dilepton Tails at the LHC*, *Eur. Phys. J. C* **80** (2020) 641 [[2002.05684](#)].
- [137] A. Greljo, J. Martin Camalich and J.D. Ruiz-Álvarez, *Mono- τ Signatures at the LHC Constrain Explanations of B -decay Anomalies*, *Phys. Rev. Lett.* **122** (2019) 131803 [[1811.07920](#)].

- [138] ATLAS collaboration, *Search for High-Mass Resonances Decaying to $\tau\nu$ in pp Collisions at $\sqrt{s}=13$ TeV with the ATLAS Detector*, *Phys. Rev. Lett.* **120** (2018) 161802 [[1801.06992](#)].
- [139] CMS collaboration, *Search for a W' boson decaying to a τ lepton and a neutrino in proton-proton collisions at $\sqrt{s} = 13$ TeV*, *Phys. Lett. B* **792** (2019) 107 [[1807.11421](#)].
- [140] K.G. Chetyrkin, J.H. Kuhn and M. Steinhauser, *RunDec: A Mathematica package for running and decoupling of the strong coupling and quark masses*, *Comput. Phys. Commun.* **133** (2000) 43 [[hep-ph/0004189](#)].
- [141] F. Herren and M. Steinhauser, *Version 3 of RunDec and CRunDec*, *Comput. Phys. Commun.* **224** (2018) 333 [[1703.03751](#)].
- [142] M.L. Waskom, *seaborn: statistical data visualization*, *Journal of Open Source Software* **6** (2021) 3021.
- [143] P. Wintz, *Results of the SINDRUM-II experiment*, *Conf. Proc. C* **980420** (1998) 534.
- [144] SINDRUM II collaboration, *Improved limit on the branching ratio of $\mu \rightarrow e$ conversion on lead*, *Phys. Rev. Lett.* **76** (1996) 200.
- [145] SINDRUM II collaboration, *A Search for muon to electron conversion in muonic gold*, *Eur. Phys. J. C* **47** (2006) 337.
- [146] N. Teshima, *Status of the DeeMe Experiment, an Experimental Search for μ -e Conversion at J-PARC MLF*, *PoS NuFact2019* (2020) 082 [[1911.07143](#)].
- [147] A. Vicente, *Computer tools in particle physics*, 2015.
- [148] MUON (G-2) collaboration, *An Improved Limit on the Muon Electric Dipole Moment*, *Phys. Rev. D* **80** (2009) 052008 [[0811.1207](#)].
- [149] MUON G-2 collaboration, *The muon EDM in the g-2 experiment at Fermilab*, *EPJ Web Conf.* **118** (2016) 01005.
- [150] T.P. Goringe and D.W. Hertzog, *Precision Muon Physics*, *Prog. Part. Nucl. Phys.* **84** (2015) 73 [[1506.01465](#)].
- [151] A. Adelman et al., *Search for a muon EDM using the frozen-spin technique*, 2, 2021.
- [152] Y.K. Semertzidis et al., *Sensitive search for a permanent muon electric dipole moment*, in *KEK International Workshop on High Intensity Muon Sources (HIMUS 99)*, 12, 1999, DOI [[hep-ph/0012087](#)].
- [153] F.J.M. Farley, K. Jungmann, J.P. Miller, W.M. Morse, Y.F. Orlov, B.L. Roberts et al., *A New method of measuring electric dipole moments in storage rings*, *Phys. Rev. Lett.* **93** (2004) 052001 [[hep-ex/0307006](#)].
- [154] BELLE collaboration, *Measurement of the decay $B \rightarrow D\ell\nu_\ell$ in fully reconstructed events and determination of the Cabibbo-Kobayashi-Maskawa matrix element $|V_{cb}|$* , *Phys. Rev. D* **93** (2016) 032006 [[1510.03657](#)].
- [155] BELLE-II collaboration, *Semileptonic B-Meson decays at Belle II*, *PoS HQL2018* (2018) 012.
- [156] BELLE collaboration, *Measurement of the CKM matrix element $|V_{cb}|$ from $B^0 \rightarrow D^{*-}\ell^+\nu_\ell$ at Belle*, *Phys. Rev. D* **100** (2019) 052007 [[1809.03290](#)].
- [157] A. Crivellin, M. Hoferichter and P. Schmidt-Wellenburg, *Combined explanations of $(g-2)_{\mu,e}$ and implications for a large muon EDM*, *Phys. Rev. D* **98** (2018) 113002 [[1807.11484](#)].
- [158] R. Parker, C. Yu, W. Zhong, B. Estey and H. Müller, *Measurement of the fine-structure constant as a test of the standard model*, *Science* **360** (2018) 191.

- [159] L. Morel, Z. Yao, P. Cladé and S. Guellati-Khélifa, *Determination of the fine-structure constant with an accuracy of 81 parts per trillion*, *Nature* **588** (2020) 61.
- [160] NL-EEDM collaboration, *Measuring the electric dipole moment of the electron in BaF*, *Eur. Phys. J. D* **72** (2018) 197 [[1804.10012](#)].
- [161] C. Bobeth, M. Bordone, N. Gubernari, M. Jung and D. van Dyk, *Lepton-flavour non-universality of $\bar{B} \rightarrow D^* \ell \bar{\nu}$ angular distributions in and beyond the Standard Model*, *Eur. Phys. J. C* **81** (2021) 984 [[2104.02094](#)].
- [162] LHCb collaboration, *Measurement of the ratio of branching fractions $\mathcal{B}(B_c^+ \rightarrow J/\psi \tau^+ \nu_\tau)/\mathcal{B}(B_c^+ \rightarrow J/\psi \mu^+ \nu_\mu)$* , *Phys. Rev. Lett.* **120** (2018) 121801 [[1711.05623](#)].
- [163] A. Crivellin and J. Matias, *Beyond the Standard Model with Lepton Flavor Universality Violation*, in *1st Pan-African Astro-Particle and Collider Physics Workshop*, 4, 2022 [[2204.12175](#)].
- [164] F.F. Freitas, J. Gonçalves, A.P. Morais, R. Pasechnik and W. Porod, *On interplay between flavour anomalies and neutrino properties*, 6, 2022.
- [165] P. Minkowski, *$\mu \rightarrow e\gamma$ at a Rate of One Out of 10^9 Muon Decays?*, *Phys. Lett. B* **67** (1977) 421.
- [166] Y. Cai, J. Herrero-García, M.A. Schmidt, A. Vicente and R.R. Volkas, *From the trees to the forest: a review of radiative neutrino mass models*, *Front. in Phys.* **5** (2017) 63 [[1706.08524](#)].
- [167] J. Davighi, A. Greljo and A.E. Thomsen, *Leptoquarks with exactly stable protons*, *Phys. Lett. B* **833** (2022) 137310 [[2202.05275](#)].
- [168] I. Esteban, M.C. Gonzalez-Garcia, M. Maltoni, T. Schwetz and A. Zhou, *The fate of hints: updated global analysis of three-flavor neutrino oscillations*, *JHEP* **09** (2020) 178 [[2007.14792](#)].
- [169] J.A. Escobar and C. Luhn, *The Flavor Group $\Delta(6n^2)$* , *J. Math. Phys.* **50** (2009) 013524 [[0809.0639](#)].
- [170] R. de Adelhart Toorop, F. Feruglio and C. Hagedorn, *Discrete Flavour Symmetries in Light of T2K*, *Phys. Lett. B* **703** (2011) 447 [[1107.3486](#)].
- [171] R. de Adelhart Toorop, F. Feruglio and C. Hagedorn, *Finite Modular Groups and Lepton Mixing*, *Nucl. Phys. B* **858** (2012) 437 [[1112.1340](#)].
- [172] S.F. King, T. Neder and A.J. Stuart, *Lepton mixing predictions from $\Delta(6n^2)$ family symmetry*, *Phys. Lett. B* **726** (2013) 312 [[1305.3200](#)].
- [173] C. Hagedorn, A. Meroni and E. Molinaro, *Lepton mixing from $\Delta(3n^2)$ and $\Delta(6n^2)$ and CP*, *Nucl. Phys. B* **891** (2015) 499 [[1408.7118](#)].
- [174] G.-J. Ding, S.F. King and T. Neder, *Generalised CP and $\Delta(6n^2)$ family symmetry in semi-direct models of leptons*, *JHEP* **12** (2014) 007 [[1409.8005](#)].
- [175] C. Hagedorn and J. König, *Lepton and quark masses and mixing in a SUSY model with $\Delta(384)$ and CP*, *Nucl. Phys. B* **953** (2020) 114953 [[1811.09262](#)].
- [176] F. Feruglio, C. Hagedorn and R. Ziegler, *Lepton Mixing Parameters from Discrete and CP Symmetries*, *JHEP* **07** (2013) 027 [[1211.5560](#)].
- [177] M. Holthausen, M. Lindner and M.A. Schmidt, *CP and Discrete Flavour Symmetries*, *JHEP* **04** (2013) 122 [[1211.6953](#)].
- [178] M.-C. Chen, M. Fallbacher, K.T. Mahanthappa, M. Ratz and A. Trautner, *CP Violation from Finite Groups*, *Nucl. Phys. B* **883** (2014) 267 [[1402.0507](#)].

- [179] W. Grimus and M.N. Rebelo, *Automorphisms in gauge theories and the definition of CP and P*, *Phys. Rept.* **281** (1997) 239 [[hep-ph/9506272](#)].
- [180] G. Ecker, W. Grimus and H. Neufeld, *Spontaneous CP Violation in Left-right Symmetric Gauge Theories*, *Nucl. Phys. B* **247** (1984) 70.
- [181] G. Ecker, W. Grimus and H. Neufeld, *A Standard Form for Generalized CP Transformations*, *J. Phys. A* **20** (1987) L807.
- [182] H. Neufeld, W. Grimus and G. Ecker, *Generalized CP Invariance, Neutral Flavor Conservation and the Structure of the Mixing Matrix*, *Int. J. Mod. Phys. A* **3** (1988) 603.
- [183] W. Grimus and L. Lavoura, *A Nonstandard CP transformation leading to maximal atmospheric neutrino mixing*, *Phys. Lett. B* **579** (2004) 113 [[hep-ph/0305309](#)].
- [184] N. Assad, B. Fornal and B. Grinstein, *Baryon Number and Lepton Universality Violation in Leptoquark and Diquark Models*, *Phys. Lett. B* **777** (2018) 324 [[1708.06350](#)].
- [185] M. Bordone, C. Cornella, J. Fuentes-Martin and G. Isidori, *A three-site gauge model for flavor hierarchies and flavor anomalies*, *Phys. Lett. B* **779** (2018) 317 [[1712.01368](#)].
- [186] M. Bordone, C. Cornella, J. Fuentes-Martín and G. Isidori, *Low-energy signatures of the PS³ model: from B-physics anomalies to LFV*, *JHEP* **10** (2018) 148 [[1805.09328](#)].
- [187] S.F. King, *Twin Pati-Salam theory of flavour with a TeV scale vector leptoquark*, *JHEP* **11** (2021) 161 [[2106.03876](#)].
- [188] S.F. King, *A Simplified Twin Pati-Salam Theory of Flavour with a TeV Scale Vector Leptoquark*, in *21st Hellenic School and Workshops on Elementary Particle Physics and Gravity*, 3, 2022 [[2203.02236](#)].
- [189] J.D. Hunter, *Matplotlib: A 2d graphics environment*, *Computing in Science & Engineering* **9** (2007) 90.
- [190] T.A. Caswell, M. Droettboom, A. Lee, E.S. de Andrade, T. Hoffmann, J. Hunter et al., *matplotlib/matplotlib: Rel: v3.4.3*, Aug., 2021. 10.5281/zenodo.5194481.
- [191] LHCb collaboration, *Measurement of the ratios of branching fractions $\mathcal{R}(D^*)$ and $\mathcal{R}(D^0)$* , [2302.02886](#).
- [192] LHCb collaboration, R. Aaij et al., *Measurement of $R(D^*)$ with hadronic τ^+ decays at $\sqrt{s} = 13$ TeV by the LHCb collaboration*, 2023.
- [193] HFLAV collaboration, Y. Amhis et al., *Preliminary average of $R(D)$ and $R(D^*)$ for Winter 2023*, 2023.
- [194] B. Grzadkowski, M. Iskrzynski, M. Misiak and J. Rosiek, *Dimension-Six Terms in the Standard Model Lagrangian*, *JHEP* **10** (2010) 085 [[1008.4884](#)].
- [195] A. Alloul, N.D. Christensen, C. Degrande, C. Duhr and B. Fuks, *FeynRules 2.0 - A complete toolbox for tree-level phenomenology*, *Comput. Phys. Commun.* **185** (2014) 2250 [[1310.1921](#)].
- [196] T. Hahn, *Generating Feynman diagrams and amplitudes with FeynArts 3*, *Comput. Phys. Commun.* **140** (2001) 418 [[hep-ph/0012260](#)].
- [197] T. Hahn and M. Perez-Victoria, *Automatized one loop calculations in four-dimensions and D-dimensions*, *Comput. Phys. Commun.* **118** (1999) 153 [[hep-ph/9807565](#)].
- [198] T. Hahn, S. Paßehr and C. Schappacher, *FormCalc 9 and Extensions*, *PoS LL2016* (2016) 068 [[1604.04611](#)].
- [199] H.H. Patel, *Package-X: A Mathematica package for the analytic calculation of one-loop integrals*, *Comput. Phys. Commun.* **197** (2015) 276 [[1503.01469](#)].

- [200] P.W. Angel, Y. Cai, N.L. Rodd, M.A. Schmidt and R.R. Volkas, *Testable two-loop radiative neutrino mass model based on an $LLQd^cQd^c$ effective operator*, *JHEP* **10** (2013) 118 [[1308.0463](#)].
- [201] M. Nowakowski, E.A. Paschos and J.M. Rodriguez, *All electromagnetic form-factors*, *Eur. J. Phys.* **26** (2005) 545 [[physics/0402058](#)].
- [202] C. Itzykson and J.B. Zuber, *Quantum Field Theory*, International Series In Pure and Applied Physics, McGraw-Hill, New York (1980).
- [203] R. Mandal and A. Pich, *Constraints on scalar leptoquarks from lepton and kaon physics*, *JHEP* **12** (2019) 089 [[1908.11155](#)].
- [204] L. Calibbi, X. Marcano and J. Roy, *Z lepton flavour violation as a probe for new physics at future e^+e^- colliders*, *Eur. Phys. J. C* **81** (2021) 1054 [[2107.10273](#)].
- [205] A. Brignole and A. Rossi, *Anatomy and phenomenology of mu-tau lepton flavor violation in the MSSM*, *Nucl. Phys. B* **701** (2004) 3 [[hep-ph/0404211](#)].
- [206] R. Fleischer, R. Jaarsma and G. Tetlalmatzi-Xolocotzi, *Mapping out the space for new physics with leptonic and semileptonic $B_{(c)}$ decays*, *Eur. Phys. J. C* **81** (2021) 658 [[2104.04023](#)].
- [207] M. González-Alonso and J. Martin Camalich, *Global Effective-Field-Theory analysis of New-Physics effects in (semi)leptonic kaon decays*, *JHEP* **12** (2016) 052 [[1605.07114](#)].
- [208] HPQCD collaboration, *B-meson decay constants: a more complete picture from full lattice QCD*, *Phys. Rev. D* **91** (2015) 114509 [[1503.05762](#)].
- [209] J. Brod, M. Gorbahn and E. Stamou, *Two-Loop Electroweak Corrections for the $K \rightarrow \pi\nu\bar{\nu}$ Decays*, *Phys. Rev. D* **83** (2011) 034030 [[1009.0947](#)].
- [210] A. Bevan et al., *Standard Model updates and new physics analysis with the Unitarity Triangle fit*, 11, 2014.
- [211] Y. Grossman and Z. Ligeti, *Theoretical challenges for flavor physics*, *Eur. Phys. J. Plus* **136** (2021) 912 [[2106.12168](#)].
- [212] E. Goudzovski et al., *New physics searches at kaon and hyperon factories*, *Rept. Prog. Phys.* **86** (2023) 016201 [[2201.07805](#)].
- [213] S. Eidelman and M. Passera, *Theory of the tau lepton anomalous magnetic moment*, *Mod. Phys. Lett. A* **22** (2007) 159 [[hep-ph/0701260](#)].
- [214] BELLE-II collaboration, *First Results and Prospects for τ Lepton Physics at Belle II*, *PoS CHARM2020* (2021) 042 [[2111.13385](#)].
- [215] W. Bernreuther, L. Chen and O. Nachtmann, *Electric dipole moment of the tau lepton revisited*, *Phys. Rev. D* **103** (2021) 096011 [[2101.08071](#)].